Title
Perimeter exchange, hydrodynamics, and scalar transport in an estuary

Author
MacVean, Lissa Jillian

Publication Date
2010

Peer reviewed|Thesis/dissertation

Perimeter exchange, hydrodynamics, and scalar transport in an estuary

by

Lissa Jillian MacVean

A dissertation submitted in partial satisfaction
of the requirements for the degree of

Doctor of Philosophy

in

Engineering – Civil and Environmental Engineering

in the

GRADUATE DIVISION

of the

UNIVERSITY OF CALIFORNIA, BERKELEY

Committee in charge:

Professor Mark T. Stacey, Chair
Professor Fotini Katopodes Chow
Professor William E. Dietrich

Fall 2010

Perimeter exchange, hydrodynamics, and scalar transport in an estuary

by

Lissa Jillian MacVean

Abstract

Perimeter exchange, hydrodynamics, and scalar transport in an estuary

by

Lissa Jillian MacVean

Doctor of Philosophy in Engineering – Civil and Environmental Engineering

University of California, Berkeley

Professor Mark T. Stacey, Chair

The exchange of flow and scalars between an estuary and its perimeter controls the hydrodynamics in the estuary's fringes as well as along its axis. The flow and scalar fields in these two regions are coupled through tidally-driven lateral exchange. The physical processes that regulate this exchange operate on tidal timescales (hours, days) and respond to perturbations such as meteorological events and morphologic changes. The long-term, or residual, effects of this system of processes define the physical and ecological functioning of an estuary by controlling its morphology, salt field, and distribution of flows. In this dissertation research, field observations and theoretical analysis are used to explore the influence of an estuary's exchange with its perimeter on flow and scalar fields at tidal and residual timescales. In-situ measurements of flow velocity and water properties were collected in a macrotidal slough in the South San Francisco Bay lined by mudflats and recently connected to former salt ponds.

The interplay between tidal flows, bathymetry, and the longitudinal salt gradient define the pattern of stratification and mixing during a tidal cycle. The mechanism of tidal straining combined with the longitudinal baroclinic pressure gradient typically work together to enhance stratification on ebb tides and break it down through active mixing on flood tides. In the presence of sharp bathymetric transitions, such as the shoal-channel interface, the typical dynamics can be overwhelmed by local exchange. On flood tides, baroclinically-driven lateral circulation between the channel and mudflats freshens the surface layer in the channel, and reduces its velocity, producing a sub-surface velocity maximum. The input of buoyancy and the velocity shear result in stable stratification. On ebb tides, outflow from the mudflats transports trapped, high-salinity water over the freshening bottom layer, producing strong lateral shear and unstable stratification near the channel-mudflat boundary. As the ebb tide progresses and the mudflat outflow decelerates, the water column becomes well-mixed, and exhibits increased turbulent motions that result from shear and buoyant production. In short, lateral exchange in this tidal channel has reversed the classical pattern of stratification at the mudflat-channel boundary.

The transport of suspended sediment through an estuary is determined by an intricate system of physical, biological, and chemical processes. The physical transport dynamics are sometimes described by a balance of particle settling and turbulent resuspension, but in a tidal channel that exchanges with a complex perimeter, this balance is overly simple. Along the channel's axis, resuspension is the main mechanism elevating suspended sediment concentrations on the flood, and particle settling reduces concentrations when slack tide arrives. On the ebb, horizontal advection results in quickly recovering concentrations of sediment before turbulent stresses increase enough to suspend material from the bed. Tidal asymmetries reflect the role of the settling and scour lags, and make this balance an unsteady one where the net transport is landward. The tidal asymmetry reverses and increases in magnitude in response to wet weather as newly deposited material works its way down-estuary on successive ebb tides. In the presence of irregular bathymetry, such as near the channel-mudflat boundary and inside a breached salt pond, much of the sediment deposited in the shallows cannot be resuspended on the ebb due to strong friction opposing tidal forcing, resulting in net deposition. The combination of low concentrations of suspended sediment in the shallows on ebb tides with bathymetrically generated shear in local velocities produces the periodic occurrence of high sediment concentrations near the water surface and low concentrations near the bed. This establishes the importance of the role of lateral advection on ebb tides. The presence of complex bathymetry therefore requires that horizontal advection and unsteadiness be accounted for when describing the mechanisms driving transport of suspended sediment.

Understanding dispersion of scalars, such as salt and sediment, in an estuary over long timescales is critical for estuarine physics as well as managing the influence of humans on the environment. An irregular shoreline and accompanying bathymetry result in tidal trapping, a dispersive mechanism that arises from differences in phasing of flow velocities and scalar concentrations between the estuary's axis and its perimeter, as well as the variations in mixing between these regions. Classical theories describing the residual effects of tidal trapping assume that exchange between the estuary and perimeter is diffusive, but this framework neglects the role of tidal advection, such as the filling and draining of side-embayments, and the branching of flows into channel networks. A new theoretical framework is developed to represent estuarine dispersion from tidal trapping driven by advective exchange. The new advective framework compares well to observations.

To Mom, Dad, Lauren,
and Ryan.

Contents

List of Figures

List of Tables

Acknowledgements

Throughout my time in graduate school, I have had the great fortune of being a part of a vibrant and supportive research group of students, postdoctoral scholars, and professors in Environmental Fluid Mechanics and Hydrology at UC Berkeley. For their many hours of fearless and cheerful fieldwork in muddy Coyote Creek, my thanks go to, in order of appearance, Mary Cousins, Matt Reidenbach, Bryce Johnson, Maureen Downing-Kunz, Mark French, Katie Lundquist, Justin Case, Wayne Wagner, Rudi Schuech, Rusty Holleman, and Audric Collignon. They provided invaluable technical expertise, physical strength, humor, and encouragement. Their many specialized skills were not limited to programming and deploying oceanographic instruments, driving boats, and intuiting complex physics on sight, but fortunately also included dodging trains, rowing boats through waterless channels, rescuing boots from monstrously sticky mud, and removing colonies of insects from buoy lines. They have my fondest memories and my deepest gratitude.

In addition to their efforts in the field, my labmates also provided lively and illuminating discussions, fresh ideas, and most importantly, friendship. Special thanks go to Mary Cousins for her scientific prowess, construction skills, patience, baked goods, and finally, her spare bedroom. She and Katie Lundquist, Maureen Downing-Kunz, Megan Daniels, Rebecca Leonardson, Wayne Wagner, Rusty Holleman, and Rudi Schuech have been excellent friends.

I owe my sincerest gratitude to my adviser, Mark Stacey, who from the beginning has treated me like the scientist I hope to become. His enthusiasm and support have been unwavering. He consistently expressed confidence in my abilities and respect for my ideas, even when I felt he was mistaken to do so. He possesses the rare combination of technical brilliance and emotional insight, and I am grateful to have had the opportunity to learn from him. I sincerely thank Tina Katopodes Chow and Bill Dietrich for reading and improving this dissertation through their thoughtful feedback. In addition, I am grateful to Jim Hunt and Stanley Berger for their insight and guidance during classes and my qualifying exam.

Finally, I thank my family. They encouraged me and listened patiently while I anxiously anticipated each milestone. They celebrated every accomplishment with me, no matter how small. I am especially thankful for the support of my husband, Ryan Logan, who not only lived the experience of graduate school with me, but inspired me to pursue this degree in the first place. He encouraged me by his own example to find the occupation I would love and be challenged by, without compromise.

CHAPTER 1

Introduction

The interaction of estuarine flows with bathymetry is manifest across all temporal and spatial scales. Pritchard (1952) classified estuaries into three groups by geomorphological structure: drowned river valleys (coastal plain estuaries), fjords, and bar-built estuaries. Dyer (1973) mentions tectonically formed estuaries, one of "the rest" that do not fall readily into this categorization. To achieve tractability, regardless of morphology, the traditional approach to understanding estuarine physics has been to collapse the estuary onto the vertical-longitudinal plane, thus conceptually creating a laterally uniform channel connecting the river to the ocean. This simplification fostered seminal analyses of tidally-averaged estuarine dynamics, such as those by Hansen and Rattray (1965) and Chatwin (1976) for the residual salt and velocity fields. These residual quantities arise from an assumed steady balance between the pressure gradient (baroclinic and barotropic) and a vertical mixing term, which consists of an effective eddy viscosity acting on the subtidal shear. Since then, authors including Geyer et al. (2000) and Scully & Friedrichs (2007) have concluded that this simple balance – and the effective eddy viscosity in particular – does not adequately represent tidal processes resulting in ebb-flood asymmetries, which, along with the longitudinal salinity gradient, are responsible for exchange flow characteristics.

The interaction between tides and bathymetry contributes greatly to tidal asymmetries as well as to dispersion and mixing of momentum and mass on all scales. Returning to the complexities of the three-dimensional tidal cycle makes it possible to diagnose the processes that should be represented in effective parameterizations for subtidal dynamics. This dissertation explores one facet of the influence of bathymetry on estuarine physics: lateral exchange with the estuarine perimeter, and its implications for the transport and dispersion of salt and sediment.

The investigative approach is based on in-situ measurements of flows, water properties, and suspended sediment concentrations in South San Francisco Bay. The field site, described extensively in the next chapter, is a macrotidal slough that is lined by shallow mudflats and recently breached salt ponds. Turbulence timescales were captured, as well as diurnal and spring-neap tides, events, and seasons. The analyses presented here are based on these field observations, and augmented with theoretical explorations.

1.1 Effects of lateral exchange on stratification at tidal timescales

The first topic examined in this dissertation is the tidal variability of the salt field in a macrotidal channel that exchanges laterally with intertidal volumes along its perimeter. Complex patterns of stratification and turbulence have been observed in estuaries of all depths, from the fjords of Puget Sound (Geyer & Cannon 1982; Mickett et al. 2004) to the shallow channels that cut through San Francisco Bay's mudflats (Ralston & Stacey 2005). Understanding the tidal cycle dynamics is critical for identifying and describing mathematically the mechanisms driving the flow of water and transport of scalars, and also for properly parameterizing them on long timescales (MacCready & Geyer 2010).

The framework that we begin with is that of the tectonically produced, partially-mixed estuary, which describes San Francisco Bay in general (Dyer 1973, p.6), and Coyote Creek in particular. The partially-mixed estuary, as described by Dyer (1973), is characterized by the tidal oscillation of the salt wedge, which is opposed by friction at the estuary bottom. Bottom friction incites turbulence, which transforms the kinetic energy of eddies into potential energy as saline water is mixed upward and freshwater downward. The increase in salinity in the surface layer requires that a volume much greater than the river inflow be discharged from the estuary, and a two-layer system is created, as landward flow compensates for the total estuarine outflow. This exchange flow helps establish an along-estuary salinity gradient, where both the surface and bottom layers are fresher near the estuary head, and saltier near the mouth; the longitudinal salinity gradient is often assumed constant with depth.

The hydrodynamics and the motion of salt in an estuary are inextricably linked through the dependence of density on salt concentration. The intra-tidal nature of this linkage was described elegantly by Simpson et al. (1990) and is referred to generally as tidal straining. This common phenomenon arises from straining of the density gradient along the estuary's axis, which varies from freshwater at the head to ocean water at the mouth, by a vertical velocity gradient, or shear. The boundary-layer structure of the tidal flows produces shear, where velocity is low near the bed and higher near the surface, and this shear tilts the estuarine isopycnals. On the ebb tide, this tilting is stratifying (see the schematic in Figure 1-1), as the faster surface flows advect fresh water from up-estuary toward the mouth over the slower near-bed flows. On the flood tide, the tilting of isopycnals is destabilizing, as the faster surface flows transport heavier water toward the estuary head over the bottom flow, which is slower to increase its salinity. On the flood tides, the destabilizing effect of tidal straining produces convective instabilities (Burchard & Baumert 1998) which are mixed out by gravity. The canonical tidal cycle therefore consists of a well-mixed flood and stratified ebb.

The lateral structure of the flow and density distribution in an estuary is inhomogeneous due to transverse variations in depth (non-uniform frictional effects), curvature, and the rotation of the earth. The emphasis of this discussion, and the analysis presented in Chapter 3, is on the effects of variable depth across the estuary. Differential advection – where flow along the shallow margins of the estuary is slower than flow in the center – can laterally strain the longitudinal density gradient in a way that is analogous to the vertical tidal straining. The result on the flood tide is that the center contains the densest water, and a two-celled lateral

baroclinic circulation is induced with divergence at the bottom and convergence at the surface (Nunes & Simpson 1985), although with increased stratification, the straining of the vertical density gradient by laterally variable vertical velocities ($\frac{\partial \rho}{\partial z}\frac{\partial w}{\partial y}$) that is induced by the circulation counteracts the circulation itself (Lerczak & Geyer 2004). The reverse circulation is not observed on the ebb tide (Nunes & Simpson 1985), despite the opposite lateral straining of the along-channel density gradient, because the divergence at the surface carries fast, core water to the estuary's edges, flattening the transverse shear and reducing differential advection (Lerczak & Geyer 2004; Turrell et al. 1996).

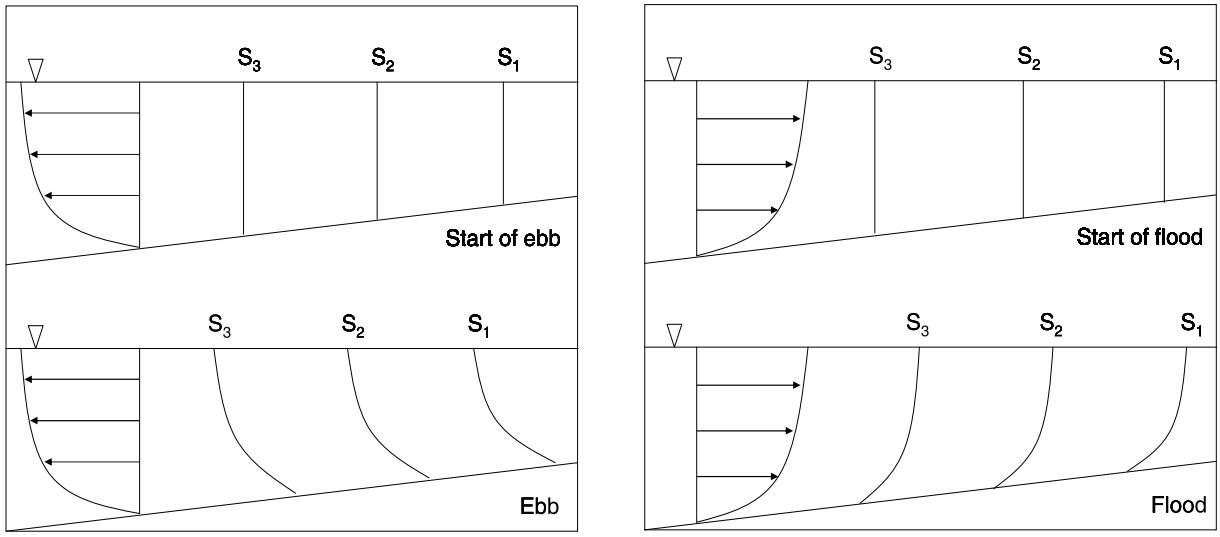

Figure 1-1: Conceptual model of tidal straining, adapted from Simpson et al (1990)
Isopycnals are marked by S, where $S_1 < S_2 < S_3$. The flood and ebb velocity profiles are shown by horizontal arrows. The straining of the longitudinal salinity gradient by the boundary-layer structure of the velocity profile leads to stable stratification on the ebb tide and unstable stratification on the flood.

Increasing the complexity of the lateral perimeter of the estuary and associated bathymetry results in less predictable interactions between bathymetry, stratification, and the tides. Distinct bathymetric features, such as mudflats and side-embayments, foster exchange that is less continuous than a gently sloping boundary. Discrete changes in frictional forcing, for example, require distinct flow regimes, and the interfaces between these regions host sharp (or frontal) lateral shears (Valle-Levinson & Atkinson 1999). Ralston & Stacey (2006) found that naturally sinuous subtidal channels in San Francisco Bay have a different orientation relative to the tidal pressure gradient than the shoals they bisect, causing shear at the shoal-channel interface. The shear in both the axial and transverse directions produces mid-water column turbulence – a feature unusual in an estuarine boundary layer, and with significant implications for the water column's ability to mix constituents into the surface layer.

Shear production of turbulence at bathymetric transitions is not the only way lateral dynamics affect vertical mixing and stratification over the tidal cycle. Lacy et al. (2003) found that shear

fronts can be generated on the flood tide from the release of flow trapped in a side-embayment into a channel, where it encounters flow that originated farther down-estuary, and that the trapping mechanism can be more important for lateral exchange than the local cross-sectional geometry. Once set up, differential advection increases the transverse density gradient as the flood tide progresses, but turbulence in the center of the channel arrests the lateral movement of the shear front. When the flood decelerates, the baroclinic exchange flow is able to vertically stratify the water column as it transports fresher, low-momentum water over faster, more saline flow. The competition between lateral baroclinicity set up by trapping and mixing from the destabilizing effects of tidal straining on the flood tide, as well as turbulence from tidal stirring, controls the occurrence of periodic density stratification in the channel. The late-flood stratification that results from this competition falls outside of the classical picture of the estuarine tidal cycle, and the unusual timing of the observed intermittent stratification has an important influence on the residual exchange flow (Stacey et al. 2001).

In addition to the lateral transport of salt, modifications to the momentum of flow at the estuary's axis by exchange with more frictional environments (shoals, mudflats, side-embayments) can be a very important factor driving stratification and mixing. Ralston & Stacey (2005) showed through observations and numerical modeling that baroclinic circulation over the shoals on flood tides – where saline flow diverges at the shoal-channel interface and fresher, low-momentum flow from the shoals converges at the surface – leads to a subsurface velocity maximum. This departure from the boundary layer structure of the along-channel velocity profile modifies traditional tidal straining and results in stable stratification on the flood tide above the maximum in velocity.

The objective of Chapter 3 of this dissertation is to examine the role of the channel-mudflat interface in producing the unexpected pattern of stable stratification on flood tides and unstable stratification on ebbs observed in spring 2006. Our data and analysis indicate that baroclinic exchange between channel and mudflat results in the observed stable stratification on the flood tide, while bathymetrically induced straining of the local horizontal density gradients produces sustained unstable stratification on the early ebb, which relaxes into a well-mixed water column for the duration of the ebb tide.

1.2 Bathymetric controls on tidal transport of suspended sediment

The field of estuarine sediment dynamics hosts many of the most complicated problems in estuarine physics today. Like salt, the presence of sediment in the water column can increase density, and gravity flows are a common occurrence in turbid estuaries (Talke et al. 2009). Layered on top of this influence on fluid density is the variability of the sediment itself and its behavior. Clay particles are disk-like rather than spherical with ionically charged surfaces, and therefore interact with each other electrostatically, exhibiting cohesion (Dyer 1986, p.202). Estuarine sediments are often high in clay, and South San Francisco Bay is no exception, with clay content exceeding 60% (Folger 1972). The flocculation of cohesive sediments changes their physical characteristics by creating aggregate particles, and size, density, and settling velocity are very distinct from those of the individual particles. Flocculation and destruction of sediment aggregates depend on material composition, total concentration of sediment (which determines the frequency of particle encounters), turbulent shear in the water column, and

salinity (Pejrup & Mikkelsen 2010), which increases the tendency to flocculate by interacting with the particles' surface charges. Salinity also affects sediment transport through stratification, which inhibits turbulent motions and limits vertical transport of sediment through the water column (Geyer 1993; Burchard & Baumert 1998). The condition of the bed influences sediment resuspension through consolidation of sediments after they have settled, and is subject to biological influences, from films to bioturbation, wetting and drying in intertidal regions, and temperature changes. In spite of these difficulties, estuarine sediment transport is extremely important for its connection to morphology – which influences all other physical estuarine processes – as well as its ability to transport contaminants such as heavy metals.

The dominant processes that drive sediment cycling through an estuary are freshwater flows, winds, and tides. These mechanisms operate on timescales of hours (diurnal tides, wind events), days (storms), weeks (spring-neap tides), and seasons. Like salt and momentum, the residual transport of sediment is most pertinent to understanding the workings of the estuary, its ecological functioning, and its response to perturbations including human activity. Patterns of scour and deposition that persist for weeks, months, and years define the estuary's morphology, which feeds back into the hydrodynamics. Also like salt and momentum, the residual distribution depends on the dynamics at all timescales *and their interactions*, from tidal to seasonal.

The exploration of sediment dynamics conducted as part of this dissertation has as its focus the influence of bathymetric irregularities and freshwater forcing on transport of suspended sediment through a tidal channel in South San Francisco Bay. This introduction, therefore, is intended to establish the broader patterns of sediment movement through the estuary, as the context into which our observations of morphologic and seasonal influences will fit. Schoellhamer (1996) used long-term observations to establish the large-scale cycling of sediment. They determined that sediment is supplied by the surrounding watersheds to the Bay during discrete events, and then redistributed among the perimeter habitats by the tides. The authors' measurements and analyses showed that during calm weather, the spring-neap cycle was responsible for the greatest variation in suspended sediment concentration at study sites in the South Bay. Suspended material accumulates in the water column as spring tide approaches, and up until two days after. The high barotropic velocities and very brief periods of slack water associated with the spring tide keep settling and bed consolidation to a minimum, creating conditions for high sediment loading. Conversely, approaching neap tide and up until two days following, the lower velocities and relatively long periods of slack water facilitate settling and discourage resuspension from the bed.

Winds play an important role in the dynamics on diurnal timescales by driving wind-wave resuspension in the shallow regions, which then exchange with the channels. In South San Francisco Bay, researchers have found that wind-waves are most effective at the shallowest tidal phases (Krone 1979), and transport is greatest on flood tides following a wind event at low water (Lacy et al. 1996; Brand et al. 2010). When these wind events are periodic, such as the warm weather afternoon winds from the northwest, they set up a predictable net sediment transport: a summer-time net landward sediment flux in the shallows, and bayward flux in the

channel, while in the winter, net sediment exchange is smaller and dependent on unpredictable rain and wind events (Schoellhamer 1996).

In Chapter 4, we explore the variability of suspended sediment concentrations over tidal and event timescales for environments with distinct bathymetries: near the channel center, at the channel-mudflat interface, and inside a breached salt pond. A simple but often first-order accurate approach to quantifying suspended sediment concentration in an estuary is to assume a mass balance of only particle settling and turbulent mass flux (Fugate & Friedrichs 2002). We explore the validity of this balance at our measurements sites with distinct morphologies and under different freshwater forcing conditions.

1.3 The influence of the perimeter on subtidal estuarine dispersion

The averaged scalar and flow fields in estuaries represent all of the physical processes that vary on turbulence, tidal (e.g. diurnal, spring-neap), and event timescales. Changes in the residual properties, such as salt excursion and exchange flow, over seasons and years are indicators of the health of the estuary, and of its response to changes in forcing due to such perturbations as meteorological events, anthropogenic activity, and climate change. The perturbation of interest here, and in Chapter 5, falls under the category of anthropogenic activity: the creation of new perimeter volumes along an estuary in the form of breached salt ponds. Longitudinal dispersion of salt is a parameter that is used to represent the tidally and cross-sectionally averaged transport mechanisms in an estuary such that the salt balance may be expressed by equating the advection of salinity (s) by river flow (U_f) with the product of the longitudinal dispersivity (K) and the along-channel salinity gradient:

$$U_f s = K \frac{\partial s}{\partial x} \tag{1-1}$$

Calculating K from data can be done by using several stations along an estuary (Banas et al. 2004), or by decomposing the salt and velocity fields through a cross-section (Fischer 1972; Fischer 1976; Fischer et al. 1979). The latter method separates velocity and salinity into cross-sectional averages (and variations from the average) and tidal averages (and variations around the average), then averages the product of velocity and salinity over the cross-section and tidally, resulting in a quantitative measure of the contribution of a number of mechanisms to the total longitudinal flux. The decomposition is performed on velocity and salinity values measured (or modeled) throughout a cross-section of an estuary over at least one 25-hour period, as done, for example, in the San Francisco Bay by Fram (2005), in the Hudson by Lerczak et al. (2006), and in the Columbia by Hughes and Rattray (1980). Each component of the sum represents a physical transport mechanism: advection by river flow, tidal trapping, Stokes drift, baroclinic steady exchange, and shear dispersion.

Fischer et al. (1979) categorize these mechanisms as either advective or dispersive. Advection by river flow, which represents the salt advected through the estuarine cross-section by freshwater inputs to the landward end of the estuary, is the unique advective term in this framework, while the effects of the remaining terms, which are often coupled, are aggregated by a single dispersion coefficient and treated as a cumulative dispersive process. In this

treatment, spreading due to all dispersive terms is represented as a dispersion coefficient multiplied by a salinity gradient, and in a steady balance, this term provides an up-estuary salt flux that balances the down-estuary advective flux from river flow.

The four dispersion terms in this decomposition vary temporally, cross-sectionally, or both. The cross-sectionally averaged, tidally varying terms are tidal trapping and Stokes drift. Tidal trapping occurs when the cross-sectionally averaged velocity and salinity signals are out of quadrature; when maximum cross-sectionally averaged salinity is not reached precisely at the end of the flood tide, the velocity and salinity signals are out of phase by an amount other than 90 degrees. Classically defined, tidal trapping results when dead zones, such as side embayments, small channels, and shoals, trap water and salt on the flood, releasing them on the ebb out of phase with the primary salinity front in the main channel. Stokes drift is especially important when the tidal range is large compared with the average depth, and arises when the cross-sectionally averaged velocity and the cross-sectional area of the flow are out of quadrature, yielding a non-zero net transport of water. The inertia of a tidal flow can delay slack velocity relative to high or low water as the tidal pressure gradient changes sign. The result is that the cross-sectional area of the flow on floods is greater than ebbs, producing a tidally averaged net landward flux of water. This flux sets up a complimentary barotropic pressure gradient directed down-estuary that balances the net transport of water.

The steady, cross-sectionally variable velocity and salinity fields interact to produce the baroclinic steady exchange term in the salt flux decomposition. This steady flux results from the residual flow and salinity fields and represents the tidally-averaged density forcing through the estuary. All remaining variability is encompassed by the shear dispersion term, which is variable in both time and space. This term accounts for an oscillatory, cross-sectionally varying velocity profile acting on the salinity field. Random phenomena that act on timescales shorter than the tidal period are captured by this term, such as rapid changes in wind forcing. In addition, other dispersive mechanisms interact with the shear dispersion term to produce a highly coupled system of fluxes.

Because of its direct dependence on the shape of the estuary's perimeter, tidal trapping is the focus of this discussion as well as Chapter 5. Tidal trapping has been observed in Holland by Schijf & Schonfeld (1953), in northern Australia by Wolanski & Ridd (1986) and Ridd et al. (1990), in Portugal's 0 Estuário do Mira by Blanton & Andrade (2001), and in Willapa Bay, Washington, by Banas & Hickey (2005), among others. Virtually every natural estuary has an irregular shoreline, providing many opportunities for dispersion from tidal trapping, particularly when these irregularities are spaced less than the length of one tidal excursion apart from one another (Geyer & Signell 1992).

The most notable analytical representation of dispersion from tidal trapping was done by Okubo (1973) for the cases of a unidirectional flow and an oscillating flow. The result of Okubo's work is a longitudinal dispersion coefficient from tidal trapping, K_{trap}, which depends on the geometry of the trap and channel, as well as a timescale for exchange between them. The timescale for exchange in Okubo's derivation represents a diffusive process, and requires that random, Fickian motions drive the transport of a scalar between the channel and the trap. There are limitations associated with this assumption. Fischer (1976) observed that the

exchange as represented by Okubo's framework is independent of the tides, which contradicts the observations made by Schijf & Schonfeld (1953). In Chapter 5, as well as a paper by MacVean & Stacey (2010), the difference in tidal trapping dispersion from advective (tidal) versus diffusive exchange is explored in detail and a new analytical formulation is presented and compared to observations.

1.4 Dissertation structure

The objective of this dissertation is to explore through in-situ measurements and theoretical analysis the impacts of the estuarine perimeter on dispersion at tidal and subtidal timescales. The experimental and analytical methods employed and a characterization of the study site are presented in Chapter 2. Chapter 3 explores the intra-tidal dynamics of stratification at our study site, and the influence of bathymetry. Sediment transport over tidal and seasonal timescales is presented in Chapter 4, and the effects of perimeter volumes on the sediment dynamics are investigated. In Chapter 5, an analytical framework for estuarine dispersion from tidal trapping over long timescales is presented, and the results are compared to measurements. Chapter 5 is adapted from published material (MacVean & Stacey 2010). Finally, Chapter 6 contains a summary of the salient findings of this research.

CHAPTER 2

Experimental methods and site characterization

The investigative approach employed for this dissertation research to discern the effects of the perimeter on estuarine flows consists of field studies and theoretical analysis. To collect in-situ measurements was a natural choice, given the opportunities for observing lateral exchange dynamics within the context of the ongoing, large-scale salt marsh restoration project in the South San Francisco Bay. This section details the collection and analyses of field measurements used to address the research questions in Chapters 3 and 4. A theoretical analysis based on these observational findings is presented in Chapter 5.

2.1 Site Description

2.1.1 South San Francisco Bay

The San Francisco Bay comprises a large and complex estuarine system, receiving freshwater primarily from the Delta, or the confluence of the Sacramento and San Joaquin rivers, and Pacific Ocean water through the Golden Gate (Figure 2-1). The San Francisco Bay supports a vast estuarine and marsh ecosystem, as well as providing water for local and remote human populations. The Bay is comprised of a series of embayments: Suisun Bay in the northeast, which receives freshwater from the Delta, San Pablo Bay at the north, Central Bay, which is connected to the Golden Gate, and finally South Bay. The southeasternmost reach of South Bay is the site of the experimental investigations described in this chapter.

The South San Francisco Bay is characterized by a shoal-channel bathymetry, with great shallow expanses (order 2 meters deep) bisected by a shipping channel of about 10 meters depth. Salinities and temperatures are controlled by mixing with the northern and Central bays which receive 90% of the system's freshwater from the Delta (Conomos 1979), as well as by local meteorological forcing. The climate in the San Francisco Bay region is Mediterranean, with wet winters and springs, and dry summers and falls. Precipitation in the Far South Bay typically totals 14.9 inches per year, with 88% occurring during October through March, and

12% during April through September (NOAA, National Climatic Data Center 2006). The years during which our studies were conducted: 2006 and 2008, were 12% wetter than normal and 31% drier than normal, respectively. Winter winds in the South Bay are episodic in response to days-long storm systems that move through the region. During the summer, solar heating of inland air masses produces winds that originate primarily from the northwest, with diurnal as well as seasonal variability (Conomos 1979; Lacy et al. 1996).

Figure 2-1: San Francisco Bay from space
NASA Image of the day: May 26, 2002

In addition to freshwater from exchange with the Delta through Central Bay and runoff from local watersheds, the South Bay receives the majority of the Bay's waste inputs, which are delivered from wastewater treatment plants through the discharge of low-salinity, high-temperature flows (Conomos 1979). The most significant is the San Jose/Santa Clara Water Pollution Control Plant, located on Artesian Slough, a tributary to Coyote Creek, and has the capacity to treat and discharge 167 million gallons per day (City of San Jose 2010). The average discharge from the pollution control plant was approximately 115 million gallons per day during the times of our experiments (Van Keuren 2008).

2.1.2 The South Bay Salt Pond Restoration Project and Coyote Creek

Presently in the South San Francisco Bay there is a major wetland restoration project underway, called the South Bay Salt Pond Restoration Project (SBR), whose mission it is to restore 15,100 acres of salt ponds to salt marsh habitat in the South San Francisco Bay (U.S. Fish & Wildlife

Service et al. 2006). The SBR goals are the formation of diverse wetland habitats, flood control for adjacent communities, and provision of wildlife-oriented public access and recreational space. The primary restoration activity has been opening salt ponds to tidal action by breaching the earth levees, allowing the marsh plain to accrete material, vegetation to establish, and the slow evolution into a viable habitat. The levee breaches reconnect thousands of acres of perimeter storage to the Bay for the first time in decades, providing an opportunity to observe the lateral exchange of the estuary with the perimeter.

The far southeastern tip of the San Francisco Bay narrows into a tidal slough called Coyote Creek (Figure 2-2). Much of the marsh land on either side of Coyote Creek was diked and converted to managed ponds for salt production in the early 1900s. The Island Ponds, which are a cluster of three salt ponds bordered by Coyote Creek on the south and Mud Slough on the north, were a pilot site of the SBR, and were among the earliest ponds to be breached as part of the restoration. In early March 2006, the levee separating the ponds from Coyote Creek was breached in five places (also shown in Figure 2-2), allowing the ponds to exchange with the Bay (via Coyote Creek) for the first time in almost a century.

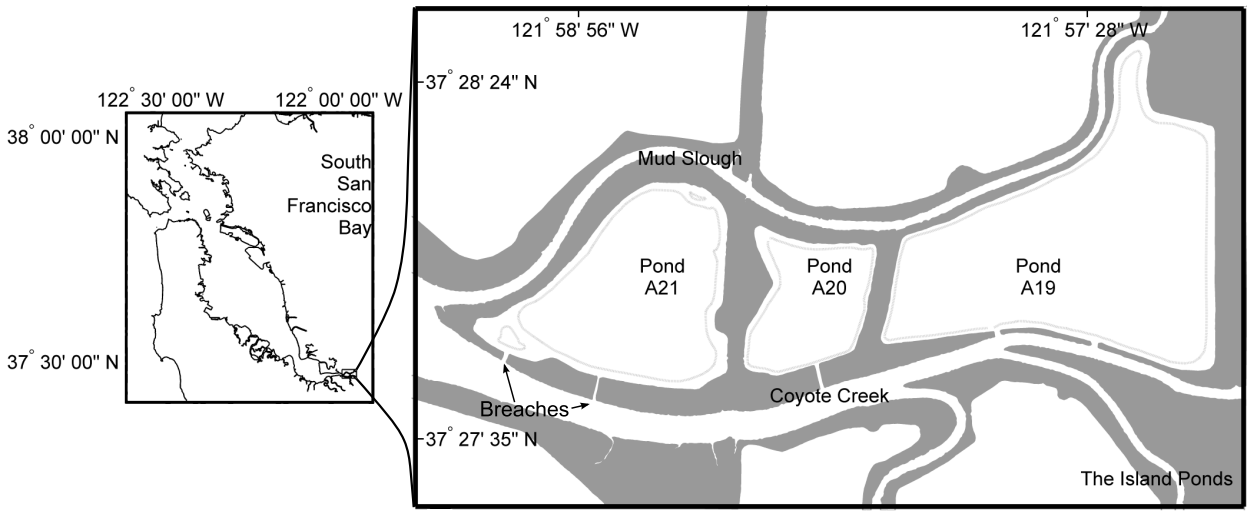

Figure 2-2: South Bay and the Island Ponds
The Island Ponds (right) were among the earliest salt ponds to be breached as part of the South Bay Salt Pond Restoration project. The levee separating them from Coyote Creek was breached in 5 places in March 2006.

The watershed that is drained by Coyote Creek is approximately 833 km^2 and contains 1078 km of creek and 293 km of engineered channels and culverts or stormdrains (Santa Clara Valley Urban Runoff Pollution Prevention Program n.d.). Coyote Creek originates in the Diablo Range, southeast of the Bay, and is impeded at the base of these hills by two dams that form the Anderson and Coyote reservoirs. The watershed is presently 50% forested and 50% developed, with 11% of its surface area impervious to water (Santa Clara Valley Urban Runoff Pollution Prevention Program n.d.). While flows in Coyote Creek were historically intermittent upstream of the lower tidally-influenced and perennial segments, and the whole system exhibited drastic seasonal flow variability, the combination of managed dam releases, increases

in impermeable area, and increased channel connectivity have resulted in reduced flow during springs and increased flow during falls, creating a flatter annual hydrograph (Grossinger et al. 2006).

Sediment entering San Francisco Bay from local tributaries is becoming more important relative to the sediment loading from the Sacramento and San Joaquin River Delta, which has been decreasing over time to a current level of 60% (McKee et al. 2006). Current sediment yields from the Coyote Creek watershed are low compared with the rest of the San Francisco Bay area: 35 tonnes km^{-2} yr^{-1}, whereas the regional average is 155 tonnes km^{-2} yr^{-1}, in part due to trapping behind the river's two dams (McKee & Lewicki 2009). Annual variability of suspended sediment concentration recorded by the USGS in creeks throughout the Bay area is best explained by peak discharge, however this does not indicate that other factors (e.g. slope, lithology, land use) are unimportant, but that adequate data are not yet available to improve regression analyses by including these variables (McKee & Lewicki 2009). Monitoring by the USGS of suspended sediment loads from the Coyote Creek watershed (at Highway 237 in Milpitas) has been performed only since 2004, which is not long enough to determine long-term trends within the context of the growth of South Bay cities. Construction in the region of the Coyote Creek watershed closest to the Bay took place in the 1960s and 1970s, and the uplands continue to be actively developed. Based on this, it is presumed that long-term trends would indicate a decrease in suspended sediment in Coyote Creek in recent decades since construction activities are significant only upstream of the Anderson and Coyote dams.

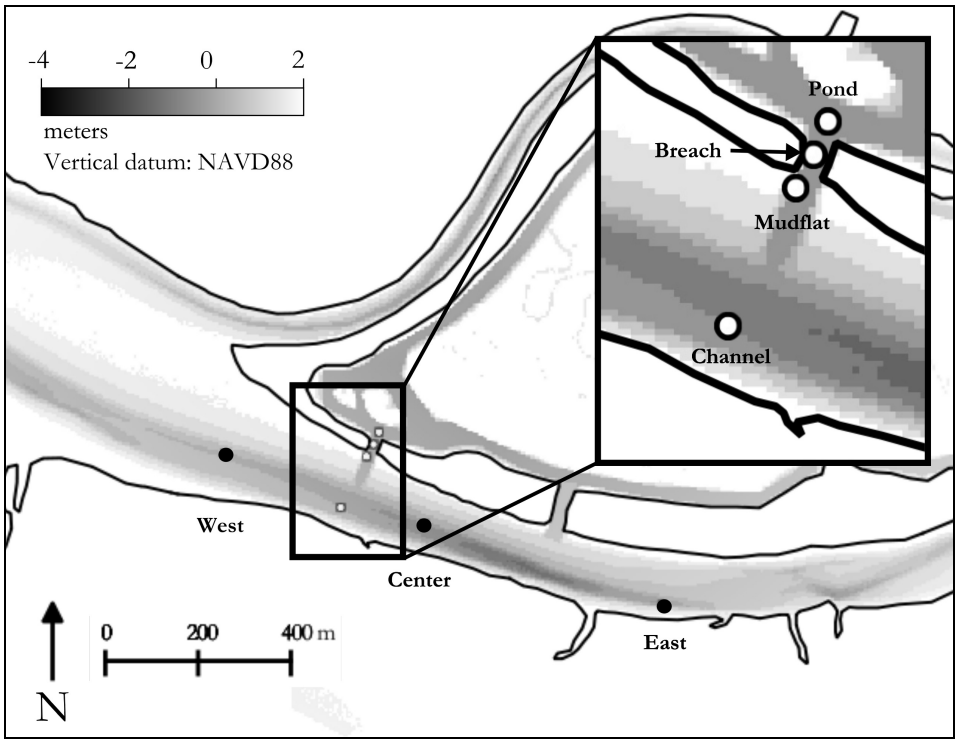

Figure 2-3: Coyote Creek bathymetry and experiment mooring locations
Spring 2006: black circles, west, center, east (left to right)
Fall 2006: white circles and inset, Channel, Mudflat, Breach, Pond (bottom to top)

The reach of Coyote Creek outside of the westernmost Island Pond (Pond A21) is the study site for the investigations into the effects of lateral exchange between an estuary and perimeter volumes undertaken as part of this dissertation. Coyote Creek is macrotidal, with a tidal range of 2.5 meters on neap tides, and 3.5 meters on springs. The dominant tidal frequencies are M2 and K1, resulting in twice daily, unequal tides. The width of Coyote Creek at this location is approximately 200 meters, including intertidal regions. The slough consists of a main channel with an average depth of 3 meters, broad intertidal mudflats on the northern border of Coyote Creek, and narrow intertidal mudflats on the southern border. Best-available bathymetry is shown in Figure 2-3. The widths of the mudflats vary along the length of Coyote Creek, but in the vicinity of the Island Ponds, our observations indicate that the mudflats are 50-70 meters wide to the north, and 20-30 meters wide to the south. Figure 2-4 shows the cross-section of Coyote Creek at the western end of the Island Ponds (location shown in inset). The black dots are measurements made by the US Army Corps of Engineers, and the line defining the cross-section is an approximate reflection of the bathymetry between measurements, based on visual inspection of the site at low-water. The elevations are shown relative to the North American Vertical Datum of 1988 (NAVD 88). The dotted portion of the cross-section, between 60 and 110 cross-channel meters, appears incongruous but reflects schematically visual observations made during boat-mounted field work. The southern mudflat approximated here is narrow compared to those to the north, and connected to the marsh above and the channel below by sharp transitions.

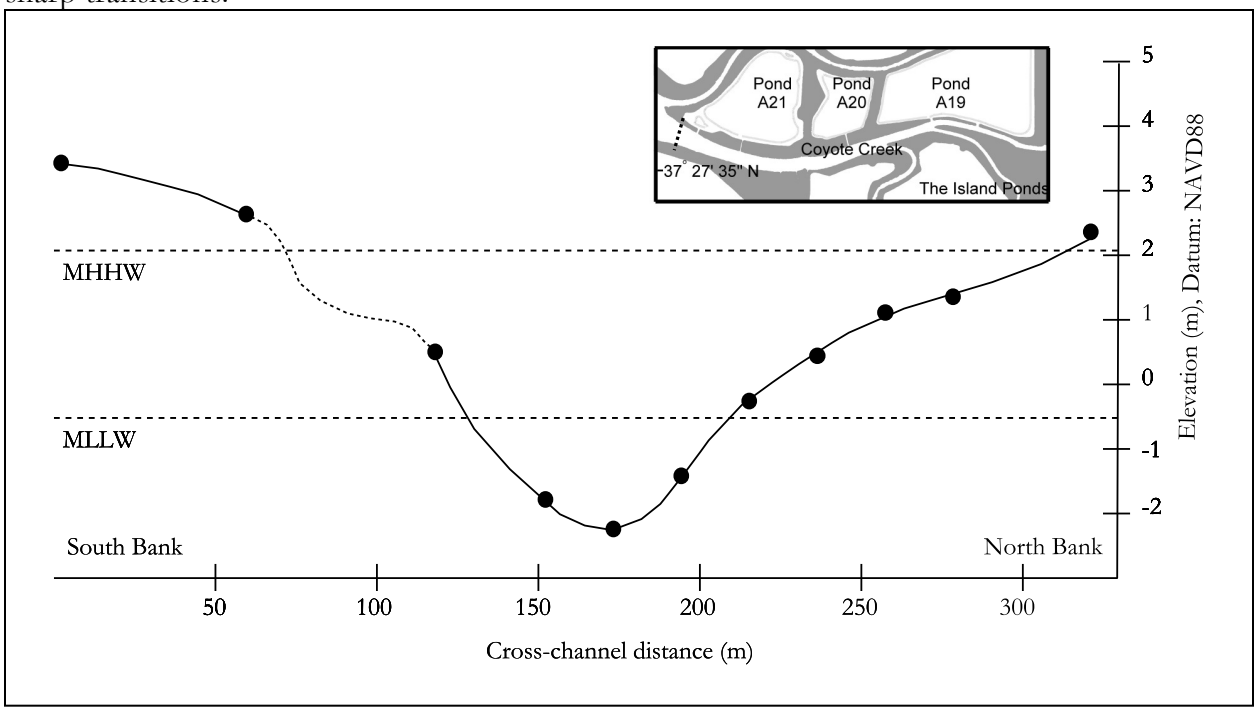

Figure 2-4: Channel cross-section.
Black dots are measurements made by USACE at the location shown by the dotted line in the inset (at the western end of the Island Ponds). The vertical datum is NAVD88, and the locations of MLLW and MHHW are shown for comparison. The line defining the cross-section was inferred by visual inspection at the site and is approximate. The dotted line between 60 and 110 cross-channel meters is used to call attention to the southern mudflat. Detailed bathymetry data are not available here, but visual observations of the site indicate that the mudflat is narrow with a gentle slope, connected to the marsh above and the channel below by sharp transitions.

Samples of bed sediment were not collected from the mudflats nor from the channel bottom, but at low tide, the mudflats appeared to be unvegetated, with coarse material resembling shells visible at the surface. Swaths of cordgrass line the intertidal zone to the north and south, with pickleweed, peppergrass, and alkali bulrush higher in the marshes and levees (per visual inspection as well as Duke et al. 2006; HT Harvey & Associates 2008). Although the marsh surface is above mean higher high water (MHHW), it is permeated by intertidal channels. Figures 2-5 and 2-6 show photographs taken on May 11, 2008 of the exposed flats and the vegetation visible from the water surface. The images were taken at 10:27am and 10:40am, when the water level was 1.38 meters relative to vertical datum NAVD88 (as in Figure 2-4), and 0.86 meters above mean lower low water (MLLW). At low tide (not pictured), greater extents of intertidal mudflats were visible, although the extremely shallow depths precluded boat-based access to all but the channel center. While the southern mudflats are certainly narrower than those to the north of Coyote Creek, this image shows that they are present, and analyses presented in later chapters indicate that they, in addition to the northern mudflats and breached salt ponds, are dynamically important.

Figure 2-5: Photographs of partially exposed mudflats on the north border of Coyote Creek
Facing the northern border of Coyote Creek. May 11, 2008, 10:40am, 100 m west of the western breach in Pond A21. Broad mudflats are visible, as well as cordgrass, and dead vegetation beyond it.

Figure 2-6: Photographs of partially exposed mudflats on the south border of Coyote Creek
Facing southern border of Coyote Creek. May 11, 2008, 10:27am, 100 m west of and across the channel from the western breach in Pond A21.

2.2 Field data collection

We conducted field measurements of velocity, salinity, temperature, pressure, and optical backscatter (a surrogate for suspended sediment concentration) near the Island Ponds in the spring and fall of 2006, as well as the summer of 2008. Data were collected via deployments of moored instruments as well as by boat-mounted surveys. The instruments used for these experiments are: acoustic Doppler current profilers for measuring profiles of velocity (ADCPs, by RD Instruments, 1200 kHz and 600 kHz, sampling in water mode 1), acoustic Doppler velocimeters for measuring velocity at a point (ADVs, by Sontek and Nortek), conductivity-temperature-depth sensors (CTDs, by RBR and Seabird Instruments), and optical backscatter sensors (OBSs, by D&A Instruments and Seapoint). Moored deployments consisted of mounting instruments to aluminum frames, weighting them with lead, and lowering them into the water from a boat. Schematics of the instruments attached to their frames are shown in Figures 2-7 and 2-8. On the ADV frames, the CTD/OBS pairs were placed at an elevation equal to that of the ADV sampling volumes. The frames were marked and recovered via surface floats. A 1200 kHz RDI ADCP in a down-looking configuration, and CTDs (RBR and Seabird Instruments) as well as OBS sensors (D&A Instruments), were used for the boat-mounted surveys.

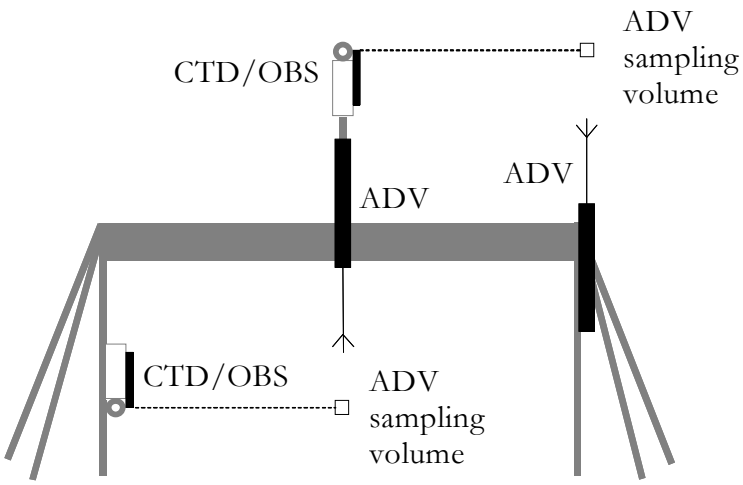

Figure 2-7: ADV Frame
The aluminum AVD frames were outfitted with 2 CTD/OBS pairs and two ADVs. The sampling volumes of the ADVs were at the same elevations as the CTD/OBS pairs.

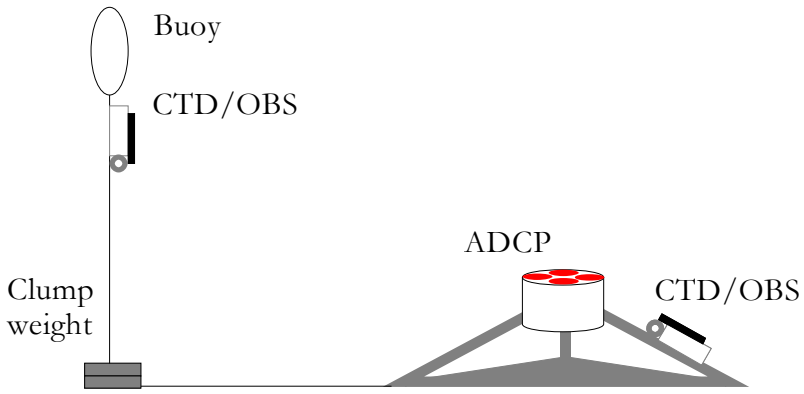

Figure 2-8: ADCP Frame
The triangular ADCP frames were outfitted with an up-looking ADCP and a CTD/OBS pair. The top CTD/OBS pair was attached to the buoy line just beneath the surface float. The lead clump weight was placed at a distance from the frame sufficient to prevent the buoy line from crossing the ADCP's sensor beams.

2.2.1 Moored experiments

The spring 2006 study

Our instruments were deployed from March to May 2006 along the thalweg of Coyote Creek outside of the western-most Island Pond (Figure 2-3). The objective of this experiment was to characterize the longitudinal structure of flows and scalar concentrations (salt, temperature, and suspended sediment). Conditions during this experiment were exceptionally wet. During March – May 2006, 9.4 inches of precipitation were recorded, which is 150% of normal for that time period. Daily streamflow was measured at the United States Geological Survey's gaging station number 11172175 on Coyote Creek (Figure 2-9).

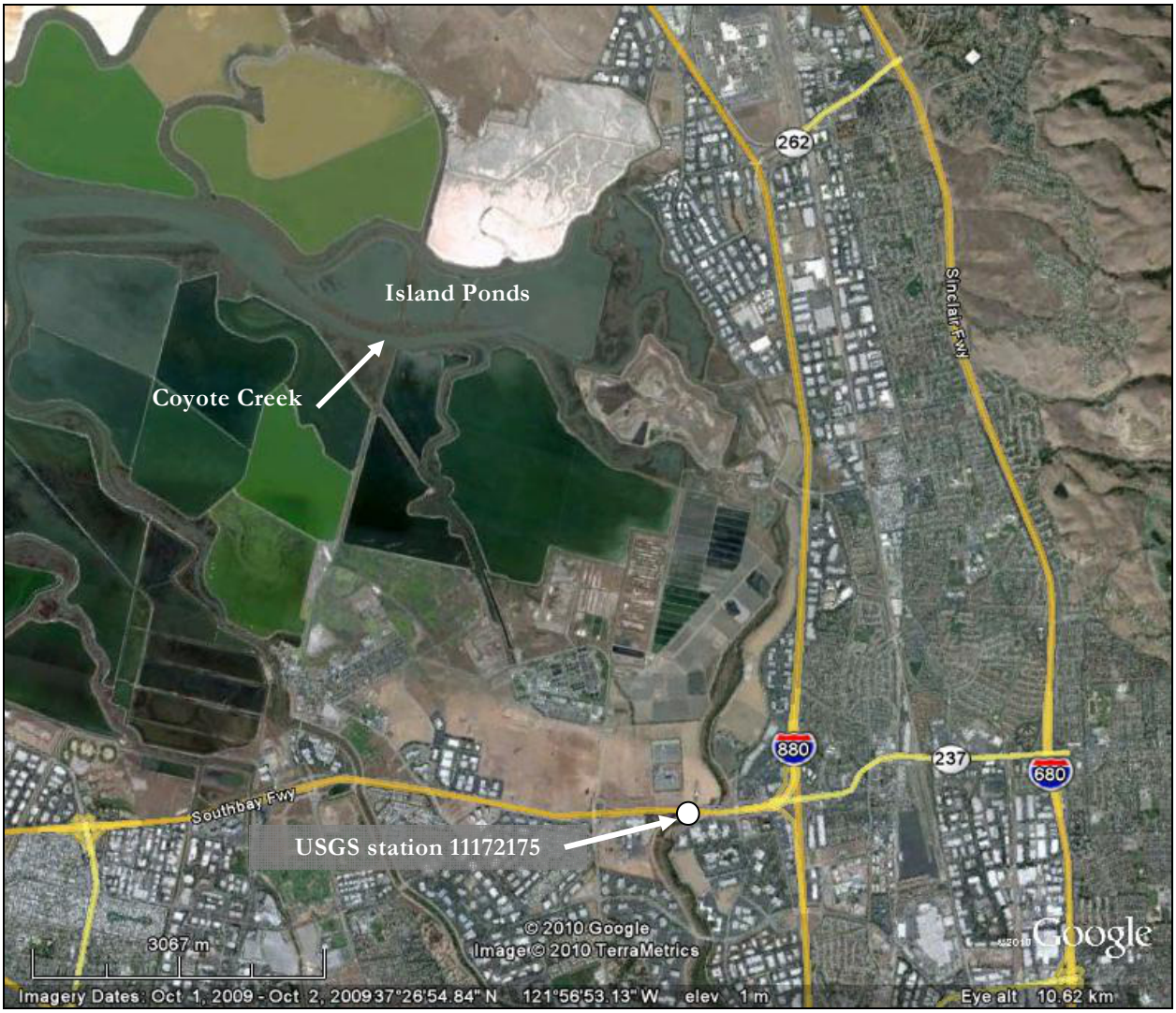

Figure 2-9: USGS Streamflow gaging station 11172175 Coyote Creek above Highway 237, at Milpitas, CA
Location: 37°25'20" N, 121°55'35" W
Gaging station is shown by the white circle.
Image from Google Earth

Figure 2-10 shows streamflow in cubic feet per second (top panel), daily precipitation in inches measured by the National Oceanographic and Atmospheric Administration (NOAA) at Newark, California (middle panel), and the wind velocity in miles per hour and direction from which it originates (bottom panel), measured by NOAA in Palo Alto, California.

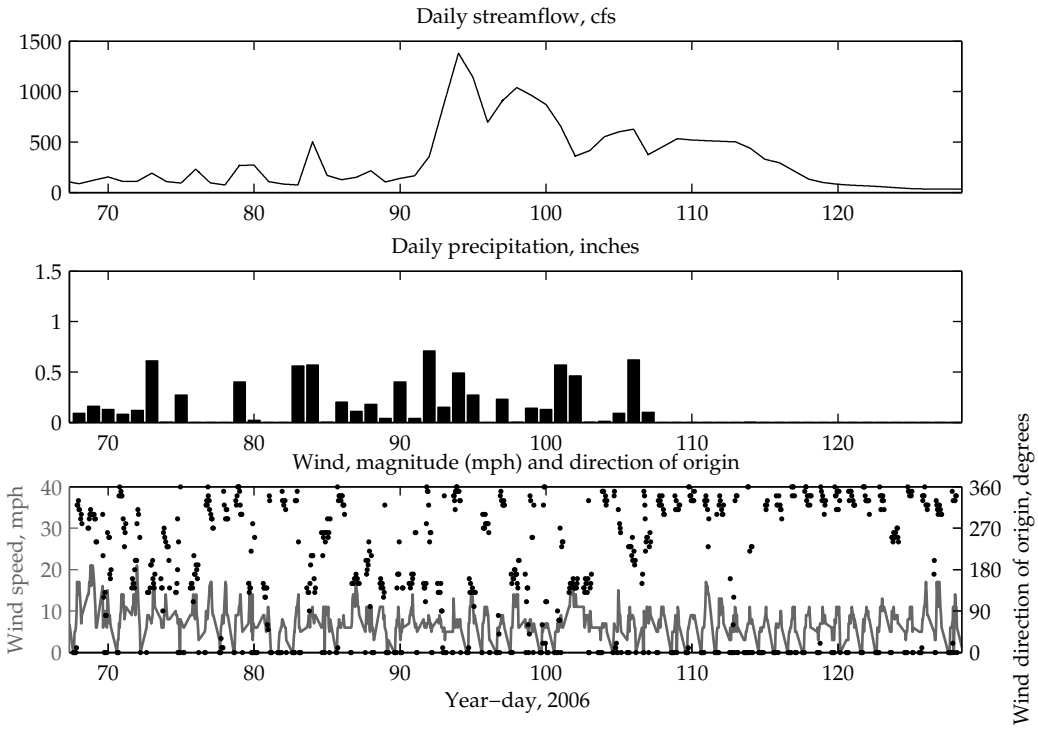

Figure 2-10: Meteorological conditions, spring 2006
Coyote Creek streamflow in cubic feet per second (top panel), precipitation in inches (middle panel), and wind magnitude in miles per hour on left axis, and direction of origin in degrees on right axis (bottom panel).

Three instrument stations were deployed (east, center, west), with the configurations presented in Tables 2-1 – 2-3.

Table 2-1: East station (37°27.582'N,121°58.723'W)

Instrument	Brand (Serial number)	Sensor Elevation	Burst frequency	Burst duration	Sampling frequency
ADV	Sontek processor/probe (G130/A342)	0.5 meters above the bed (mab)	15 minutes	48 seconds	10 Hz
ADV	Nortek (4132)	1.5 mab	15 minutes	30 seconds	16 Hz
CTD/OBS	Seabird Seacat 19/D&A Instruments (2837/unknown)	0.5 mab	15 minutes	30 seconds	4 Hz
CTD/OBS	Seabird Microcat/D&A Instruments (1542/ unknown)	1.5 mab	15 minutes	48 seconds	4 Hz

Both ADVs deployed at the east station (Table 2-1) were programmed to sample at their maximum frequency: 10 and 16 Hz for the Sontek and Nortek, respectively. Although the sampling rates differ, the burst duration was adjusted so that the total number of samples per burst for each ADV would be equivalent. We also note that the serial numbers for the D&A

optical backscatter sensors were not recorded during this spring 2006 deployment. This did not present a problem as the sensors were attached to CTDs, through which all OBS data were conveyed.

Table 2-2: Center station (37°27.677'N, 121°59.064'W)

Instrument	Brand (Serial number)	Sensor Elevation	Burst frequency	Burst duration	Sampling frequency
ADV	Sontek processor/probe (G149/A349)	0.5 mab	15 minutes	30 seconds	16 Hz
ADV	Nortek (4142)	1.5 mab	15 minutes	30 seconds	16 Hz
CTD/OBS	Seabird Microcat/D&A Instruments (1617/ unknown)	0.5 mab	15 minutes	30 seconds	4 Hz
CTD/OBS	RBR/D&A Instruments (9621/ unknown)	1.5 mab	10 minutes	15 seconds	4 Hz

The Seabird CTD mounted at 0.5 mab at the center station stopped collecting reliable salinity data after year-day 75, while the temperature and depth readings continued. This suggests that the conductivity cell filled with mud or other debris, preventing accurate measurements of salinity, while the pressure and temperature sensors (located externally) remained unaffected. The batteries in the RBR CTD mounted at 1.5 mab were depleted after 6 weeks of the 8 week duration.

Table 2-3: West station (37°27.760'N, 121°59.350'W)

Instrument	Brand (Serial number)	Sensor Elevation	Burst frequency	Burst duration	Sampling frequency
600 kHz ADCP	RDI (1161)	Up-looking, on bottom	3 minutes	3 minutes	1/3.6 Hz (water mode 1)
CTD/OBS	RBR/D&A Instruments (10364/ unknown)	0.3 mab	15 minutes	30 seconds	4 Hz
CTD/OBS	RBR/D&A Instruments (9620/ unknown)	0.5 meters below the surface	15 minutes	30 seconds	4 Hz

The fall 2006 study

From October – December 2006 our instrument frames were moored in a lateral configuration across Coyote Creek, through the western-most breach of the western-most pond, and into salt pond A21 (Figure 2-3). The objective of this study was to capture lateral exchange of flows and scalars between the pond and the channel. Conditions during the fall moored experiment were 30% drier than normal, with 3.4 inches of precipitation falling during October – December 2006. Figure 2-11 shows Coyote Creek streamflow (top panel), precipitation (middle panel), and wind speed and direction of origin (bottom panel) with the same axes as

Figure 2-10 for comparison with the spring experiment. Streamflow, precipitation, and wind speed were markedly lower during the fall experiment.

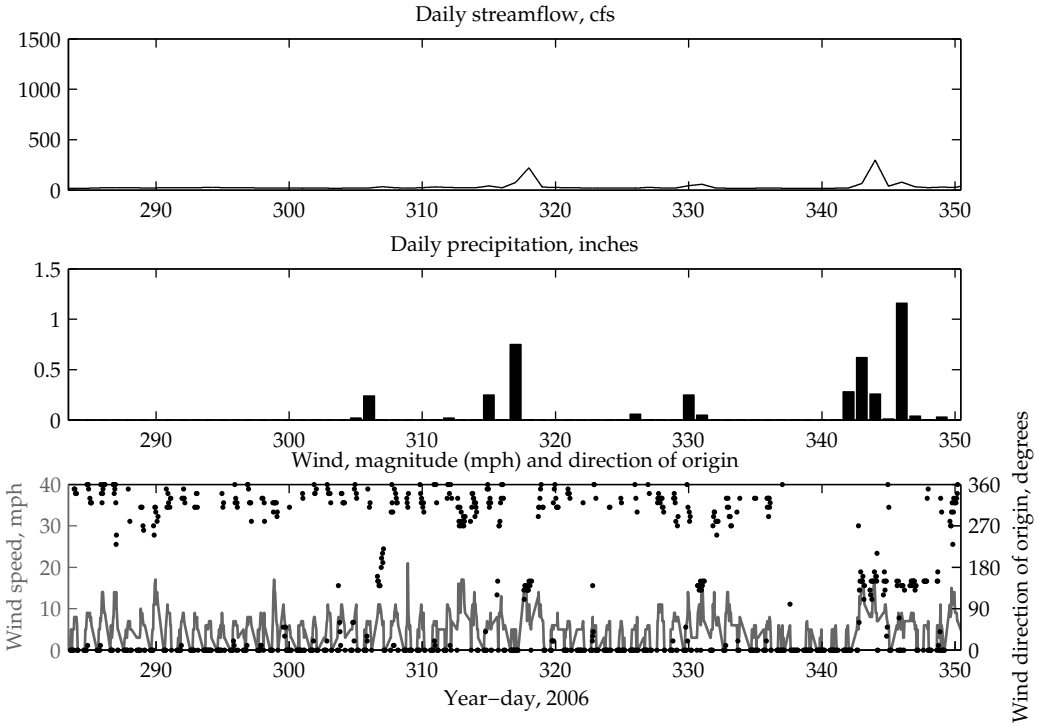

Figure 2-11: Meteorological conditions, fall 2006
Coyote Creek streamflow in cubic feet per second (top panel), precipitation in inches (middle panel), and wind magnitude in miles per hour on left axis, and direction of origin in degrees on right axis (bottom panel).

Four instrument stations were deployed, with the configurations listed in Tables 2-4, 2-5, 2-6, and 2-7.

Table 2-4: Channel station (37°27.697'N, 121°59.184'W)

Instrument	Brand (Serial number)	Sensor Elevation	Burst frequency	Burst duration	Sampling frequency
600 kHz ADCP	RDI (1161)	Up-looking, on bottom	3 minutes	3 minutes	1/3.6 Hz (water mode 1)
CTD/OBS	RBR/D&A Instruments (9621/1559)	0.5 meters below the surface	10 minutes	15 seconds	4 Hz

The CTD at the channel station exhausted its batteries at year-day 327. The location of the water surface was deduced from the echo amplitude and correlation matrices recorded by the ADCP for each beam.

Table 2-5: Mudflat station (37°27.755'N, 121°59.146'W)

Instrument	Brand (Serial number)	Sensor Elevation	Burst frequency	Burst duration	Sampling frequency
1200 kHz ADCP	RDI (2020)	Up-looking, on bottom	1 minute	1 minute	1 Hz (water mode 1)
CTD/OBS	RBR/D&A Instruments (10364/2019)	0.3 mab	10 minutes	15 seconds	4 Hz
CTD/OBS	RBR/D&A Instruments (9620/1426)	0.5 meters below the surface	10 minutes	15 seconds	4 Hz

The mudflat instrument station was located within the breach that laterally traverses the mudflat on the northern border of Coyote Creek in the vicinity of the Island Ponds, connecting Pond A21 with the main channel of the slough. During year-day 309, an unknown event caused the pitch and roll to change drastically and the depth to jump approximately one meter, as evident in Figure 2-12 which shows the pitch, roll, and tilt recorded by the ADCP's compass (top panel), and pressure (bottom panel). The shift is also visible in the bottom and water surface velocities plotted in Figure 2-22.

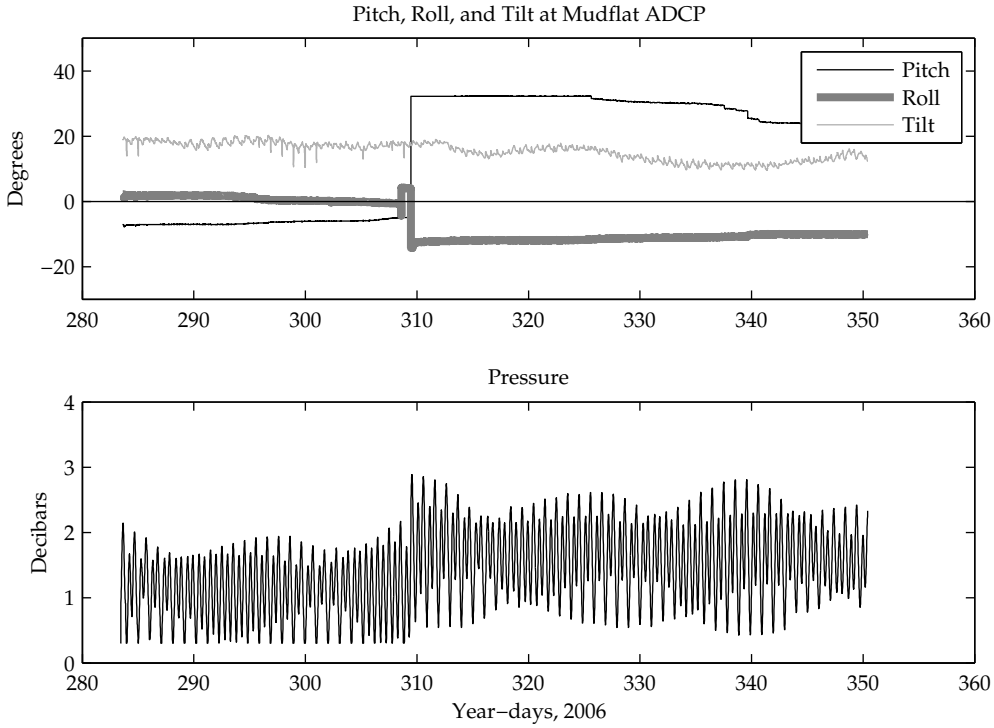

Figure 2-12: Pitch, roll, and tilt, mudflat station

We speculate that either spring tide velocities pushed the frame into a nearby depression in the bed, or that curious boaters recovered the frame briefly and returned it to a slightly different

location. If it was the latter, it must have taken place in less than 10 minutes (between CTD measurements), or the pressure record would have shown a brief but drastic decrease in depth. In either case, the position from which we ultimately recovered the instrument frame was not noticeably different from where we deployed it; however, due to the apparent change in position, ADCP and bottom CTD data from after day 309 are regarded as a separate deployment from data prior to day 309. In all subsequent analyses, velocity data after day 309 is used only sparingly (to examine mean flow characteristics) due to the extreme angles of pitch and roll, in spite of the fact that the ADCP was programmed to collect data in east-north-up coordinates. The CTDs at the mudflat station performed well with the exception of the battery failure of the water surface CTD two weeks prior to the end of the experiment.

Table 2-6: Breach station (37°27.769'N, 121°59.136'W)

Instrument	Brand (Serial number)	Sensor Elevation	Burst frequency	Burst duration	Sampling frequency
ADV	Sontek processor/probe (G130/A342)	0.5 mab	15 minutes	48 seconds	10 Hz
ADV	Nortek (unknown SN)	1.5 mab	15 minutes	30 seconds	16 Hz
CTD/OBS	Seabird Seacat 19/D&A Instruments (2837/2018)	0.5 mab	15 minutes	30 seconds	4 Hz
CTD/OBS	Seabird Microcat/D&A Instruments (1542/1645)	1.5 mab	15 minutes	48 seconds	4 Hz

As during the spring deployment, the ADVs at the breach station sampled at different frequencies, but the burst duration was adjusted such that the number of samples per burst was equivalent; however, velocity data from this station had to be discarded because unexpectedly high velocities tilted the frame drastically with the tides, and caused overranging of the ADVs, as described by Wahl (2000). The pitch and roll measurements confirm that the frame was tilted by the tidal flows. The salinity sensors also indicate that the frame was unstable; both sensors appear to have filled with mud early in the deployment (see Figure 2-25, discussed in the next section), possibly reflecting contact with the bed. Interestingly, the four pressure sensors (from 2 CTDs and 2 ADVs) agree, suggesting that they were not adversely impacted by the motion of the frame.

Table 2-7: Pond station (37°27.783'N, 121°59.128'W)

Instrument	Brand (Serial number)	Sensor Elevation	Burst frequency	Burst duration	Sampling frequency
ADV	Sontek processor/probe (G149/A349)	0.5 mab	15 minutes	30 seconds	16 Hz
ADV	Nortek (4132)	1.5 mab	15 minutes	30 seconds	16 Hz
CTD/OBS	Seabird Microcat (1617/2017)	1.5 mab	15 minutes	30 seconds	4 Hz

There were no problems with the pond station mooring.

The summer 2008 study

During June 26 – July 27, 2008, two CTD/OBS pairs were moored in Coyote Creek, 20 cm above the bed, at the Channel and Mudflat stations from the fall 2006 study. Standalone depth sensors were deployed in addition to the CTDs after prior experiments (not part of this research) suggested that the CTD pressure gages needed servicing. This was a small-scale deployment for the purpose of complementing boat-mounted velocity and salinity/temperature/backscatterance measurements made during this 1-month period. No moored velocity measurements were collected. Conditions during the summer 2008 moored experiment were 100% drier than normal, with almost no precipitation falling during the June – July 2008 period. Figure 2-13 show Coyote Creek streamflow (top panel), precipitation (middle panel), and wind speed and direction of origin (bottom panel). Note that all axes have been changed relative to Figures 2-10 and 2-11 to make the data visible. Streamflow and precipitation were extremely low (top and middle panels). Winds were predominantly out of the northwest (bottom panel).

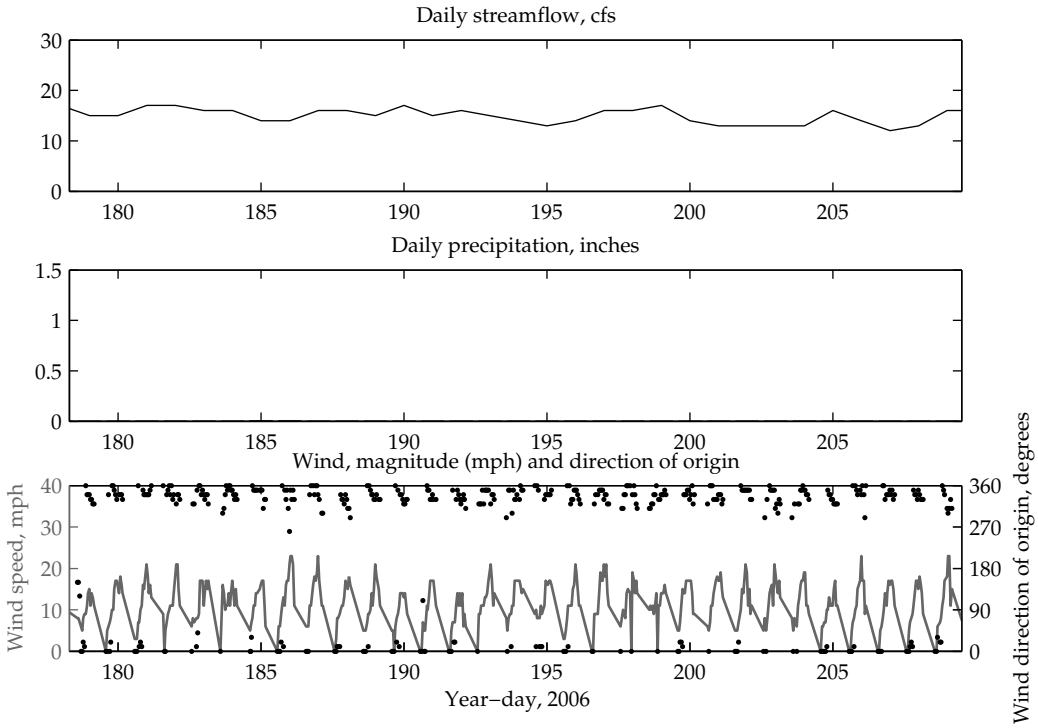

Figure 2-13: Meteorological conditions, summer 2008
Coyote Creek streamflow in cubic feet per second (top panel), precipitation in inches (middle panel), and wind magnitude in miles per hour on left axis, and direction of origin in degrees on right axis (bottom panel).

Tables 2-8 and 2-9 show the instrument configurations for the two moorings deployed in the summer of 2008.

Table 2-8: Channel station (37°27.697'N, 121°59.184'W)

Instrument	Brand (Serial number)	Sensor Elevation	Burst frequency	Burst duration	Sampling frequency
CTD/OBS	RBR/D&A Instruments (10364/2017)	0.2 mab	5 minutes	5 seconds	4 Hz
Depth sensor	RBR (9782)	0.2 mab	5 minutes	(no averaging)	1 sample per burst

Table 2-9: Mudflat/Breach station (37°27.755'N, 121°59.146'W)

Instrument	Brand (Serial number)	Sensor Elevation	Burst frequency	Burst duration	Sampling frequency
CTD/OBS	RBR/D&A Instruments (9621/1559)	0.2 mab	5 minutes	5 seconds	4 Hz
Depth sensor	RBR (9783)	0.2 mab	5 minutes	(no averaging)	1 sample per burst

2.2.2 Boat-mounted experiments

During the spring and fall experiments in 2006, water samples were collected at each backscatter sensor for calibration to suspended sediment concentration. Each sampling session was conducted from a boat using a battery powered pump. The hose was placed such that the intake was at the same distance from the bottom as the backscatter sensors (optical and acoustic). There was a horizontal separation between the water sample and the sensors due to shifting boat position that we estimated to be less than ten meters.

During the summer of 2008, three boat-mounted surveys of velocity and surface water properties were conducted (May 11, June 26, and July 27). A 1200 kHz RDI ADCP in a down-looking configuration (water mode 1), CTDs (RBR and Seabird Instruments), and OBS sensors (D&A Instruments), were deployed. A programming error on May 11 resulting in useless velocity data, which was discarded.

2.3 Data analysis techniques

The following data analysis methods were used for each field experiment, and provide the foundation for subsequent, more detailed analyses that are described in later chapters.

2.3.1 Principal axes

Velocity measurements for all experiments were rotated onto principal axes using the technique described by Emery & Thomson (2001, pp. 325-328) that is the convention for tidal flows. For the spring 2006 study, the major axis was defined for each instrument frame as the direction that maximizes the variance in depth-averaged velocity, and was oriented roughly along-

channel. The minor axis contained the minimum variance and was oriented across the channel. In the fall 2006 study, principal axes were defined solely based on the depth-averaged velocity at the channel station. All velocity measurements at the other three stations were rotated onto these axes. The principal axes for the boat-mounted velocity measurements were defined such that mass is conserved in the lateral direction: the cross-channel velocity integrates to zero. For along-channel velocities, the flood tide velocity is positive, and ebbs are negative.

2.3.2 Calibration to suspended sediment concentration

Calibration of optical and acoustic backscatterance to suspended sediment concentration was performed using a combination of field and laboratory techniques. Water samples were collected and analyzed for total suspended solids following US EPA Method 160.2 (US EPA 1999), which involves filtering the water sample through a washed, dried, and weighed glass fiber filter, drying the sample of solids, and weighing it to obtain a final mass of solids per volume of water filtered. The optical instruments were calibrated using water samples collected at the field site during the deployment, and the acoustic instruments were calibrated in the laboratory using previously collected sediment samples from the South San Francisco Bay. The lab calibrations were performed by Brand et al. (2010). The insensitivity of the acoustic backscatter signal to biological fouling provided a significant advantage of the SSC measurements derived from the ADV (acoustic) data relative to the OBS (optical) data. In addition, ADV backscatter is less sensitive to particle size than that from OBS sensors, resulting in better estimates of total mass of particles in suspension (Fugate & Friedrichs 2002). For these reasons, wherever ADV backscatter data are available, they are used in place of OBS data from the same stations. Suspended sediment concentrations derived from OBS are used at locations where no ADVs were deployed.

The issues associated with the backscatter-to-SSC calibrations are significant. For both acoustic and optical backscatter, the water samples used for calibration in the field and in the lab contained concentrations of suspended sediment much lower than the maximum values of the calibrated backscatter; the highest estimates of SSC from backscatter time series data are based on an extrapolation of the calibration data. Uncertainty is compounded for the acoustic calibration due to the fact that the water and sediment samples used were collected at a different field site, approximately 30 km north of the Island Ponds in the South San Francisco Bay, at instrument stations in intertidal, shallow subtidal, and channel bottom regions (Brand et al. 2010). While the sediments at the two sites appear visually to be very similar, and the calibrations obtained by the authors of that study were quite good ($R^2 > 85$ for the linear fit between backscatter voltage and the logarithm of the concentration), the error in estimates of SSC presented here is likely significant. For these reasons, the analysis presented in Chapter 4 emphasizes temporal variability and minimizes discussion of spatial gradients when the differences in SSC between sensors are small.

2.3.3 Turbulence quantities

Reynolds stresses

Reynolds stresses were calculated from the ADV data. Each burst was 30 (or 48, for Sontek with probe SN A342) seconds in duration, and 480 measurements were collected per burst, at a rate of 16 Hz (or 10 Hz, for Sontek with probe SN A342). Since the burst duration is short, the Reynolds averaging window (which is temporal and not over realizations) is the entire length of the burst. The deviations in velocity from the burst average were correlated with one another and averaged, resulting in the Reynolds stresses, as follows, where an overbar indicates a burst average, and prime indicates the deviation from the average. In the following equations, the longitudinal, lateral, and vertical velocity components are represented by u, v, and w, respectively.

(2-1) $$u = u' + \bar{u},\ v = v' + \bar{v},\ w = w' + \bar{w}$$

(2-2) $$\overline{u'w'} = \overline{(u - \bar{u})(w - \bar{w})}$$

(2-3) $$\overline{u'^2} = \overline{(u - \bar{u})(u - \bar{u})},\ \overline{v'^2} = \overline{(v - \bar{v})(v - \bar{v})},\ \overline{w'^2} = \overline{(w - \bar{w})(w - \bar{w})}$$

This calculation was performed for $\overline{u'w'}$, which represents the vertical turbulent flux of longitudinal momentum, and $\overline{v'w'}$, which is the vertical turbulent flux of lateral momentum. The normal Reynolds stresses are shown in equations 2-3, and their sum is defined as the turbulent kinetic energy (TKE), or q^2.

Turbulent fluxes of sediment

In addition to correlations of turbulent components of momentum, the vertical turbulent flux of sediment concentration was also calculated. In this case, the calibrated suspended sediment concentration (c) measured acoustically was decomposed into mean and fluctuating components, and the correlations could be calculated because the velocity and concentrations were collocated (both measured by the ADV).

(2-4) $$\overline{w'c'} = \overline{(w - \bar{w})(c - \bar{c})}$$

2.4 Data summary and site characterization

Our measurements yield a picture of hydrodynamics and sediment concentrations in Coyote Creek near the Island Ponds. This section reports measured quantities with discussion of seasonal and spring-neap variability, but detailed analyses that include vertical and horizontal scalar gradients are presented in Chapters 3, 4, and 5. The plots of data included in this chapter are intended to show the maximum and minimum magnitudes of velocities, water properties, and suspended sediment concentrations, and therefore they include up to two months of data per plot.

2.4.1 The spring 2006 study

Velocities

Velocities measured in Coyote Creek vary over the approximate ranges listed in Table 2-10, and the time series are shown in Figures 2-14, 2-15, 2-16. Generally, lateral velocities were on the order of 10% of the longitudinal velocities. We recall that positive along-channel velocities (U) are floods, and negative U reflects ebbs.

Table 2-10: Spring 2006 velocity ranges

Station	Along-channel velocity (U, m s^{-1})		Across-channel velocity (V, m s^{-1})	
	Springs	Neaps	Springs	Neaps
East				
1.5 mab	-0.8 – 0.7	-0.6 – 0.3	-0.05 – 0.15	-0.05 – 0.1
0.5 mab	-0.7 – 0.5	-0.5 – 0.2	-0.1 – 0.15	-0.05 – 0.05
Center				
1.5 mab	-1 – 0.7	-0.6 – 0.3	-0.05 – 0.05	-0.05 – 0.05
0.5 mab	-0.5 – 0.6	-0.5 – 0.3	-0.15 – 0.2	-0.1 – 0.1
West				
Water surface	-1.1 – 0.7	-0.7 – 0.4	-0.05 – 0.25	-0.07 – 0.05
1.6 mab	-1 – 0.7	-0.6 – 0.4	-0.1 – 0.25	-0.1 – 0.05

The primary limitation of the velocity dataset collected during this study that must be considered is the spatial resolution of the measurements. At the east and center stations, only two elevations were sampled. At the west station, profiles of velocity were measured, but the ADCP model (600 kHz) has a 1.35 meter blanking distance, which places the middle of the lowest 50-cm bin at 1.6 meters above the bed. In water depths that vary over the range of 2 to 5 meters, this means that the top 20 – 70% of the water column was sampled. Additionally, the contaminating effects of the water surface on the top bin of ADCP velocity measurements require that velocities in the top 10% of the water column be discarded. The result is that at lower low water on spring tides, no velocity measurements are used in analysis.

In addition to vertical spatial resolution of velocity data, the horizontal placement of each instrument frame must be considered. The west and center stations were deployed near the channel center, but the east station was situated in the channel near the southern mudflat. The

close proximity of the east instrument frame to the bank of the low-tide channel is considered in all subsequent analysis, such as that presented in Chapter 3.

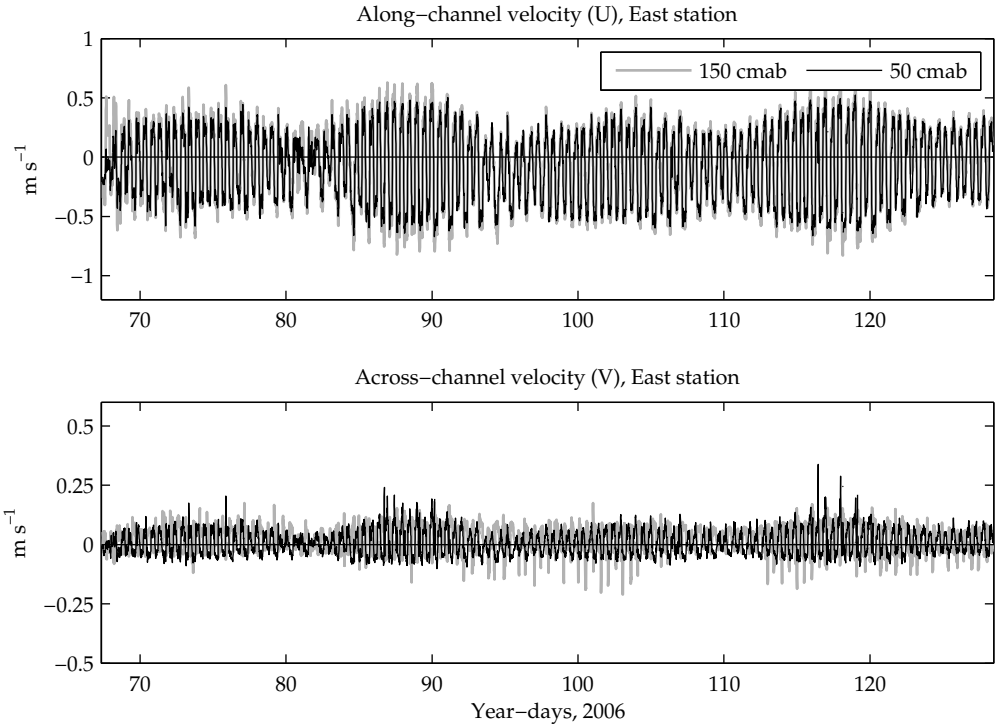

Figure 2-14: Velocities, East station, Spring 2006
Along-channel velocities (U) at 150 cmab (grey line) and 50 cmab (black line) are shown in the top panel. Cross-channel velocities (V) at the same elevations are shown in the bottom panel.

Field measurements indicate that Coyote Creek is ebb-dominant, with along-channel velocities 15 – 40% higher in magnitude on ebbs compared with floods. Fortunato & Oliveira (2005) pose an analytical scaling analysis based on cross-sectional dimensions to weigh the competing implications of tidal flats (which lead to ebb-tide dominance) and great tidal range (which leads to flood-tide dominance). Applying the Fortunato & Oliveira (2005) scaling to Coyote Creek requires estimating the three dimensionless parameters derived by the authors: β: the ratio of the tidal flat half-width to the channel half-width, η: the ratio of the depth of the tidal flats below the mean water depth (positive when the flats are submerged at mean water depth) to the mean water depth, and ε: the ratio of the tidal amplitude (half the tidal range) to the mean water depth. For Coyote Creek, accounting for the width and depth of tidal flats, but neglecting the ponds, these parameters are as follows: $\beta \sim 1/2$, $\eta \sim 0$, $\varepsilon \sim 1/2$, resulting in a balance between flood- and ebb-dominance. Our measurements outside of the Island Ponds indicate that the intertidal storage provided within the ponds may tip the tidal asymmetry toward ebb-dominance, as we observe at all three instrument stations, and at all measurement depths.

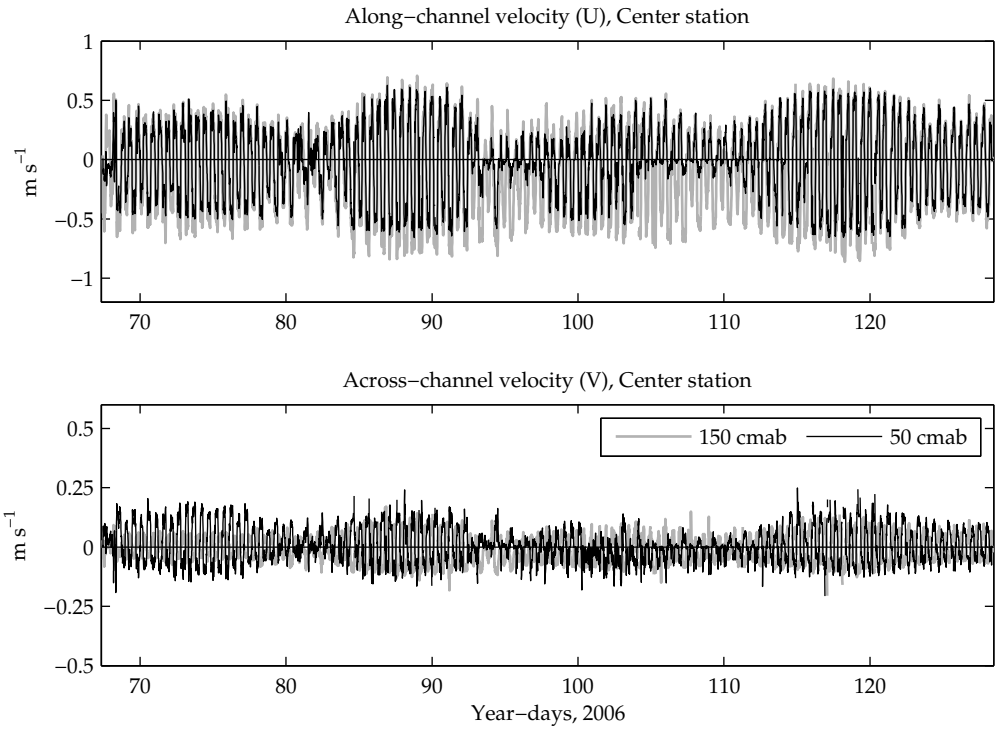

Figure 2-15: Velocities, Center station, Spring 2006
Along-channel velocities (U) at 150 cmab (grey line) and 50 cmab (black line) are shown in the top panel. Cross-channel velocities (V) at the same elevations are shown in the bottom panel.

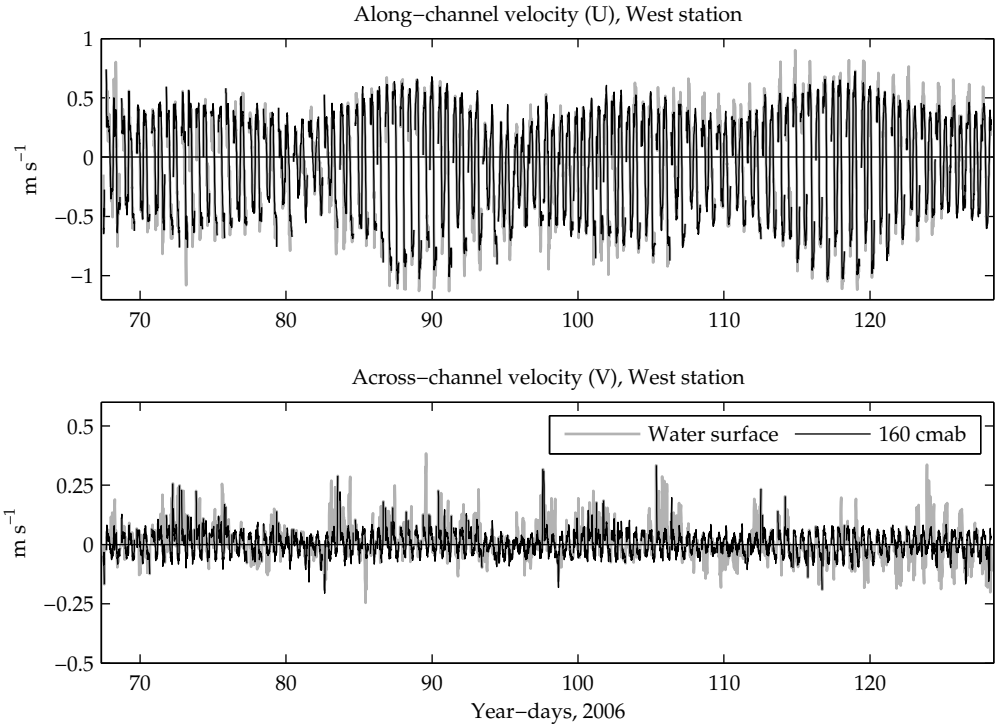

Figure 2-16: Velocities, West station, Spring 2006
Along-channel velocities (U) at the water surface (grey line) and 160 cmab (black line) are shown in the top panel. Cross-channel velocities (V) at the same elevations are shown in the bottom panel.

Salinity, temperature, and depth

Salinities measured during the spring 2006 experiment varied over the range of 2 to 32 ppt. Figures 2-17, 2-18, 2-19 show the salinities, temperatures, and depths recorded at each station.

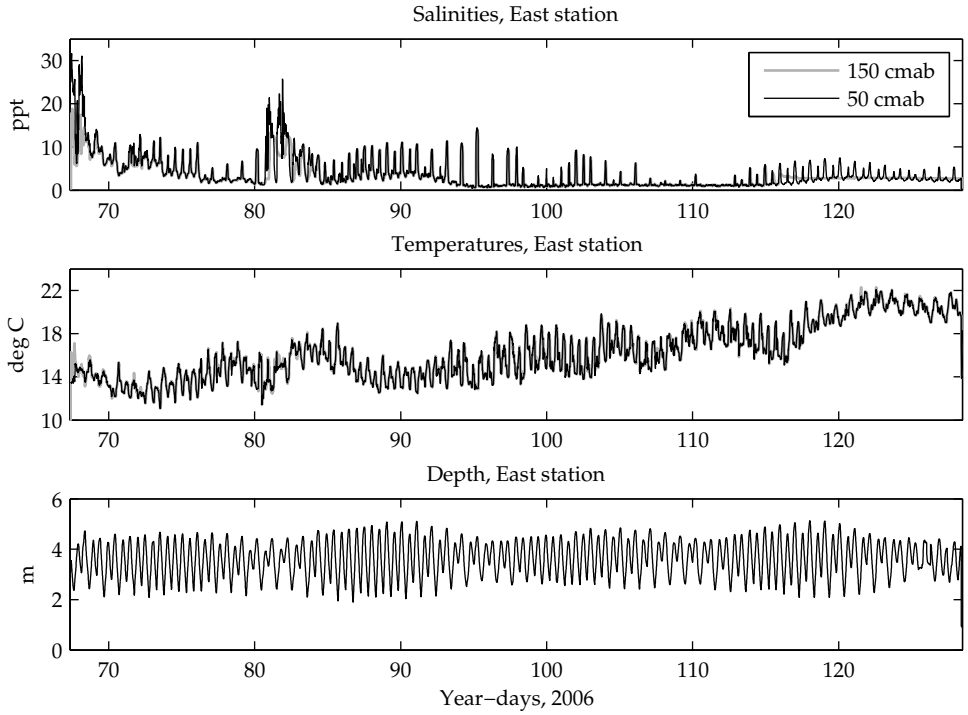

Figure 2-17: Water properties, East station, Spring 2006
Salinity and temperature (top and middle panels) were measured at two elevations (150 and 50 cmab). The differences between the two sensors are small and therefore not apparent on this plot which shows longer-term variability.

Freshwater input from heavy rains, spring-neap tides, and twice daily tides contribute to the observed variability in salinity. The highest values of salinity, which approach undiluted ocean water, correspond to the breaching of the levees. The elevated salinities are observed on both floods as well as ebbs, which points to two driving mechanisms. The first is the dissolution and flushing of the residual salt layer within the ponds. The second is the estuary's response to new subtidal volumes, which in this case are the borrow ditches and subterranean pore spaces beneath the subsided salt ponds. With the increased capacity, a greater volume of Bay water is forced by the tidal wave into Coyote Creek, resulting in greater peak salinities on the flood tides. This effect would diminish after the subtidal volumes were occupied. Determining the magnitude of the contribution of each of these mechanisms would require a complete mass balance of salt, and is not readily calculable with the data collected.

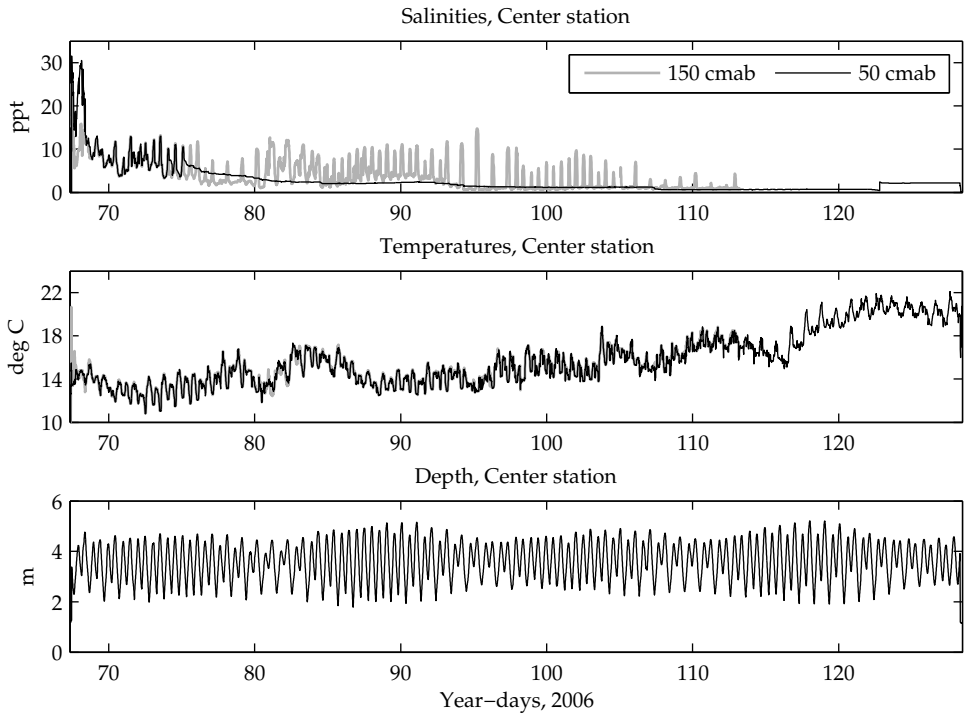

Figure 2-18: Water properties, Center station, Spring 2006
Note that the conductivity cell 50 cmab (top panel) filled with mud around day 75. Seasonal warming is evident in the temperature signal.

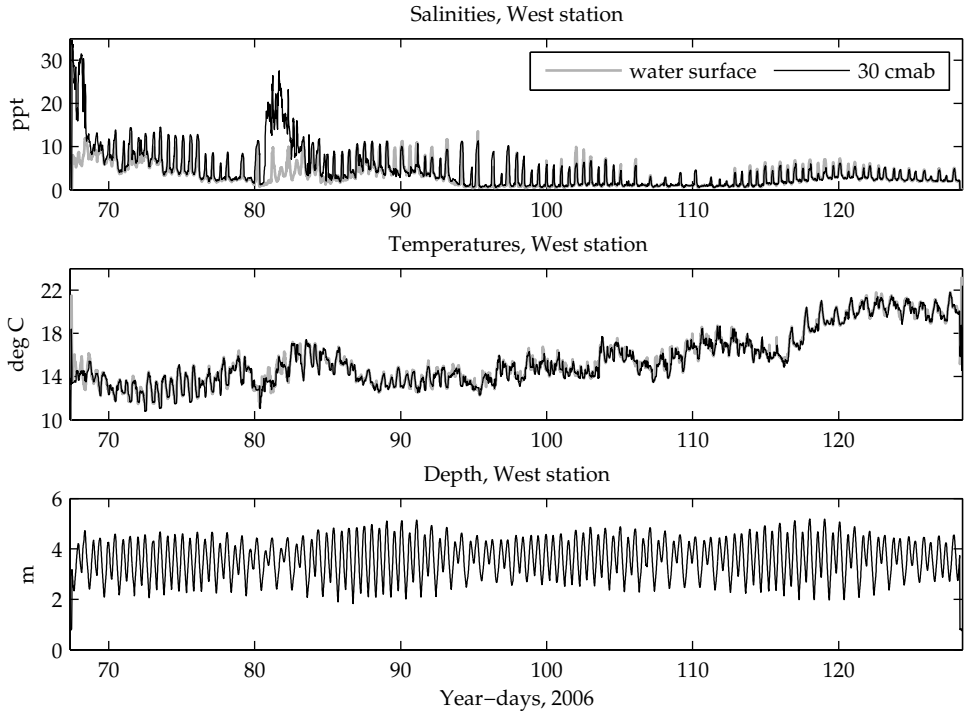

Figure 2-19: Water properties, West station, Spring 2006
Salinity and temperature signals show long-term variability.

The specific breaching schedule is as follows (Santa Clara Valley Water District et al. 2010): Pond A19 was the first to be breached on March 7 (eastern and western breaches, year-day 66), followed by Pond A20 on March 13 (single breach, day 72), with Pond A21 finally breached on March 21 (western breach, day 80) and March 29 (eastern breach, day 88). Comparing the year-days of the levee breaches with the salinities plotted in the top panel of Figures 2-17, 2-18, 2-19 shows the response of the Island Ponds region to the breaches. The greatest spikes in salinity occur on days 67-68, following the breaching of Pond A19, and days 80-82, following the formation of the western breach in Pond A21. Ponds A19 and A21 are significantly greater in surface area (and volume) than Pond A20, and the peaks in salinity from initial tidal exchange with these ponds reflects the difference in mass of residual salt as well as subtidal volume. The second breach in Pond A21 produced a practically imperceptible response in the measured salinities in Coyote Creek because the pond's volume had been filled and stored salt had been flushed through the first breach, formed 8 days prior.

Temperatures show a seasonal warming trend of about 7 degrees over the 2-month deployment: from 13 degrees to 20 degrees Celsius. Spring-neap and diurnal tidal variability, as well as daily warming, are also evident in the temperature signals.

Fluctuations in water depth at each station were measured as changes in pressure by the moored CTDs and by pressure sensors installed on the Nortek and Sontek ADVs. Absolute depths, however, had to be inferred, since the recorded pressures are relative to an arbitrary and unknown datum. The depth of water at the east station was measured from a boat on April 26, 2006, at 13:44-13:47, with a value of 412 centimeters, and the pressure time series at this location was offset to match the measured value. The water depths at the center and west stations were offset using the same method from boat-mounted depths measured during the same April 26 survey.

Depths recorded at the three instrument stations show that the tidal wave has an amplitude of 1 meter on neap tides and 1.7 meters on spring tides (where amplitude is defined as half of the difference in depth at high-water versus low-water). South San Francisco Bay tidal ranges have been documented in many studies which have also found similar values for tidal wave amplitude in the Far South Bay and Coyote Creek (e.g.Cheng & Gartner, 1985; NOAA, Tides and Currents, 2006).

Suspended sediment concentration from optical and acoustic backscatterance

Optical backscatter measurements proved problematic due to biological fouling of the optical sensors in the spring 2006 study, and these data were discarded at the east and center instrument stations in favor of acoustic backscatter, measured by the ADVs. No ADVs were deployed at the west station, and so we must rely on optical backscatter to estimate suspended sediment concentrations (SSC) at this site; however, due to biological fouling, all but the first week of OBS data were discarded. In the present discussion, we observe the temporal variability of the SSC signals. Figure 2-20 shows a dependence on spring-neap and diurnal tides, as well as freshwater flow. Specifically, spring-tide peaks in SSC are evident at days 73-75, 85-87, and 116-118. On year-day 94, when Coyote Creek riverflow reaches a maximum as shown in the top panel of Figure 2-10, there is an initial spike in the SSC measured at the east

and center stations; however, while riverflow toward the estuary remains relatively high for the next 20 days, SSC is depressed at east (50 and 150 cmab) and center (50 cmab), and the spring-tide that occurs during this time does not correspond with a peak in the SSC signal. The implication that the spring-neap variability was overwhelmed by high flows in the channel, as well as additional analyses, will be discussed in detail in Chapter 4 of this dissertation.

The concentrations of suspended sediment in the water column reach very high values – occasionally 2000 mg L^{-1}, and we must note that these are outside of the range of concentrations used for calibration in the field, which were generally less than 400 mg L^{-1}, and in the lab by Brand et al. (2010), which were less than 1000 mg L^{-1}. This introduces additional uncertainty to the calibration, and for this reason, caution is used in comparing concentrations between sensors.

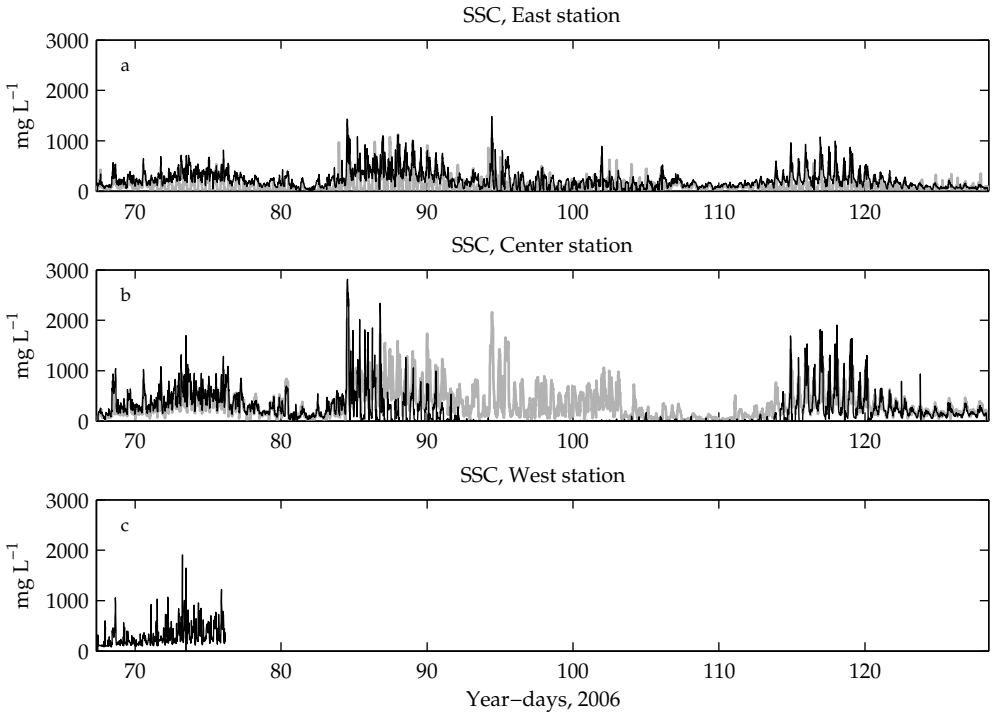

Figure 2-20: Suspended sediment concentration, Spring 2006
Panels a and b: 150 cmab (grey line), 50 cmab (black line). SSC is from acoustic backscatter. Panel c: 30 cmab. SSC is from optical backscatter, which fouled after the first week. The remaining data were discarded.

2.4.2 The fall 2006 study

Velocities

Velocities measured across Coyote Creek and into the westernmost breach of Pond A21 vary over the ranges shown in Table 2-11. Note that the velocities were rotated onto the principal axes of the channel station. These axes are approximately perpendicular to the orientation of the breach.

Table 2-11: Fall 2006 Velocity Ranges

Station	Along-channel velocity (U, m s^{-1})		Across-channel velocity (V, m s^{-1})	
	Springs	Neaps	Springs	Neaps
Pond				
1.5 mab	-0.25 – 0.5	-0.15 – 0.45	-0.2 – 0.2	-0.1 – 0.05
0.5 mab	-0.2 – 0.3	-0.15 – 0.25	-0.2 – 0.1	-0.1 – 0.05
Breach/Mudflat				
Water surface	-0.1 – 0.4	-0.1 – 0.3	-1.2 – 0.7	-0.8 – 0.4
0.75 mab	-0.2 – 0.05	-0.15 – 0.05	-1 – 0.8	-0.7 – 0.6
Channel				
Water surface	-1 – 0.9	-0.8 – 0.5	-0.08 – 0.05	-0.08 – 0.04
1.6 mab	-0.8 – 0.8	-0.7 – 0.5	-0.05 – 0.03	-0.04 – 0.03

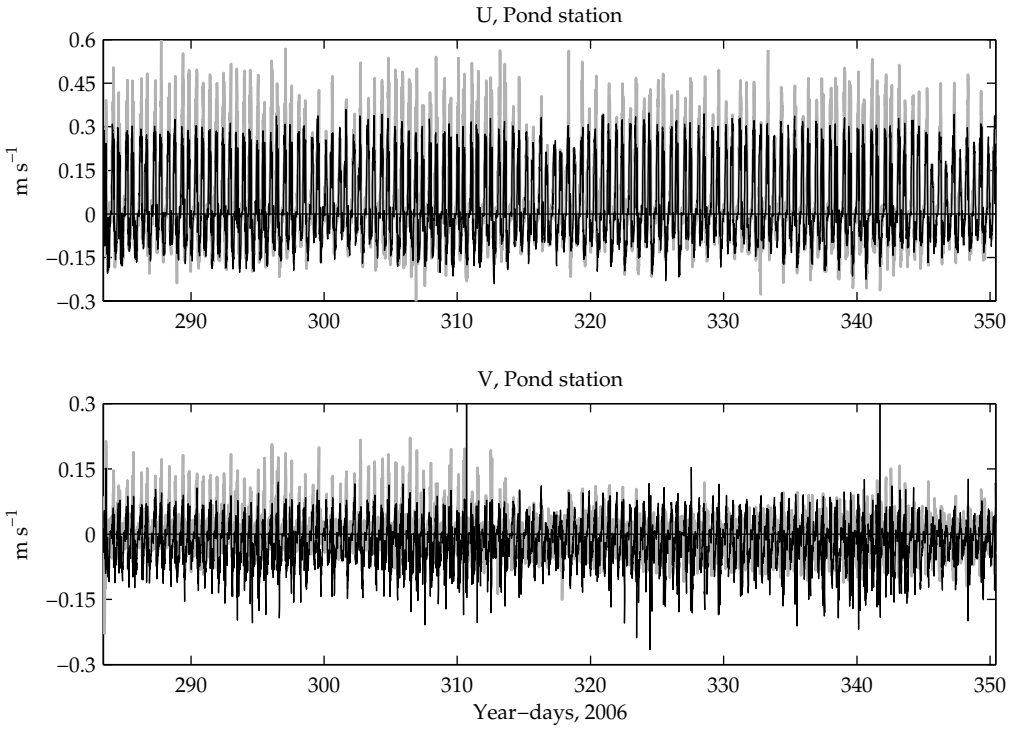

Figure 2-21: Velocities, Pond station, Fall 2006
150 cmab (grey line), 50 cmab (black line)

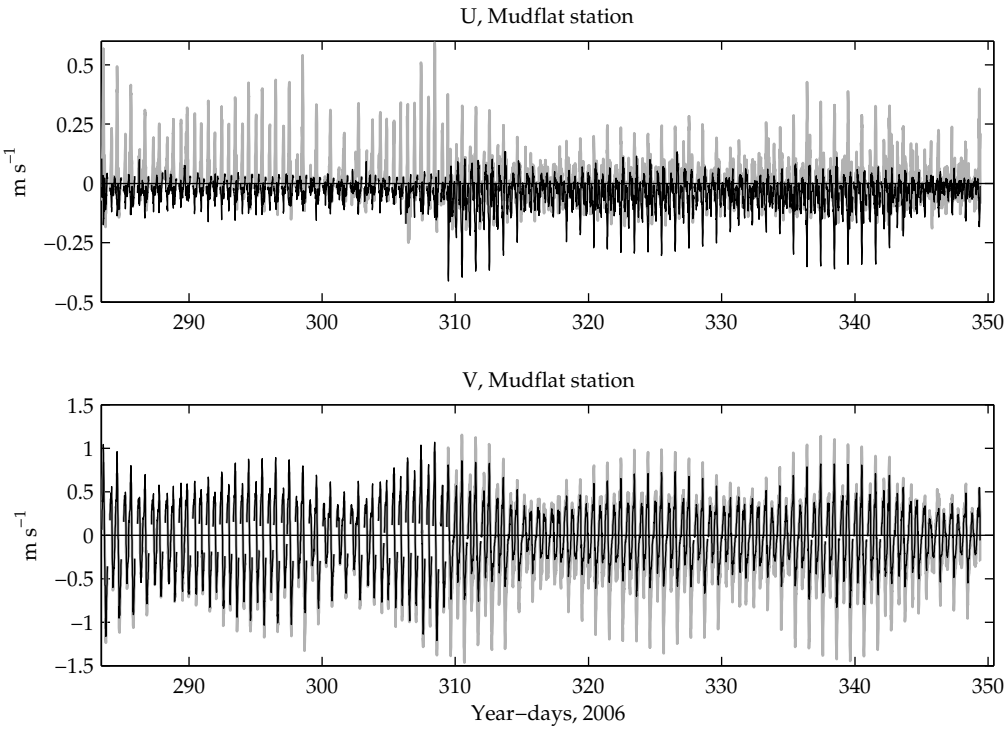

Figure 2-22: Velocities, Mudflat station, Fall 2006
Water surface (grey line), 75 cmab (black line). The frame was disrupted at day 309, which is evident in the signals; all analyses are based on the record before that time.

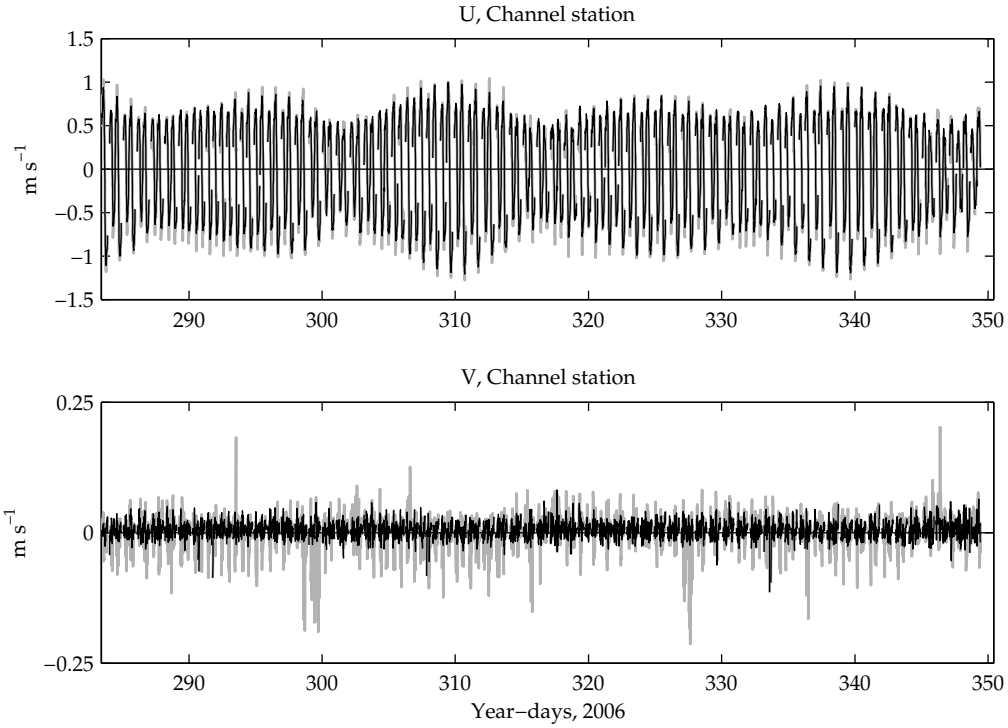

Figure 2-23: Velocities, Channel station, Fall 2006
Water surface (grey line), 160 cmab (black line).

Salinity, temperature, and depth

Salinities during the fall 2006 deployment reflect the dry conditions and vary over a range of 8 to 25 ppt. The diurnal and spring-neap tidal cycles are evident in the plots of salinity at all four instrument stations (Figures 2-24, 2-25, 2-26, and 2-27). In addition to the tidal variability, seasonal dependencies are evident when salinity plots are compared from the spring and fall 2006 experiments. We recall that the salinity varied between 2 and 32 ppt during the wet spring experiment, but note that the high salinities were the result of the flushing of the newly breached salt ponds. The purely tidal variation in salinity during the spring experiment, from inspection of Figures 2-17, 2-18, and 2-19, was about 2 – 13 ppt.

Depths at the four stations vary from approximately 1 to 4 meters, with differences due to bathymetry at the mooring locations. The characteristics of the tidal wave are the same as the spring experiment: the tidal amplitude on spring tides is 1.7 meters, and 1 meter on neap tides.

The axes are the same for the following four figures.

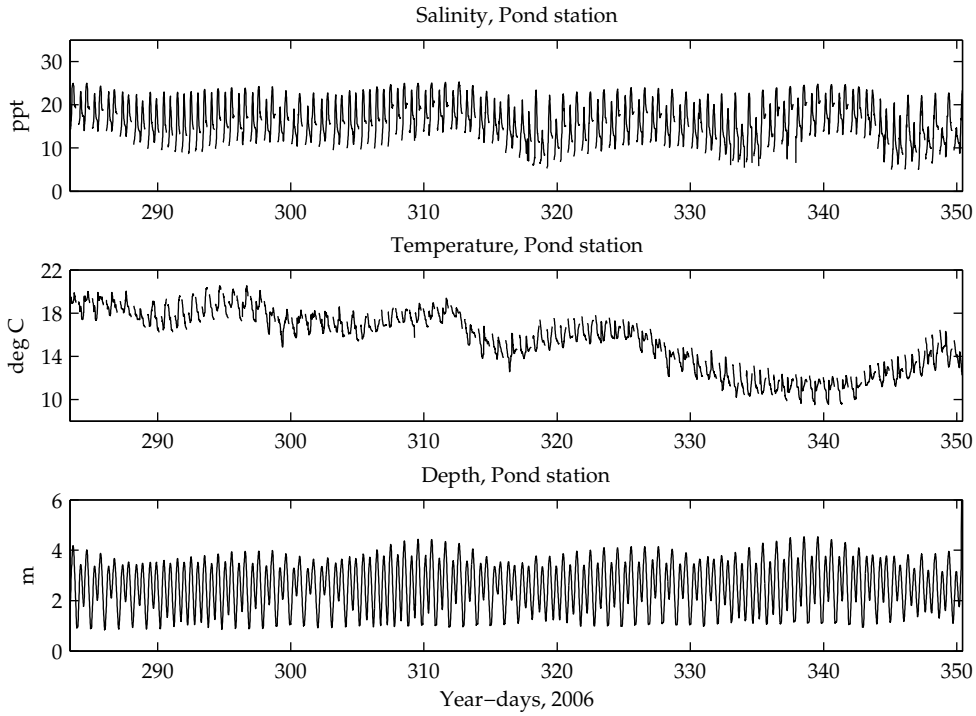

Figure 2-24: Water properties, Pond station, Fall 2006
Salinity and temperature recorded at 150 cmab.

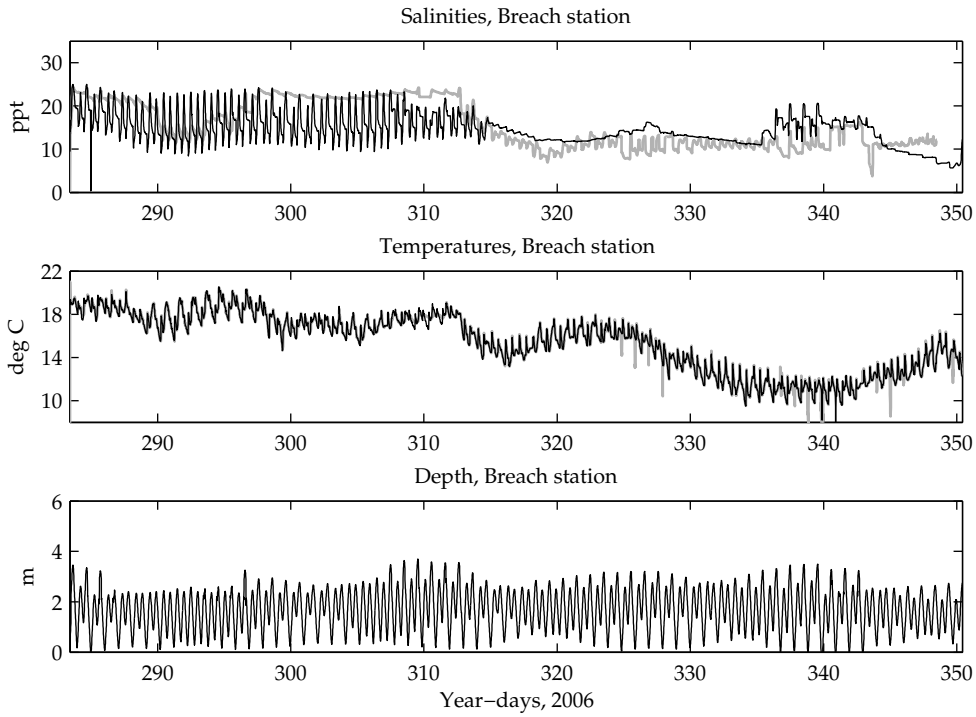

Figure 2-25: Water properties, Breach station, Fall 2006
Salinities and temperatures recorded at 150 cmab (grey line) and 50 cmab (black line), although vertical position changed through time as a result of tidal rocking of the frame. Only depth from this station is used for analyses.

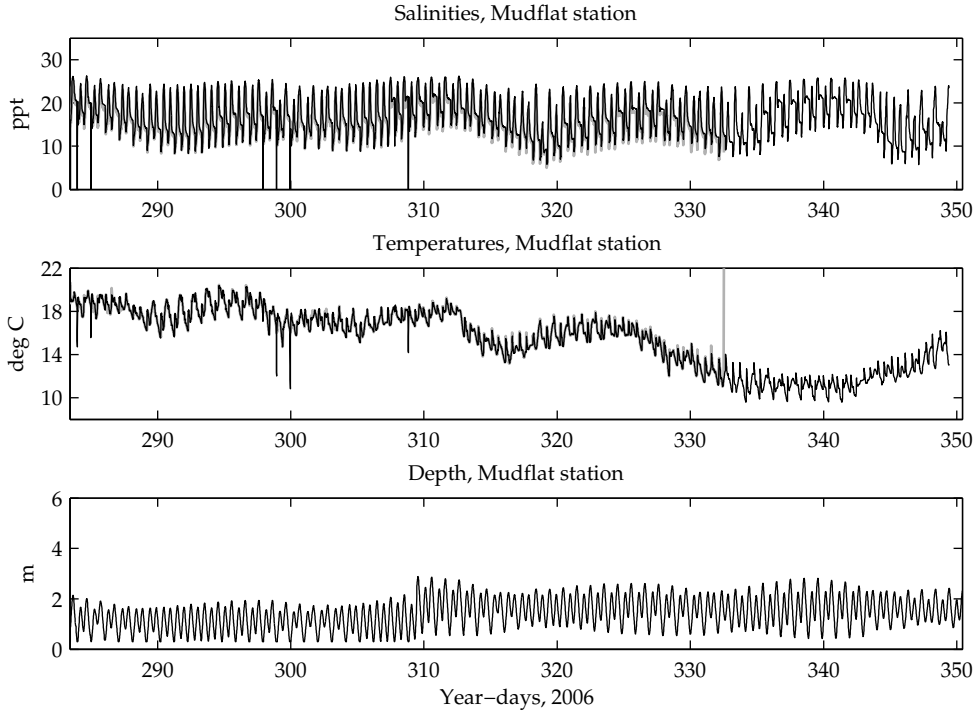

Figure 2-26: Water properties, Mudflat station, Fall 2006
Salinities and temperatures recorded at the water surface (grey line) and 30 cmab (black line). Disruption to frame at day 309 is evident in the depth record.

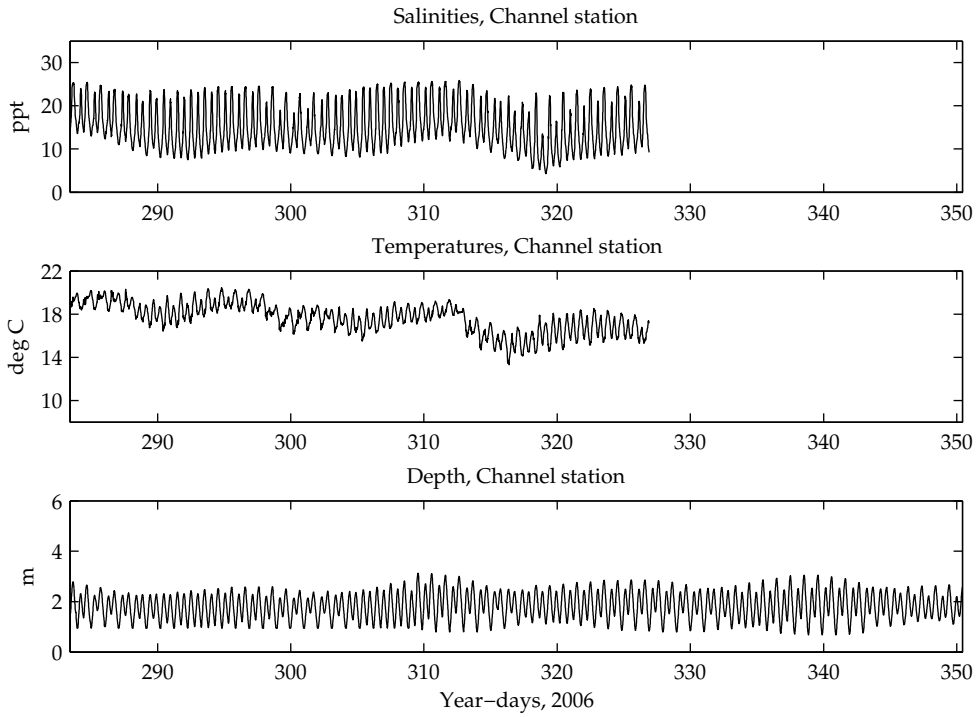

Figure 2-27: Water properties, Channel station, Fall 2006
Salinity and temperature recorded at the water surface. A battery failure occurred at day 327.

Suspended sediment concentration from optical and acoustic backscatterance

The calibrated SSC is shown for all instrument stations in Figure 2-28. Please note that limits of the vertical axes are not consistent because the values of SSC vary significantly. The lowest values of SSC were recorded at the water surface at the channel station (bottom panel): an unsurprising result. SSC at the mudflat and breach stations are of similar magnitudes, with the greater concentrations recorded inside the breach. This could be due to the very high concentrations present in the pond (top panel) or due to the frame possibly on its side, or a combination of these factors. These SSC data are used with caution since the location of the sampling volume is unknown with the range of 0 to 1.5 mab. The high SSC values recorded inside the pond are also used carefully, since the peak values fall well outside the calibrated region for these instruments. This is discussed in detail in the SSC Calibration section.

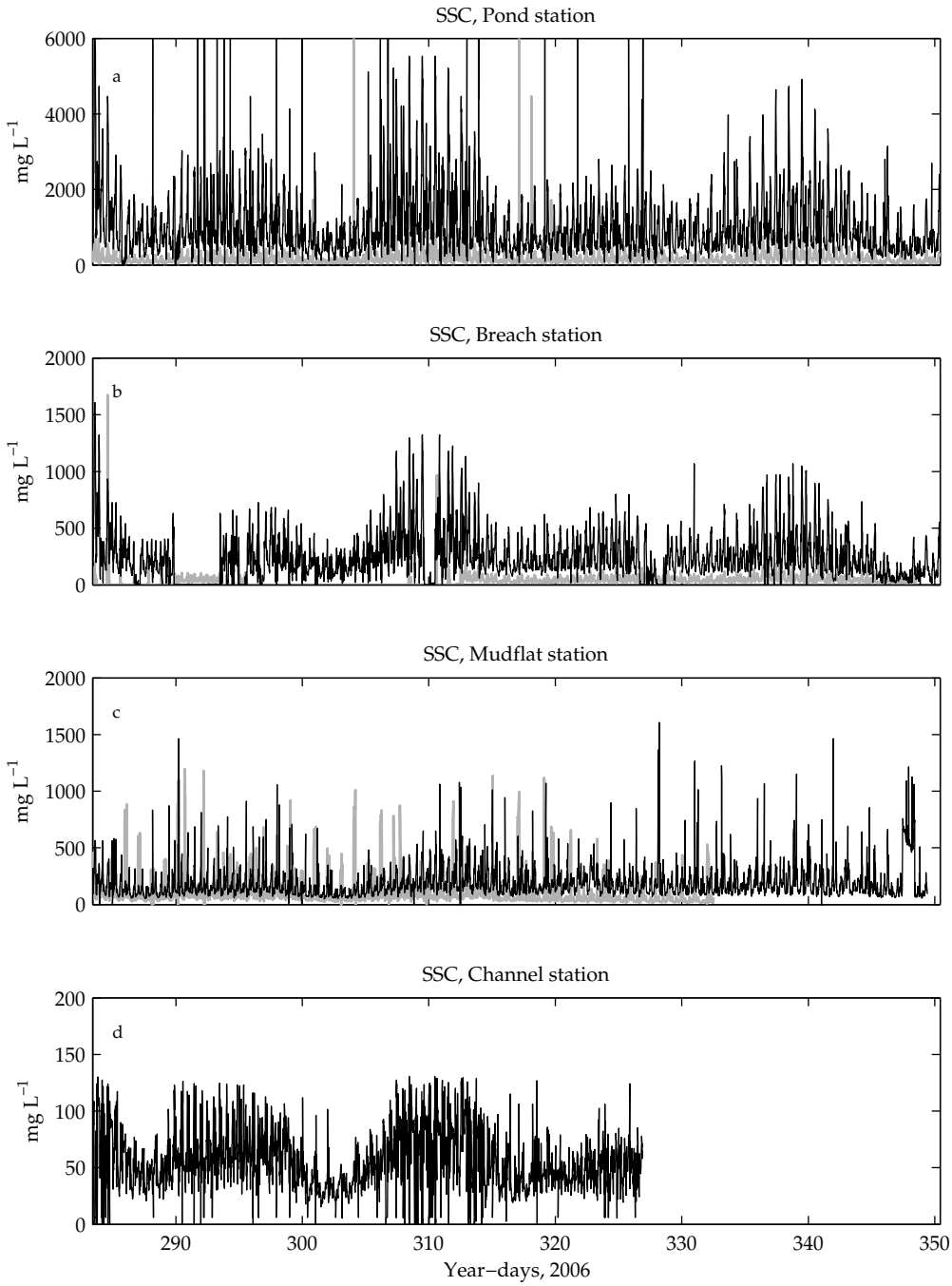

Figure 2-28: Suspended sediment concentration, Fall 2006
Panels a and b: SSC measured at 150 cmab (grey line) and 50 cmab (black line). Panel c: SSC measured at the water surface (grey line) and 30 cmab (black line). Panel d: SSC measured at the water surface (black line). Note that the vertical scale varies between panels.

2.4.3 The summer 2008 study

The summer 2008 study was composed of two simple moorings, measuring bottom salinities, temperatures, depths, and optical backscatter at the same channel and mudflat stations as the fall 2006 experiment. The results are described below.

Salinity, temperature, and depth

Our moorings were deployed during the period of June 26 – July 27, 2008: a very dry summer. Essentially zero rain fell during this period, and streamflows in Coyote Creek were very low (Figure 2-13). Salinity levels vary over the range of 12 – 30 ppt and 10 – 28 ppt at the Mudflat and Channel stations, respectively, reflecting the dry conditions, as shown in Figure 2-29. The higher values at the Mudflat station suggest that there is lateral variability in Coyote Creek and that higher salinities in the channel were not sampled by our mooring. The possibility that salt is still dissolving from within the salt ponds and elevating salinity levels at our instrument station is unlikely; the Island Ponds accumulated 11.5 cm of sediment between the formation of the breaches and summer 2008 (Callaway et al. 2009), and the salinities at the Mudflat station are higher on floods as well as ebbs, when water from the channel is flowing past the sensors.

Temperatures vary at the Mudflat station between 19 and 27 degrees, and between 20 and 26 degrees at the Channel station. Tidal variability on diurnal and spring-neap timescales is apparent in the middle panel of Figure 2-29.

Tidal wave characteristics are the same as recorded in the fall 2006 study, and depths are shown in the bottom panel of Figure 2-29.

Suspended sediment concentration from optical backscatterance

SSC from optical backscatter at the Mudflat and Channel stations shows a strong disparity between concentrations at the two locations (Figure 2-30). We refrain from concluding that the whole of the channel has concentrations of suspended sediment as low as those recorded at our mooring; it is likely that significant lateral variability exists in SSC across Coyote Creek. At both locations, concentrations are elevated on springs, and depressed on neap tides. Details of these time series are explored in Chapter 4.

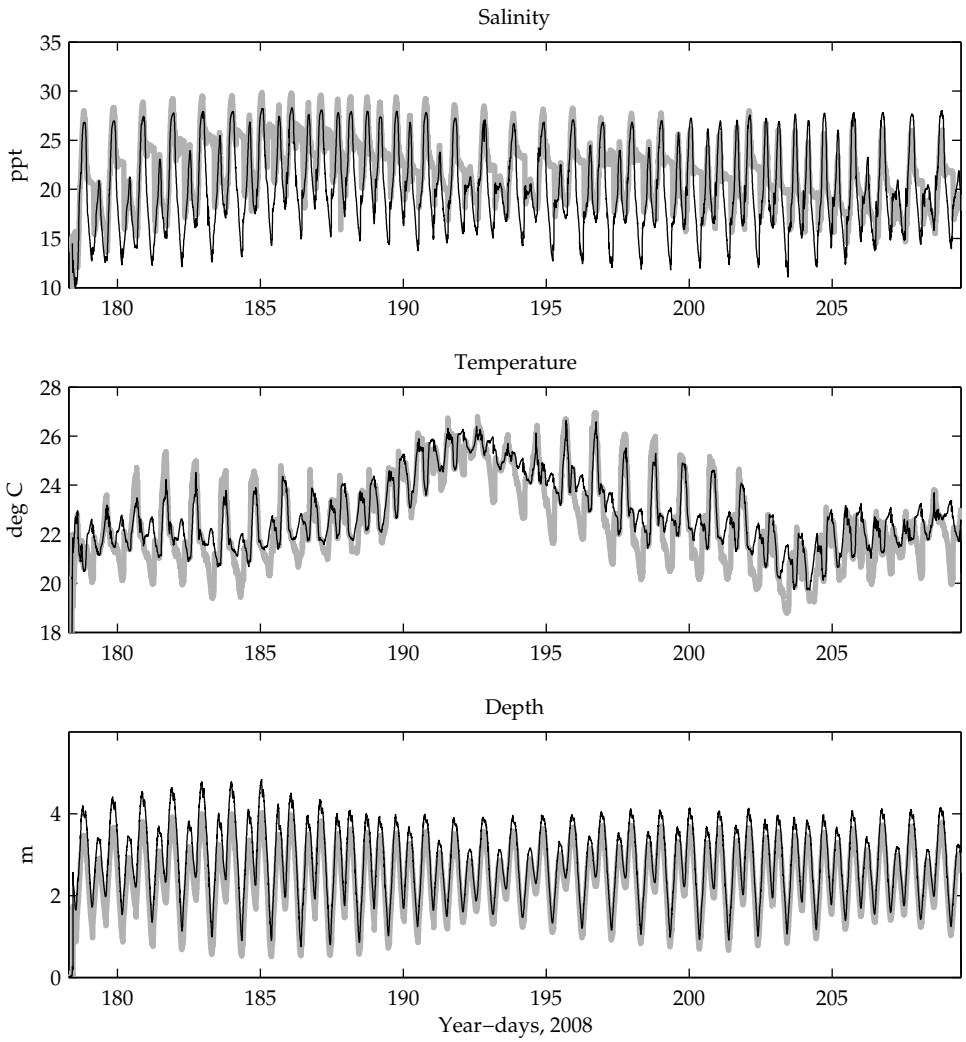

Figure 2-29: Water properties, Mudflat & Channel stations, Summer 2008
Mudflat station: grey line, Channel station: black line

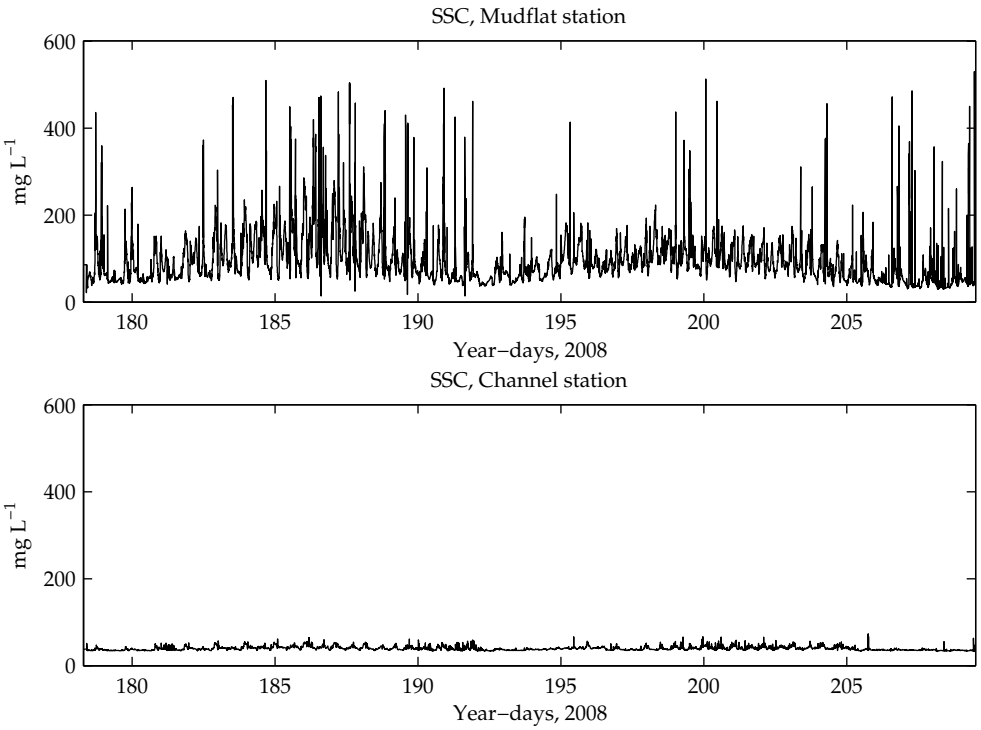

Figure 2-30: Suspended sediment concentration, Mudflat & Channel stations, Summer 2008
SSC from OBS was measured at both mooring locations at 20 cmab. Spring tides occur around days 183 – 188 and 198 – 203. Calibration for these backscatter signals was performed with water samples collected at the locations of the sensors during the deployment.

2.4.4 Boat-mounted surveys

Three boat-mounted experiments were undertaken during the summer of 2008. On May 11, surface water properties were measured from mid-ebb to mid-flood. On June 26 and July 27, velocity profiles and surface water properties were sampled from mid-ebb to mid-flood, and from early-ebb to mid-ebb, respectively. During each survey, a distance of 500 – 800 meters just down-estuary of the westernmost breach of the westernmost Island Pond (A21) was sampled. The lateral extent of each survey was determined by water depth; at lower tidal stages, the mudflats could not be traversed and only the channel was sampled.

The following figures (2-31, 2-32, and 2-33) show examples of the measurements collected during the three surveys of the summer of 2008. Each east-west or (west-east) pass took approximately 30 minutes, and 10-20 passes were conducted during each survey. A square-wave path, such as those pictured, was followed in each case, with lateral channel crossings lasting for approximately 2-3 minutes.

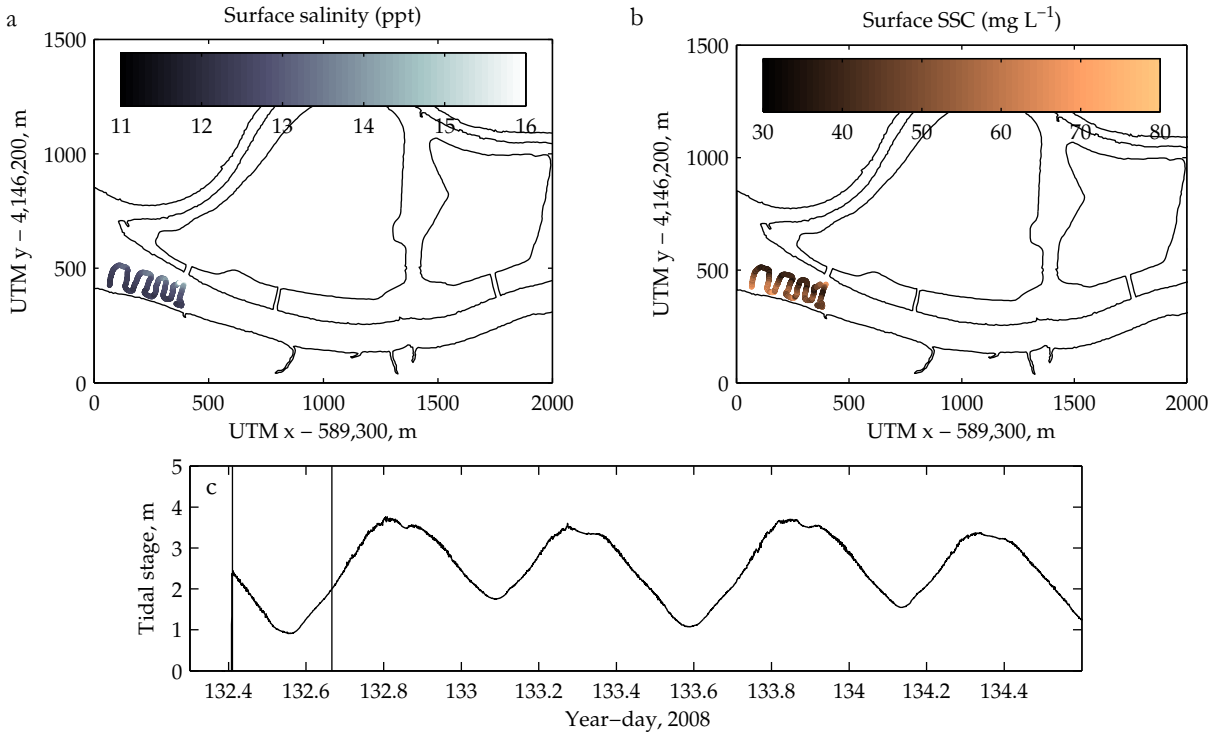

Figure 2-31: 11 May 2008 survey
One pass from east to west is shown as an example of surface salinity (a) and SSC (b). The duration of the survey is shown by vertical lines on the plot of tidal stage (c).

During the May 11 survey, surface salinities varied over the range of 8 – 16 ppt. Surface concentrations of suspended sediment were in the range of 40 – 120 mg L^{-1}.

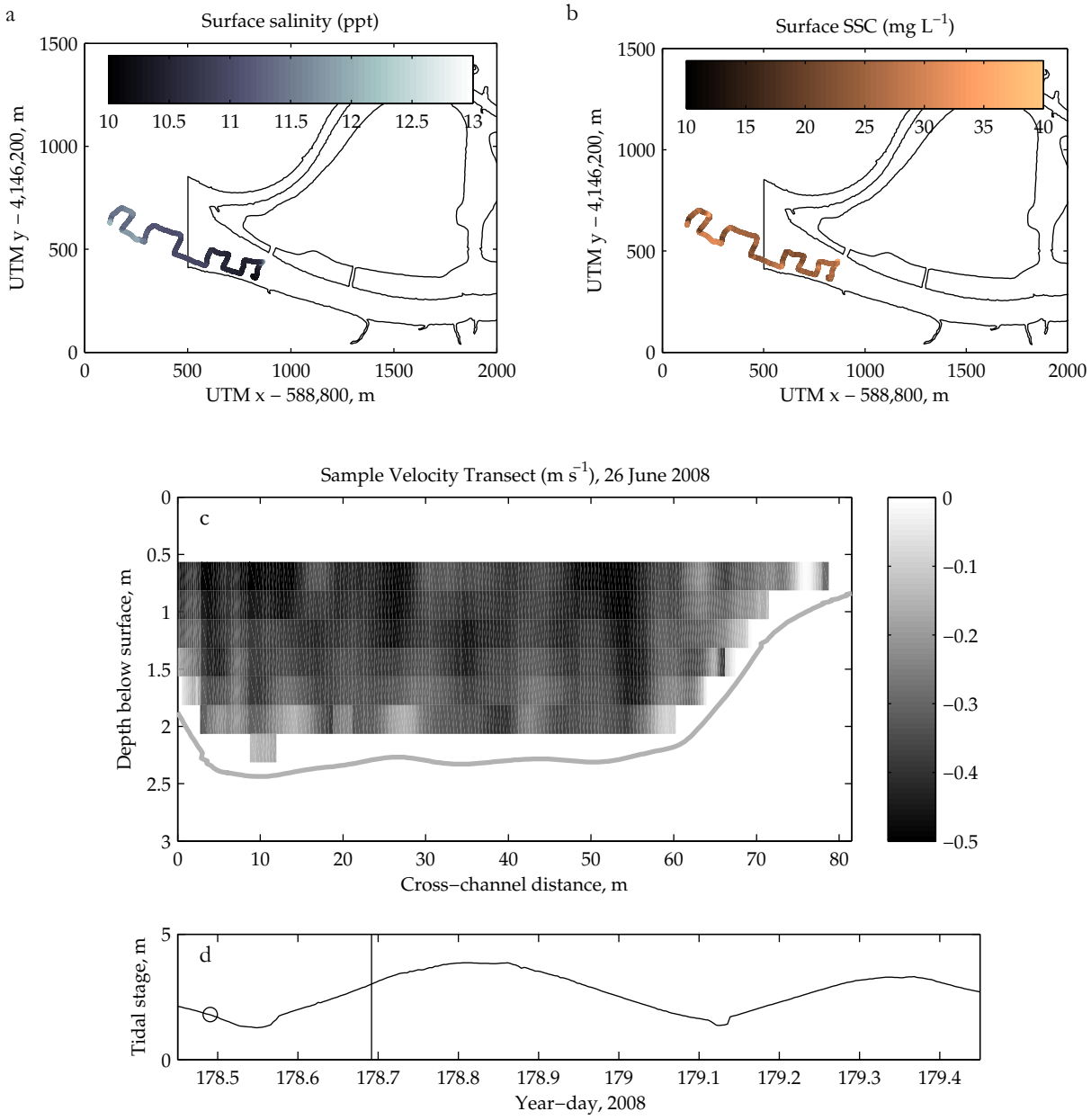

Figure 2-32: 26 June 2008 survey
In addition to examples of surface salinities (a) and SSC (b), one lateral transect of along-channel velocity is shown (c). The duration of the survey is bracketed by vertical lines on the plot of tidal stage (d), and the time of the velocity transect is shown by the circle.

During the June 26 survey, salinities varied from 10 – 18 ppt, and SSC varied from 15 – 60 mg L^{-1}. This survey captured velocities during the ebb-to-flood transition, with values of -1 to 1.3 m s^{-1} along-channel, where flood velocities are positive.

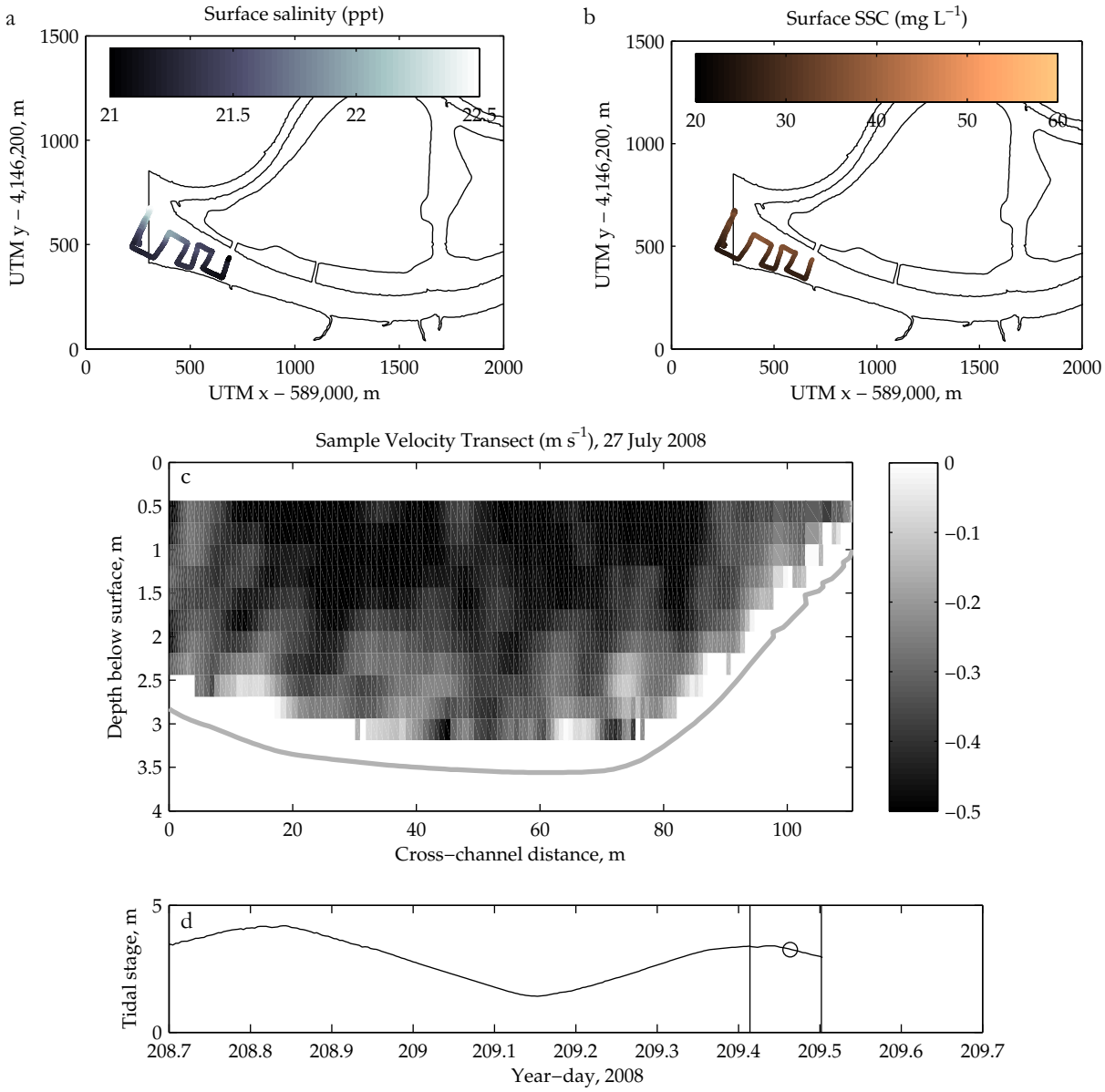

Figure 2-33: 27 July 2008 survey
Examples of surface salinity (a) and SSC (b) are shown, as well as one lateral transect of along-channel velocity (c). Vertical lines on the plot of tidal stage (d) indicate the temporal limits of the survey, and the sample velocity transect was collected at the time marked by the circle.

During the July 27 survey, salinities varied from 19 – 23 ppt, and SSC varied from 20 – 60 mg L^{-1}. This survey captured velocities during the ebb-to-flood transition, with values of -0.9 to 0.5 m s^{-1} along-channel, where flood velocities are positive.

2.5 Summary

Field experiments were performed in a tidal slough outside of newly breached salt ponds in order to study the dynamics of exchange between the channel and side volumes, and the influence of this exchange on hydrodynamics and scalar transport. The field site is located in the southeastern-most reach of San Francisco Bay, in Coyote Creek, which exchanges with the Island Ponds through breaches formed in early 2006. Coyote Creek is a macrotidal channel that varies in depth over a range of 1 to 4 meters. The tidal wave has an amplitude of 1 meter on neaps and 1.7 meters on springs. Coyote Creek is tidally forced via the Bay to the west, and receives freshwater flow from surrounding watersheds, as well as the San Jose/Santa Clara Water Pollution Control Plant, which is located on a tributary of Coyote Creek. The climate of the greater San Francisco Bay/Delta system and of the Coyote Creek region is Mediterranean, with dry summers and rainy winters. Moored experiments were performed during a rainy spring (2006), a dry fall (2006), and a dry summer (2008) during which velocity, salinity, temperature, depth, and suspended sediment concentrations were measured. These deployments of moored instruments were augmented by boat-mounted surveys of the same quantities.

Our measurements indicate that barotropic velocities vary from approximately -1 to 0.75 m s^{-1} along the main channel of Coyote Creek, with lateral velocities from -0.25 to 0.25 m s^{-1}. Inside one of the salt pond breaches, velocities were measured over the range of -1.5 to 1 m s^{-1} along the breach, with across-breach velocities of -0.25 to 0.5 m s^{-1}. Velocities measured during the spring of 2006 along the axis of the channel show that Coyote Creek is ebb-dominant, which is assumed to be caused by the intertidal storage provided within the salt ponds.

The results of these experiments show that water properties vary in response to season, where salinity and temperature are depressed during rainy winter periods and elevated during dry summers. Water properties also vary strongly on the spring-neap and diurnal tidal timescales. We measured a tidal range in salinity of 2-13 ppt during the wet spring of 2006, 8-25 ppt during the dry fall of 2006, and 10-30 ppt during one completely dry month of the summer of 2008. Average water temperatures during these periods were 17, 15, and 23 degrees C, respectively.

Suspended sediment concentrations show strong tidal variability on diurnal and spring-neap timescales, with maximum SSC occurring on spring tides. SSC in the channel shows a seasonal dependence as well, with values exceeding 2000 mg L^{-1} during rainy weather, and generally less than 1000 mg L^{-1} during dry weather.

The results presented in this chapter provide a context for the detailed exploration of hydrodynamics and spatial gradients of scalar fields in Coyote Creek described in subsequent chapters.

CHAPTER 3

Effects of lateral exchange on stratification at tidal timescales

3.1 Introduction

This chapter explores the motion of water and salt through a tidal slough connected to large intertidal volumes along its perimeter in the context of the physics of a partially mixed estuary. In his classification of estuaries based on salinity structure, Dyer (1973) describes a partially mixed estuary as one where tides oscillate the system of freshwater overlying saline, producing turbulent eddies from the work of the tides against bottom friction (known as tidal stirring). These eddies are dissipated through heat and by increasing the potential energy of the stratified fluid – lifting heavy water above light – which mixes salt into the surface layer and dilutes the bottom layer. The vertical stratification of the salt-wedge estuary, on the other hand, suppresses vertical turbulent motions, such that the surface layer remains fresh. Relatively constant longitudinal salinity gradients are commonly observed over long reaches of the partially mixed estuary, unlike the frontal salinity structure of a salt-wedge estuary.

Tidal straining, which is the straining of the longitudinal density gradient by shear in the velocity profile, acts on the estuary to produce an asymmetry between flood and ebb of stratification and turbulent mixing (Simpson et al. 1990). Simple schematics of tidal straining on ebb and flood tides are shown in Figure 3-1. For both phases of the tide, differential advection arises from the boundary-layer structure of the velocity profile, wherein flow near the bottom is slower than surface flows due to frictional resistance. On the ebb tide, when the barotropic pressure gradient opposes the longitudinal density gradient, surface flows carry lighter, fresher water down-estuary over the relatively slow and dense near-bottom flows. Tidal straining, in this case, strengthens stratification and dampens vertical turbulent motions. On the flood tide, the barotropic and baroclinic pressure gradients are aligned, and the boundary-layer shear in the velocity profile advects saline water over fresher water, creating a convective instability that enhances vertical mixing (Burchard & Baumert 1998). In the case of a partially-mixed estuary, where stratification may be present at the start of flood and ebb, tidal straining strengthens existing stratification on ebbs and breaks it down on floods.

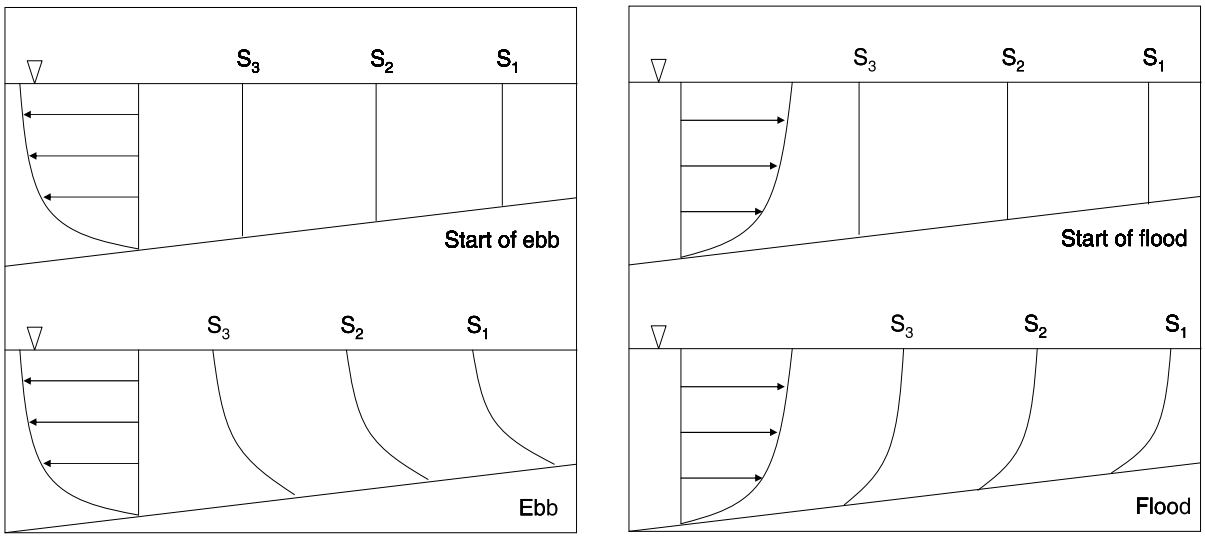

Figure 3-1: Conceptual model of tidal straining, adapted from Simpson et al (1990)
Isopycnals are marked by S, where $S_1 < S_2 < S_3$. The flood and ebb velocity profiles are shown by horizontal arrows. The straining of the longitudinal salinity gradient by the boundary-layer structure of the velocity profile leads to stable stratification on the ebb tide and unstable stratification on the flood.

The implications of this tidal asymmetry in stratification and mixing reach beyond intra-tidal analyses and are critical for determining residual, or tidally averaged, estuarine flows and scalar fields in partially-mixed estuaries (Geyer et al. 2000; Stacey et al. 2001). It is the distributions of flow and scalars over long timescales that define the ecological functioning of an estuary: the length of salt intrusion up-estuary, the tidally-averaged transport of sediment, and the distance traveled over days or weeks by seeds, larvae, and contaminants. Traditional models assume that the residual estuarine exchange flow is determined by the strength of the along-estuary baroclinic pressure gradient (Chatwin 1976; Hansen & Rattray 1965), however, Geyer et al. (2000) found that in fact the estuarine exchange flow on tidal and subtidal timescales was dependent on vertical mixing (although, interestingly, well represented by bottom stress alone). Observations made by (Stacey et al. 2001) in northern San Francisco Bay show that the vertical structure of stratification and mixing set up intermittent pulses of flow, and these pulses determined the residual estuarine exchange flow.

On tidal timescales, periodic stratification can alter mixing within the water column, leading to periodic decoupling of the bed and the water surface. The timing of this decoupling has important implications for many ecologically significant scalars, including sediment. During periods of stratification, elevated bed stresses may resuspend sediment, but the pycnocline limits the vertical transport of the sediment, preventing the sediment from accessing higher habitats such as mudflats and marshes. In the traditional model, the flood tide hosts the lowest stratification, suggesting that resuspension during this phase of the tide determines sediment concentrations that access the highest elevations. Over successive tidal cycles, this periodicity will determine patterns of erosion and deposition and, therefore, the geomorphic structure of the estuary.

In this chapter, we explore modifications by bathymetry of local patterns of vertical shear and stratification that have implications for flow and transport on tidal and residual timescales. Coyote Creek, a macrotidal slough in the Far South San Francisco Bay, functions as an estuary unto itself and provides the context for this research. The channel-mudflat-pond morphology generates vertical shear in horizontal velocities, which strain local salinity gradients to produce patterns of stratification that do not adhere to the classical model of partially-mixed estuaries. Field experiments were conducted to measure these interactions and create a conceptual model of the intra-tidal dynamics, as well as the implications for scalar transport on longer timescales. The site, conditions, and field experiments are discussed extensively in Chapter 2, and summarized in the following section.

3.2 Observations

Measurements of velocity, salinity, and depth were collected in Coyote Creek during the spring of 2006. The experiments took place in the vicinity of the Island Ponds, which are a cluster of three former salt ponds breached to tidal action via Coyote Creek in March 2006 (Figure 3-2). Coyote Creek is oriented approximately along an east-west line in this region; Bay water enters from the west on floods, and freshwater is supplied from watersheds to the east and south, and from a local wastewater treatment plant.

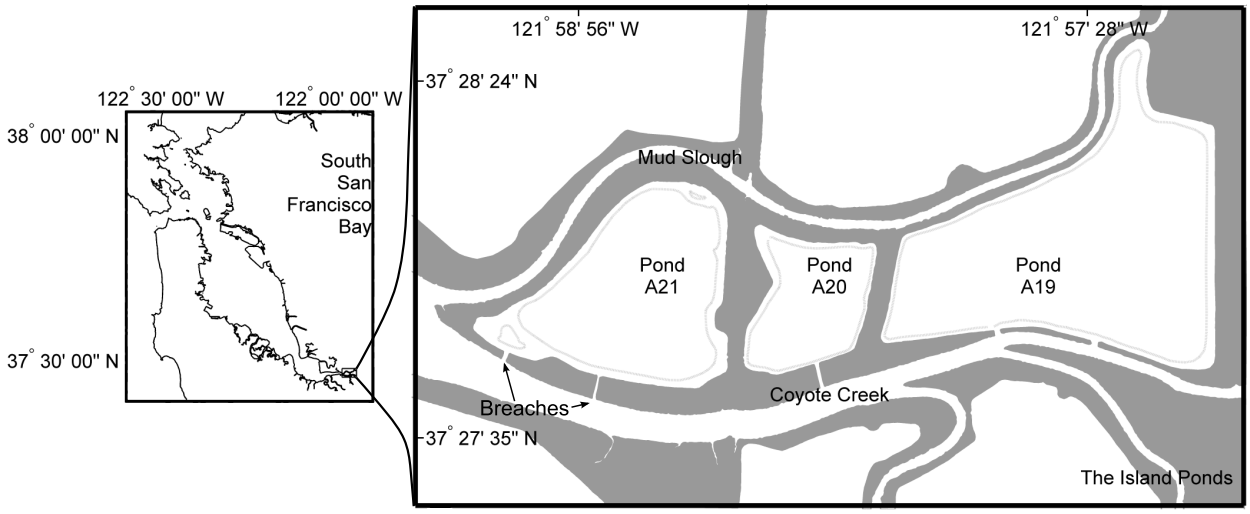

Figure 3-2: South San Francisco Bay and the Island Ponds
The Island Ponds (right) were among the earliest salt ponds to be breached as part of the South Bay Salt Pond Restoration project. The levee separating them from Coyote Creek was breached in 5 places in March 2006.

Coyote Creek consists of a main channel flanked by intertidal mudflats and marsh. The width at this location is approximately 200 meters, including intertidal regions. The main channel has an average depth of 3 meters, with broad intertidal mudflats on the northern border of Coyote Creek, and narrow intertidal mudflats on the southern border. Best-available bathymetry is shown in Figure 3-4. The widths of the mudflats vary along the length of Coyote Creek, but in

the vicinity of the Island Ponds, our observations indicate that the mudflats are 50-70 meters wide to the north, and 20-30 meters wide to the south. Figure 3-3 shows the cross-section of Coyote Creek at the western end of the Island Ponds (location shown in inset). The black dots are measurements made by the US Army Corps of Engineers, and the line defining the cross-section is an approximate reflection of the bathymetry between measurements, based on visual inspection of the site at low-water. The elevations are shown relative to the North American Vertical Datum of 1988 (NAVD 88). The dotted portion of the cross-section, between 60 and 110 cross-channel meters, is a schematic representation of visual observations made during boat-mounted field work. The southern mudflat is narrow compared to those to the north, and connected to the marsh above and the channel below by sharp transitions.

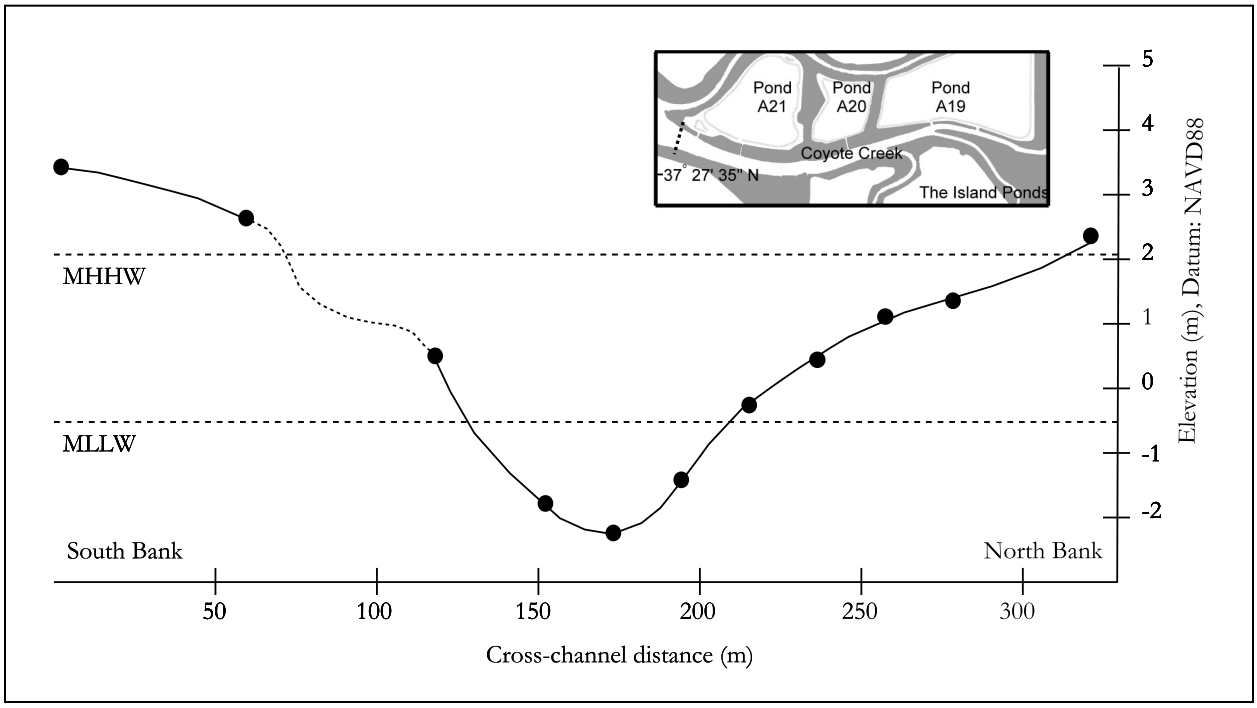

Figure 3-3: Channel cross-section.
Black dots are measurements made by USACE at the location shown by the dotted line in the inset (at the western end of the Island Ponds). The vertical datum is NAVD88, and the locations of MLLW and MHHW are shown for comparison. The line defining the cross-section was inferred by visual inspection at the site and is approximate. The dotted line between 60 and 110 cross-channel meters is used to call attention to the southern mudflat. Detailed bathymetry data are not available here, but visual observations of the site indicate that the mudflat is narrow with a gentle slope, connected to the marsh above and the channel below by sharp transitions.

The spring 2006 experiment was a longitudinal study composed of one ADCP mooring (at the west station) and two ADV moorings (center, east). Mooring locations and bathymetry are shown in Figure 3-4 (filled black circles). In addition to the 600 kHz ADCP, the west station also had a CTD/OBS pair located 30cm above the bed, and a CTD/OBS pair 50cm below the surface (attached to the buoy line). The two ADV frames at the center and east stations were identical, with ADV sampling volumes and CTD/OBS pairs located at 0.5 and 1.5 m above the bed (mab). The ADVs were programmed to sample at 16 Hz in 30-second bursts every 15

minutes such that mean flows as well as turbulence characteristics could be measured. Data from the center station is not discussed since the bottom CTD filled with mud approximately one week after deployment, rendering those data unusable. The west station was deployed in the center of the channel, and the east station was situated near the transition to mudflat at the southern edge of the channel.

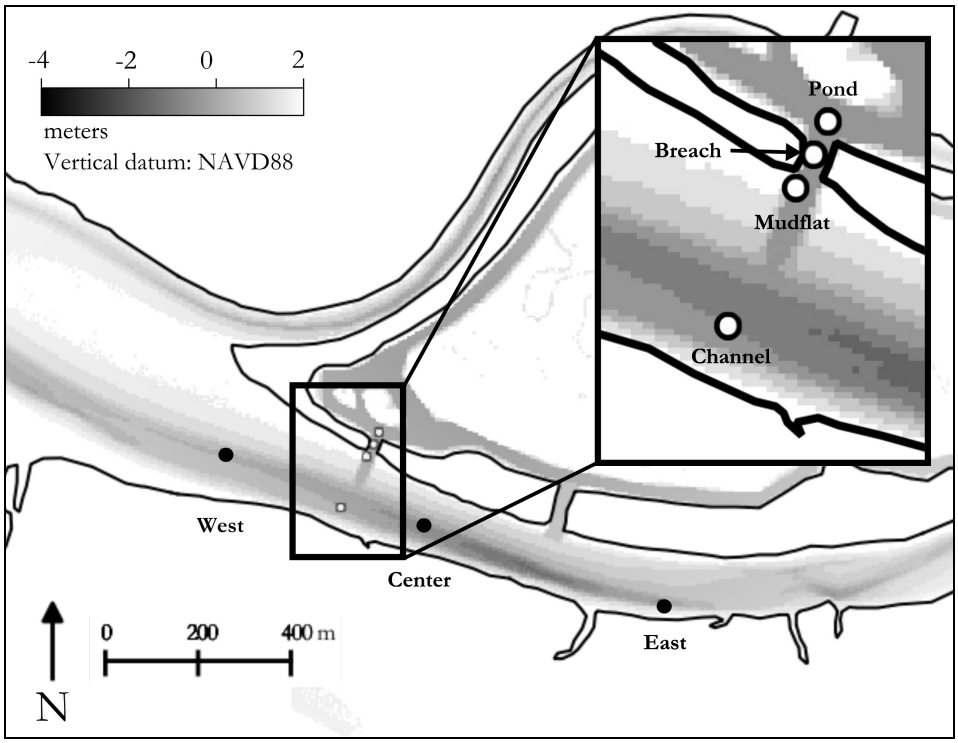

Figure 3-4: Coyote Creek bathymetry and experiment mooring locations
Spring 2006: black circles, west, center, east (left to right)
Fall 2006: white circles and inset, Channel, Mudflat, Breach, Pond (bottom to top)

3.2.1 Salinity and stratification

Salinities in Coyote Creek increase as the flood tide enters from Far South Bay to the west and recede on the ebb. Figure 3-5 shows salinities recorded over five tidal cycles at the east and west instrument stations during the spring 2006 study. In this and all plots in this chapter, floods are designated by the shaded areas and ebbs are unshaded. For the first half of the flood tide, the salinity increases gradually at both measurement locations as shown, for example, during year-days 74.8 – 75 and 75.3 – 75.5. During the later portion of the flood tide (e.g. year-days 75 – 75.1 and 75.5 – 75.6), the salt wedge passes by the sampling stations, arriving first at the west station (bottom, then top), followed by the east station. The arrival of the salt wedge is marked by a rapid increase in salinity that begins around year-days 75 and 75.5 and is sustained for about 2 hours, until salinities reach their peak values of 10-13 ppt. The reversal of the transport of the salt wedge on the ebb tide is steeper than its arrival on the flood; the salinity signals from each instrument station are not symmetric about the flood-ebb transition, with the decline in salinity occurring in less time than the rise. The passage of the

salt wedge on the ebb tide occurs in the reverse order as its arrival, as we would expect, with salinities diminishing first at the east station, then the west, returning to the range of 3 ppt at the end of the ebb tide.

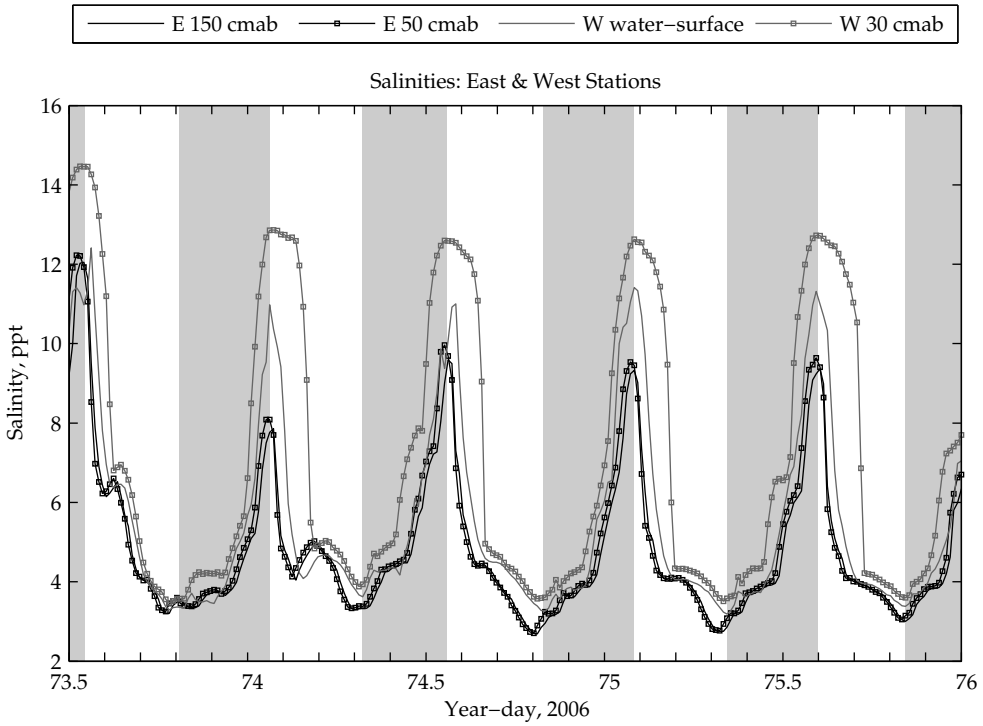

Figure 3-5: Salinities, spring 2006
East station: black lines, West station: grey lines. Floods are shaded, ebbs are unshaded. 5 tidal cycles are shown. The flood carries salty water up-estuary, and it recedes on the ebb.

Stratification in Coyote Creek is predominantly due to salt, as temperature varies over about 3 degrees C per tidal cycle, and salinity over 10 or more parts per thousand per tidal cycle. Figure 3-6 shows the vertical salinity gradient calculated as a difference between salinity sensors, divided by the vertical distance between them. For the east station (thick grey line), the CTDs were fixed to aluminum frames, separated vertically by one meter. At the west station (thin black line), the lower CTD was fixed to the frame 0.3 meters above the bed, and the upper CTD was attached to the surface line, 0.5 meters below the buoy. The measured water depth at this station was used to determine $\Delta z(t)$. During the early flood (year-days 74.8 – 75 and 75.3 – 75.5), the water column is slightly stably stratified (salinity difference of <1 ppt m^{-1}); "stable" is indicated as a negative value of $\partial s/\partial z$, where z is positive upward. As the salt wedge arrives, the stratification intensifies, starting at year-days 75 and 75.5. During the later portions of these two flood tides, the vertical salinity gradient reaches -1 ppt m^{-1}.

As the tide transitions from flood to ebb, the stratification measured at the east and west stations diverge. An unstably stratified water column rapidly develops at the east station, which persists for 1-1.5 hours (0.8 ppt m^{-1} starting around 74.6 and 75.1, respectively, in Figure 3-6). At 1-1.5 hours into the ebb tide, the salt wedge has passed by the east station (as is evident in

Figure 3-5), and the water column at the east station becomes better-mixed, with the vertical salinity gradient bouncing between -0.3 and 0.3 ppt m^{-1} for the duration of the ebb tide.

The ebb tide salinity gradient is distinct at the west station. Instead of unstable stratification developing early in the ebb, as was observed at the east station, the stable stratification intensifies with the transition from flood to ebb, reaching -3 ppt m^{-1} at year-days 74.7 and 75.2, for example. Directly after this peak in stable stratification occurs, and coincident with the passage of the salt wedge, the stratification at the west station drops to between 0 and -0.5 ppt m^{-1}, which is relatively well-mixed.

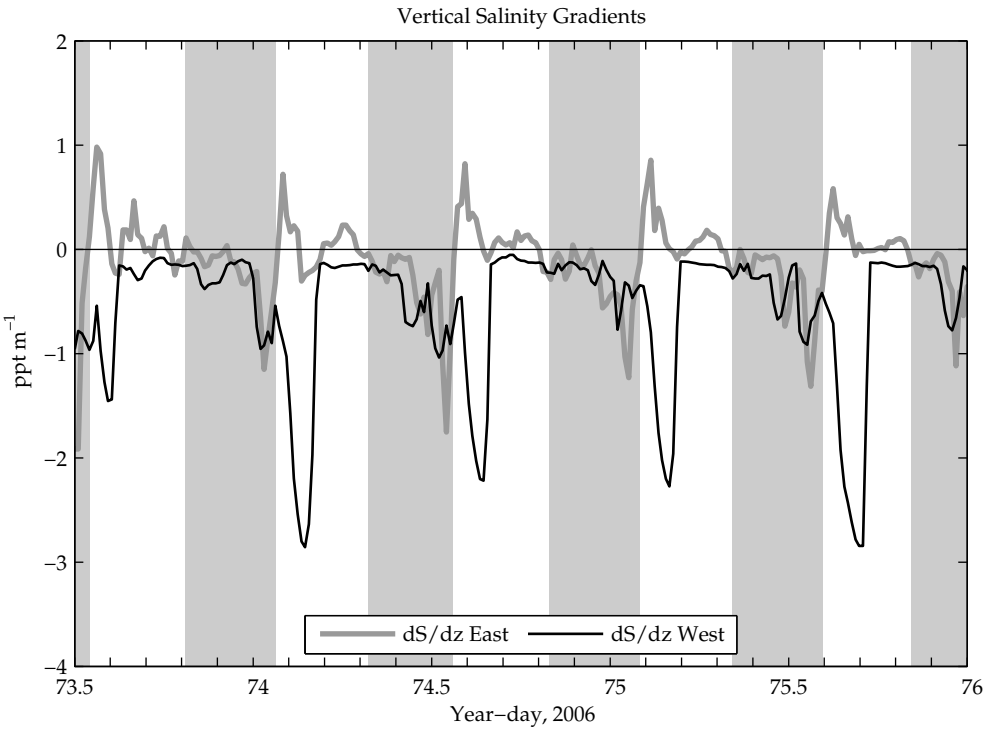

Figure 3-6: Vertical salinity gradients
Gradients are calculated as a difference between two points per vertical distance. East: grey line, West: black line. Floods are shaded and ebbs are unshaded.

3.2.2 Lateral salinity gradients

Lateral salinity differences also exist throughout the tidal cycle, as observed during boat-mounted transects in 2008. Although the measurements described here were collected at different times than the spring 2006 experiment, they are useful for establishing the pattern of lateral salinity gradients throughout the tidal cycle, particularly during the ebb. We use care not to make quantitative comparisons between experiments, but simply explore qualitatively the cycle of filling and draining of the mudflats and ponds.

The results of continuous sampling at the surface from a boat-mounted surveying experiment in July 2008 show gradients of salinity across the channel through the early ebb tide. This

survey was conducted during an extremely dry summer (0 inches of rainfall fell during May – July 2008, per NOAA, National Climatic Data Center 2008), and the surface salinities reflect the absence of freshwater: hovering around 20 ppt at high-water. Plots of salinity vs. cross-channel distance from the southern bank, as well as depth, and tidal stage, are plotted in Figure 3-7. This survey was conducted on the falling tide, and the figures show instances from the flood-to-ebb transition, and just after. At this tidal stage, salinities are slightly elevated at the banks, and depressed near the channel center.

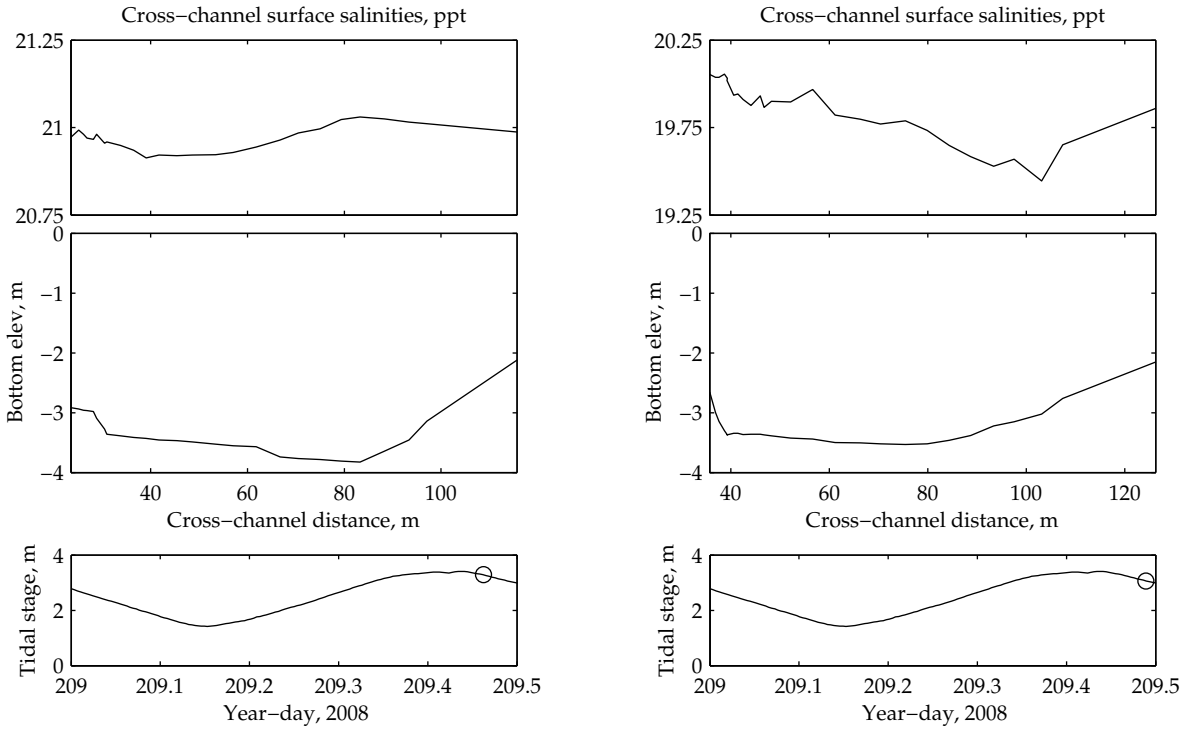

Figure 3-7: Cross-channel surface salinities: July 27, 2008
Surface salinity is shown (top panel) at two times just after high-water on July 27. The south bank is on the left of the figure, and the north is on the right. The topography of the channel cross-section is shown in the middle panel, with the bottom elevation relative to the water surface. Tidal stage is shown in the bottom panel.

Survey data collected on June 26, 2008 between mid-ebb and mid-flood show surface salinity gradients late in the ebb tide. Salinities were in the range of 10-12 ppt, and although there is variability across the channel, the shallow edges of the channel show elevated salinities during the mid and late ebb, similar to the early-ebb data collected on July 27. Figure 3-8 shows samples of cross-channel transects of surface salinity, with the channel bottom and tidal stage shown for reference.

In summary, surveys of surface salinity in Coyote Creek suggest that the shallow mudflats generally have higher salinity than the main channel on ebb tides.

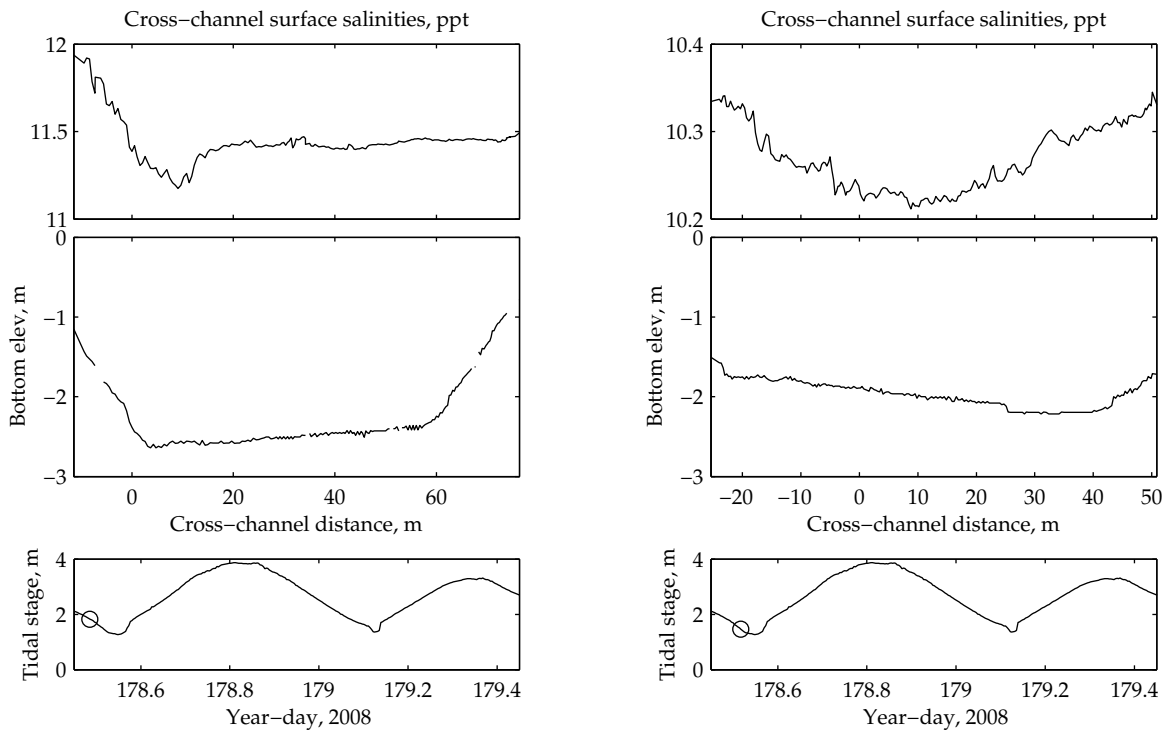

Figure 3-8: Cross-channel surface salinities: June 26, 2008
Surface salinity is shown (top panel) at two times just after high-water on June 26. The south bank is on the left of the figure, and the north is on the right. The topography of the channel cross-section is shown in the middle panel, with the bottom elevation relative to the water surface. Tidal stage is shown in the bottom panel.

3.2.3 Velocities

Velocities and vertical shear at the east station are shown in Figure 3-9. Shear, $\partial u/\partial z$, was calculated as the difference between velocity at 1.5 and 0.5 meters above the bottom, divided by 1 m, and a 1.5-hour moving average was applied prior to plotting. Flood velocities are positive and ebbs are negative. Along-channel velocities are slightly ebb-dominant, with magnitudes approximately 0.1 m s^{-1} greater than on floods (-0.5 m s^{-1} vs. 0.4 m s^{-1}). Slack tides at both high and low water are very brief, as is evident from the steeply changing velocity signals at all of the pictured tidal transitions (at each of the borders between shaded and unshaded regions). A lagged correlation of the velocities at 0.5 and 1.5 mab shows that the bottom velocity changes direction at flood-to-ebb and ebb-to-flood transitions 2-3 minutes before the velocity at 1.5 mab.

Inspection of the velocities in the top panel of Figure 3-9 gives the impression that shear resembling a boundary layer is present for most of the tidal cycle, and this is generally true; however, the shear shown in the bottom panel makes it clear that this is not always the case, particularly during ebb tides. We would expect the shear to be negative on the ebb tide (where velocities at 1.5 mab are more negative than velocities at 0.5 mab), but it is positive for brief periods, such as 74.8 and 75.8, indicating that at these times, the flow closer to the bed is moving faster down-estuary than the flow 1 m higher. This also contradicts the expected

phasing of flows at the ebb-to-flood transition, which for a boundary layer would involve low-momentum bottom flows changing direction before the high-inertia flow at the top of the water column, producing negative shear.

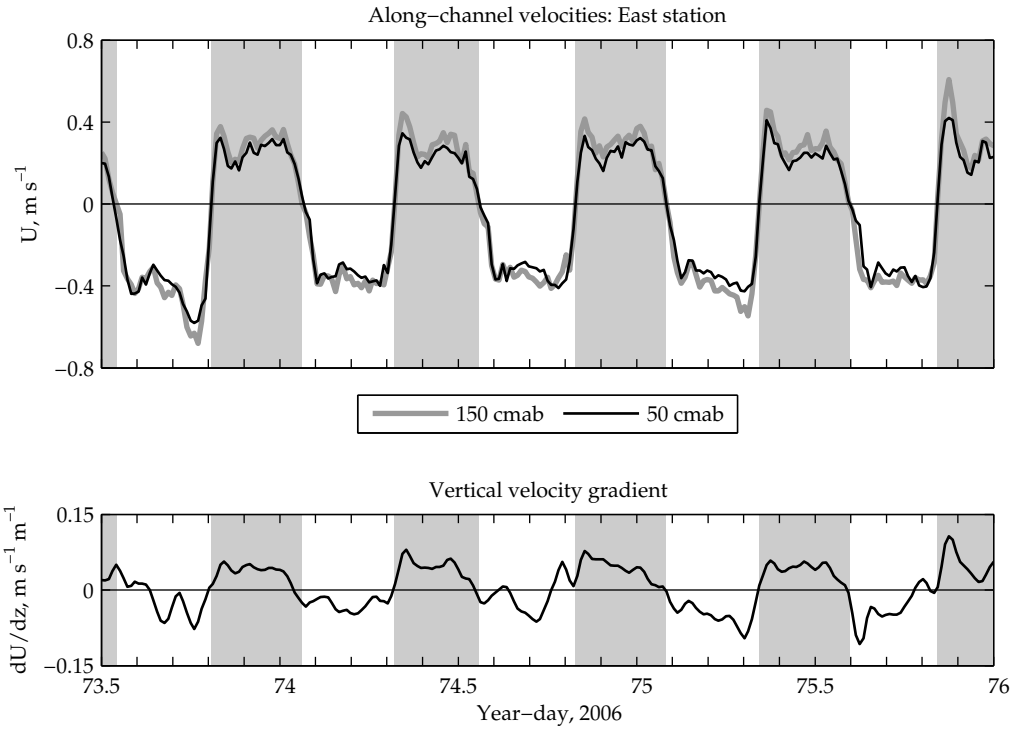

Figure 3-9: Along-channel velocities, East station
Velocities at east station (top panel) and vertical velocity gradient (bottom panel) calculated as a difference per vertical distance. Floods are shaded and ebbs are unshaded.

3.2.4 Turbulence

Reynolds stresses

Reynolds stresses were calculated from the ADV data collected at the east instrument station. Each burst was 30 seconds in duration, and 480 measurements were collected per burst, at a rate of 16 Hz. Since the burst duration is short, the Reynolds averaging window (which is temporal and not over realizations) is 30 seconds long. The deviations in velocity from the burst average were correlated with one another and averaged, resulting in the Reynolds stresses, as follows, where an overbar indicates a 30-second average, and prime indicates the deviation from the average. In the following equations, the longitudinal, lateral, and vertical velocity components are represented by u, v, and w, respectively.

(3-1) $$u = u' + \overline{u}, \; v = v' + \overline{v}, \; w = w' + \overline{w}$$

(3-2) $$\overline{u'w'} = \overline{(u - \overline{u})(w - \overline{w})}$$

(3-3) $$\overline{u'^2} = \overline{(u-\bar{u})(u-\bar{u})},\ \overline{v'^2} = \overline{(v-\bar{v})(v-\bar{v})}\ ,\ \overline{w'^2} = \overline{(w-\bar{w})(w-\bar{w})}$$

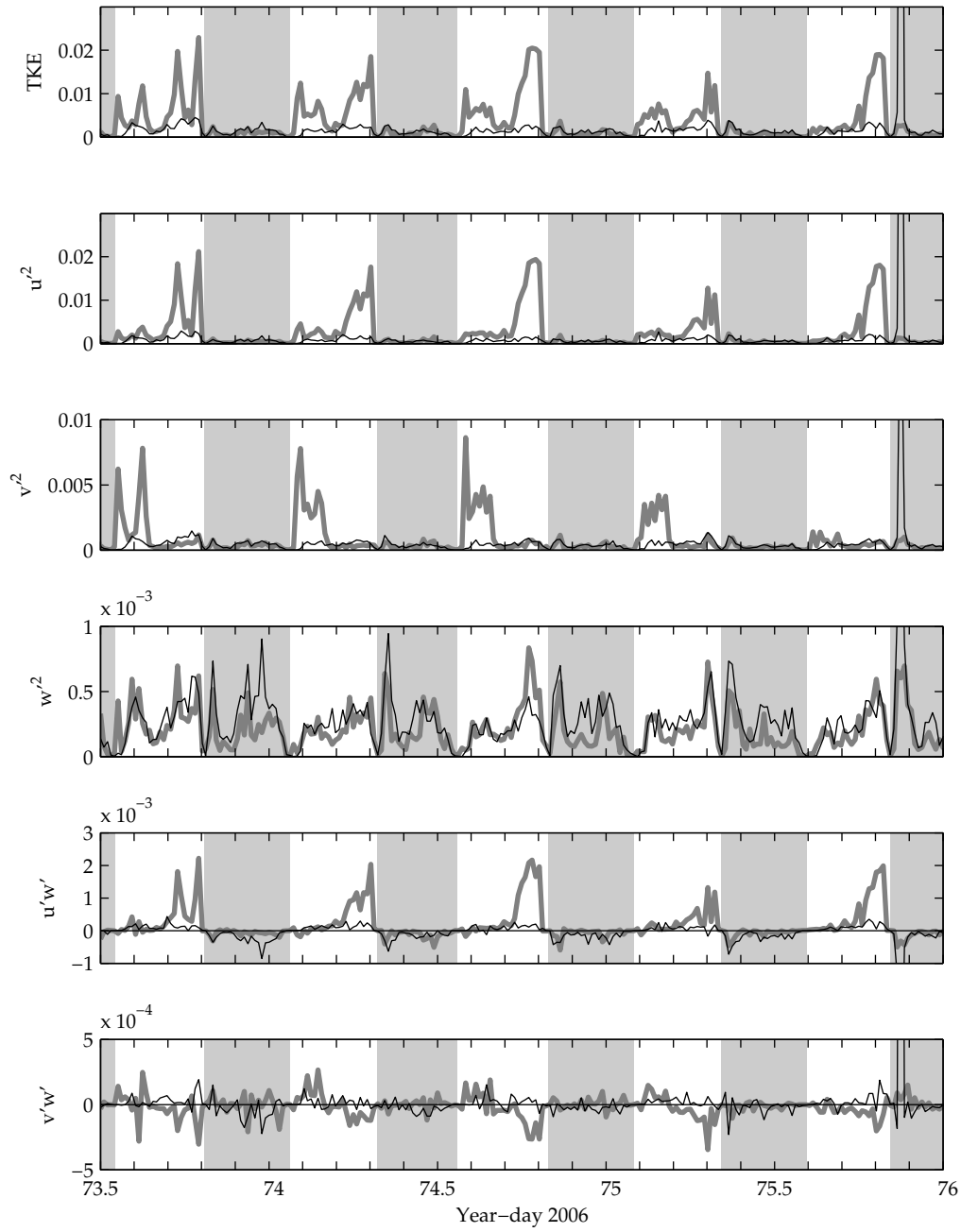

Figure 3-10: Reynolds stresses and TKE from ADVs at East station
All panels: 150 cmab (thick grey line), 50 cmab (thin black line). Units: $m^2\ s^{-2}$. Horizontal normal stresses at 150 cmab exhibit strong ebb-flood asymmetries; vertical normal stresses are mostly symmetric. Floods are shaded and ebbs are unshaded.

This calculation was performed for $\overline{u'w'}$, which represents the vertical turbulent flux of longitudinal momentum, and $\overline{v'w'}$, which is the vertical turbulent flux of lateral momentum. The normal Reynolds stresses are shown in equation 3-3, and their sum is defined as the turbulent kinetic energy (TKE), or q^2. Figure 3-10 shows the variation of turbulent kinetic energy as well as the shear and normal stresses over the five tidal cycles within the spring 2006 experiment which are the focus of this chapter. TKE, shown in the top panel, is much greater on ebbs than floods at 150 cmab; this asymmetry is present but much less pronounced at 50 cmab. There are two distinct peaks in magnitude on each ebb tide for the top ADV. The second and third panels show $\overline{u'^2}$ and $\overline{v'^2}$, respectively. Both are higher on ebbs than floods for both ADVs. At 150 cmab, $\overline{u'^2}$ reaches a maximum late in the ebb tide of around 0.02 m^2 s^{-2}, and $\overline{v'^2}$ reaches its peak early in the ebb tide of about 0.01 m^2 s^{-2}. $\overline{w'^2}$ is an order of magnitude lower than the other two normal stresses, and is more symmetric over floods and ebbs, with slightly higher values on ebbs (4th panel of Figure 3-10). Also, the vertical variation in $\overline{w'^2}$ is much lower than the other components of the Reynolds stresses. The turbulent shear stresses are shown in the 5th and 6th panels, and at 150 cmab, the flux of longitudinal momentum, or $\overline{u'w'}$, is an order of magnitude higher than $\overline{v'w'}$. Shear stresses on floods and ebbs are more symmetric at the lower ADV. Turbulent fluxes of lateral momentum do not exceed 3×10^{-4} m^2 s^{-2}, or 3 cm^2 s^2. Fluxes of along-channel momentum, however, reach values of -5 cm^2 s^{-2} on floods and 20 cm^2 s^{-2} during the second half of the ebb tides. (Note that the signs of the along-channel Reynolds stresses make sense: the vertical and longitudinal fluctuations are inversely correlated, and since u is positive on floods and negative on ebbs, $\overline{u'w'}$ is negative on floods and positive on ebbs.) TKE and the Reynolds stresses that are shown in Figure 3-10 indicate that the ebbs contain more energetic turbulence than floods, with the greatest asymmetry measured at 150 cmab.

The stark tidal asymmetry in Reynolds stresses at 150 cmab and the great difference between measurements at the two ADVs warrant further investigation. The elevated Reynolds stresses at the ADV at 150 cmab compared with the lower stresses at 50 cmab point to a mechanism that acts from the top of the water column, and wind-wave contamination is a possibility. To assess the general importance of wind speed and direction on the magnitude of the Reynolds stresses, we compared wind measurements collected in Palo Alto, California (NOAA, National Climatic Data Center 2008), the closest wind data available, with observed Reynolds stresses. Figure 3-11 shows the shear stresses, $\overline{u'w'}$ and $\overline{v'w'}$, versus wind magnitude in miles per hour in the top panel. The bottom panel shows the dependence of the stresses on the components of wind in the same direction as the along-channel velocity (U) and the cross-channel velocity (V). The wind speed and direction of origin were rotated onto the principal flow axes. Inspection of Figure 3-11 shows that there is no convincing relationship between wind and turbulent motions. While there are elevated stresses that correspond to high wind speeds, there are just as many instances of elevated stress and low wind speed.

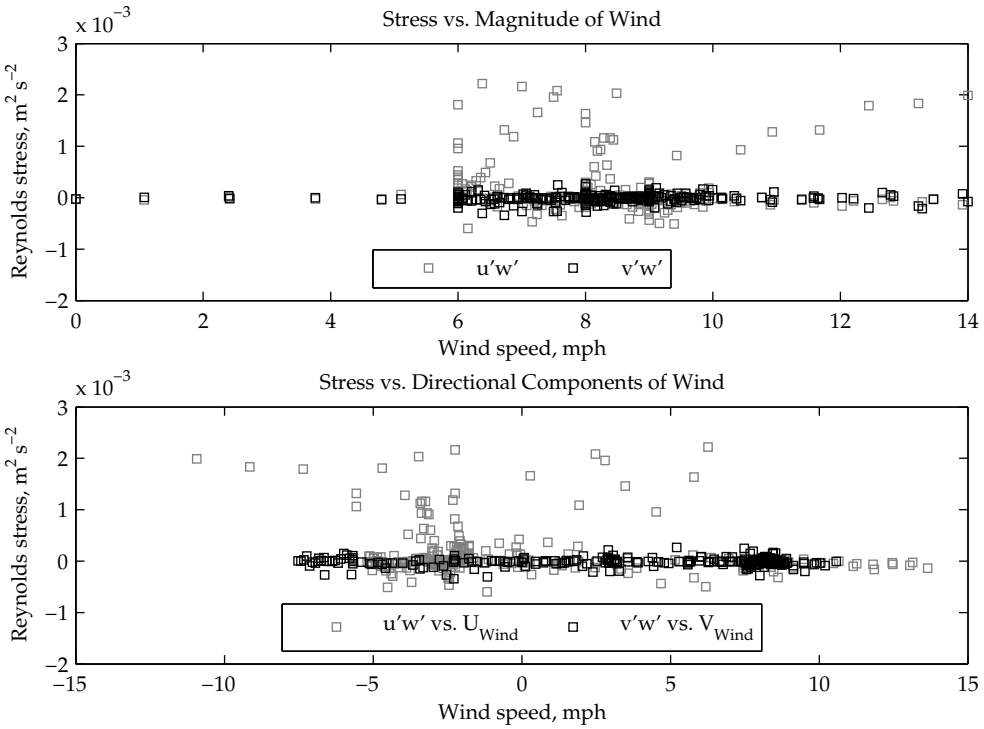

Figure 3-11: Wind and shear stresses
Shear stresses are plotted against wind magnitude (top panel) and wind speed (bottom panel). Wind was measured 15 km from the field site which could explain the lack of a coherent dependency.

In addition to looking for a general dependency on wind, waves due to wind were also investigated. Two methods of decomposing wave-generated motions from turbulence were employed, referred to here as the "Bricker" method (Bricker & Monismith 2007) and the "Benilov" method (Benilov et al. 1974). The Bricker method is a spectral method that uses data from a single ADV to separate wave motions from turbulence records. The Benilov method uses collocated measurements of velocity and pressure to identify wave-driven velocity fluctuations, which are assumed to be correlated with changes in water surface elevation detected by the pressure sensor. Figure 3-12 shows the turbulent stress that remains after wave motions were removed, as well as the original data for comparison. The difference is minimal. Applying these methods far from the bed (e.g. > 1 m) carries the risk of confusing wave-stretched turbulence with wave-motions, with the result that turbulent stresses are removed during the decomposition (Bricker & Monismith 2007). Given this, and the very minor difference between the measured stresses and the decomposed stresses, we conclude that the observed Reynolds stresses at the end of the ebb tides are not wave motions.

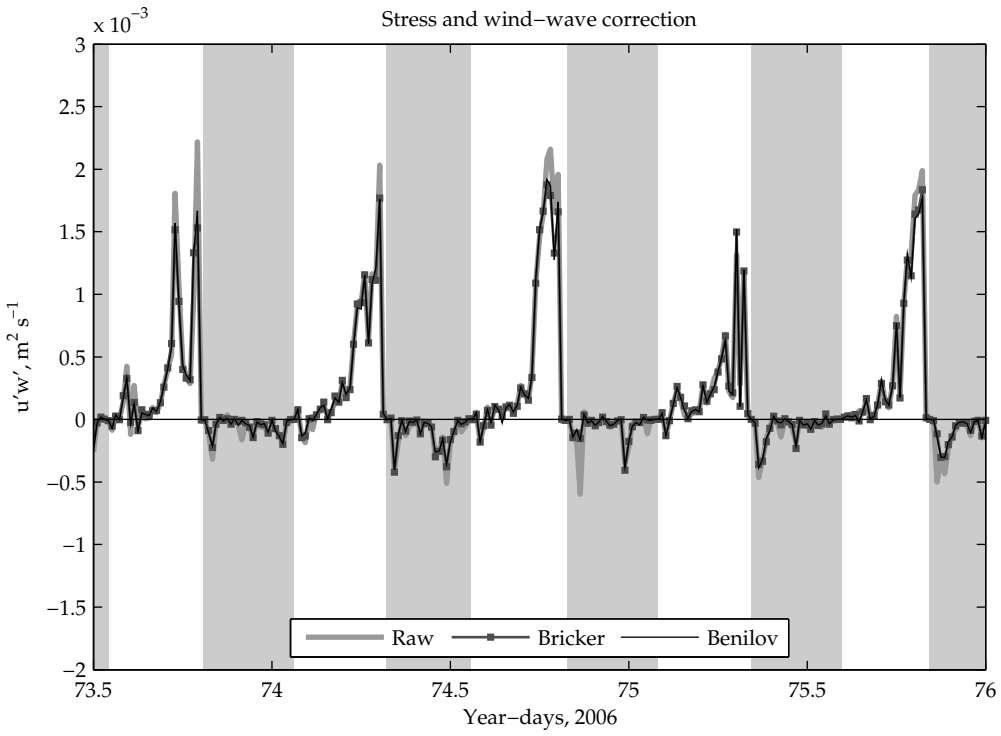

Figure 3-12: Wave/turbulence decomposition
The stresses as measured by the East 150 cmab ADV (thick grey line) are compared to the stresses with wind-waves removed using the Bricker (line with square marker) and Benilov (thin black line) decompositions. The similarity between the raw and decomposed stresses indicates that wind-wave contamination was not significant.

It is not surprising that a correlation between Reynolds stresses and wind speeds measured in Palo Alto is not discernable, given that they are separated by 15 km over variable topography; however, the fact that Reynolds stresses are not contaminated by wind waves as shown by two turbulence-wave decomposition analyses is compelling evidence that wind is not the mechanism responsible for the high Reynolds stresses at 150 cmab. In light of this, the most plausible explanation for these motions is an interaction with topography that produces persistent generation and shedding of vortices. Examination of the Reynolds stresses shows that the vertical fluctuations ($\overline{w'^2}$) do not exhibit the same degree of tidal asymmetry as the horizontal motions, and that the vertical motions at 150 cmab are very similar in magnitude and structure to those at 50 cmab. If we assume that the anisotropies of turbulent shear and normal Reynolds stresses at our instrument station can be closely represented by those measured in open channel flow experiments (Stacey et al. 1999a; Stacey et al. 1999b), then we can estimate the contribution of turbulence to the stresses without the effects of vortex shedding from a local topographic feature. Ratios of normal stress to TKE of $\overline{w'^2}/q^2 = 0.17$ (Nakagawa & Nezu 1993) and shear stress to TKE of $\overline{u'w'}/q^2 = 0.1$ (Soulsby 1981; Roussinova et al. 2009) were used to estimate TKE and $\overline{u'w'}$, and these values are compared to the measurements at 50 cmab in Figure 3-13. This method provides very good agreement between measured values of TKE and vertical fluctuations at 50 cmab and estimated values at 150

cmab. This method also shows that stresses are fairly symmetric between ebb and flood. For the analysis that follows, these values of the Reynolds stresses will be used.

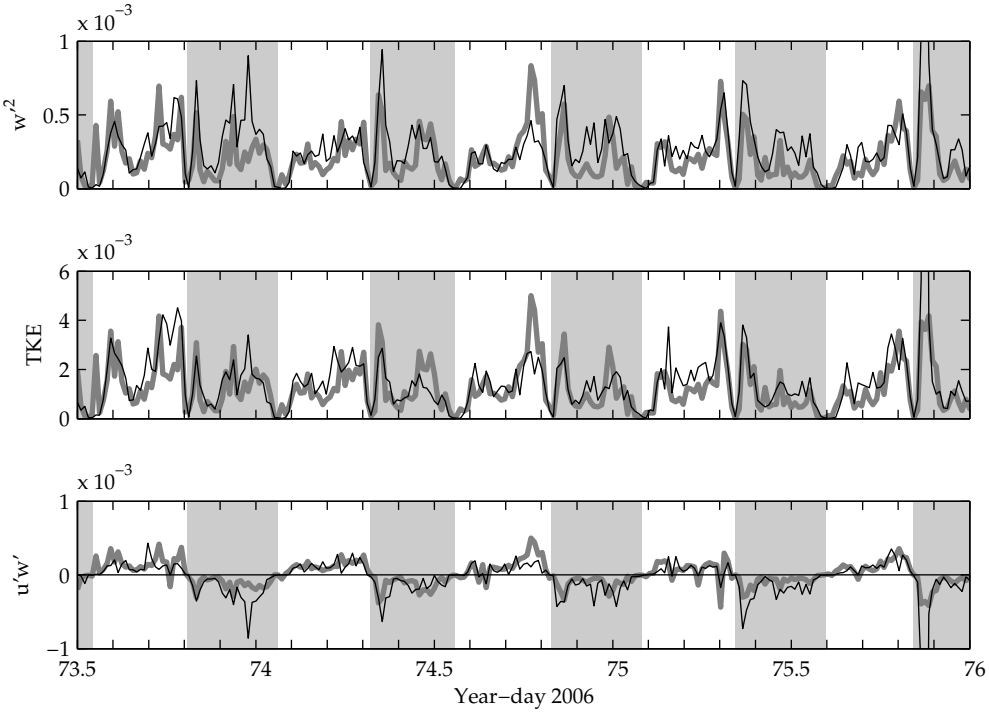

Figure 3-13: Reynolds stresses from anisotropies
Top panel: measured values at 50 (thin black line) and 150 cmab (thick grey line).
Middle and bottom panels: measured values at 50 (thin black line), calculated values at 150 cmab (thick grey line) using published anisotropies. Bottom panel: the sign at 150 cmab was assumed to be the same as the sign at 50 cmab. Floods are shaded and ebbs are unshaded.

Drag coefficient

Turbulence quantities are an integral part of the dynamics of stratification, and since they were not measured with the ADCP, scaling arguments are used to provide insight into turbulent processes at the west station. Specifically, a drag coefficient is calculated as a function of Reynolds stresses measured by the ADVs and the velocity at 1.5 mab:

$$C_D = \frac{\overline{u'w'}}{U^2} \tag{3-4}$$

The velocity at 1.5 mab was used for this calculation because this is the elevation of the lowest velocity measurement made by the 600 kHz ADCP and will provide a consistent quantity to use for scaling across instrument stations. By definition, the drag coefficient C_D is a function of the bed stress, and so the $\overline{u'w'}$ values used here were recorded at 0.5 mab – the sampling location closest to the bed. Bed stresses ought to be measured at a distance from the bed that is less than 10% of the water depth, but such data are not available. The resulting drag

coefficient is 0.002, which is similar to the value of 0.0022 for mud reported by Dyer (1986, p.77).

Friction velocities were computed for each instrument station and the results throughout the tidal cycle are compared. The friction velocity, u_*, is defined as a function of the bottom shear stress, τ_b, (equation 3-5a) and can be scaled using a drag coefficient, C_D, (equation 3-5b):

$$u_* = \sqrt{\frac{\tau_b}{\rho}} \quad \text{(3-5a)}$$

$$u_* = C_D^{1/2} U \quad \text{(3-5b)}$$

Where Reynolds stresses were measured (east and center stations), equation 3-5a was used to calculate the friction velocity, and where they were not (west station), equation 3-5b was used. The results of these calculations are shown in Figure 3-14. The estimates of friction velocity have reasonable agreement in terms of structure. Magnitudes vary by as much as a factor of two, however this difference would not change the outcome of analyses presented in later sections.

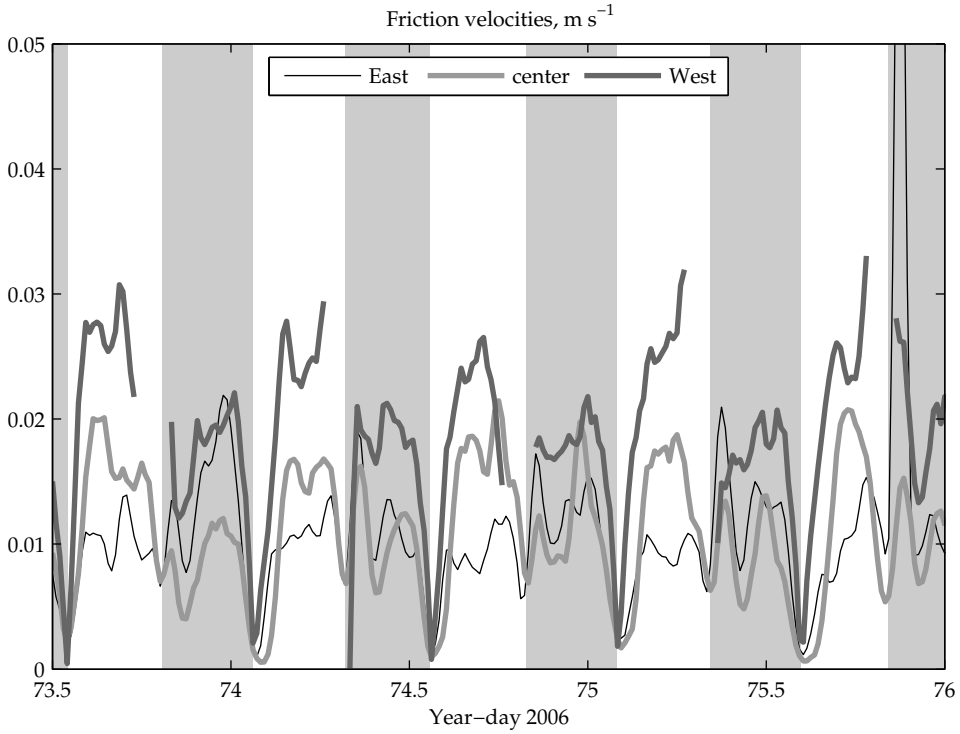

Figure 3-14: Friction velocities, spring 2006
Friction velocities calculated from measured Reynolds stresses are shown for the east (thin black line) and center (thick light grey line) stations. Friction velocity estimated using a drag coefficient is shown for the west station (thick dark grey line) where stresses were not measured. Floods are shaded and ebbs are unshaded.

In summary, our field experiments depict a tidal channel that is stratified on flood tides and has moderate turbulent fluxes of momentum. On ebb tides, two pictures emerge: the down-estuary (west) instrument station experiences strengthened stable stratification, while the up-estuary (east) station becomes strongly unstably stratified, and then well-mixed. Turbulent fluxes are not damped on ebb tides.

3.3 Discussion

This section provides a conceptual model of stratification and the evolution of the salt field based on our field measurements. The goal is to reconcile our observations in Coyote Creek with the established understanding of a tidally strained, partially-mixed estuary. While no single experiment of either moored or boat-mounted instruments yielded adequate spatial and temporal coverage to construct this conceptual model, an integrated view of the observations described in the previous section provides a description of the complex interaction between flows and bathymetry that produces these dynamics. The general picture is one of a primary salinity gradient, or salt wedge, that is advected up- and down-estuary with the tides. Our spring 2006 deployment of instruments was positioned at the up-estuary reach of the salt wedge. Vertical mixing is periodically important, consistent with partially-mixed estuarine dynamics, but interactions with bathymetry result in major departures from the classical framework. Specifically, exchange with the salt ponds and mudflats results in modifications to velocities (both longitudinal and lateral) as well as density gradients, which are described here in the context of one tidal cycle.

3.3.1 Tidal straining

The differences between our data and the classical model of tidal straining warrant a detailed investigation. Simpson et al. (1990) first parameterized the competition that arises from turbulent mixing due to tidal stirring and stratification that results from straining of the salinity field with what is now known as the Simpson Number (Stacey 2009). Also referred to as the horizontal Richardson number, this dimensionless quantity is high when stratification from straining cannot be overcome by tidal stirring, and low when barotropic velocities are high enough to overwhelm stratification from freshwater inflow.

$$Si = \frac{g\beta \frac{\partial S}{\partial x} H^2}{u_*^{\,2}} \qquad (3\text{-}6)$$

The numerator contains the gravitational constant, g; the saline expansivity, β (with a value of 7×10^{-4} ppt^{-1} per El-Shaarawi & Piegorsch 2002, p.1862); the longitudinal salinity gradient, $\partial S/\partial x$; and the square of the depth, H^2. The denominator contains the square of the friction velocity, u_*. In their experiment in Northern San Francisco Bay, Stacey et al. (2001) find that the threshold value of the Simpson Number is order 1, but in a subsequent numerical study, Li et al. (2008) find a much lower value of 0.2.

It is important to note that the interpretation of the Simpson number on floods is different than on ebbs. Stacey et al. (2001) explain that the idea of a threshold between mixing from tidal stirring and stratification from straining is premised on the assumption that buoyancy is a sink for turbulent energy – that tidal straining leads to stable stratification, as is expected on ebb tides. On typical flood tides, however, when the longitudinal salinity gradient is strained such that convective instabilities are created (Burchard & Baumert 1998), both buoyancy and shear production are responsible for the creation of turbulence. In this instance, high Simpson numbers *do not* indicate that stable stratification overwhelms turbulent motions, but rather that buoyancy – in addition to shear production – is a significant source of turbulent energy. Simplistically speaking, the distinction lies in whether the barotropic and baroclinic pressure gradients are aligned (typical floods) or opposed (typical ebbs).

In an effort to lend clarity to the difference between floods and ebbs, we multiply the Simpson number by the sign of the along-channel velocity. This results in negative Simpson numbers for flood tides (when $ds/dx < 0$ and $u > 0$), and positive values for ebb tides (when $ds/dx < 0$ and $u < 0$). Negative Simpson numbers should be interpreted as the balance between turbulence from buoyancy vs. shear production, and positive Simpson numbers represent the competition between turbulence from shear in tidal flows and stratification from straining of the longitudinal salinity gradient.

The signed Simpson number is shown for the east (thin black line) and west (thick grey line) stations in Figure 3-15 (panel a). The longitudinal salinity gradient (panel b) was calculated as a difference of depth-averaged salinities at the east and west stations, which are 980 meters apart. The squared friction velocities are shown in panel c. The vertical salinity gradient is also shown (panel d) to provide a complete picture of the degree of stratification present at these times for comparison with the Simpson number. While the precise threshold value isn't clear from the data, periods of high and low Simpson numbers stand out, and they contrast with the level of stratification measured in Coyote Creek. For example, late in each flood, the magnitude of the Simpson number is very high, and the sign is negative, suggesting that buoyancy is an important source of turbulence at these times; however, Coyote Creek is stably stratified late in the floods at both instrument stations (panel d), and buoyancy therefore is a sink for turbulence. In addition, turbulent motions are relatively small at these times compared to ebb tides and early floods (as represented by the friction velocities shown in panel c). Early in the ebb tides (e.g. times 74.1, 74.6 and 75.1), when the Simpson number is high and positive, we would expect to find stable stratification and damped turbulence. At the west station, this is what was observed, and the stable stratification (panel d) reaches a maximum during the early ebb tides. At the east station, however, stratification is unstable (1 ppt m^{-1}), and fluctuations of vertical velocity are on the order of 3 – 5 cm^2 s^{-2}.

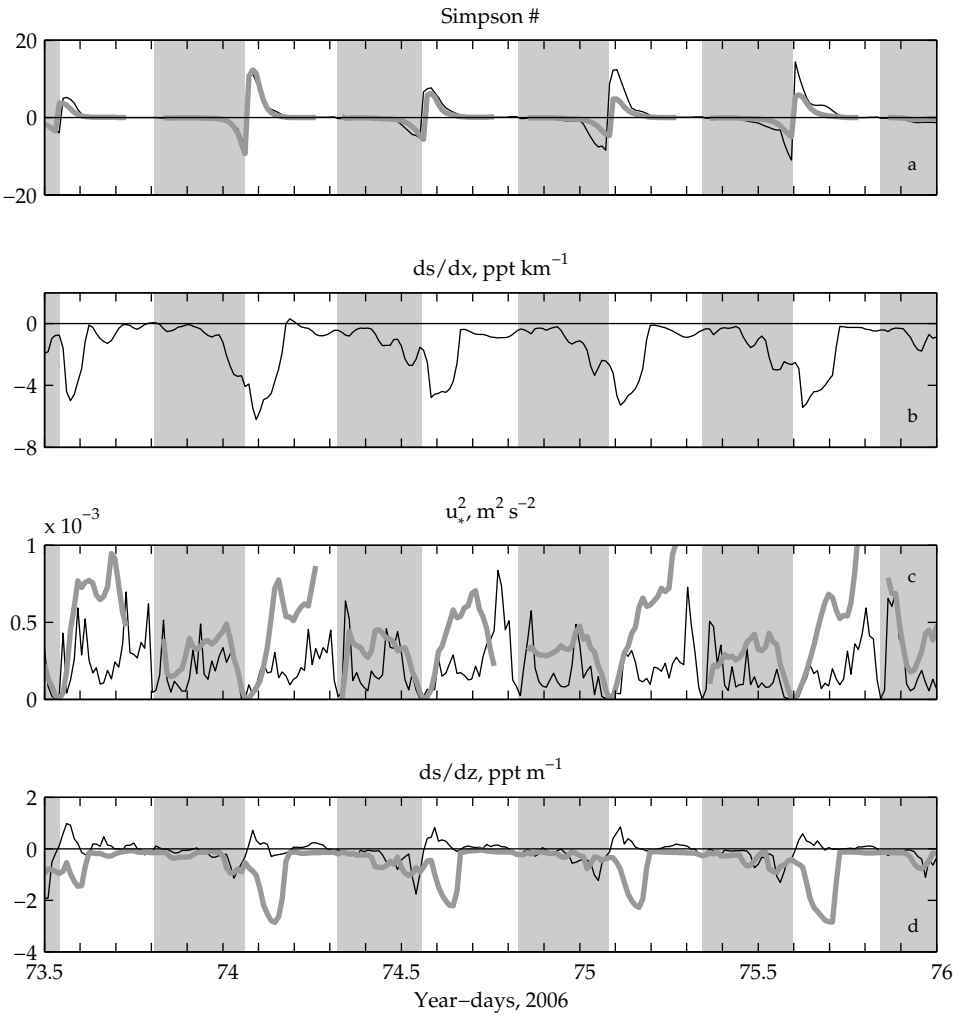

Figure 3-15: Simpson numbers
East station: thin black line, West station: thick grey line

To discern what these measurements mean for mixing, the potential for turbulence to work against stratification must be considered. A useful parameter for expressing this balance is the dimensionless gradient Richardson number, which compares the strength of turbulence generated by vertical shear in the water column to the strength of stratification to dampen turbulent motions, as follows (Dyer 1973):

$$Ri_g = -\frac{g}{\rho}\frac{\partial \rho}{\partial z}\Big/\left(\frac{\partial u}{\partial z}\right)^2 \qquad (3\text{-}7)$$

In this equation, g is gravitational acceleration, ρ is density, u is longitudinal velocity, and z is distance above the bed. The water column is stably stratified if Ri_g is positive and unstably stratified if it is negative, and the critical value for mixing is taken to be approximately 0.25; above 0.25, buoyancy inhibits turbulence from shear and stratification remains. Gradient

Richardson numbers were calculated for both east and west instrument stations, and are shown in Figure 3-16. Note that the vertical axis is a log scale, and therefore doesn't show periods of unstable stratification; the critical value of 0.25 is plotted as a horizontal line. A 1.5-hour moving average was applied to the calculation prior to plotting. This calculation shows that at the east station, the balance between turbulence and stratification favors stratification on floods, and turbulence on ebbs, which contradicts tidal straining theory. The highest Richardson numbers occur late in the flood tides, such as at times 74 and 75.6 in Figure 3-16, indicating that at these times, stratification inhibits turbulent mixing; however, on ebb tides, Richardson numbers at the east station are largely negative (and therefore not shown in the figure) or positive but lower than 0.25, indicating that the velocity shear is adequate to mix out the vertical salinity gradient. At the west station, Richardson numbers are highest at mid-ebb, and are generally below the value of 0.25 around low-water: during the late ebb and early flood.

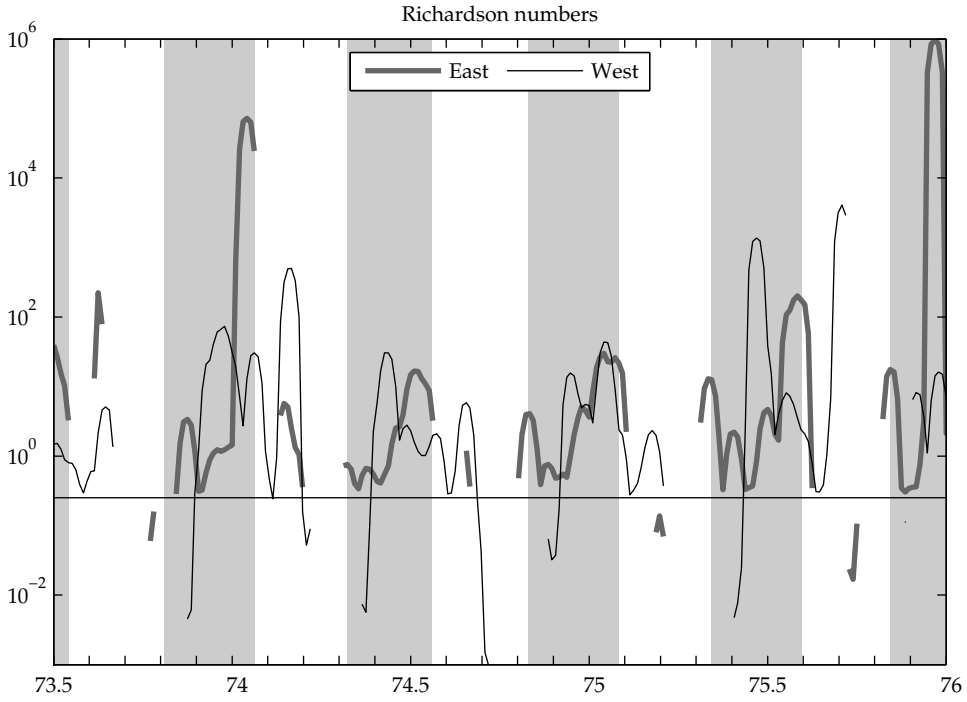

Figure 3-16: Richardson numbers
The typical threshold for mixing is Ri_g < 0.25, plotted as a horizontal line. Grey shading denotes flood tides.

In summary, the magnitude of the Simpson number, which is a function of the ratio of the longitudinal salinity gradient to the friction velocity, is high at the end of the floods and the start of the ebbs. The longitudinal salinity gradient is also great at these times, reaching values of -5 ppt km^{-1}, while typical values for San Francisco Bay are on the order of -0.5 ppt km^{-1}. (This is not the first time such high values have been observed in tidal sloughs in San Francisco Bay; Ralston & Stacey 2005a; Ralston & Stacey 2005b.) The elevated Simpson numbers are therefore unsurprising, however, their interpretation contrasts with calculated gradient Richardson numbers, particularly at the east instrument station. The following sections will explore the role of bathymetry in producing these unexpected results.

3.3.2 The flood tide

The tidal straining mechanism, combined with bottom stirring, would normally be expected to produce a well-mixed water column for the duration of the flood tide, but this is not what the data show in Coyote Creek. Rather, vertical salinity gradients shown in Figure 3-6 indicate that the flood tides are well-mixed to start (where $\partial s/\partial z < -0.5$ ppt m^{-1}), but become stably stratified when the salt wedge arrives, reaching values of -1 ppt m^{-1}.

Measured Reynolds stresses (shown in Figure 3-10) are low on the flood tides, particularly in the latter portion when the salt wedge is present, and along with the non-dimensional Richardson numbers, they corroborate the picture that mixing is inhibited on flood tides. This is in direct contrast with the accepted model of tidal straining, in which the alignment of the pressure gradients from the incoming tidal wave and the along-estuary density gradient lead to convective instabilities and mixing (Burchard & Baumert 1998). Nevertheless, this is not the first time stratification has been observed to be enhanced on the flood tide in a tidal channel (Lacy et al. 2003; Ralston & Stacey 2005; Ralston & Stacey 2005). Ralston & Stacey (2005b) observed a similar pattern of intensification of stratification behind the salt wedge on the flood tide in tidal channels that cut through mudflats in northern San Francisco Bay. Through idealized numerical modeling, the authors confirmed that it was a result of lateral exchange with adjacent shoals. We propose that the same dynamics are present in Coyote Creek. On the flood tide, differential advection concentrates the highest salinity flow along the channel center, with fresher water over the mudflats (Nunes & Simpson 1985; Lerczak & Geyer 2004). Superposed onto the barotropically-driven filling and draining of the system, this sets up a density-driven, lateral exchange, which enhances stable stratification in the channel in two ways: first, heavy waters flow outward onto the mudflat, and lighter water is returned to the channel at the surface, which creates stratification directly by delivering a source of buoyancy to the surface layer. Second, the lateral exchange causes flow with diminished momentum to enter the channel, modifying the upper portion of the vertical velocity profile to produce a maximum that occurs beneath the surface. This modified velocity profile then strains the longitudinal density gradient such that stratification is created and reinforced above the velocity maximum.

The observations collected in Coyote Creek show that near-surface along-channel velocities in Coyote Creek on the flood tide were lower than the maximum, which occurred deeper in the water column. Figure 3-17 shows velocity profiles collected by a 600 kHz ADCP at the west station. This instrument, operating in Water Mode 1, was bottom-mounted and sampled the flow velocity from 1.6 mab to 30-40 cm below the water surface, in 50 cm increments. The distance from the instrument face to 1.6 mab is called the "blanking distance", and no measurements are recorded by the ADCP within this range. Therefore, Figure 3-17 shows only roughly the top half of the water column, and vertical axes for panels a – c reflect the blanking distance. While this vertical coverage is limited, it does clearly show that the flood velocity maximum occurs below the water surface, which is a result of the low-momentum water entering the channel surface from the mudflats. Panels a – c show three profiles of longitudinal velocity for each of three flood tides. The profiles are 15 minutes apart and the specific timing is shown in panel d, which plots tidal stage (depth) versus time. The flood

velocity is positive (up-estuary), and for each flood tide, the velocity diminishes upward of 1.5 mab.

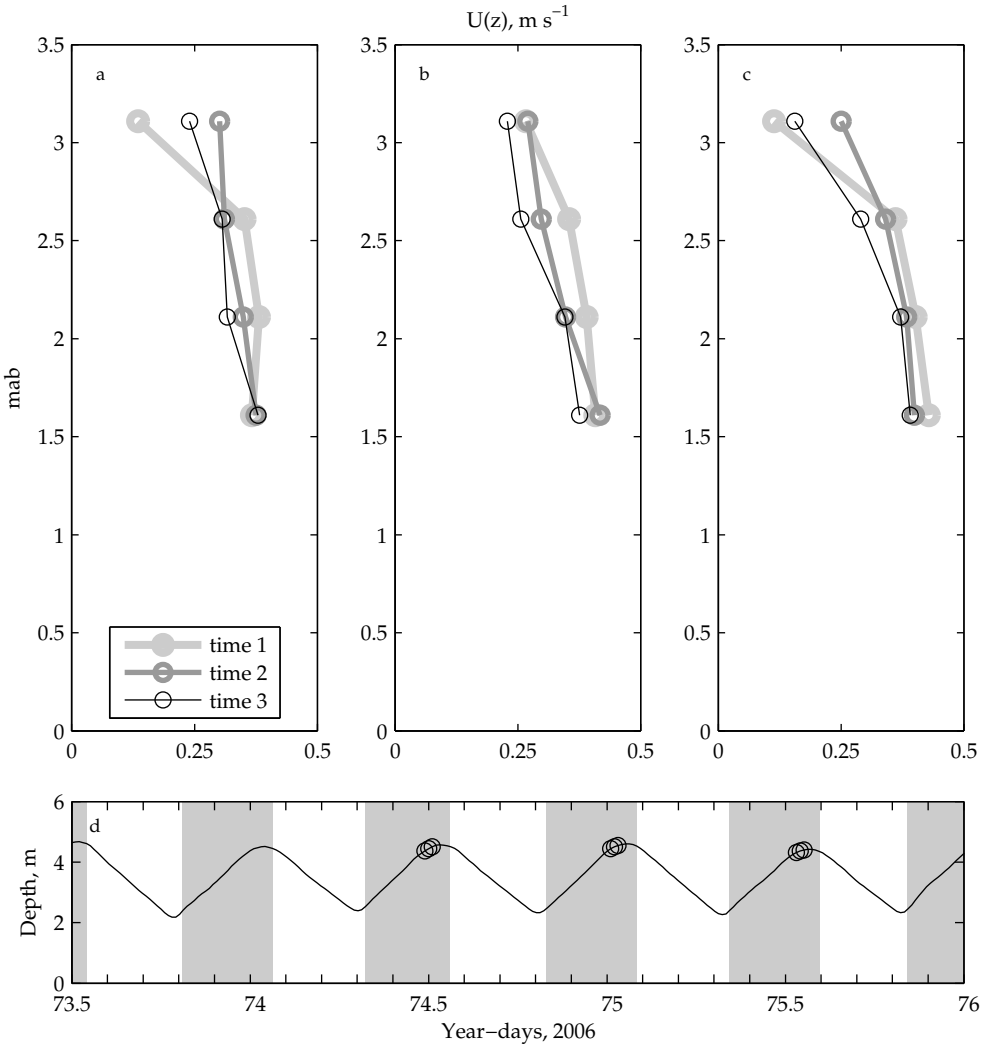

Figure 3-17: U(z), West station
Panels a – c show velocity profiles during three late flood tide periods, which are shown as circles on the plot of depth in panel d. The time between profiles within a panel is 15 minutes. Flood velocities are positive. For each period shown, the maximum velocity occurs beneath the water surface, at or below 1.6 mab.

Equivalent plots of lateral velocity profiles for the same times are shown in Figure 3-18. Zero velocity is shown for reference (vertical lines, panels a – c), and positive values indicate flow toward the ponds and broad mudflats on the north bank of Coyote Creek. While the lateral velocity is visibly sheared, a distinct and consistent lateral circulation is not discernable with this coverage and resolution. The instrument station would have had to be located within one of the two lateral circulation cells in order to capture the exchange, and ours was likely near the convergence/divergence zone between the cells. Winds, which were predominantly out of the

south during the period shown (NOAA, National Climatic Data Center 2006), could also be a confounding factor.

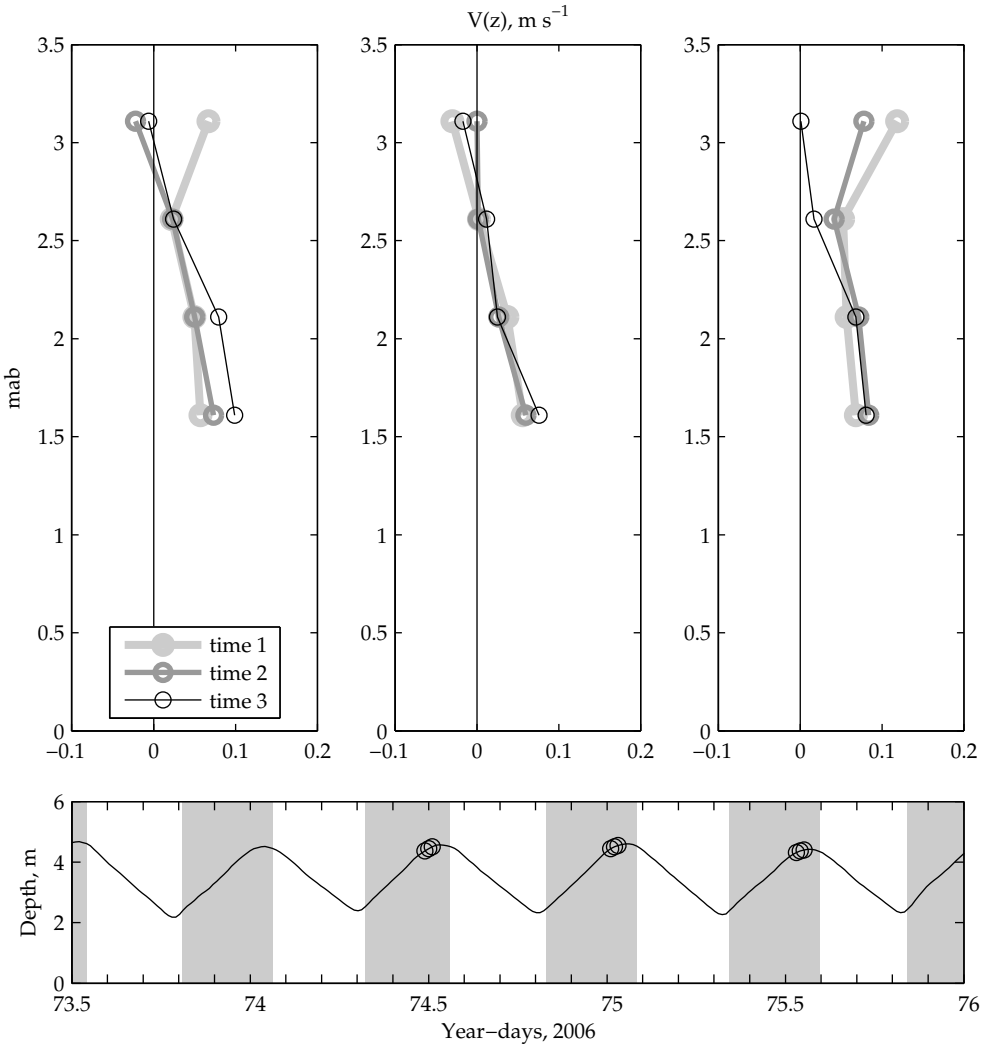

Figure 3-18: V(z), West station
Panels a – c show velocity profiles during three late flood tide periods, which are shown as circles on the plot of depth in panel d. The time between profiles within a panel is 15 minutes. Flood velocities are positive. For each period shown, the maximum velocity occurs beneath the water surface, at or below 1.6 mab.

While the lateral velocity data do not directly illustrate a consistent exchange with the mudflats, the observations of the modification to the along-channel velocity profile support the conclusion that lateral circulation is responsible for the stratified flood tides in Coyote Creek. This circulation (shown in Figure 3-19) and subsequent modification of the velocity structure have been observed previously, and are evident in field observations as well as numerical models (Ralston & Stacey 2005; Ralston & Stacey 2005; Lerczak & Geyer 2004). The authors concluded that the velocity modification by lateral exchange was responsible for the stable stratification they measured on the flood, where the fastest-moving flow brought salty water

up-estuary, underneath the slower transport at the surface. They assumed that the portion of the water column below the velocity maximum was well-mixed, consistent with the destabilizing straining of the salinity field within the boundary-layer shear described above.

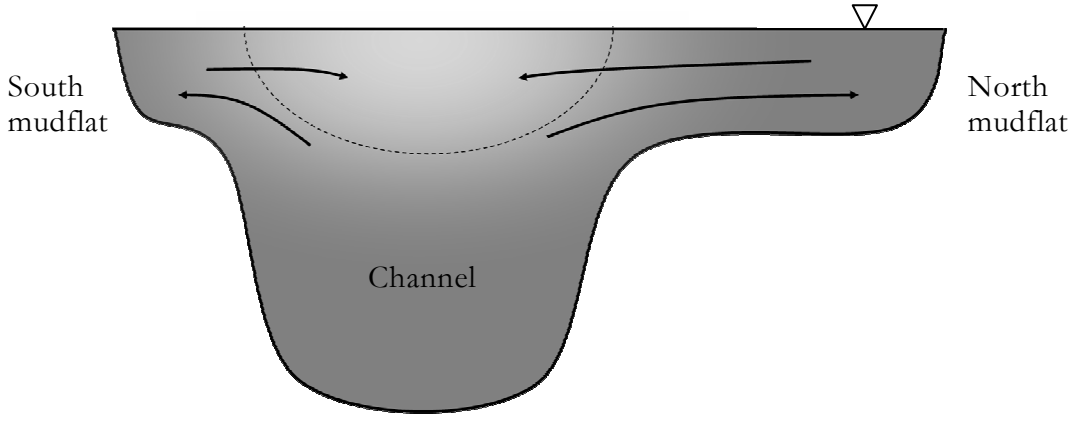

Figure 3-19: Schematic of lateral circulation between channel and mudflats
Lighter shading indicates locations of low salinity water, and darker shading shows regions of high salinity. On flood tides, differential advection leads to a transverse salinity gradient which drives a baroclinic two-celled circulation. Fresher water is delivered to the surface of the channel, creating a convergence. Arrows show the direction of the circulation.

3.3.3 The ebb tide

The ebb tide in Coyote Creek at the east instrument station is characterized by levels of turbulence equal to or exceeding those observed on the floods, and a salinity profile that transitions from unstably stratified to well-mixed, while the theory of tidal straining predicts stable stratification and diminished mixing on ebb tides. The west station adheres to a more standard ebb-tide model of stratification, and the remainder of this chapter will focus on the east instrument station. Our measurements show that interaction with bathymetry overwhelms the classical picture of the ebb tide by shearing horizontal velocities, which then strain local density gradients.

Bathymetrically generated velocity shear

At the east instrument station in Coyote Creek, the influence of the local bathymetry on the ebb-tide flow velocity is clear in the measurements. The east station was positioned inside the channel, close to the transition between the channel and the southern mudflat. Specifically, as the ebb begins, flow at 0.5 mab reverses in the along-channel direction with an almost-zero lateral component. Flow at 1.5 mab, on the other hand, experiences a strong pulse of cross-channel velocity as the along-channel component reverses direction. Vectors of velocity at 50 and 150 cmab measured around high-water at 15-minute intervals are plotted in Figures 3-20 and 3-21. Depth is shown as a function of time in the bottom panel, and the color of the depth value corresponds to the color of the velocity vector, showing tidal stage for each vector. Two individual flood-ebb transitions are shown. For both periods pictured, velocity vectors at both elevations are oriented up-estuary (to the east) at high water. As the depth decreases and the transition to ebb proceeds, the velocity vectors at the upper ADV (150 cmab) swing

through a counter-clockwise rotation. In both cases, two to three vectors have a significant northward component, indicating that the marsh to the south of the instrument station is draining into the channel and that the draining takes place over 30 to 45 minutes. This northward flow is not observed at 50 cmab, where the velocity vectors change direction within one 15-minute timestep.

To determine more specifically the depth at which the northward flows occur, we examine Figure 3-22, a plot of tidal stage at the east station versus the direction of velocity of the ADV at 150 cmab. The time period represented here is year-day 73.5 – 76; this is the same period shown in all plots versus time in this chapter. Magnetic declination, or the difference between magnetic north and true north, has been accounted for in this figure as well as in the velocity vectors plotted in Figures 3-20 and 3-21. The velocity direction is shown in degrees clockwise from north. The flood tide enters at approximately 93 degrees, and the ebb flows down-estuary at about 277 degrees. At the end of the flood tide, which occurs at high-water, the flow direction turns northward (decreases) by about 15 degrees. As the ebb begins, the flow direction is westward (along-channel), but with significant lateral variability, and a particularly large northward component. When the water depth drops to 3.5 meters, the flow direction converges on 277 degrees for the remainder of the ebb tide.

The relationship between depth and flow direction is interpreted as a reflection of flow that exchanges with the adjacent mudflats to the south and flow that is confined to the channel. The northward bias of late-flood flows reflects the phase-lag between the channel and mudflats: the mudflats begin to drain before the channel flow has changed direction, resulting in an up-estuary velocity with a northward component. As the channel flow responds to the reversal in the tidal (barotropic) pressure gradient, the mudflats continue to drain to the north, until the water depth has dropped below the elevation of the mudflats. It should be noted that the lateral variability is highest just after high-water, and that there is southward flow as well as northward, indicating that exchange with the mudflats continues.

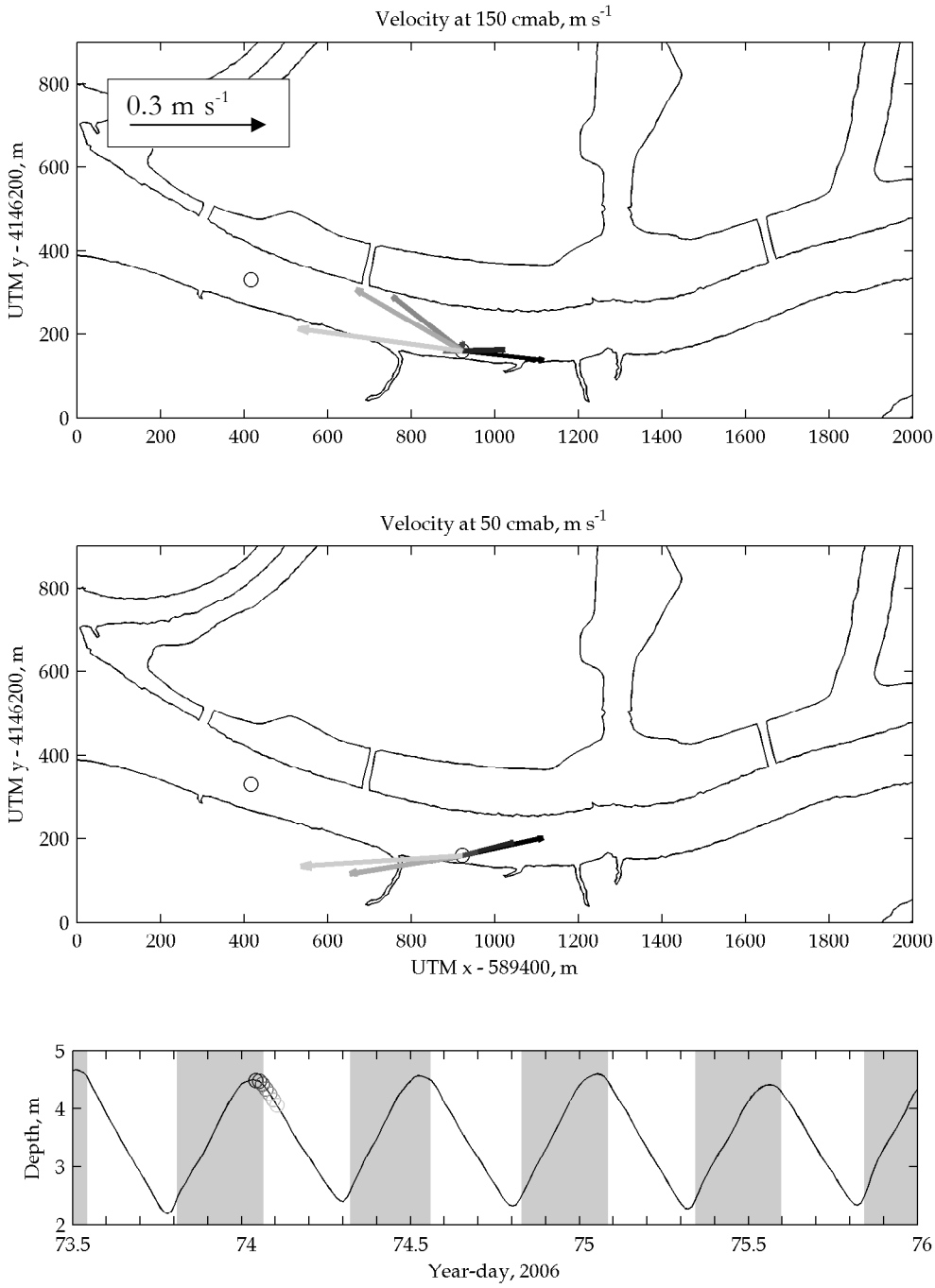

Figure 3-20: Flood-to-ebb velocity vectors, year-day 74
Velocity vectors measured at 150 cmab (top panel) and 50 cmab (middle panel) are shown over the local coastline for one flood-to-ebb transition (year-day 74). The tidal stage (bottom panel) for each velocity measurement is shown as a circle in the same shade of grey as the velocity vector. There is a large northward velocity component at 150 cmab that is not observed at 50 cmab, indicating the presence of lateral shear.

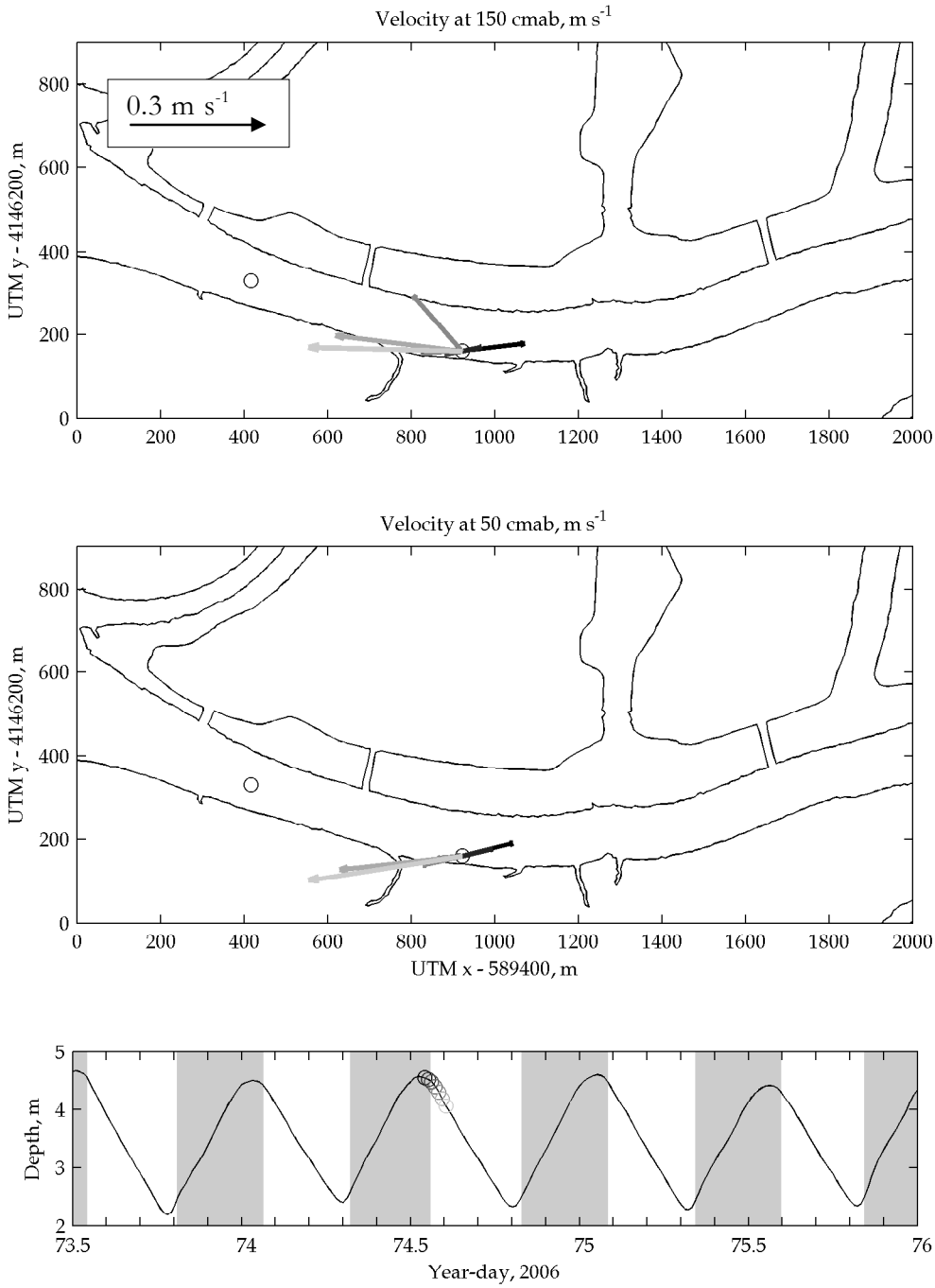

Figure 3-21: Flood-to-ebb velocity vectors, year-day 74.5
Velocity vectors measured at 150 cmab (top panel) and 50 cmab (middle panel) are shown over the local coastline for one flood-to-ebb transition (year-day 74.5). The tidal stage (bottom panel) for each velocity measurement is shown as a circle in the same shade of grey as the velocity vector. There is a large northward velocity component at 150 cmab that is not observed at 50 cmab, indicating the presence of lateral shear.

This phase-lag can be represented using the momentum equations in the longitudinal and transverse directions. The simplest possible balance for a tidal system is composed of the pressure gradient opposed by the frictional force. In the longitudinal (x) direction, the tidal pressure gradient ($\partial P/\partial x$, divided by density ρ) is counteracted by friction ($\frac{\partial}{\partial z}\nu_T\,\partial u/\partial z$), but the balance is unsteady (equation 3-8a); our data show that there is a 30-minute lag between the change in direction of the tidal wave and the reversal of the velocity. The balance in the lateral (y) direction consists of the lateral pressure gradient ($\partial P/\partial y$) and the lateral frictional force ($\frac{\partial}{\partial z}\nu_T\,\partial v/\partial z$) and can be assumed steady ($\partial v/\partial t = 0$), as shown in equation 3-8b, or at least *more* steady than the longitudinal momentum balance; the directional change in the transverse velocity happens closer to the time of slack water than does the along-channel velocity reversal. This difference in timing – the phase-lag – is captured by $\partial u/\partial t$ in the equations below.

(3-8a) $$\frac{\partial u}{\partial t} = -\frac{1}{\rho}\frac{\partial P}{\partial x} + \frac{\partial}{\partial z}\nu_T\frac{\partial u}{\partial z}$$

(3-8b) $$0 = -\frac{1}{\rho}\frac{\partial P}{\partial y} + \frac{\partial}{\partial z}\nu_T\frac{\partial v}{\partial z}$$

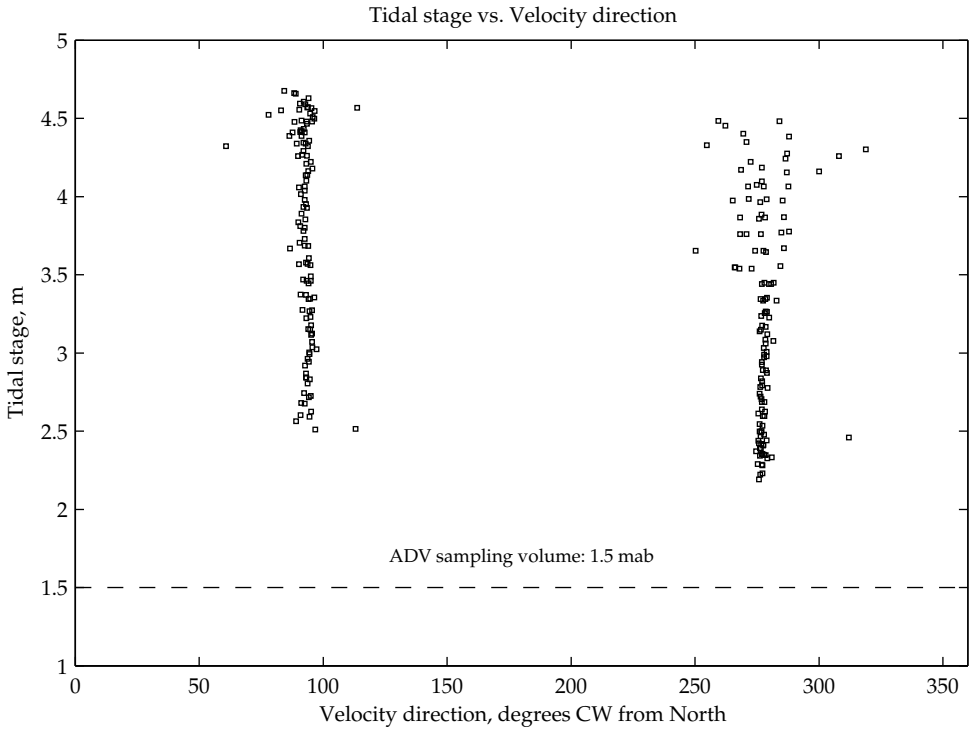

Figure 3-22: Tidal stage vs. Velocity Direction
Data from the ADV at 150 cmab, east station. Ebb flow direction is about 277 degrees clockwise from north; flood flow direction is about 93 degrees clockwise from north. Flow direction is variable as the tide begins to fall (ebb tide, depths above 3.5 meters).

The result of the interaction between flow and the channel-mudflat interface is vertical shear in the horizontal velocities. Figures 3-20 and 3-21 show that the velocities at 50 cmab do not deviate significantly from the along-channel principal axis. Contrastingly, the velocity vectors plotted in Figures 3-20 and 3-21 at 150 cmab as well as the relationship between tidal stage and velocity direction in Figure 3-22 illustrate that cross-channel flows are significant early in the falling tide at 150 cmab. The directional discrepancy between transverse flows at 50 cmab and 150 cmab indicates that the water column is vertically sheared. Figure 3-23 shows magnitude and direction of the velocity shear, which for simplicity is assumed linear, and is calculated as follows:

(3-9a) Shear: $$\mathbf{s} = \frac{\mathbf{v}_{150cm} - \mathbf{v}_{50cm}}{\Delta z} = \left(\frac{u_{150cm} - u_{50cm}}{\Delta z}, \frac{v_{150cm} - v_{50cm}}{\Delta z} \right)$$

(3-9b) Shear magnitude: $$\|\mathbf{s}\| = \sqrt{\mathbf{s} \cdot \mathbf{s}}$$

(3-9c) Shear direction: $$\theta = \arctan\left(\frac{u_{150cm} - u_{50cm}}{v_{150cm} - v_{50cm}} \right)$$

Figure 3-23 indicates that the magnitude of the shear approaches zero at slack tides, and generally reaches local peaks just before and after slack. The direction of the shear also peaks just before and after the reversal of the flow direction at flood-to-ebb transitions (high-water). These transitions – such as the ones shown at 74.1, 74.6, and 75.1 – are dynamically important; at these times, the peaks in shear interact with local horizontal density gradients to produce unstable density stratification.

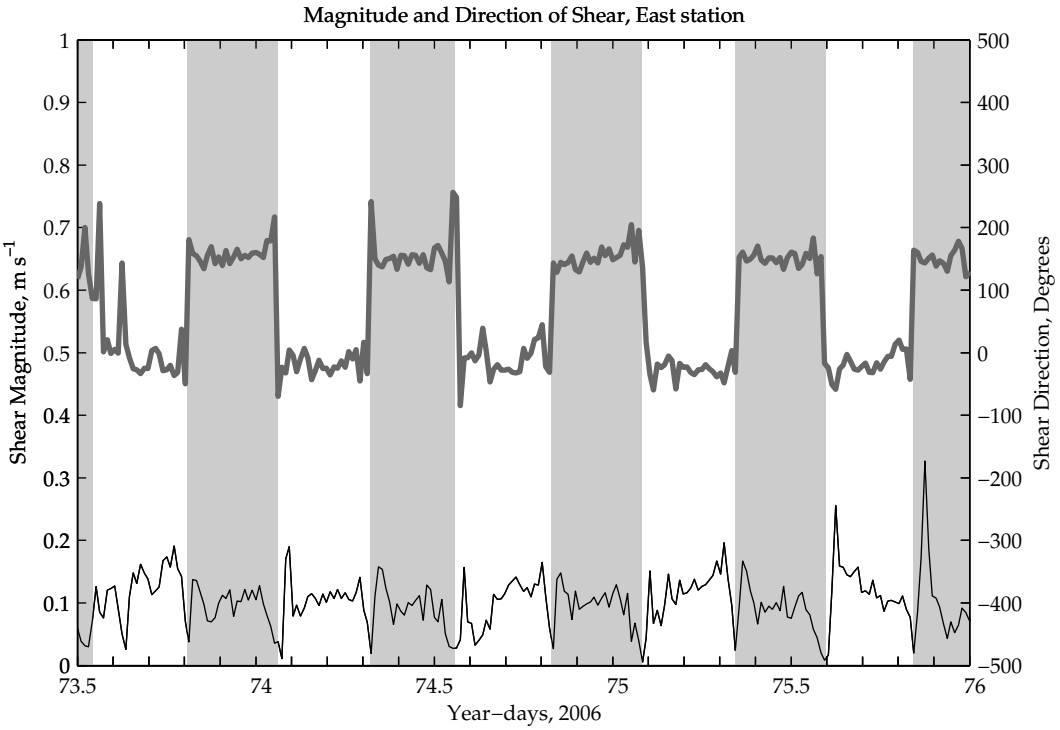

Figure 3-23: Shear magnitude and direction
Shear magnitude (thin black line, left axis) and shear direction (thick grey line, right axis) are shown at the east station, 150 cmab. Floods are shaded and ebbs are unshaded.

Generation of unstable stratification

At the beginning of each ebb tide, unstable density stratification is observed at the east instrument station in Coyote Creek, as is shown in Figure 3-6. This observation was unexpected given that tidal straining theory predicts that boundary layer shear in the ebb-tide velocity profile strains the longitudinal salinity gradient to bring fresher water over saline, producing stable stratification. Contrary to this theory, observations show that unstable stratification reaches 0.5 – 1 ppt m^{-1}, and lasts for 1-2 hours. The buoyancy timescale, which is the inverse of the frequency of gravity waves in an unstably stratified environment, can be interpreted as a timescale for the rectification of unstable stratification due to gravity alone, and is defined as follows (Tennekes & Lumley 1972, p.99):

$$(3\text{-}10) \quad T_b = \left(\frac{g}{\rho_0} \frac{\partial \rho}{\partial z} \right)^{-1/2}$$

The inverse square of the buoyancy timescale (T_b) is proportional to the gravitational acceleration (g), the inverse of the average density (ρ_0), and the vertical density gradient ($\partial\rho/\partial z$). Scaling equation 3-10 with a salinity difference of 0.5 ppt over 1 meter between

sensors produces a buoyancy timescale of approximately 14 seconds. The fact that the unstable stratification is sustained for over one hour indicates that it is being actively maintained by some dynamic process.

Measurements suggest that the mechanism responsible for creating and maintaining this instability is the bathymetry-induced straining of local horizontal density gradients whereby shear in the velocity profile differentially advects water masses of differing salinities. Conceptually, the sequence of events is as follows: lateral exchange with the mudflats late in the flood tide results in salty water spreading out over the shallows, which pushes fresher water into the main channel at the surface. The spatially variable frictional force produces a phase lag between the change in direction of the velocity in the channel and the velocity over the mudflats. The mudflats begin to drain while the channel flow is still directed up-estuary, and a northward velocity component is observed as the channel flow at 150 cmab rotates from up- to down-estuary. The salty water stored on the mudflats is then advected into the channel, over the near-bottom flow that begins to freshen as the ebb tide accelerates. The structure and phasing of the velocities were discussed in the previous section, and the objective of this discussion is to establish the presence of the horizontal density gradients acted upon by the velocity shear to produce the observed instability.

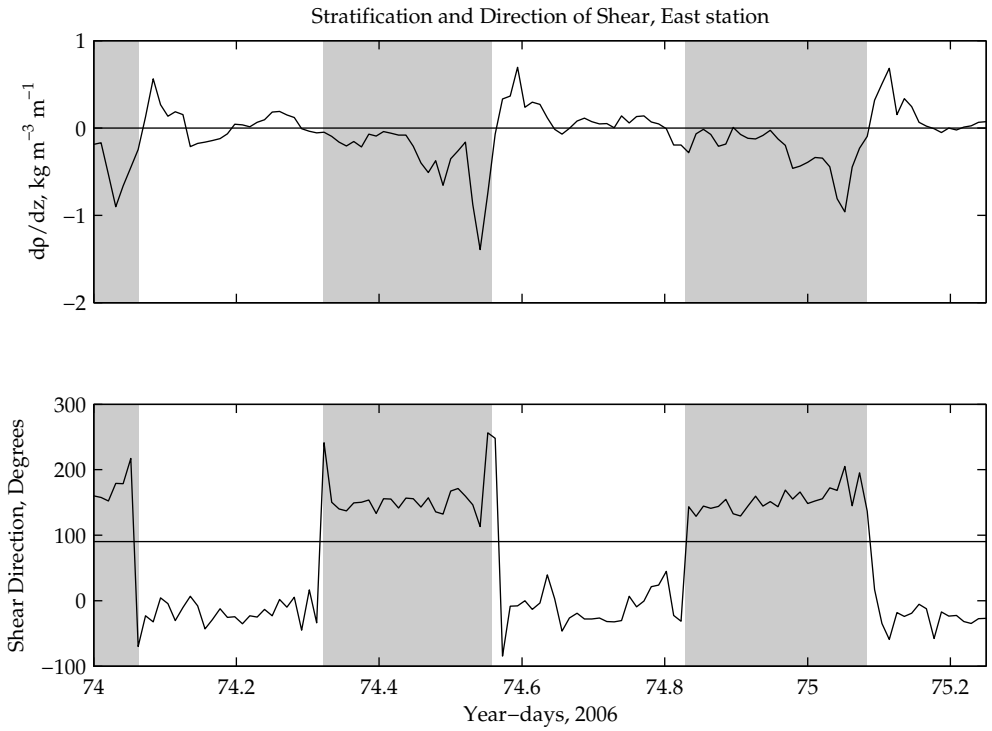

Figure 3-24: Stratification and shear direction
The vertical density gradient is shown in the top panel, and the direction of shear is in the bottom panel. Floods are shaded and ebbs are unshaded, and the time period shown is 2.5 tidal cycles to provide better visibility of the time series. At the flood-to-ebb transitions, the time at which the shear direction drops below 90 degrees (horizontal line) corresponds to the time at which the stratification becomes unstable.

The correlation between the shear direction and the unstable stratification at the flood-to-ebb transitions can be seen qualitatively in Figure 3-24. The vertical density gradient is shown in the top panel, and the direction of shear is shown in the bottom panel. The 90-degree threshold for shear direction is marked with a horizontal line, and represents the boundary between northward and southward shear. The time period shown in this plot is shorter than other plots in this chapter to provide better visibility. At each transition from flood to ebb, the point at which the shear turns to the north (or goes below 90 degrees) is the point at which unstable (positive) stratification is observed. The correlation is minimal at other tidal stages; we assert that the straining mechanism is not the dominant process at times other than the early falling tide.

This picture is one of lateral straining superposed onto the longitudinal straining described originally by Simpson et al. (1990). The channel-mudflat interface requires that the lateral dynamics be considered; this is not a problem that can be reduced to the vertical/along-channel plane. Nevertheless, in spite of its complexity, the tidal straining framework, which is based on the evolution of the potential energy anomaly, is useful for understanding the mechanisms at work in this 3-dimensional problem.

Simpson et al. (1990) define the potential energy anomaly, ϕ, as:

(3-11a) $\phi = \frac{1}{h}\int_{-h}^{0}\left(\overline{\rho}-\rho\right)gz\,dz$, where the vertically averaged density is:

(3-11b) $$\overline{\rho} = \frac{1}{h}\int_{-h}^{0}(\rho)\,dz$$

h is the flow depth; ρ and $\overline{\rho}$ are the density and depth-averaged density, respectively; g is the gravitational constant; z is the vertical spatial dimension.

The time evolution of the potential energy anomaly is therefore:

(3-12) $$\frac{\partial\phi}{\partial t} = \frac{g}{h}\int_{-h}^{0}\left(\frac{\partial\overline{\rho}}{\partial t}-\frac{\partial\rho}{\partial t}\right)z\,dz$$

Simpson et al. (1990) assume that the sheared velocity as well as the horizontal density gradient is only important in the along-channel direction, but here, we include both horizontal directions in the transport equation of density (3-13a). t is time; x and u are the longitudinal spatial dimension and velocity, respectively; y and v are the lateral spatial dimension and velocity, respectively. We also assume that the horizontal density gradients are independent of depth, yielding 3-13b, where an overbar indicates depth-averaged quantities:

(3-13a) $$\frac{\partial\rho}{\partial t} = -u\frac{\partial\rho}{\partial x} - v\frac{\partial\rho}{\partial y}$$

(3-13b) $$\frac{\partial\overline{\rho}}{\partial t} = -\overline{u}\frac{\partial\rho}{\partial x} - \overline{v}\frac{\partial\rho}{\partial y}$$

The result is the time evolution of the potential energy anomaly in terms of the straining of the horizontal density field.

(3-14) $$\frac{\partial \phi}{\partial t} = \frac{g}{h}\frac{\partial \rho}{\partial x}\int_{-h}^{0}\left(u-\bar{u}\right)z dz + \frac{g}{h}\frac{\partial \rho}{\partial y}\int_{-h}^{0}\left(v-\bar{v}\right)z dz$$

This equation is simplified by assuming that the vertical density and velocity gradients are linear, and defined by the two measured points, 50 and 150 cmab. The depth-dependent variables can then be replaced by linear equations, and the integrals can be solved. m and b represent the slope and z-intercept, respectively, of the linear equations, and the subscripts denote density, along-channel velocity, or cross-channel velocity.

(3-15a) $$\rho = m_\rho z + b_\rho,\ \bar{\rho} = \frac{m_\rho}{2}h + b_\rho,\ \phi = -\frac{g}{h}\frac{7m_\rho}{12}, \text{ and } \frac{\partial \phi}{\partial t} = -\frac{g}{h}\frac{7}{12}\frac{\Delta m_\rho}{\Delta t}$$

(3-15b) $$u = m_u z + b_u,\ \bar{u} = \frac{m_u}{2}h + b_u, \text{ and } \int_{-h}^{0}\left(u-\bar{u}\right)z dz = \frac{7m_u}{12}$$

(3-15c) $$v = m_v z + b_v,\ \bar{v} = \frac{m_v}{2}h + b_v, \text{ and } \int_{-h}^{0}\left(v-\bar{v}\right)z dz = \frac{7m_v}{12}$$

With these simple expressions, we can solve for the stratification that would result from the straining of both horizontal salinity gradients. $\Delta m_\rho / \Delta t$ is the change in the slope of the vertical density distribution per the change in time, and is a function of the products of the slope in the velocity profile and the horizontal density gradient, in both lateral and longitudinal directions.

(3-16) $$\frac{\Delta m_\rho}{\Delta t} = -\frac{\partial \rho}{\partial x}m_u - \frac{\partial \rho}{\partial y}m_v$$

However, there are a number of problems associated with estimating the lateral and longitudinal density gradients from our experiments. The most obvious is the fact that our spring 2006 experiment was a longitudinal study and neglected lateral gradients entirely. We do have salinity and temperature at three points along Coyote Creek, but the $\partial\rho/\partial x$ calculated from the data is imperfect for two reasons: first, the measurements are ~500 meters apart, which is too far to capture local, frontal gradients, and second, the gradient is not centered on our station of interest (east). This means that the estimate of $\partial\rho/\partial x$ reflects a salt wedge that arrives too early on the flood, and recedes too late on the ebb. Another option is to use an advective balance to estimate $\partial\rho/\partial x$ as a function of unsteadiness and velocity, but this quantity is undefined when the velocity goes through zero, and doing so assumes variability in only one horizontal direction (*x* or *y*).

Given these complications, we proceed by solving equation 3-16 for $\partial\rho/\partial y$, which is the only quantity we cannot estimate from our spring 2006 moorings, and scaling it to estimate the lateral density gradient required to produce the observed stratification. The objective then is to assess whether $\partial\rho/\partial y$ fits within our conceptual model of exchange between the channel and

mudflat, and whether similar values were observed during boat-mounted sampling across that interface.

$$\frac{\partial \rho}{\partial y} = -\frac{1}{m_v}\left(\frac{\Delta m_\rho}{\Delta t} + \frac{\partial \rho}{\partial x} m_u\right) \quad (3\text{-}17)$$

The time period of interest is the very early ebb, when the strongest unstable stratification is developing, and measurements are used to scale each component in 3-17. At this phase of the tide, the stratification increases at a rate of approximately 0.5×10^{-3} kg m^{-3} s^{-1}. The longitudinal density gradient is on the order of -3 kg m^{-3} km^{-1}, and the shear in the longitudinal and lateral velocities are -0.05 and 0.2 m s^{-1} m^{-1}, respectively, indicating that the flow at 150 cmab is more westward and northward relative to that at 50 cmab. These quantities make physical sense; the flow at the top ADV is ebbing slightly more strongly than the flow closer to the bed, and the mudflats are draining to the north near the surface. Using 3-17 to calculate the lateral density gradient, we obtain: $\partial\rho/\partial y \approx -3\times10^{-3}$ kg m^{-3} m^{-1}. This result corresponds to a salinity gradient of about -6×10^{-3} ppt m^{-1}, and indicates that the salinity over the mudflats must be higher than the channel in order to produce the observed stratification through straining.

This negative lateral salinity gradient during the early-ebb is conceptually consistent with lateral exchange between the channel and mudflats. Similar to the flood tide dynamics, differential advection on the ebb leads to a slower freshening of the mudflats relative to the channel, resulting in the highest-salinity flow being located in the shallows (marshes and mudflats). This flow drains out of the marsh and into the channel during the ebb tide, while the flow near the channel bed begins to freshen as the ebb tide transports up-estuary water toward the Bay.

In the absence of moored measurements of the lateral salinity gradient across the channel-mudflat interface, we rely on boat-mounted sampling of surface salinities performed during the summer of 2008 as an indication of whether these gradients do indeed set up at the flood-to-ebb transition. On July 27, 2008, we measured gradients across the southern channel-mudflat interface to vary over a range of -24×10^{-3} to -0.6×10^{-3} ppt m^{-1} over the first two hours of the falling tide, with an average of -7×10^{-3} ppt m^{-1} (see Figure 3-7). These measurements reflect temporal as well as longitudinal variability along the channel-mudflat interface, but we can conclude that early in the ebb tide, a negative lateral salinity gradient of the strength required to produce unstable stratification from straining is realistic.

Straining and increased mixing from buoyancy and shear production

The final phase of the tide to be discussed is the second half of the ebb, during which elevated turbulent motions and a well-mixed water column are observed. Tidal straining of a partially mixed estuary predicts that the late ebb should see the greatest stratification, since by then, the ebb-tide boundary layer has had the most time to tilt the isopycnals toward the Bay at the water surface. In contrast, our observations of salinity show a water column that is well-mixed or slightly unstably stratified at the east and west stations (-0.1 ppt m^{-1} $< \partial\rho/\partial y <$ 0.2 ppt m^{-1} and $\partial\rho/\partial y \sim$ -0.2 ppt m^{-1}, respectively). Figure 3-13 shows that Reynolds stresses reach a maximum late in the ebb tide (e.g. 73.8, 74.8, 75.3, 75.8).

The field measurements collected in Coyote Creek suggest that straining of the water column provides buoyancy to the water surface, which incites turbulent motions, and results in a relatively well-mixed water column. Buoyancy is a sink for turbulent kinetic energy (TKE) when the water column is stably stratified (buoyant destruction), but is a source of TKE when unstable stratification is present (buoyant production). Measuring this term in the TKE budget requires high-frequency, collocated sampling of velocity and density which is not available in the Coyote Creek datasets; however, the elevated turbulent stresses (both shear and normal) in the presence of a slightly unstably stratified water column suggest that buoyant production is important.

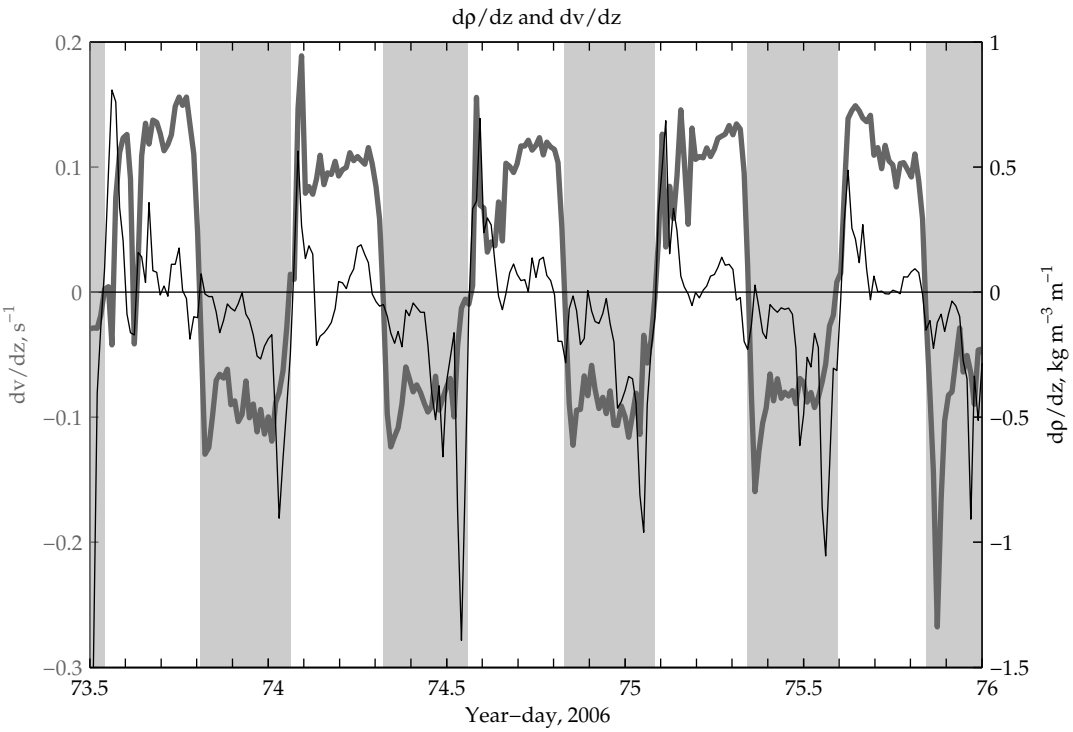

Figure 3-25: Stratification and lateral shear
Cross-channel shear (thick grey line, left axis) and density gradient (thin black line, right axis) are shown. Positive shear in the transverse velocity on ebb tides reflects the draining of the mudflats, and unstable (positive) stratification results.

As during the early ebb, the draining of the mudflats plays a major role in defining the salinity field at the east station. The source of the unstable stratification at this location, and the buoyant production of turbulence, is the advection of higher salinity water from the mudflats into the channel to the north. Figure 3-25 shows the time series of density stratification and transverse shear. During the latter portion of each ebb tide, the shear in the transverse velocity (v) is positive, meaning that velocity at 150 cmab is more northward than the velocity at 50 cmab, which reflects the effects of the draining of the mudflats in the upper part of the water column. The weak but slightly unstable stratification measured in the late ebbs takes place during this sustained shear. The stratification returns to stable at the very end of the ebbs

(times 74.3, 74.8, 75.3) at the same time that the transverse shear begins to diminish. Recall that measurements of the lateral surface salinity gradient show that the shallows have higher salinity than the channel during the late ebb tide (Figure 3-8); this gradient in combination with the persistent shear in the water column result in transport of saline water into the channel's surface and the opportunity for buoyant production of turbulence.

There is an important distinction in buoyant production of turbulence between the early ebb and late ebb. During the early ebb, the unstable stratification is significantly stronger, and yet an increase in Reynolds stresses equivalent to the late ebb is not observed. In both cases, flow off of the mudflats is a prominent mechanism. We attribute this apparent discrepancy to the evolution of the flow off of the mudflat. Early in the ebb, when water over the shallows is deeper, lateral (northward) velocities are at their peak, as shown in Figure 3-26. The high momentum of the initial mudflat effluent pushes the mixing zone beyond our instrument station. Later in the ebb, when velocities and momentum are lower, the mixing zone is closer to the bank, and our measurements detect higher turbulent motions. This process is analogous (although relatively miniscule in scale) to the study of flow over a sill in Knight Inlet, British Columbia, performed by Farmer & Armi (1999).

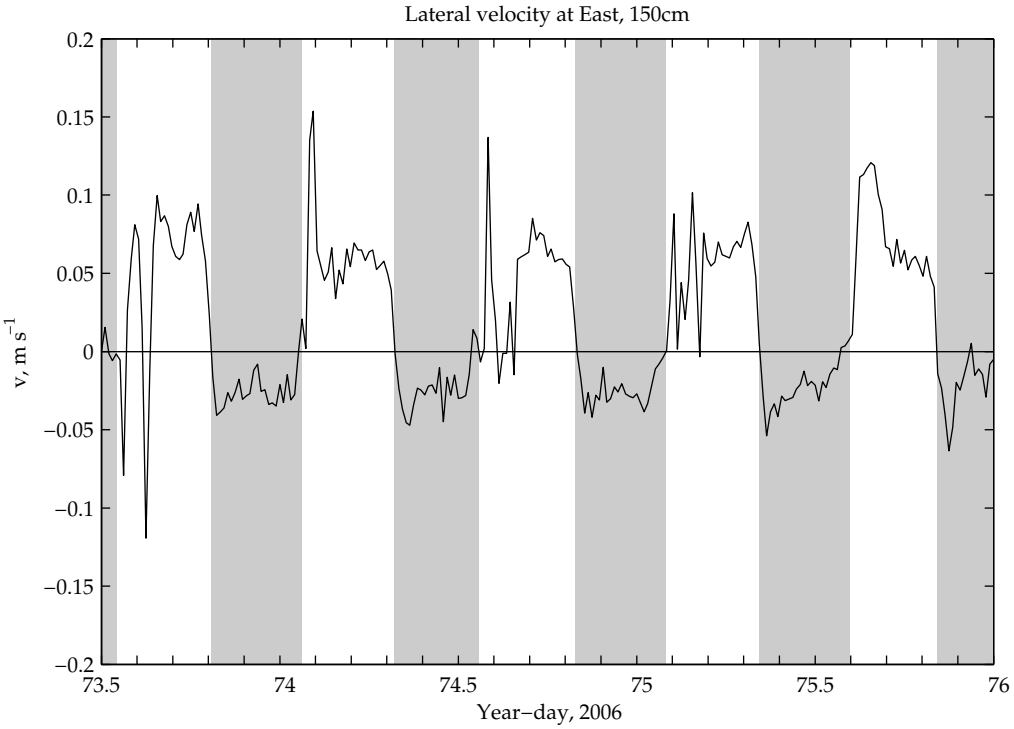

Figure 3-26: Lateral velocity, East station, 150cm
Pulses of northward (positive) flow off of the mudflats are evident early in the ebb tides, and while the flow generally remains positive, the velocity diminishes to about half of the pulse magnitude. Flood are shaded and ebbs are unshaded.

In addition to buoyant production, shear production of turbulence appears to be important for elevating Reynolds stresses during the late ebbs. Figure 3-27 shows $\overline{u'w'}$ plotted versus magnitude of velocity shear (top panel), and the vertical density gradient versus magnitude of shear (bottom panel). The range of data shown is between year-day 73.5 and 76, which is the same time period analyzed throughout this chapter. The magnitude of shear is defined in equation 3-9b, and is the magnitude of the vector that is the difference between the top velocity and the bottom velocity, divided by the vertical distance between them. The units are s^{-1}. The top panel shows that the magnitude of $\overline{u'w'}$ increases as the total shear increases. In the bottom panel, there is a trend toward zero and then positive (unstable) stratification with increasing shear.

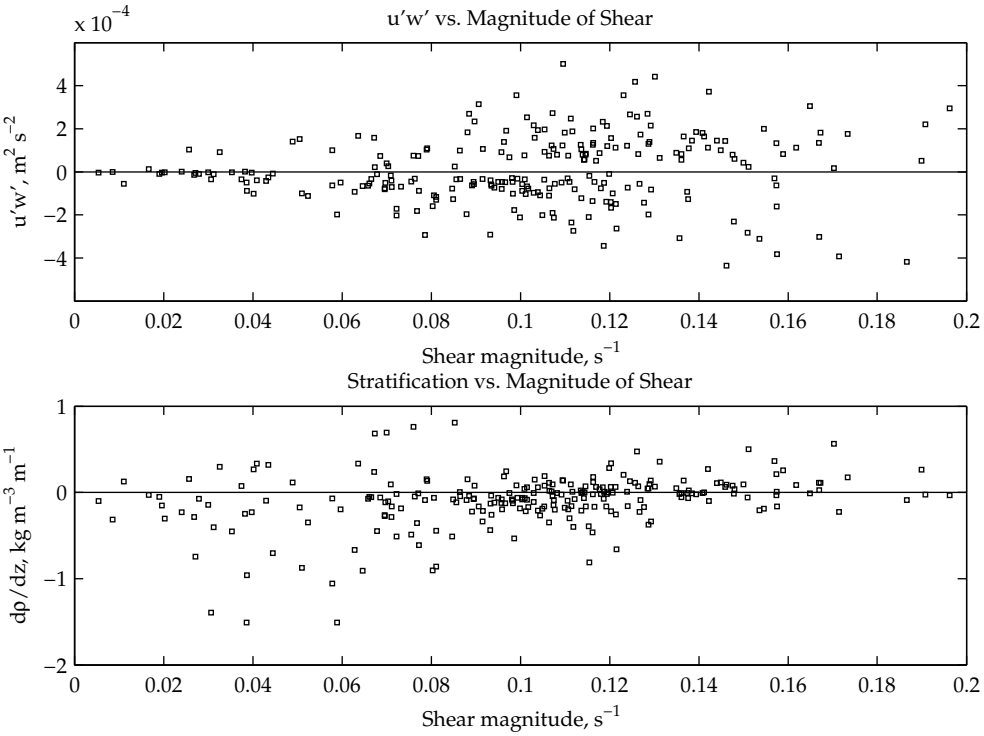

Figure 3-27: Stress and stratification vs. shear magnitude
Stresses increase with increasing shear (top panel), and stratification becomes more positive with increasing shear (bottom panel). The time period shown is year-days 73.5 – 76.

Mixing due to buoyant and shear production appears to be an important mechanism at the end of the ebb tides. In order to link the physics at this phase of the tide to the analysis performed for the early ebb, we return to the framework of the evolution of the potential energy anomaly (Simpson et al. 1990) and modify 3-14 to include vertical turbulent diffusion of mass, where K is the eddy diffusivity:

$$(3\text{-}18)\quad \frac{\partial \phi}{\partial t} = \frac{g}{h}\frac{\partial \rho}{\partial x}\int_{-h}^{0}\left(u-\bar{u}\right)z\,dz + \frac{g}{h}\frac{\partial \rho}{\partial y}\int_{-h}^{0}\left(v-\bar{v}\right)z\,dz + \frac{g}{h}\int_{-h}^{0}\left(\frac{1}{h}\int_{-h}^{0}\frac{\partial}{\partial z}K\frac{\partial \rho}{\partial z}\,dz - K\frac{\partial \rho}{\partial z}\right)z\,dz$$

Calculating or scaling the diffusion terms in 3-18 would require at least three measurements of density in the vertical, and only two were collected at the east station. Without more detailed data, estimating the value of the terms in the equation for the time evolution of the potential energy anomaly is not possible, and this obscures the details of the mechanisms behind the observations. Nevertheless, this relationship provides a theoretical framework to describe the complex development of the density field at the channel-mudflat boundary in Coyote Creek.

3.4 Summary and Conclusions

In estuarine physics there exists a strong understanding of the tidal variability of stratification and mixing in a partially-mixed estuary, but our measurements show that the effects of bathymetry can locally overwhelm the effects of tidal straining. Typically, flood tides are well-mixed and ebb tides are stratified as the boundary-layer structure of tidal flows strains the along-channel salinity gradient. Differential advection on flood tides between the channel and the shallow mudflats on its perimeter results in a lateral circulation which produces stable stratification in the channel, overcoming the destabilizing effects of the interaction between the longitudinal salinity gradient and the up-estuary flood flow. On ebb tides, the draining of the mudflats into the channel generates unstable stratification as trapped water of high salinity is discharged into the channel, over the top of the freshening bottom flow. The strength of the instability decreases as the ebb tide progresses and the velocity of the mudflat effluent weakens. Lateral exchange with the perimeter can therefore produce a tidal pattern of stratification that is opposite to the classical theory. This exchange can have important implications for tidal and residual flows and transport, eddy viscosity and diffusivity, and local bed stresses. These parameters control morphology through erosion and deposition of sediment, as well as the ability of other ecologically pertinent scalars to mix from the surface to the bed, and the bed to the surface. For all of these reasons, it is critical to fundamentally understand and properly parameterize the role of perimeter exchange in estuarine flows.

CHAPTER 4

Bathymetric controls on tidal transport of suspended sediment

4.1 Introduction

Sediment transport in estuaries is a complex balance of physical, chemical, and biological forces, and quantifying these forces and their interactions (through measurements and/or numerical modeling) is riddled with difficulties. In spite of the challenges, the motivation to understand sediment transport in estuaries is great. The erosion and deposition of sediment defines the estuary's morphology, which influences the hydrodynamics, salt regime, ecology, and the transport of scalars – including sediment. The transport of sediment is inexorably linked to all other physical processes in an estuary, in addition to many that are chemical and biological, including mobilization of, and subsequent exposure to, contaminant-laden sediments. The objective of this study is to examine sediment transport through a tidal slough in South San Francisco Bay with a highly irregular perimeter. Variability is investigated over timescales ranging from turbulence to meteorological events. The dependence on bathymetry of flows and sediment concentrations is explored in the vicinity of the slough's axis, its border with an intertidal mudflat, and inside of a breached salt pond.

4.1.1 Salt marsh restoration

Presently in the South San Francisco Bay there is a major wetland restoration project underway, called the South Bay Salt Pond Restoration Project (SBR, for South Bay Restoration), whose mission it is to restore 15,100 acres of salt ponds to salt marsh habitat in the South San Francisco Bay (U.S. Fish & Wildlife Service et al. 2006). The SBR goals are the formation of diverse wetland habitats, flood control for adjacent communities, and provision of wildlife-oriented public access and recreational space. The primary restoration activity has been opening salt ponds to tidal action by breaching the earth levees, allowing the marsh plain to accrete material, vegetation to establish, and the slow evolution into a viable habitat. The levee breaches reconnect thousands of acres of perimeter storage to the Bay for the first time in

decades, representing a major perturbation to the Bay with unknown impacts on flows and transport mechanisms.

Sediment dynamics, and how they will be impacted by the restoration, are a concern of the restoration managers for three primary reasons: 1) the success of the restoration depends upon adequate accretion of sediment; 2) historic mining has led to contamination of sediments with legacy heavy metals in the vicinity of the restoration (Conaway et al. 2004; Flegal et al. 2005), and scour that leads to renewed exposure to these contaminates would be an undesirable outcome of the restoration, as would be 3) erosion of existing intertidal habitats as a result of restoration activities. The SBR therefore provides the opportunity and the motivation to study the motion of sediment through the South Bay's existing channels, as well as the impacts of lateral exchange with new perimeter habitats.

4.1.2 Site description

The far southeastern tip of the San Francisco Bay narrows into a tidal slough called Coyote Creek (Figure 4-1). Coyote Creek is macrotidal, with a tidal range of 2.5 meters on neap tides, and 3.5 meters on springs. The dominant tidal frequencies are M2 and K1, resulting in twice daily, unequal tides. Field experiments were conducted in the vicinity of the Island Ponds, which are a cluster of three former salt ponds breached to tidal action via Coyote Creek in March 2006 (Figure 4-1). Coyote Creek is oriented approximately along an east-west line in this region; Bay water enters from the west on floods, and freshwater is supplied from watersheds to the east and south, and from a local wastewater treatment plant.

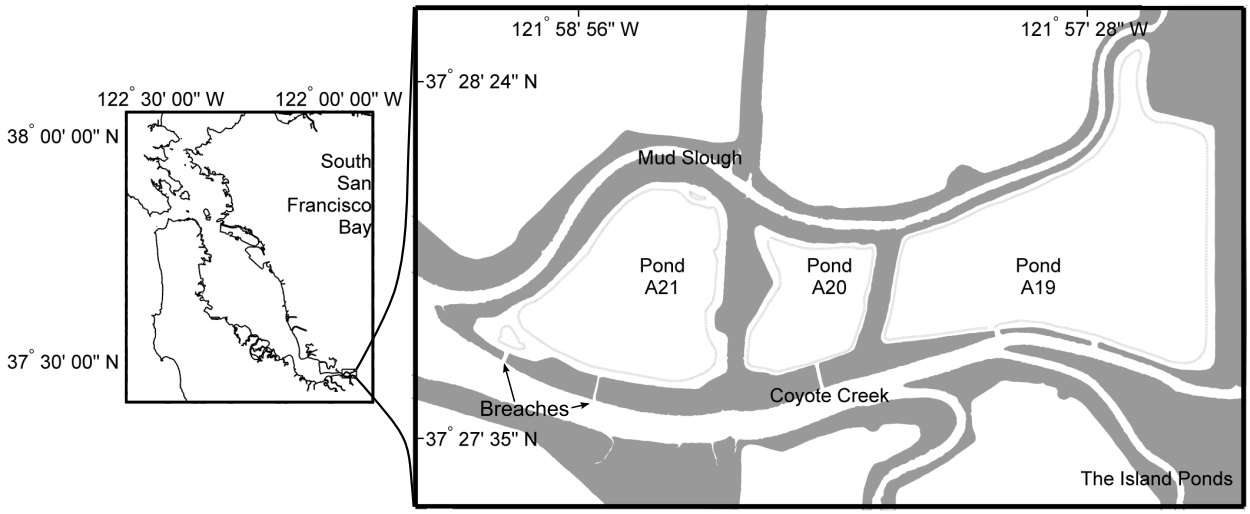

Figure 4-1: South San Francisco Bay and the Island Ponds
The Island Ponds (right) were among the earliest salt ponds to be breached as part of the South Bay Salt Pond Restoration project. The levee separating them from Coyote Creek was breached in 5 places in March 2006.

Much of the marsh land on either side of Coyote Creek was diked and converted to managed ponds for salt production in the early 1900s. The Island Ponds were a pilot site of the SBR, and were among the earliest ponds to be breached as part of the restoration. The reach of Coyote Creek outside of the westernmost Island Pond (Pond A21) is the study site for the investigations into the effects of lateral exchange between an estuary and perimeter volumes on sediment transport. The width of Coyote Creek at this location is approximately 200 meters, including intertidal regions. The slough consists of a main channel with an average depth of 3 meters, broad intertidal mudflats on the northern border of Coyote Creek, and narrow intertidal mudflats on the southern border. Best-available bathymetry is shown in Figure 4-2. The widths of the mudflats vary along the length of Coyote Creek, but in the vicinity of the Island Ponds, our observations indicate that the mudflats are 50-70 meters wide to the north, and 20-30 meters wide to the south. Figure 4-3 shows the cross-section of Coyote Creek at the western end of the Island Ponds (location shown in inset). The black dots are measurements made by the US Army Corps of Engineers, and the line defining the cross-section is an approximate reflection of the bathymetry between measurements, based on visual inspection of the site at low-water. The elevations are shown relative to the North American Vertical Datum of 1988 (NAVD 88). The dotted portion of the cross-section, between 60 and 110 cross-channel meters, is a schematic representation of visual observations made during boat-mounted field work. The southern mudflat is narrow compared to those to the north, and connected to the marsh above and the channel below by sharp transitions.

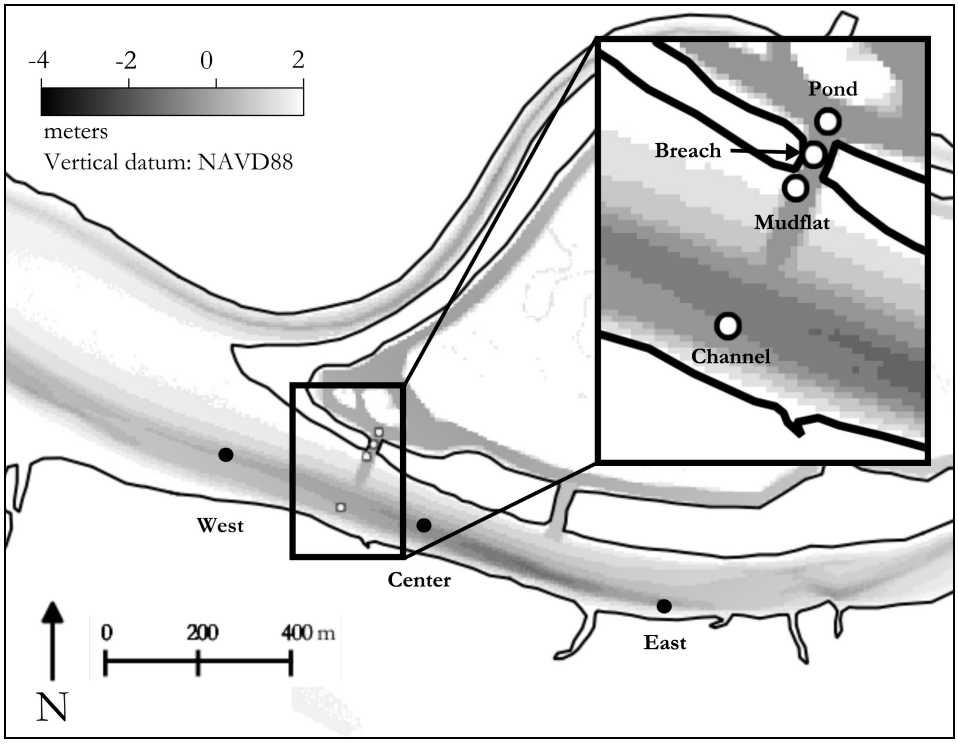

Figure 4-2: Coyote Creek bathymetry and experiment mooring locations
Spring 2006: black circles, west, center, east (left to right)
Fall 2006: white circles and inset, Channel, Mudflat, Breach, Pond (bottom to top)

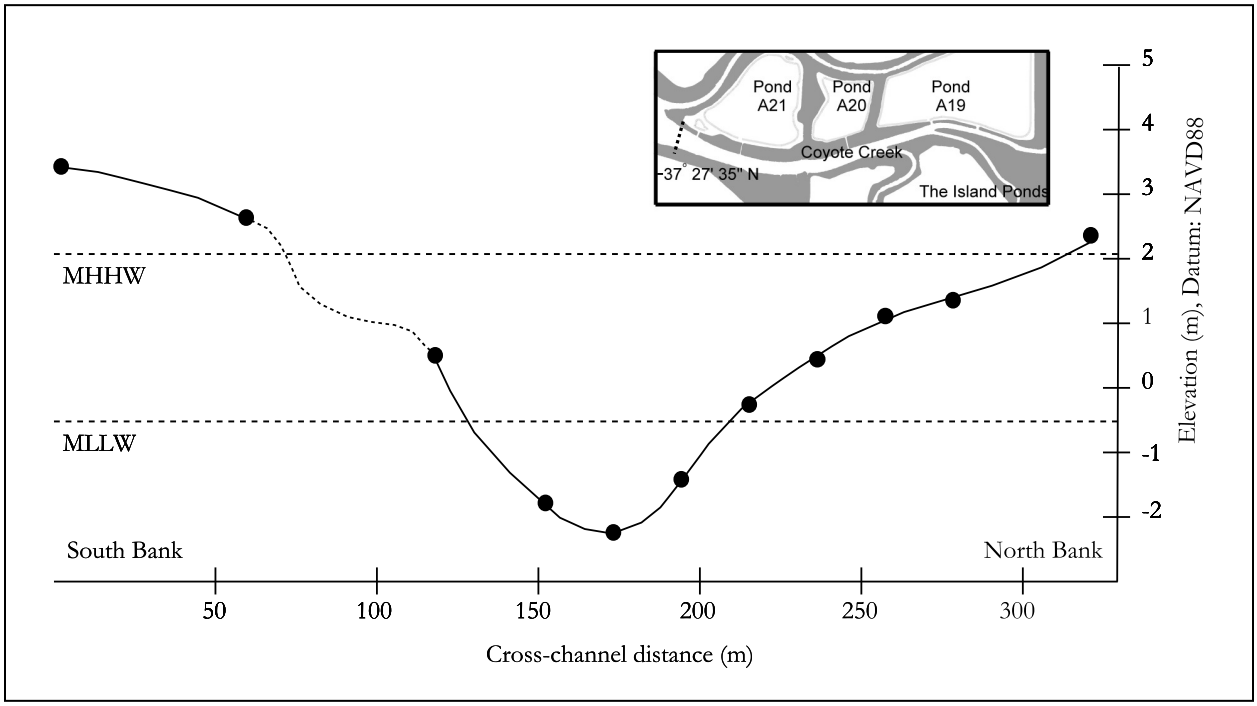

Figure 4-3: Channel cross-section.
Black dots are measurements made by USACE at the location shown by the dotted line in the inset (at the western end of the Island Ponds). The vertical datum is NAVD88, and the locations of MLLW and MHHW are shown for comparison. The line defining the cross-section was inferred by visual inspection at the site and is approximate. The dotted line between 60 and 110 cross-channel meters is used to call attention to the southern mudflat. Detailed bathymetry data are not available here, but visual observations of the site indicate that the mudflat is narrow with a gentle slope, connected to the marsh above and the channel below by sharp transitions.

Samples of bed sediment were not collected from the mudflats nor from the channel bottom, but at low tide, the mudflats appeared to be unvegetated, with coarse material resembling shells visible at the surface. Swaths of cordgrass line the intertidal zone to the north and south, with pickleweed, peppergrass, and alkali bulrush higher in the marshes and levees (per visual inspection as well as Duke et al. 2006; HT Harvey & Associates 2008). Although the marsh surface is above mean higher high water (MHHW), it is permeated by intertidal channels. Figures 4-4 and 4-5 show photographs taken on May 11, 2008 of the exposed flats and the vegetation visible from the water surface. The images were taken at 10:27am and 10:40am, when the water level was 1.38 meters relative to vertical datum NAVD88 (as in Figure 4-3), and 0.86 meters above mean lower low water (MLLW). At low tide (not pictured), greater extents of intertidal mudflats were visible, although the extremely shallow depths precluded boat-based access to all but the channel center.

Figure 4-4: Photographs of partially exposed mudflats on the north border of Coyote Creek
Facing the northern border of Coyote Creek. May 11, 2008, 10:40am, 100 m west of the western breach in Pond A21. Broad mudflats are visible, as well as cordgrass, and dead vegetation beyond it.

Figure 4-5: Photographs of partially exposed mudflats on the south border of Coyote Creek
Facing southern border of Coyote Creek. May 11, 2008, 10:27am, 100 m west of and across the channel from the western breach in Pond A21.

Morphology inside the ponds is characterized by an interior intertidal island surrounded by a subtidal channel (Figures 4-1 and 4-2). The channel, called the "borrow-ditch", was the location from which material was excavated to construct the levees surrounding the ponds. Before the breaches, and for at least the first year post-breaching, the interior island of Pond A21 was covered in 15-18 cm of gypsum (Callaway et al. 2009).

Sediments in South San Francisco Bay are predominantly silt and clay, with clay content exceeding 60% (Folger 1972). Proportions by weight of clay in estuarine sediments of greater than 5-10% lead to cohesion becoming dynamically significant (Dyer 1986, p.202), so it can be concluded that sediments in South San Francisco Bay are cohesive. Analyses of bed sediment grain sizes and mineral content were not performed at the Coyote Creek study site. Visual observations of sediment in intertidal regions (mudflats, ponds) and sediment recovered from the channel bed indicate that the grain sizes are very fine and the clay content of these materials is high.

4.1.3 Classical dynamics of estuarine sediment transport

The physical mechanisms that govern the motion of sediment that travels in suspension in an estuary can be described by the mass balance equation for sediment:

$$\frac{\partial C}{\partial t} + u\frac{\partial C}{\partial x} + v\frac{\partial C}{\partial y} + w\frac{\partial C}{\partial z} + w_s\frac{\partial C}{\partial z} = \frac{\partial}{\partial z}\left(-\overline{w'C'}\right) \quad \text{(4-1)}$$

The terms in 4-1 are, from left to right, unsteadiness in the sediment concentration (C), advection in the longitudinal, lateral, and vertical directions (x, y, z), particle settling, and the turbulent sediment flux. The settling velocity, w_s, is always negative. The final term is a general expression for turbulent motions in the water column, and incorporates the effects tidal flows, shear generated by wind at the water surface, and turbulence from wind-wave driven increases in near-bed currents, depending on the vertical location of the mass balance control volume. Sophisticated numerical modeling formulations include all of these terms, in some cases with additional horizontal dispersion parameterizations, meant to capture advective processes at timescales short relative to those resolved by the model (Schuttelaars & De Swart 1997; Lumborg & Pejrup 2005). When the objective is not a representative numerical model, but rather simply to understand the mechanisms at work, some authors neglect lateral advection but retain vertical advection (Jay & Musiak 1994), others do the opposite (Fugate & Friedrichs 2002), while others neglect both transverse and vertical advection (D Pritchard 2005).

The simplest expression of the sediment budget assumes a local balance of particle settling and resuspension through turbulent motions (equation 4-2); unsteadiness and advection are relatively unimportant in this framework (Wiberg et al. 1994; Fugate & Friedrichs 2002; Fugate & Friedrichs 2003). When these assumptions are deemed satisfactory, 4-2 can be vertically integrated to produce 4-3, and the settling velocity can be calculated using collocated

measurements of high-frequency concentration and velocity, as with an Acoustic Doppler Velocimeter (ADV) (Fugate & Friedrichs 2002).

$$w_s \frac{\partial C}{\partial z} = \frac{\partial}{\partial z}\left(-\overline{w'C'}\right) \tag{4-2}$$

$$w_s C = -\overline{w'C'} \tag{4-3}$$

The objective of this study is to assess the important transport mechanisms for suspended sediment in the vicinity of distinct topographies, and the modification to these balances from seasonal changes.

4.2 Observational methods

Moored measurements of velocity, depth, and water properties (salinity, temperature, and suspended sediment concentration) were made during two experiments in the spring and fall of 2006, each lasting two months. One small-scale deployment of one-month duration was performed to measure water properties during the summer of 2008.

The spring 2006 experiment was a longitudinal study composed of one acoustic Doppler current profiler (ADCP) mooring (at the west station) and two acoustic Doppler velocimeter (ADV) moorings (center, east). Mooring locations are shown in Figure 4-2. Filled circles represent spring 2006 mooring sites, and open circles represent the fall 2006 moorings. In addition to the 600 kHz ADCP, the west station also had a conductivity-temperature-depth sensor with an optical backscatter sensor (CTD/OBS pair) located 30cm above the bed, and a CTD/OBS pair 50cm below the surface (attached to the buoy line). The two ADV frames at the center and east stations were identical, with ADV sampling volumes and CTD/OBS pairs located at 0.5 and 1.5 m above the bed. The ADVs were programmed to sample at 16 Hz in 30-second bursts every 15 minutes such that mean flows as well as turbulence characteristics could be measured. The bottom CTD at the center station filled with mud approximately one week after deployment, and was discarded after that time.

The fall 2006 experiment consisted of four instrument stations deployed in a lateral configuration across Coyote Creek, through the western-most breach in Pond A21, and just inside the pond. In addition to the two 2006 experiments, two CTD/OBS pairs were moored at the southern stations from the fall 2006 deployment during the month of July 2008. Velocities were not measured during this deployment.

Suspended sediment concentrations (SSC) were measured using optical and acoustic backscatter signals that were calibrated to concentrations of total suspended solids. The optical instruments were calibrated using water samples collected at the field site during the deployment, and the acoustic instruments were calibrated in the laboratory using previously collected sediment samples from the South San Francisco Bay. The lab calibrations were performed by Brand et al. (2010). The acoustic and optical backscatter signals were measured using ADVs and OBS sensors, respectively. The insensitivity of the acoustic backscatter signal

to biological fouling provided a significant advantage of the SSC measurements derived from the ADV data relative to the OBS data. In addition, ADVs are less sensitive to particle size than OBS sensors, resulting in better estimates of total mass of particles in suspension (Fugate & Friedrichs 2002). For these reasons, wherever ADV backscatter data are available, they are used in place of OBS data from the same stations. Suspended sediment concentrations derived from OBS are used at locations where no ADVs were deployed.

The issues associated with the backscatter-to-SSC calibrations are significant. For both acoustic and optical backscatter, the water samples used for calibration in the field and in the lab contained concentrations of suspended sediment much lower than the maximum values of the calibrated backscatter; the highest estimates of SSC from backscatter time series data are based on an extrapolation of the calibration data. Uncertainty is compounded for the acoustic calibration due to the fact that the water and sediment samples used were collected at a different field site, approximately 30 km north of the Island Ponds in the South San Francisco Bay, at instrument stations in intertidal, shallow subtidal, and channel bottom regions (Brand et al. 2010). While the sediments at the two sites appear visually to be very similar, and the calibrations obtained by the authors of that study were quite good ($R^2 > 85$ for the linear fit between backscatter voltage and the logarithm of the concentration), the error in estimates of SSC presented here is likely significant. For these reasons, the discussion is limited to characteristics of the data and dynamics that do not require accurate quantification of spatial gradients in SSC.

Meteorological conditions during the three experiments were variable. The spring of 2006 was exceptionally wet; during March – May 2006, 9.4 inches of precipitation were recorded, which is 150% of normal for that time period. The fall experiment occurred during a period 30% drier than normal, with 3.4 inches of precipitation falling during October – December 2006. The summer 2008 study was completely dry, with no rain falling during July 2008.

4.3 Results and discussion

A detailed overview of the results of these experiments is presented in Chapter 2, and the findings pertinent to this analysis are summarized here. The magnitudes of peak velocities in the channel of Coyote Creek reach 1.2 m s^{-1} mid-channel and 0.5 m s^{-1} close to the channel-mudflat boundary. Coyote Creek is ebb-dominant, with ebb velocities 10-20% higher than flood velocities. Salinities vary tidally and seasonally, over a range of 2-12 ppt during wet weather, and 12-30 ppt during dry weather. There is a standing wave in Coyote Creek, and outside of the Island Ponds, times of high and low water lead slack tide in the channel by approximately 30 minutes. Lateral baroclinic exchange (Chapter 3) and tidal trapping (Chapter 5) between the main channel and the mudflats and salt ponds lead to persistent transverse salinity gradients.

4.3.2 Temporal variability

Seasonal timescales

Suspended sediment concentrations vary on tidal timescales (diurnal, spring-neap) as well as seasonal timescales (days, months). The spring-neap and seasonal variability in the main channel of Coyote Creek can be assessed by comparing SSC during the rainy spring of 2006 with the very dry summer of 2008 shown in Figure 4-6. Note that the axes on the two panels are different. It is clear that levels of SSC are elevated during wet weather compared with dry weather, as the concentrations during spring 2006 vary over the range of 100 – 1000 mg L^{-1}, and during summer 2008, they do not exceed 75 mg L^{-1}. The dependence on wet weather becomes more complex when wet conditions are sustained and sequential storms arrive in this area. Around year-day 93 of 2006 (top panel), the stream flow reaches its peak, increasing from around 200 cfs to 1400 cfs. This is coincident with a drop in SSC. Diurnal tidal fluctuations are still visible during the 22-day period of elevated stream flow, but the range of SSC values is depressed. The spring-neap signal is visible in both panels of Figure 4-6. The top and bottom panels show 2 months of data (4 spring-neap cycles), and 1 month of data (2 spring-neap cycles), respectively. Springs are evident in 2006 at year-days 75, 89, and 117. The spring tide at day 103 is not evident in the SSC signal, and appears to have been overwhelmed by the high freshwater flows in Coyote Creek. This suggests that while sediment is supplied to the system during rain events, the sediment load may diminish with successive storms, and high freshwater flows that occur with sustained rainfall prevent the up-estuary advection of Bay-sourced sediments that defines the steady-state tidal variability.

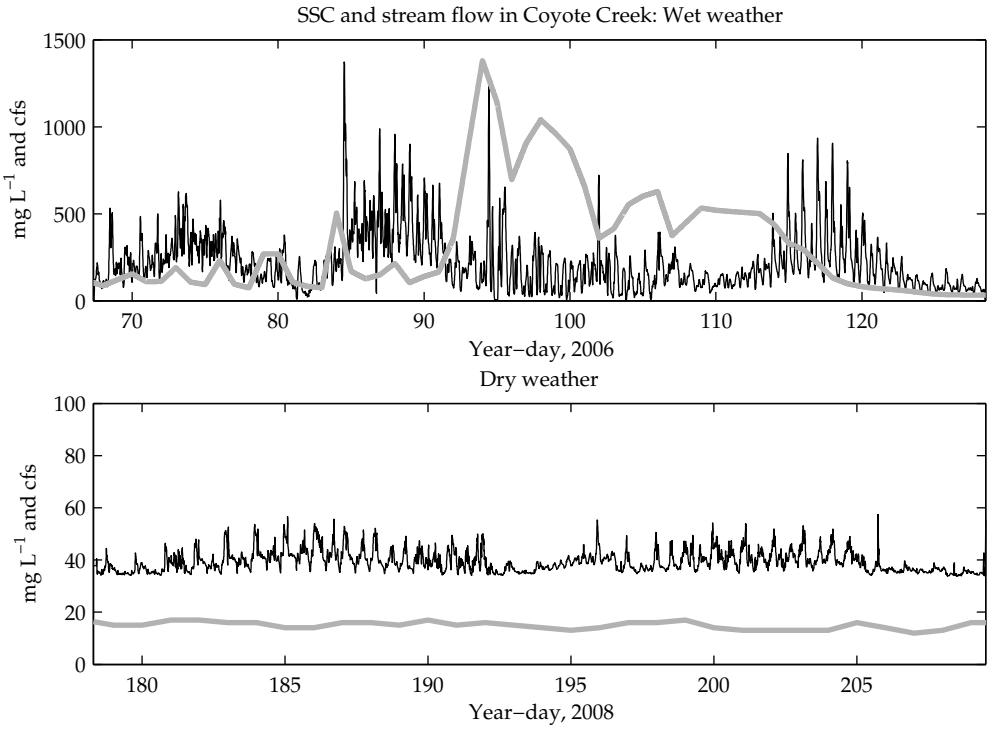

Figure 4-6: SSC in wet and dry weather
SSC in Coyote Creek (thin black line) and stream flow measured by USGS (thick grey line). Top panel: Spring 2006 – wet weather, East station, 50 cmab; Bottom panel: Summer 2008 – dry weather, Channel station, 20 cmab

The relationship between wind speed and SSC in Coyote Creek is unclear from our measurements. While wind waves are important for elevating bed stresses and thus resuspending sediment from the bed in general (Sanford 1994; Cacchione & Drake 1982), and in San Francisco Bay in particular (Lacy et al. 1996; Schoellhamer 1996; Brand et al. 2010), we did not find a strong relationship between them. Figure 4-7 shows time series of the spring 2006 and summer 2008 experiments and the wind speeds recorded during those times at NOAA's Palo Alto station. The variability that may be due to wind is masked by the influence of the spring-neap and daily tidal cycles and freshwater inflow.

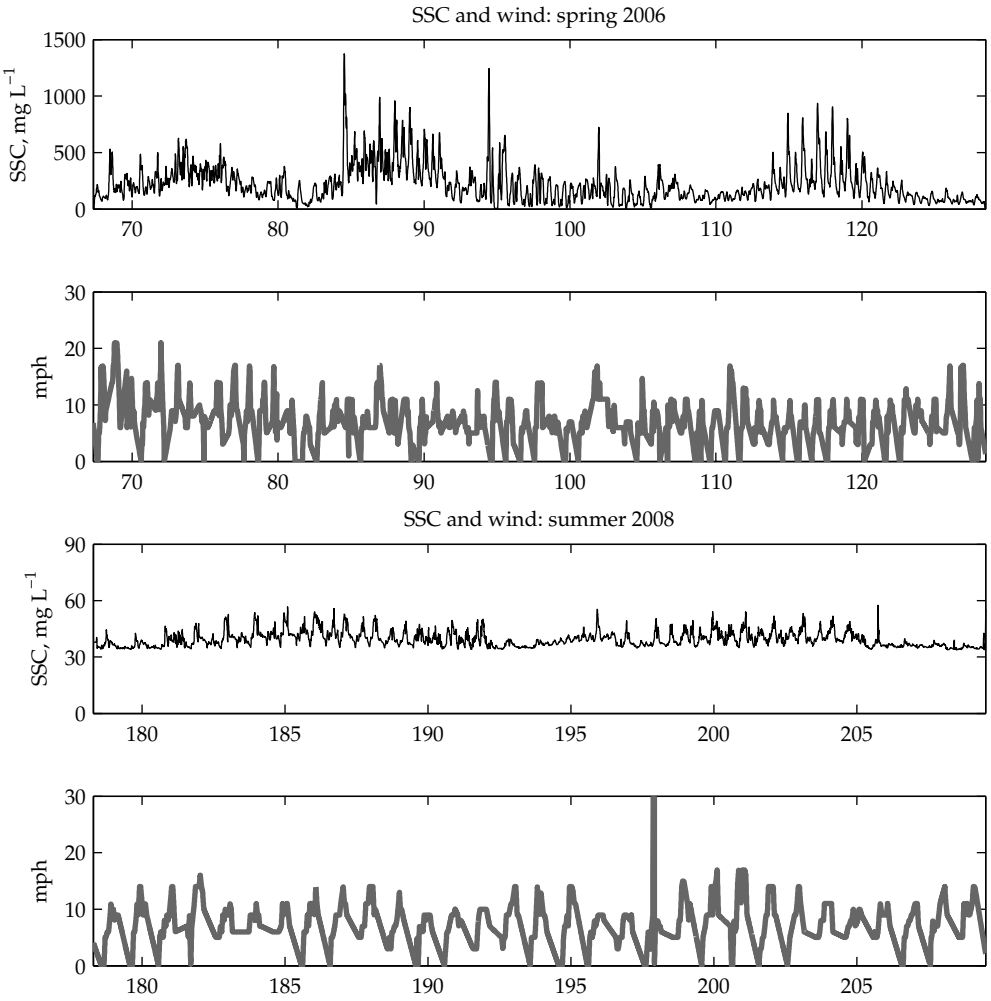

Figure 4-7: SSC and wind speed for fall and spring 2006

While a general dependency on wind measured 15 km away from the study site is, unsurprisingly, not discernable, the decomposition of waves from turbulence is compelling evidence that wind waves were not active at the site. Details of the decomposition using two methods are presented in Chapter 3, with the result that turbulent stresses were largely unaffected by wind waves. Limited fetch in this narrow channel could explain the absence of the influence of wind in our experiments.

Tidal variability in Coyote Creek's main channel

The intra-tidal variability in SSC is examined first during a low-rainfall period at the center station of the spring 2006 experiment (Figure 4-8). This station hosted two ADVs (50 cmab and 150 cmab) and was deployed near the center of the channel (relative to the east station, which was deployed near the bank between the channel and mudflat), making it helpful for providing a baseline of SSC conditions in Coyote Creek. The spring of 2006 was extremely wet, and flows in Coyote Creek as measured by the USGS were elevated (around 150 cfs rather than the dry-weather value of 20 cfs as shown in Figure 4-6, Station 11172175, United States Geological Survey 2006), even though precipitation was low for the days preceding the period pictured. This indicates that the time period considered here does not represent steady-state, but, when compared to the full dataset, it is clearly outside of the estuarine adjustment period that follows major storms.

Flood tides in this figure and all figures in this dissertation are shown by the shaded areas, and ebb tides are unshaded. The tidal variability shown in Figure 4-8 consists of SSC increasing through the flood with maximum concentration reached at the end of the flood tide (such as year-day 74.5), followed by a period of depressed concentration for the first hour of the ebb (74.6). The concentration then increases rapidly, reaching the ebb-tide maximum, and diminishes slightly for the remainder of the ebb. There is a low concentration period at the ebb-to-flood transition (low water) that is much briefer than the one observed at the flood-to-ebb transition (high water). The signal is approximately symmetric about the slack tides.

The intra-tidal structure of SSC in Coyote Creek is distinct from the commonly observed pattern of elevated suspended sediment concentrations in the presence of fresher water. The significance of the timing of high SSC relative to the salt wedge is its association with mechanisms driving sediment transport. The presence of salt stratification inhibits vertical turbulent motions, and therefore suspension and upward mixing of particles, leading to higher SSC up-estuary of the salinity front, and lower SSC down-estuary (Burchard & Baumert 1998; Geyer 1993). If SSC increases with the arrival of the salt wedge and ensuing stable stratification, then the levels of SSC are most likely not driven by a local resuspension event, but advected into the region from another location.

Figure 4-9 shows the timing of the arrival of high suspended sediment and salt concentrations (top and bottom panels, respectively). The highest suspended sediment concentrations arrive in the later portion of the flood, with the arrival of the salt wedge (e.g. year-days 74.5, 75). SSC decreases significantly just before the flood-to-ebb transition, at which point the salt wedge has been present for 1-2 hours. Early in the ebb tide, SSC remains depressed for over an hour (e.g. 74.6, 75.1). SSC then increases to a level similar to – but slightly lower than – the peak attained during the previous late flood. SSC diminishes for the remainder of the ebb tide in a manner loosely symmetric to the increase on the prior flood.

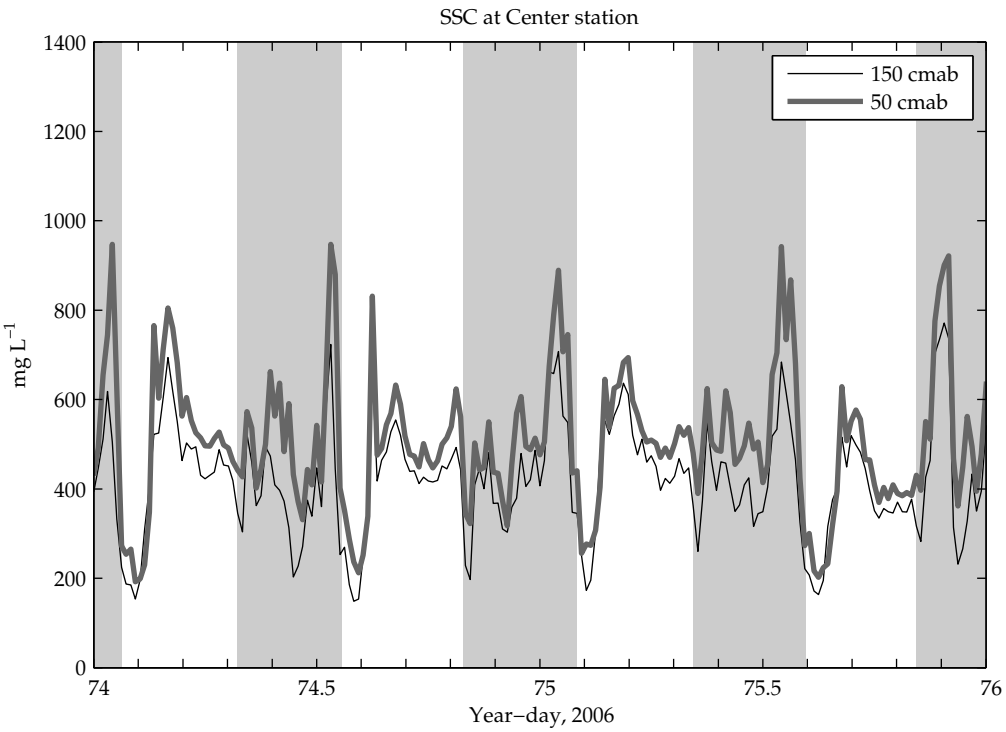

Figure 4-8: SSC at center station
This dataset provides a baseline for tidal variability in the thalweg of Coyote Creek. Floods are shaded and ebbs are unshaded, and 4 tidal cycles are shown.

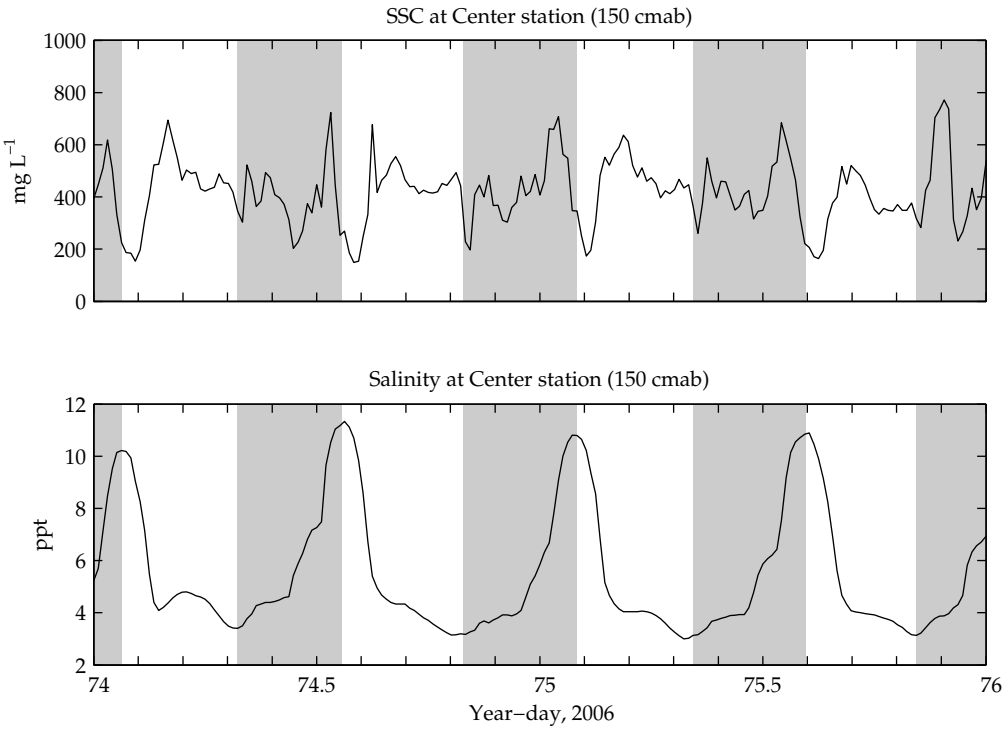

Figure 4-9: SSC and Salinity at Center station

Our measurements preclude calculation of the density stratification at this time since the salinity cell of the CTD at 50 cmab was filled with mud, however, we do have at our disposal a more direct measurement of the strength of mixing: the turbulence quantities themselves. Instead of comparing SSC to stratification, Figure 4-10 shows the suspended sediment concentration time series with those of the vertical turbulent motions, $\overline{w'^2}$, at the upper and lower ADVs. Consider the two complete flood tides pictured (grey shading), where $\overline{w'^2}$ at both ADVs peaks just before year-day 75 and right at 75.5 (solid gray line and dotted grey line). Meanwhile, SSC is still increasing, and peaks at 75.05 and 75.55, or about 1.2 hours after the decline of the Reynolds stresses. The substantial lag in the peak in SSC relative to the peaks in the vertical normal stresses indicates that although turbulence is damped in the presence of the salt wedge, another mechanism continues to drive the concentration of suspended sediment upward. Tidal advection of Bay-sourced sediment transported up Coyote Creek along with the salt wedge is a likely candidate.

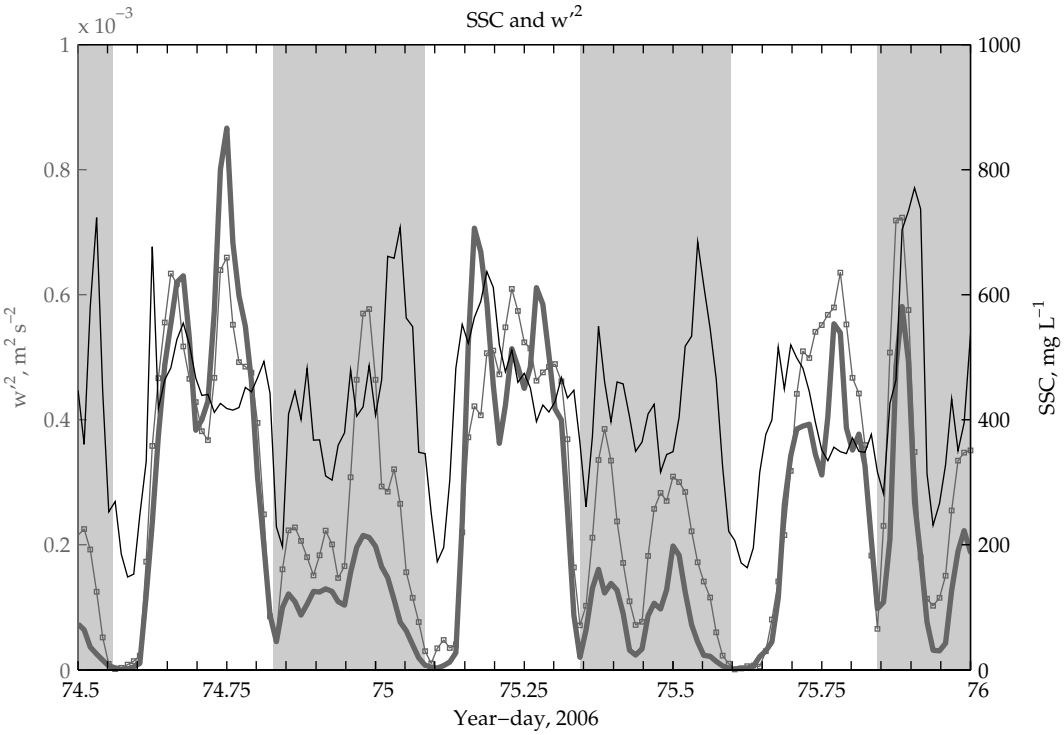

Figure 4-10: SSC and turbulent stresses

Center station: SSC at 150 cmab (thin black line, right axis), $\overline{w'^2}$ at 150 cmab (thick grey line, left axis), $\overline{w'^2}$ at 50 cmab (dotted grey line, left axis). Peaks in $\overline{w'^2}$ precede the peak in SSC by over 1 hour, suggesting that another mechanism (such as tidal advection) continues to drive SSC even though turbulence is inhibited by salinity stratification.

The settling lag must be considered when comparing the phasing of stresses (or velocity) with concentration. The settling lag is defined as the time required for a particle to fall to the bed when the decelerating current can no longer hold it in suspension (Dyer 1986, p.262), and in

conjunction with scour lag, it is considered an important factor in producing landward net transport of sediment (van Straaten & Kuenen 1958; D Pritchard 2005). In the simplest case of a lagged (unsteady) balance between particle settling and turbulent sediment flux, the settling lag would show up in time series measurements of SSC as a decrease in concentration when the water column above the sensor clears. For the center station during the period pictured, the total depth around high water is 4 – 4.75 meters. Sediment aggregates in San Francisco Bay have been measured to have settling velocities on the order of 0.1 – 1 cm s^{-1} (Kranck & Milligan 1992) and are used here for rough approximation in the absence of sediment samples from the field site. The maximum settling lag calculable given these parameters is therefore 4.75 – 1.5 m / 0.001 m s^{-1} = 54 minutes, where SSC is measured 1.5 m above the bottom. Having measured the lag between maxima in the vertical stress and SSC to be 1.2 hours (72 minutes) and noting that the particles would most likely begin to fall sometime after the maximum in $\overline{w'^2}$ when stresses are lower, we cannot conclude that the settling lag is not the reason SSC is elevated in the presence of the salt wedge.

While the end of the flood tide is inconclusive with regard to the role of tidal advection versus settling lag, the early ebb tide provides more substantial insight. Turbulent stresses in the water column are very low until 1.5 hours after slack tide (74.6, 75.1, 75.65), but SSC begins to increase within about 30 minutes after the flood-to-ebb transition. It has been concluded that the scour lag is often significantly shorter than the settling lag (D Pritchard 2005), but even if it is zero, the increase in SSC when turbulent activity is essentially non-existent points to the importance of other transport mechanisms.

The vertical gradient in SSC, as approximated linearly by the difference in concentrations at the two sensors divided by the distance between them (1 m), is shown in Figure 4-11. Although the backscatter to SSC calibrations are uncertain, examination of this gradient is useful to qualitatively assess the mechanisms driving the temporal changes in concentration. For most of the tidal cycle, the vertical concentration gradient is negative, indicating that SSC is higher closer to the bed, which is to be expected under the assumption that the bed is a source of sediment that is suspended by the tidal flows; however, during the early ebb (e.g. 74.1, 75.15, 76.65), the gradient reverses, suggesting that SSC is higher in the upper portion of the water column. This indicates that at this time, local bed resuspension is not the dominant mechanism driving sediment transport at the center station. This is consistent with the conclusions drawn from examining vertical turbulent stresses (Figure 4-10), which are too low to suspend particles from the bed during the very early ebbs.

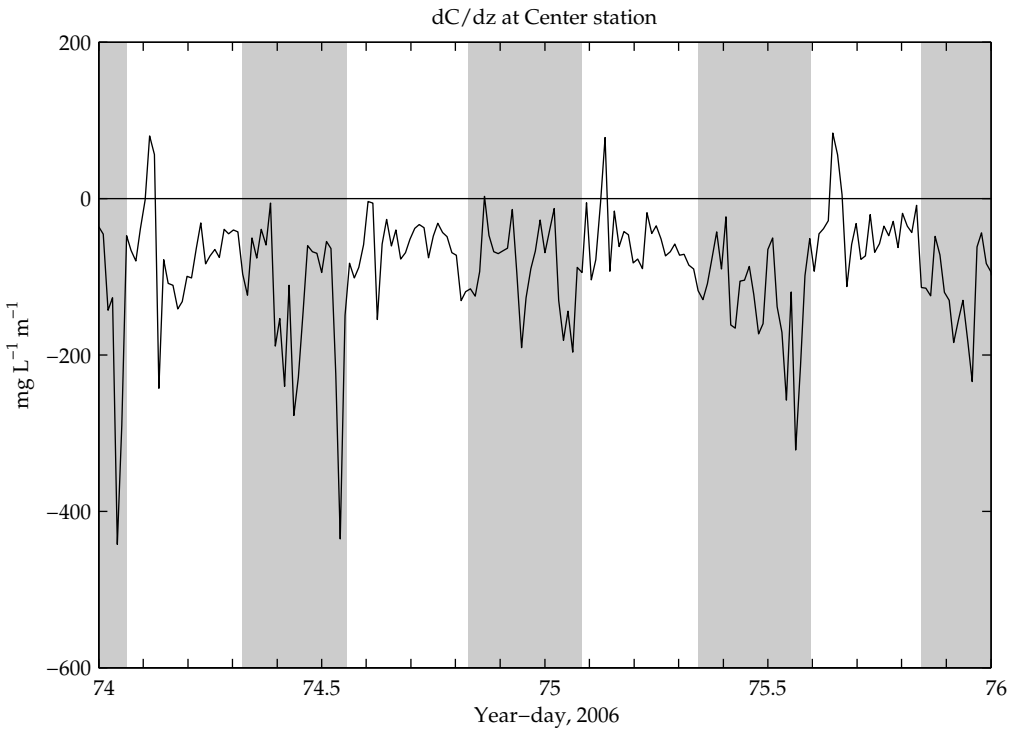

Figure 4-11: dC/dz at Center station
The gradient (or difference) in SSC becomes more positive in the early portion of each ebb tide (ebbs are unshaded).

Considering the periods of positive vertical SSC gradient in the context of horizontal flows provides insight into why these gradients develop. Figure 4-12 shows the vertical SSC gradient and the velocities recorded at the center station (50 cmab: dotted grey, 150 cmab: thick solid grey). One 24-hour period is shown so that the details are visible. The velocities are indicative of a boundary-layer structure, with the 50 cmab velocity always lower in magnitude than the 150 cmab velocity. The most unusual feature of the velocities occurs at the early ebb – coincident with the positive SSC gradient and low $\overline{w'^2}$. The velocity at 50 cmab transitions to negative after low water, but then plateaus at a magnitude of 0.1 – 0.2 m s^{-1}, while the velocity at the upper ADV accelerates almost linearly throughout this period. When the lower velocity finally accelerates (e.g. 75.15 and 75.655), the positive gradient in SSC drops rapidly and becomes negative. This suggests that two mechanisms are at work: low near-bottom velocities during the early ebb are slow to resuspend bed material that settled at slack tide, while the flows higher in the water column advect sediment that did not settle out of suspension during slack tide back down-estuary. The combined effect of these mechanisms is a period where the concentration of suspended sediment in the upper water column is higher than the concentration closer to the bed.

Although we cannot calculate salt stratification from measurements at this time and location, the shear in the early-ebb velocity suggests that stratification is indeed present at this time from the mechanism of tidal straining (Simpson et al. 1990). Essentially, tidal straining typically produces stable stratification on ebb tides by rotating the longitudinal salinity gradient to produce a vertical component; faster velocities high in the water column advect fresher water from up-estuary over the top of slower-moving near-bed flows. Figure 4-12 shows that velocities are strongly strained at this location, and this straining combined with the depressed vertical turbulent motions indicate that stable stratification exists during these early-ebb periods.

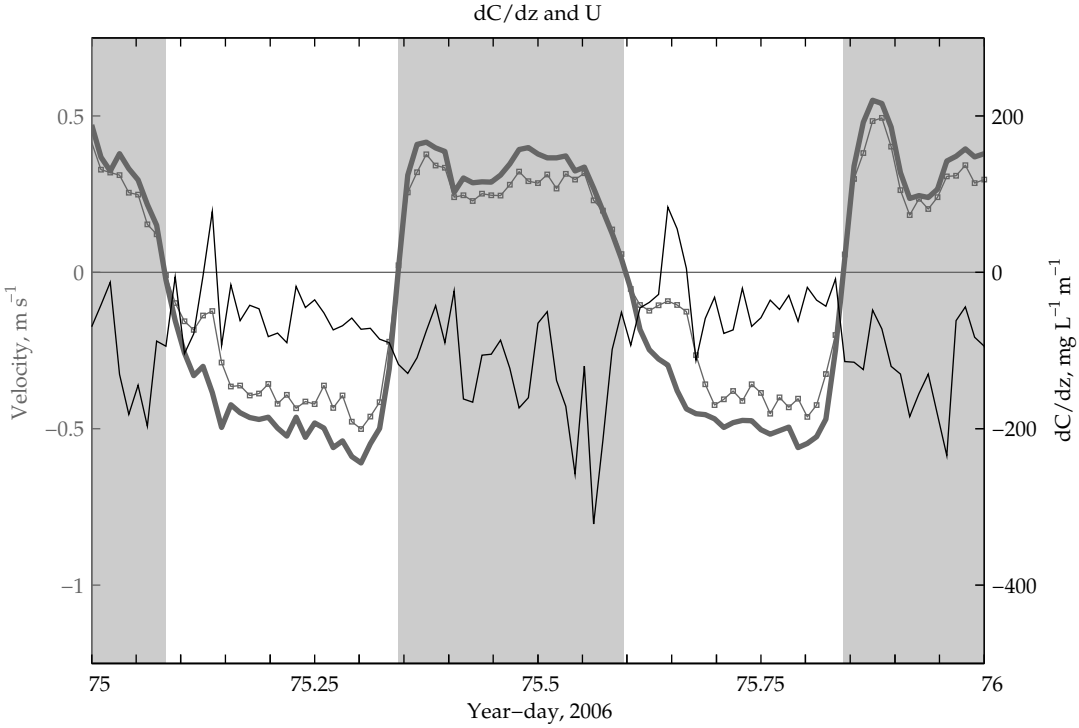

Figure 4-12: dC/dz and along-channel velocities at 150 cmab and 50 cmab
Center station: Vertical SSC gradient (thin black line, right axis), longitudinal velocity at 150 cmab (thick grey line, left axis), longitudinal velocity at 50 cmab (dotted grey line, left axis)

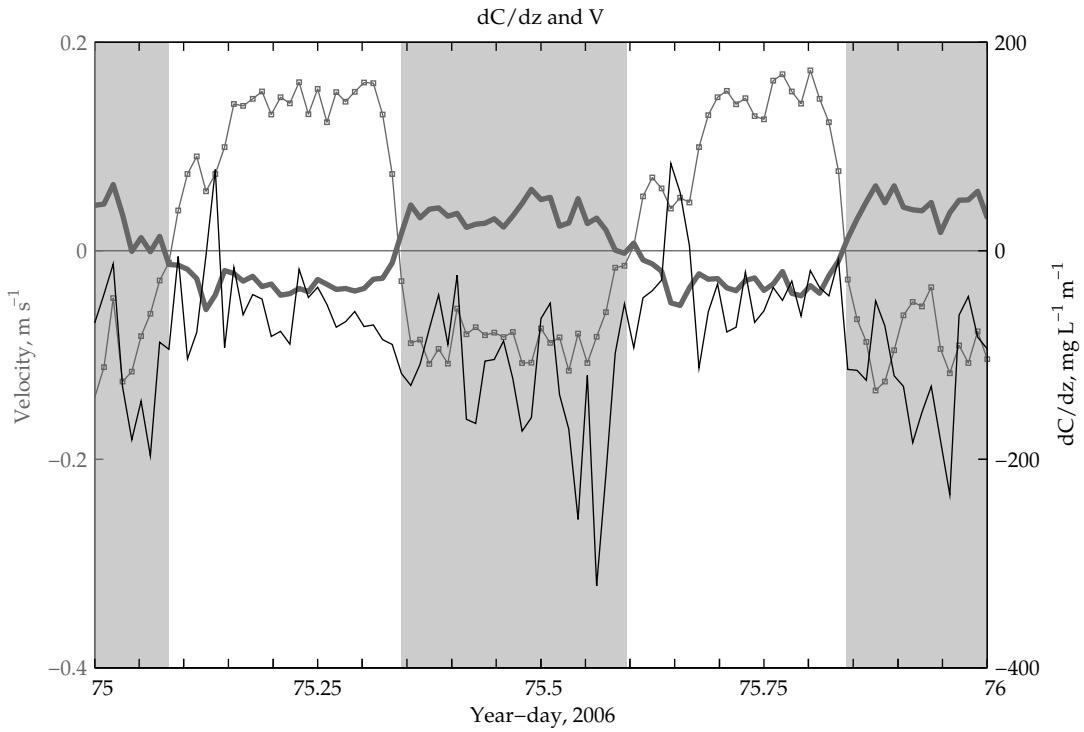

Figure 4-13: dC/dz and cross-channel shear
Center station: Vertical SSC gradient (thin black line, right axis), lateral velocity at 150 cmab (thick grey line, left axis), lateral velocity at 50 cmab (dotted grey line, left axis)

While the primary flow direction is along-channel, the three-dimensional nature of velocities in Coyote Creek must not be ignored. Figure 4-13 shows vertical gradient in SSC (same as Figures 4-12 and 4-11), with transverse velocities overlaid. The structure of the figure is equivalent to Figure 4-12, where the velocity (V) is shown at the ADV at 50 cmab (dotted grey line) and 150 cmab (thick solid grey line) on the left axis, and the SSC gradient (thin black line) is shown on the right axis. Generally at the center station on ebb tides, lateral velocities are directed roughly northward at the lower ADV (positive V) and southward at the upper ADV; however, during the occurrence of the positive SSC gradient, both lateral velocities experience a southward dip; flow at 150 cmab becomes more strongly negative, and flow at 50 cmab becomes less positive (times 75.15 and 75.65). This feature is presumably a result of the draining of the salt ponds or the broad mudflats along the north bank of Coyote Creek.

In summary, at the center station during a dry several-day period within a wet season, elevated levels of SSC accompany the arrival of the salt wedge on the flood tide. SSC begins to fall as the flood decelerates and turbulent motions diminish. After the start of the ebb, SSC rises approximately one hour before any appreciable increase in turbulent motions, and SSC at the upper ADV rises more rapidly than at the lower ADV. These observations indicate that local resuspension is not the dominant mechanism driving SSC during the early ebb. Velocities measured at these elevations show shear in the water column, in both horizontal directions, but most strongly in the along-channel velocity, and the periodic nature of the observed shear suggests that it is controlled bathymetrically. (Vertical velocities are approximately 2% of the

longitudinal component, which is the same order of magnitude as the measurement error, and therefore not considered dynamically.) It is concluded based on these data that horizontal advection is an important mechanism of sediment transport in Coyote Creek, particularly on early ebb tides when turbulence is not strong enough to resuspend sediment locally. It appears that at these times, horizontal velocity fields are advecting sediment that was suspended elsewhere into our measurement locations. In addition, similar to the salinity dynamics explored in Chapter 3, vertical shear in horizontal velocities may be straining gradients of SSC, producing periods where SSC is higher in the upper water column than the lower water column. This conclusion contradicts the often-invoked assumption that a balance of settling and resuspension represents estuarine sediment transport.

Tidal variability near Coyote Creek's channel-mudflat boundary

The proximity of the mudflat-channel boundary to the east instrument station has a pronounced effect on sediment concentrations in the upper water column. Figure 4-14 shows SSC measured at 50 and 150 cmab during the same time-period plotted in Figure 4-8 (year-days 74-76). In general, concentrations of suspended sediment are lower than at the center station. The most distinctive difference, though, is the clearing of the upper water column on ebb tides. On floods, the signals at 50 and 150 cmab track closely, with a persistent negative vertical gradient (where bottom concentration is higher than the upper ADV). On ebbs, however, SSC drops to very low levels (10-20 mg L^{-1}) at 150 cmab while it recovers to values similar to the flood tide at 50 cmab.

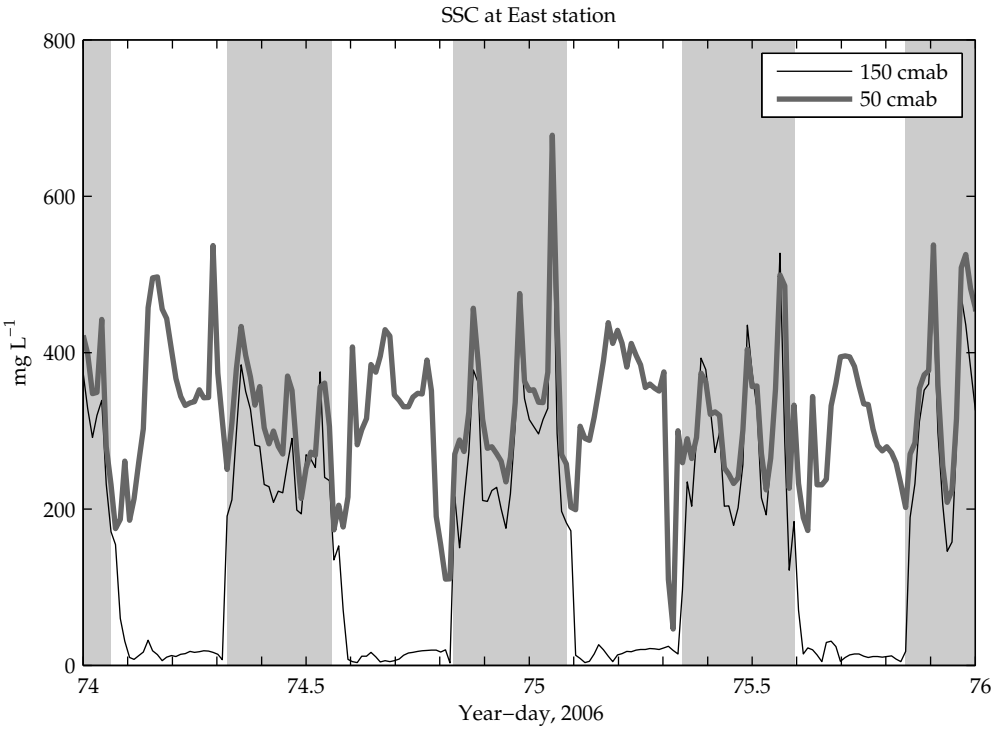

Figure 4-14: SSC at East station
On flood tides (shaded) the SSC signals at 50 and 150 cmab track closely, but on ebb tides, the SSC at the upper ADV drops to 5-10% of the concentration at the lower ADV.

In Chapter 3 we established that measurements at this station at 150 cmab are affected by mudflat outflow throughout the ebb tide, and we conclude that this outflow is producing the unusual time series of SSC as well. Dyer et al. (2000) found that on mudflats in calm weather, ebb concentrations of sediment are lower than flood concentrations, even in ebb-dominant environments, due to the settling lag. On flood tides, when the velocity drops below the critical value for keeping sediment in suspension, it continues to be advected up-estuary while it falls toward the bed (van Straaten & Kuenen 1958). The sediment that eventually settles on the mudflats has landed in a region with a different flow regime from where it originated, and typically, much lower velocities than the channel. Therefore, on the ensuing ebb tide, velocities over the mudflats are too low to resuspend an amount of material equivalent to that deposited during the flood, producing the well-known tidal asymmetry. In Chapter 3, the draining of the mudflats into the channel at the east station was explored in detail, and found to be influential throughout the ebb tide. We conclude based on that analysis as well as the SSC data presented here that the flow sampled by the east ADV at 150 cmab on ebb tides is low in suspended sediment because it consists of low-SSC mudflat effluent.

Modification of intra-tidal structure by storms

During dry weather in Coyote Creek's main channel, the general variability reflects suspension of bed sediments and landward advection on floods, settling around high water, and resuspension and down-estuary advection on ebb tides. Figure 4-15 shows SSC plotted against along-channel velocity (m s^{-1}) for all three instrument stations of the spring experiment (East, center, and West). The right column of plots (a-c) shows a dry-weather period, and the left column (d-f) shows a period of heavy rainfall.

During dry weather, sediment concentration generally increases with increasing velocity, but peak SSC values occur at velocities of lesser magnitude than peak flood and ebb, reflecting the time required to travel vertically through the water column after the elevation of bed stresses due to tidal flows. Another salient feature of the dry-weather plots is that the maximum values of SSC occur on flood tides (positive velocities), in spite of the fact that Coyote Creek is ebb-dominant, and ebb velocities are 10-20% greater than floods at our instrument stations. This suggests that some sediment is trapped in the shallow ponds and mudflats after the flood tide, from which it is only partly resuspended on ebb tides (Dyer et al. 2000). This observation fits within the context of other studies in South San Francisco Bay that have concluded that tidally-averaged sediment transport in South San Francisco Bay is landward, and that sediment travels from the Bay to be redistributed amongst perimeter habitats over subsequent tidal cycles (Schoellhamer 1996).

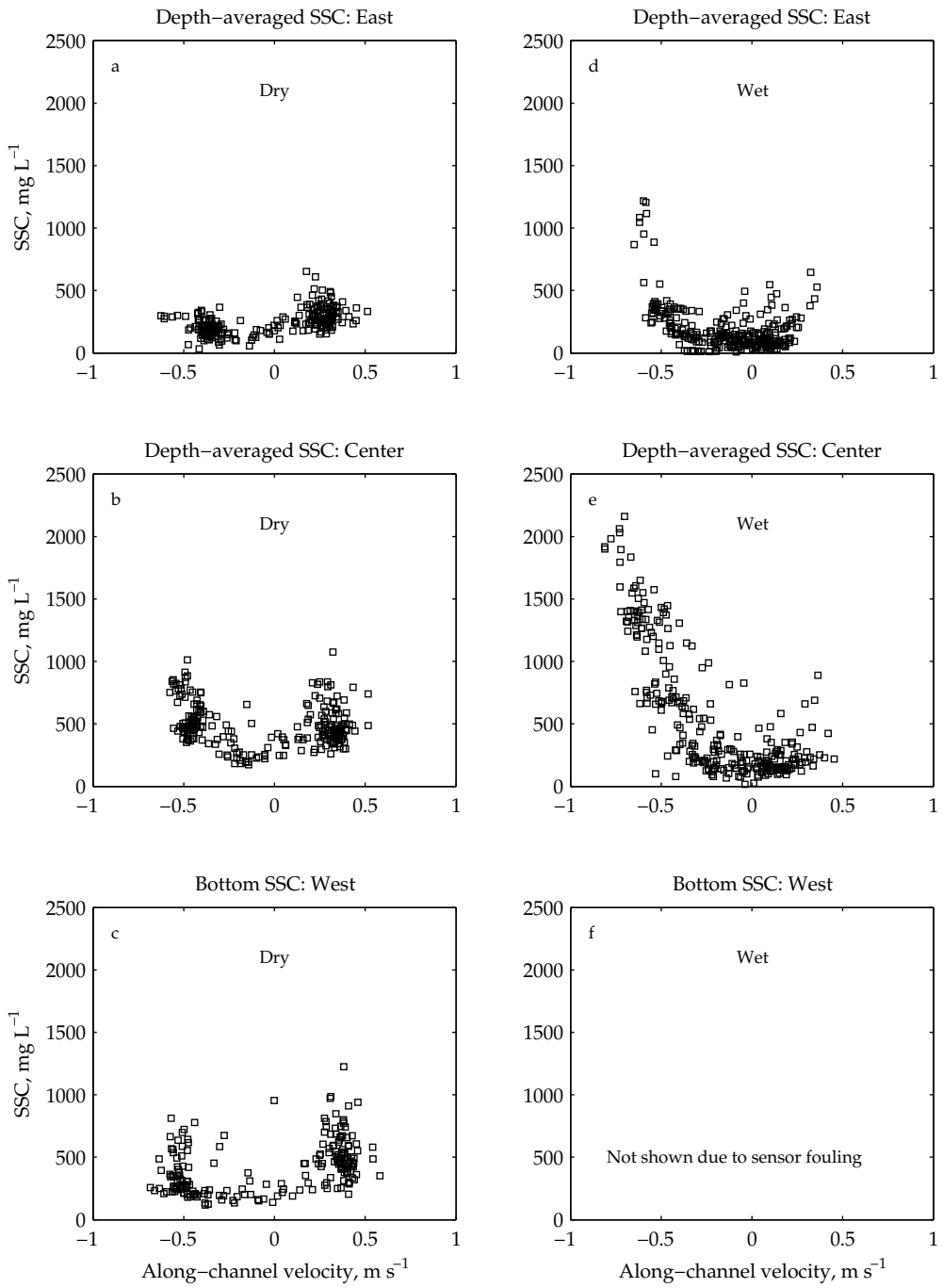

Figure 4-15: SSC vs. U, spring 2006

During wet weather, the relationship between SSC and along-channel velocity changes (panels d and e). The peak values of SSC are much higher than during dry weather, and occur during ebb tides (negative velocities). The implication is that the rain event brings a new supply of sediment to the upper reaches of the estuary, which is being advected toward the Bay on ebb tides. Peak concentrations on flood tides during wet weather are not markedly different from

those attained during dry weather, suggesting that the new supply of sediment was deposited in the channel up-estuary of the Island Ponds, or in the higher elevation habitats, such as the mudflats and marshes. On ebb tides, it is resuspended and transported down-estuary in great concentrations, past our moored instruments.

4.3.3 Spatial variability: pond, breach, and channel

Magnitudes of suspended sediment increase between the channel and breach. Figure 4-16 shows SSC measured during the fall 2006 experiment at the pond station (50 cmab) and the mudflat station (30 cmab) in the left panel. The right panel shows SSC collected during the summer 2008 experiment at the mudflat station (20 cmab), and at the channel station (20 cmab). Note the distinct vertical axes. There is a seasonal difference reflected in the two time-periods, but there is a clear increase in SSC from the channel to the mudflat, and again into the pond. Magnitudes of SSC at the channel station are an order of magnitude lower than those recorded in the mudflat and pond for all phases of the tide. This indicates that sediment is being scoured from regions between the channel thalweg and the breach, and further resuspension is occurring within the breach and pond.

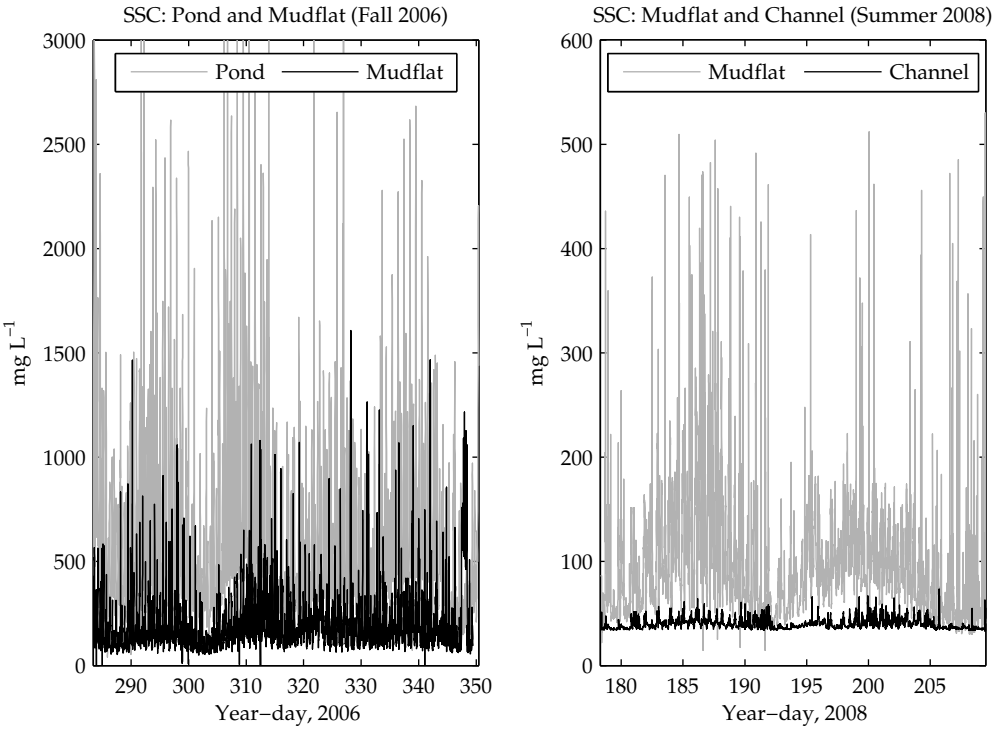

Figure 4-16: SSC in the Pond, Mudflat, and Channel
There is a general increase in SSC from the channel toward the pond

There is variability in sediment transport between the channel and pond in addition to magnitudes of concentration. Figure 4-17 shows the relationship between velocity and SSC for three moorings during the fall 2006 experiment. For this experiment, velocities at all stations were rotated onto the principal axes of the channel station. The breach is oriented roughly 90

degrees from the main axis of Coyote Creek, so the along-breach direction is aligned with the transverse component of velocity in the channel. Velocities shown in Figure 4-17 contain the maximum variance locally; at the channel station, the along-channel velocity is shown (floods are positive and toward the east), at the mudflat station the along-breach velocity is shown (floods are positive and toward the north), and in the pond, the along-borrow ditch velocity is shown, which in this region is parallel to the channel's main axis (floods positive to the east). Note that the vertical axes for each plot vary, reflecting a lateral (along-breach) gradient in suspended sediment concentration, where concentrations are highest in the pond and lowest in the channel.

The velocity-SSC relationship shows an ebb-flood asymmetry that gets more pronounced from the channel (panel c) to the pond (panel a). In the channel, surface SSC reaches similar peaks on floods compared with ebbs. In the mudflat/breach region, the SSC is elevated on floods compared to ebbs, and within the pond, the flood concentrations of suspended sediment are significantly higher than those on ebbs. While these discrete point measurements do not make it possible to calculate a mass flux of sediment into and out of the ponds, the implication is that more sediment enters the breach and pond than exits. As flood waters fill the pond, sediment is carried through the breach and along the borrow ditch while the tide rises. As flows cover the broad, interior island near high tide, sediment drops out, and ebb velocities atop the island are too low to resuspend it before the water level falls and it is exposed to air, producing an asymmetry similar to what has been observed on mudflats (Dyer et al. 2000). This conceptual model is corroborated by accretion observations within Pond A21 that show that sediment accumulated at a rate of 130 mm yr^{-1} for the first year after breach construction in the southern half of the pond, where the breaches are located (Callaway et al. 2009).

Another lateral transition visible in this plot is the elevated SSC at slack tide in the pond that diminishes at the breach, and does so further in the channel. We must note that the channel backscatter from the fall 2006 experiment were collected about 0.5 meters beneath the water surface, but the slack-tide peak in SSC is also missing from the spring 2006 channel data at all three stations (near-bottom and depth-averaged). These peaks at low velocities occur at both the flood-to-ebb and ebb-to-flood transitions. Depths around low water (defined here as less than 1.75 meters in the pond) are shown by black squares, and all other depths are shown by grey squares, indicating that the slack-tide peaks occur at low water as well as high water. The low-water peak is unexpected based on the tidal variability in the channel, where high SSC occurs with the arrival of the salt wedge, and reflects a dynamic process that is distinct to the interior of the pond.

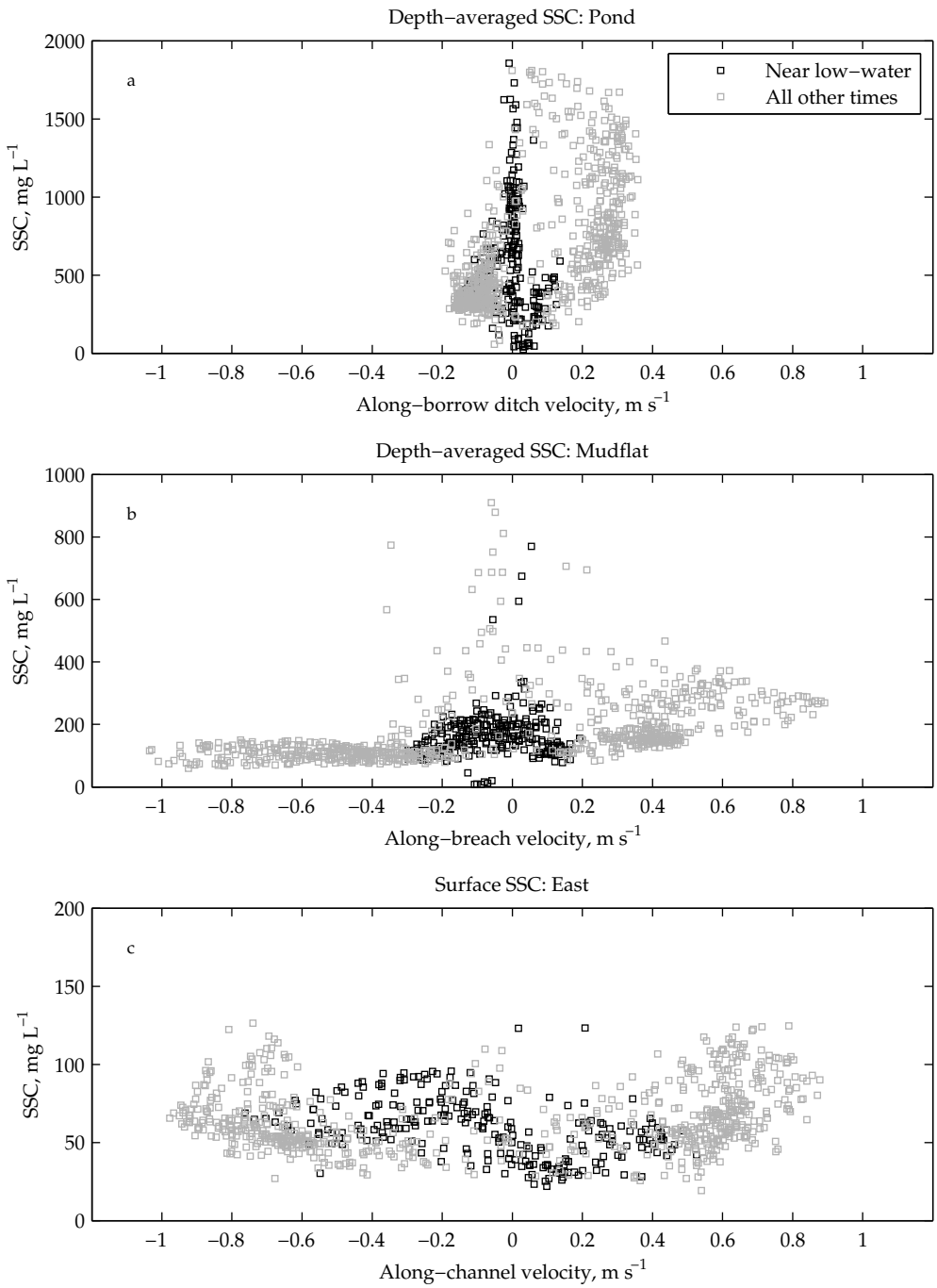

Figure 4-17: SSC vs. U, Fall 2006
Black markers indicate measurements near low water, and grey markers are all other times. The flood dominance becomes more pronounced from channel to pond.

Identifying this process specifically is not possible with the existing data, but the most probable explanation is advection of a cloud of sediment from a nearby location. We can use the data to rule out certain other processes. Wind is most effective at elevating SSC at low depths by generating bed stresses that are capable of resuspending sediment (Lacy et al. 1996). Figure 4-

18 shows the relationship between SSC and wind magnitude (left panel) and the relationship between SSC and the vertical turbulent flux of sediment (right panel), specifically at depths less than 2 m. There is not a clear dependence of SSC on either wind speed or turbulent mass flux, and as discussed in Chapter 3, wind-waves have not elevated measured turbulent stresses, so we conclude that wind waves are not the dominant mechanism driving high SSC at low water. The low velocities late in the ebb combined with the ill-defined relationship between SSC and turbulent flux also rule out tidal resuspension.

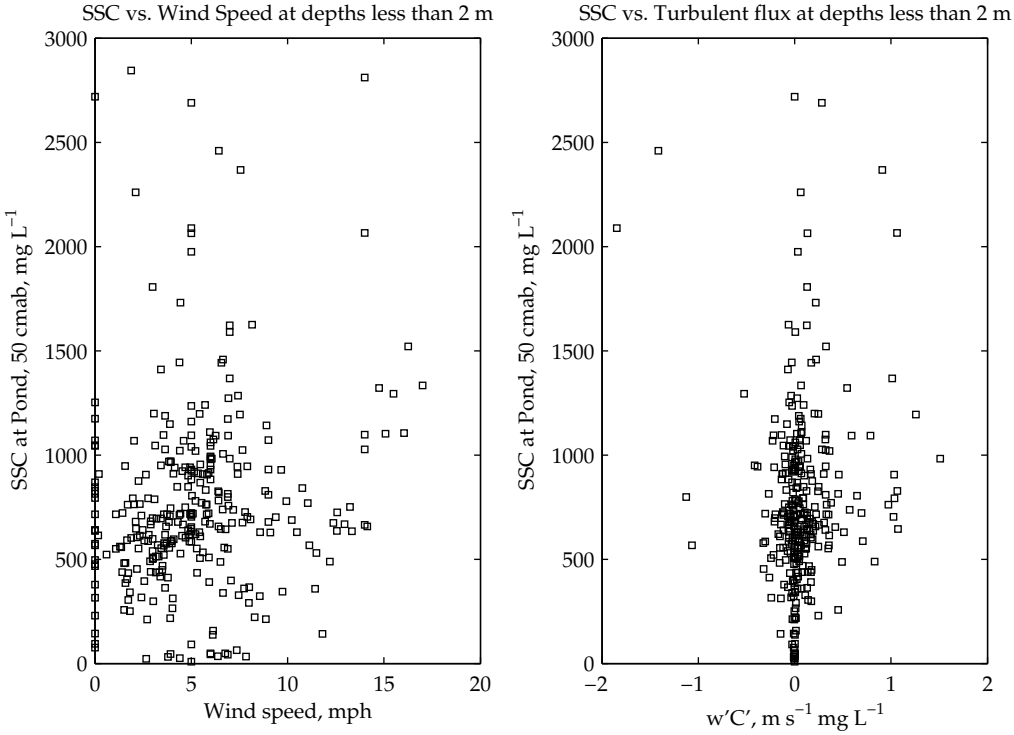

Figure 4-18: SSC and wind at low water

Another possible mechanism to explain the high SSC at low water is particle settling as the ebb tide decelerates. To consider this, we must examine the time series of SSC at the Pond station (shown in Figure 4-19). Low-water spikes of sediment concentration at the 50 cmab ADV appear, for example, at times 295.8, 296.9, 297.9, and 298.9 (each lower-low water). If settling particles are passing by the sensor at these times, they must be originating from higher in the water column. The ADV at 150 cmab went dry at these low depths, so we do not have an indication of SSC at that elevation. Nevertheless, examination of the times of higher-low water, such as 296.3 and 297.4, shows a small but similar increase in SSC at both ADVs at the end of the ebb. This suggests that particle settling could be occurring throughout the water column, but the disparity between the two SSC values casts further doubt on the calibration, and we cannot determine conclusively the contribution of settling.

We have concluded that the low-water spikes are not due to tidal or wind wave resuspension, and the contribution of particle settling is unresolved. What we do know is that since these high values of SSC appear as spikes that are not being scoured from the bed, sediment is being

advected horizontally into the vicinity, either directly, or into a layer higher in the water column, from which it settles past the ADV at 50 cmab.

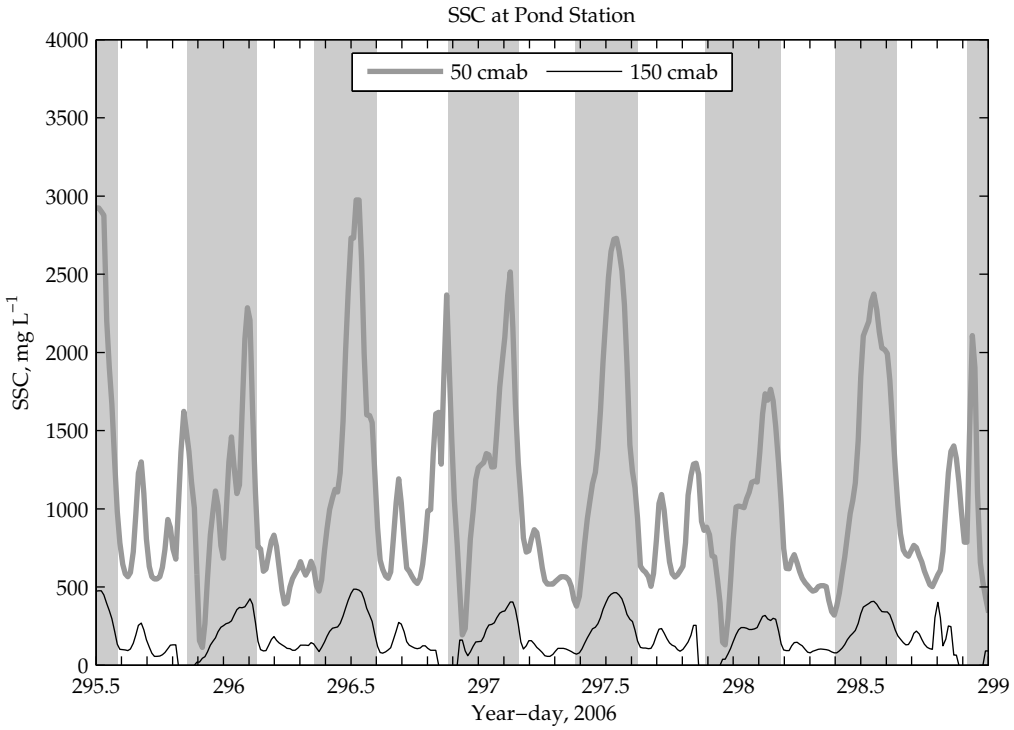

Figure 4-19: SSC at Pond station, Fall 2006
Particle settling may be elevating SSC at 50 cmab at each lower-low water.

4.3.4 Sediment budget considerations

Having explored the mechanisms of suspended sediment transport that control the dynamics reflected in our data, we now examine them in the context of the sediment mass balance (equation 4-1). The objective is to determine which transport terms are necessary to achieve first order accuracy in representing sediment transport in our data collection locations in Coyote Creek and Island Pond A21. Reducing the complexity of equation 4-1 for these locations provides value by allowing conceptual insight into the mechanisms which can get lost when regarding the full expression. Calculation or scaling of the terms in the full sediment budget is not possible without accurate estimates of spatial gradients of suspended sediment concentration; however, starting with the simple case, it is possible to determine the mechanisms that are missing and formulate a more complete dynamical model.

The balance between particle settling and turbulent mass flux (equation 4-2) has been found to provide a very good first order approximation of sediment dynamics in estuaries, and has even been used to identify sediment characteristics based on calculated settling velocities (Fugate & Friedrichs 2002). This calculation must be performed with an ADV, which collects collocated, high-frequency measurements of velocity and concentration (via backscatter). In Coyote Creek and the Island Ponds, however, this balance only sometimes achieves first order accuracy. The

results discussed in previous sections indicate that the sediment budget at our field site was not simply a balance of settling and turbulent flux under at least the following specific conditions: in the presence of the salt wedge; during wet weather; and at low water inside the pond.

The most straightforward way to diagnosis this balance is to calculate the settling velocities (w_s) using equation 4-3, and determine if they are (1) downward (negative) and (2) of appropriate orders of magnitude. This approach does not address the many complexities of the settling velocity, including its critical dependence on total concentration, grain size distribution, and turbulent shear (e.g. Pejrup & Mikkelsen 2010), but it does provide some basic insight. Two ADVs from the spring 2006 experiment are used for this analysis: center station, 150 cmab, and east station, 50 cmab. The other two ADVs deployed during this experiment are not used for this analysis because they were affected by exchange with the mudflat (east 150 cmab) or showed an unexplained drop in SSC during heavy rain (center 50 cmab). Figure 4-20 shows the negative of the turbulent mass flux versus concentration for dry weather (panels a and b) and wet weather (panels c and d). The slope is equal to the settling velocity (assuming this balance is valid). Note that the vertical axes are the same (units of m s^{-1} mg L^{-1}), and the horizontal axes are different for wet and dry weather (units of mg L^{-1}). The data are grouped by flood and ebb: circles indicate floods and pluses indicate ebb tides.

During dry weather, the slope is negative, but the data do not fall onto one line, suggesting that particles and aggregates of multiple sizes are present. The ranges are -1.5 to 0 mm s^{-1} at Center 150 cmab and -2.5 mm s^{-1} to 0 at East 50 cmab. These ranges are equivalent to fall velocities of estuarine flocs of 10s to 100s of microns in diameter (Gibbs 1985), which are in the range – albeit the low end – of flocs observed in San Francisco Bay (Kranck & Milligan 1992). Another feature of the dry-weather plots is the minimum concentration of about 200 mg L^{-1}. This can be interpreted as the "background" concentration of particles too small to settle out during slack tides (Fugate & Friedrichs 2002).

Turning to the wet-weather cases, the relationship between turbulent flux and concentration is quite different. Most importantly, the settling velocity is not consistently negative, which is impossible by definition. The highest positive "settling velocities" inferred from these plots occur during ebb tides, which are marked by pluses. The implication is that instead of suspending sediment from below, the turbulent flux is transporting it downward, or out of our mass balance control volume. Since the settling velocity is always negative, there must be an additional process that is supplying sediment to the control volume during wet weather, and particularly during ebb tides.

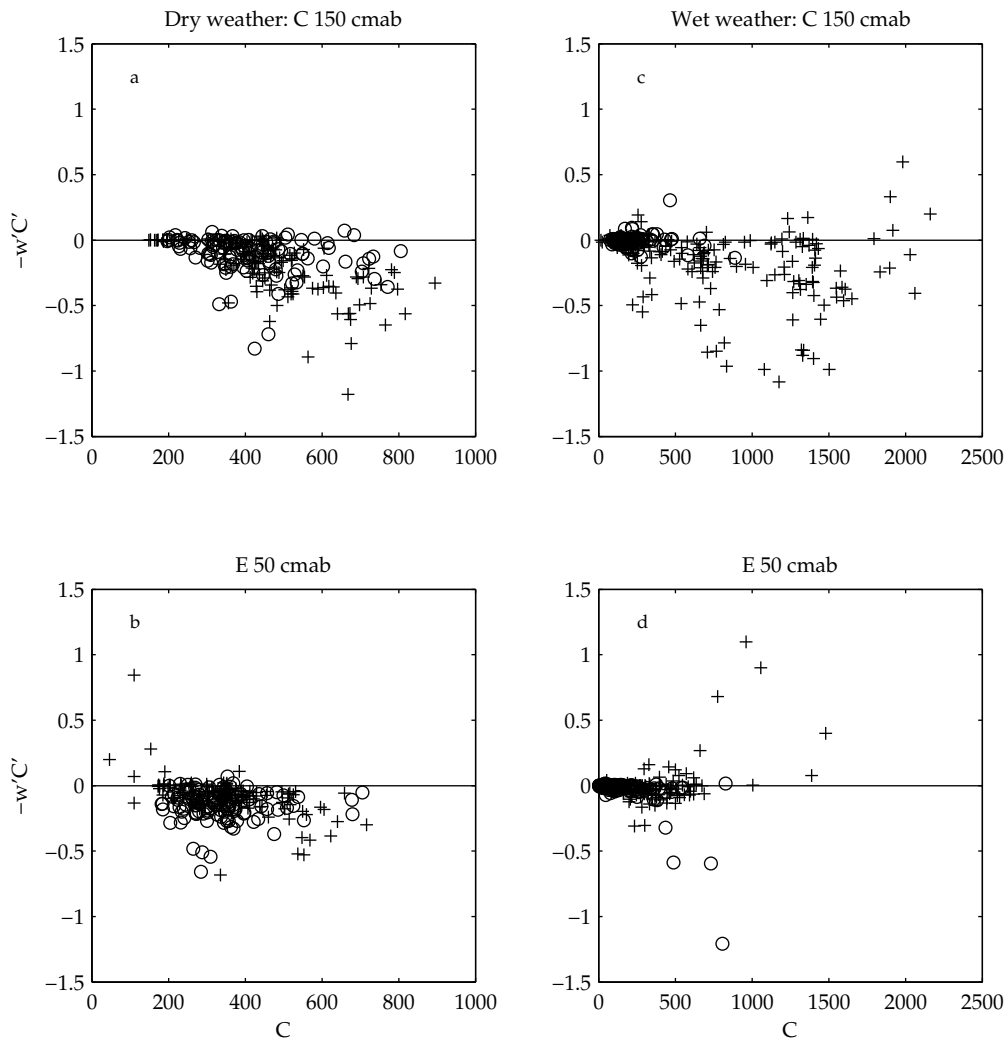

Figure 4-20: Settling velocity, wet and dry weather
Floods: o; Ebbs: +
For equation 4-3 to be valid for these data, the slope of resuspension versus concentration must always be negative. Based on this, we can conclude that 4-3 is not valid *at least* during wet weather (panels c and d).

An additional balance that can be explored using this simple framework is the one inside the salt pond. Figure 4-21 shows the turbulent mass flux plotted versus the concentration for both ADVs inside Pond A21 (a: 150 cmab and b: 50 cmab). Again, the sign of the inferred settling velocity from this balance is not consistently negative, showing that the balance is invalid inside the pond. Note that positive values of $-\overline{w'C'}$ occur on floods and ebbs, which is distinct from the wet weather case in the channel, during which they mainly occurred on ebbs.

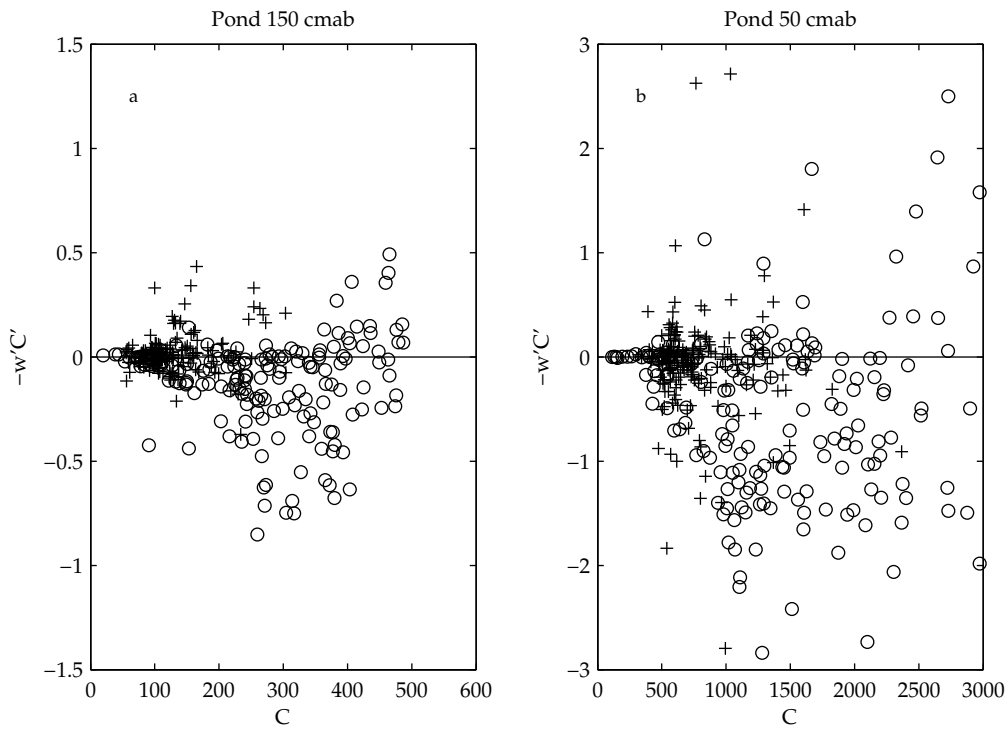

Figure 4-21: Settling velocity in Pond A21
Floods: o; Ebbs: +
The slope of resuspension versus concentration is not always negative, indicating that equation 4-3 does not describe the sediment budget for these data.

Consideration of these inferred settling velocities as well as the exploration of mechanisms in the last section suggest that in addition to settling and local resuspension, unsteadiness and horizontal advection play an important role in transporting suspended sediment. Settling and scour lags are difficult to quantify in general, and impossible to parse from our data, but their importance to estuarine sediment transport is significant. These lags have been determined to be responsible for the tidal asymmetry of SSC that leads to net landward sediment transport (van Straaten & Kuenen 1958; Dyer et al. 2000), and are represented in the mass balance for sediment by unsteadiness. The tidal asymmetry in Coyote Creek's main axis in the absence of rainfall is slight, but present, and this asymmetry is compounded if subtidal timescales are considered. The asymmetry in dry weather near irregular bathymetry, such as within the pond and at the channel-mudflat interface, is great, even on timescales of individual tidal cycles. Settling lag and the unsteadiness term in the mass balance are therefore assumed important factors in transporting sediment in this region.

Horizontal advection also should not be eliminated from the mathematical description of sediment transport in Coyote Creek and in Pond A21. In the case of wet weather, ebb-tide velocities advect the newly input sediment load Bay-ward. In the channel axis (the center station of the spring 2006 experiment), SSC during early ebb tides is differentially advected to the instrument station from up-estuary and possibly from the mudflats to the north. At the southern channel-mudflat boundary (east station, spring 2006 experiment), lateral advection is

particularly important in supplying very low concentrations of SSC in mudflat effluent on the ebb tides. Within the ponds, highly irregular bathymetry causes frontal features to develop and advect into the vicinity of our sensors on both phases of the tide.

$$\frac{\partial C}{\partial t} + u\frac{\partial C}{\partial x} + v\frac{\partial C}{\partial y} + w_s\frac{\partial C}{\partial z} = \frac{\partial}{\partial z}\left(-\overline{w'C'}\right) \tag{4-4}$$

We conclude that unsteadiness and horizontal advection in addition to particle settling and turbulent resuspension are needed to understand sediment transport in Coyote Creek (equation 4-4), where the contribution of these additional terms is heightened with freshwater inflows and close proximity to topographic irregularities. In the presence of a complex perimeter or after meteorological events, the simplest and widely used sediment budget, in which settling balances resuspension, does not adequately describe estuarine sediment transport.

4.4 Summary and Conclusions

Velocities, water properties, and acoustic and optical backscatter were measured in a macrotidal slough in South San Francisco Bay in the vicinity of irregular topography. Measurements were conducted over a variety of wet weather conditions: a rainy spring, an average fall, and a very dry summer. Our measurements show that the variability in morphology and freshwater flow impact total levels of suspended sediment concentration, direction of subtidal transport (as indicated by flood or ebb dominance in SSC), as well as the balance of mechanisms driving sediment transport on tidal timescales. The classical balance of particle settling and turbulent resuspension provides reasonable estimates of particle settling velocity for unperturbed locations and time periods, such as in a straight channel during dry weather, but the small tidal asymmetries in SSC indicate that the balance should be unsteady to account for settling and scour lags. The importance of including unsteadiness grows as longer timescales are considered. For the unperturbed case, horizontal advection is important during early ebb tides. During wet weather and in the presence of complex bathymetry, horizontal advection and unsteadiness are critical, and the complicated dynamics preclude estimating particle fall velocities based a balance of settling and turbulent resuspension.

CHAPTER 5

The influence of the perimeter on subtidal estuarine dispersion

5.1 Introduction

Exchange between an estuary and its perimeter habitat greatly influences transport and concentrations of scalars throughout the system, and depends on complex interactions between bathymetry, tides, winds, and inputs of freshwater. Supplies of salt, sediment, nutrients, and contaminants to fringe sloughs and marshes have immense ecological implications for the viability of those habitats. Likewise, dispersion of scalar concentrations along the main axis of the estuary is impacted by lateral processes (Fischer 1972; Fischer et al. 1979; Geyer et al. 2008), and is pertinent to the estuary's productivity (Jassby et al. 1995), morphology (Ralston & Stacey 2007), and level of contamination (Smith 1976). This study addresses the physical processes driving lateral exchange between an estuary and its perimeter habitat, as well as the implications of this exchange for flow and transport dynamics along the estuary, and was published in a 2010 journal article by MacVean & Stacey.

5.1.1 Dispersion in estuaries

The decomposition of estuarine dispersion into longitudinal salt fluxes was formally presented by Fischer (1972; 1976; Fischer et al. 1979). The framework separates velocity and salinity into cross-sectional averages (and variations from the average) and tidal averages (and variations around the average), then averages the product of velocity and salinity over the cross-section and tidally, resulting in a quantitative measure of the contribution of a number of mechanisms to the total longitudinal flux. The decomposition is performed on velocity and salinity values measured (or modeled) throughout a cross-section of an estuary over at least one 25-hour period, as done, for example, in the San Francisco Bay by Fram (2005), in the Hudson by Lerczak et al. (2006), and in the Columbia by Hughes and Rattray (1980). Each component of the sum represents a physical transport mechanism: advection by river flow, tidal trapping, Stokes drift, baroclinic steady exchange, and shear dispersion.

Fischer et al. (1979) categorize these mechanisms as either advective or dispersive. Advection by river flow, which represents the salt advected through the estuarine cross-section by freshwater inputs to the landward end of the estuary, is the unique advective term in this framework, while the effects of the remaining terms, which are often coupled, are aggregated by a single dispersion coefficient and treated as a cumulative dispersive process. In this treatment, spreading due to all dispersive terms is represented as a dispersion coefficient multiplied by a salinity gradient, and in a steady balance, this term provides an up-estuary salt flux that balances the down-estuary advective flux from river flow.

The four dispersion terms in this decomposition vary temporally, cross-sectionally, or both. The cross-sectionally averaged, tidally varying terms are tidal trapping and Stokes drift. Tidal trapping occurs when the cross-sectionally averaged velocity and salinity signals are out of quadrature; when maximum cross-sectionally averaged salinity is not reached precisely at the end of the flood tide, the velocity and salinity signals are out of phase by an amount other than 90 degrees. Classically defined, tidal trapping results when dead zones, such as side embayments, small channels, and shoals, trap water and salt on the flood, releasing them on the ebb out of phase with the primary salinity front in the main channel. Traditional treatment of tidal trapping, as well as a new framework for quantifying its effects, will be explored in detail in subsequent sections. Stokes drift is especially important when the tidal range is large compared with the average depth, and arises when the cross-sectionally averaged velocity and the cross-sectional area of the flow are out of quadrature, yielding a non-zero net transport of water. The inertia of a tidal flow can delay slack velocity relative to high or low water as the tidal pressure gradient changes sign. The result is that the cross-sectional area of the flow on floods is greater than ebbs, producing a tidally averaged net landward flux of water. This flux sets up a complimentary barotropic pressure gradient directed down-estuary that balances the net transport of water.

The steady, cross-sectionally variable velocity and salinity fields interact to produce the baroclinic steady exchange term in the salt flux decomposition. This steady flux results from the residual flow and salinity fields and represents the tidally-averaged density forcing through the estuary. All remaining variability is encompassed by the shear dispersion term, which is variable in both time and space. This term accounts for an oscillatory, cross-sectionally varying velocity profile acting on the salinity field. Random phenomena that act on timescales shorter than the tidal period are captured by this term, such as rapid changes in wind forcing. In addition, other dispersive mechanisms interact with the shear dispersion term to produce a highly coupled system of fluxes.

5.1.2 The objective of this study

Our study explores the salinity dynamics of a tidal slough that exchanges with volumes along its perimeter. This exchange, which is tidally-forced, is dynamically equivalent to a branching channel, and the analysis presented here is suitable for both environments. The perimeter volumes (or channel branches), which temporarily retain water and constituents it carries, alter the phasing of flows and scalar concentrations in the slough's main channel. Longitudinal dispersion in the slough is affected by this exchange largely through the mechanism of tidal trapping. While dispersion due to tidal trapping has been estimated in other studies, most

notably by Okubo (1973) for traps that exchange diffusively with the main flow, we have found that the classical formulation misrepresents exchange driven by tidal advection. We propose a distinct formulation to quantify the effects of changes in phasing resulting from perimeter exchange on estuarine dispersion, and we suggest a dimensionless number that helps discern the suitability of these formulations.

In order to explore this new framework, we first summarize the physics that dominate an estuary's exchange with its perimeter and the resulting shifts in phasing of velocities and scalar concentrations. The following section addresses the effects of spatially varying frictional forcing, the interaction of the pressure gradient, velocity, and salinity signals, and the ensuing tidal trapping flux. Subsequently, we present field observations of these phenomena and the ways in which the existing treatment of tidal trapping misrepresents the physics of exchange and dispersion for the present environment. Finally, we derive an alternative formulation for estuarine dispersion driven by perimeter exchange and changes in phasing, and we explore its implications.

5.1.3 The physics of tidal trapping

The phasing of a flow's velocity relative to tidal stage depends on the regional tidal dynamics and the retarding force exerted on the flow by friction. As the tides interact with a basin, the degree of reflection of the tidal wave determines whether the tides are standing waves or progressive waves. Inviscid analysis shows that in standing waves, the velocity and stage are exactly 90 degrees out of phase; in progressive waves, velocity and stage are in phase.

Locally, the effects of friction become important in establishing variability in the phasing of flows. Regions that experience relatively high levels of friction, such as those that are shallow, vegetated, or have an otherwise rough substrate, lose a considerable amount of momentum, and tidal velocities in these regions respond quickly to changes in the barotropic pressure gradient. In comparison, deeper areas exert less friction on the flow, and after reversing, the tidal pressure gradient must increase until it is able to overcome the flow's inertia before changing the flow direction. Equation 5-1 shows the along-channel balance of momentum from unsteadiness, the barotropic pressure gradient, and the vertical divergence of the Reynolds stress.

$$\frac{\partial u}{\partial t} = -g\frac{\partial \eta}{\partial x} + \frac{\partial}{\partial z}\left(\nu_t \frac{\partial u}{\partial z}\right) \tag{5-1}$$

In the shallow regions, unsteadiness is small, and the along-channel velocity (u) is 90 degrees out of phase with the pressure gradient. In the deep regions, unsteadiness is important, and the pressure gradient and velocity signals are no longer 90 degrees out of phase; in these regions, the velocity's response to tidal forcing is delayed, so that the pressure gradient lags the velocity by less than 90 degrees. The time between a change in forcing and a corresponding change in flow is referred to as the phase lag.

Spatial variation in the amount of friction exerted on a tidal flow will lead to variations in the phasing of the local velocity relative to tidal stage, and can cause the cross-sectionally averaged

velocity and salinity time-series to be out of quadrature. We describe this process using an example of a tidal channel lined by relatively shallow shoals. The channel's response to the changing tidal pressure gradient lags that of the shoals, such that during the flood-to-ebb transition, the main channel continues to carry high-salinity water up-estuary, while the flow over the shoals reverses and freshens. A lateral salinity gradient is thus created. Mixing processes act on this gradient to homogenize the cross-section, which reduces the salinity of the flow in the channel. By the time the velocity changes direction to flow down-estuary, the peak salinity has already passed, and the velocity signal lags the salinity by less than 90 degrees. In this example, the departure from quadrature yields a landward tidal trapping flux of salt.

Fischer et al. (1979) illustrate this phenomenon using an example of a branching tidal channel. The flood waters and a theoretical scalar cloud enter both branches, one small and one large, and upon the transition to the ebb, the flow in the small channel reverses before the flow in the large channel. The result is the fraction of the scalar cloud that traveled into the small channel rejoins the main channel prior to the arrival of the fraction of the scalar cloud that traveled into the large channel. The differential phasing that acts on the two stems of a branching channel divides the original scalar cloud into two portions with differing phase lags, causing both a longitudinal spreading of the scalar, as well as a lateral gradient of scalar concentration across the main channel.

There is a subtle, but important, distinction, however, between the examples described in the previous two paragraphs. In the first case, two subregions of the channel are out of phase with one another due to differential effects of friction, but those subregions are continuously exchanging with one another in a diffusive manner. In the second case, the merging channels are out of phase, but now that phase shift directly affects the phasing of the exchange between the two channels. The distinction lies in the process that is providing the exchange between the channel and the storage volume: in the first the two are diffusively coupled; in the second they are advectively coupled but with a variable phase shift.

5.2 Observations of tidal trapping

5.2.1 South Bay Salt Pond Restoration Project in San Francisco Bay

In the South San Francisco Bay, a landscape-scale marsh restoration project underway at the time of this study provided an opportunity to investigate an estuary's exchange with volumes along its perimeter – in this case, breached ponds formerly used for salt production. We conducted field experiments to examine the physics of tidal trapping and estuarine dispersion in a tidal slough connected to former salt ponds through levee breaches. The Island Ponds are a cluster of three adjacent former salt ponds, located in the southeastern-most reach of South San Francisco Bay, as shown in Figure 5-1. They are bounded by Coyote Creek on the south and Mud Slough on the north. The levees on their southern border were breached in March 2006, allowing exchange with Coyote Creek for the first time in approximately a century, according to the California Coastal Conservancy, California Department of Fish and Game, and Fish and Wildlife Service, which are the state and federal agencies responsible for the restoration. There were five breaches, two in each of the larger ponds (A21, A19) and one in the smaller pond (A20). The tidal prism within the ponds, which are on average 1 km^2 in area

and 1 meter deep, is on the same order as that of the adjacent reach of Coyote Creek: about 10^6 m^3. Coyote Creek is flanked by broad intertidal mudflats to the north, and narrow mudflats to the south. The total width of the sub- and intertidal cross-section is on the order of 150 meters. Our study focused on the western-most breach in Pond A21.

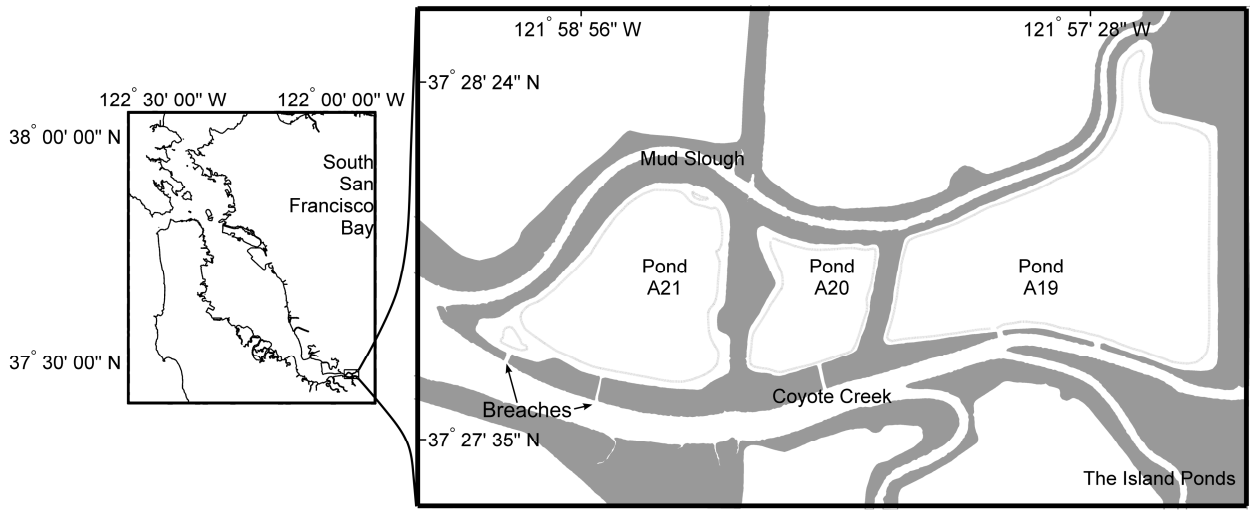

Figure 5-1: South San Francisco Bay and the Island Ponds. Breaches, formed in March 2006, allow ponds A19, A20, and A21 to exchange with Coyote Creek.

5.2.2 Field experiments

Field measurements collected in Coyote Creek were used to characterize flow velocity, conductivity, temperature, and depth. We performed a deployment of moored instruments, lasting two months (mid-October to mid-December 2006), with sampling frequencies from 3 to 15 minutes. Four instrument frames were moored in a lateral configuration extending from the thalweg of Coyote Creek, across the channel, through the breach, and into Pond A21 (see Figure 5-2). The shallowest stations, inside the pond and inside the breach, were instrumented with 2 Acoustic Doppler Velocimeters (ADVs, Sontek and Nortek), which measure velocities at a point, with sampling volumes at 0.5 and 1.5 meters above the bed. Conductivity-Temperature-Depth (CTD, RBR and Seabird) sensors outfitted with Optical Backscatter (OBS, D&A) sensors, to measure conductivity (salinity), temperature, pressure (depth), and backscatter (suspended sediment concentrations) were placed at the same elevations. Acoustic Doppler Current Profilers (ADCPs, RD Instruments), which measure vertical velocity profiles, were deployed at the deeper channel stations, along with CTD/OBSs pairs near the surface and bottom.

In addition to the moored instrument deployment, boat-mounted profiling and surveying were conducted in Coyote Creek in the spring and fall of 2006, as well as the summer of 2008, to improve spatial resolution over a limited time period. We measured bathymetry and profiles of velocities using a down-looking ADCP, and a CTD/OBS package was mounted to the boat to measure water properties 25cm below the surface.

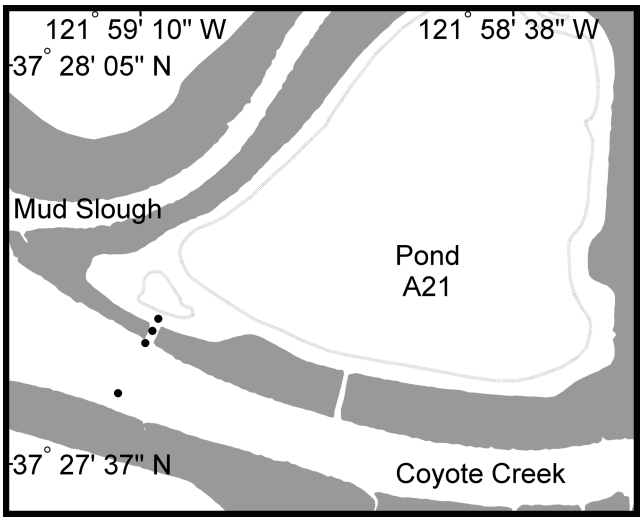

Figure 5-2: Coyote Creek and Mooring Locations. Moorings are shown by filled black circles.

5.2.3 Results of field experiments

Our measurements yield a picture of flows along Coyote Creek and lateral exchange with the Island Ponds. The experiment duration and sampling frequencies allowed us to capture diurnal and semi-diurnal timescales for tides and wind, as well as the fortnightly spring-neap tidal frequency. The dominant tidal frequencies are M2 and K1, resulting in twice daily, unequal tides. Coyote Creek is a macrotidal slough with an average depth in the main channel of 3 meters. Tidal range is 2.5 meters on neap tides to just over 3 meters on springs.

Velocity and salinity ranges

In Coyote Creek, depth-averaged along-channel velocities vary over the range of about ± 1 m s^{-1}, while cross-channel flows vary between approximately ± 0.1 m s^{-1} (Figure 5-3a). In the western-most breach of Pond A21, depth-averaged along-breach velocities vary over about -1.3 m s^{-1} to 1 m s^{-1}, and cross-breach velocities vary from -0.2 m s^{-1} to 0.3 m s^{-1} (Figure 5-3b). Noting that the breach is oriented approximately perpendicularly to the axis of Coyote Creek, we define the sign convention as follows: Positive along-channel (or cross-breach) velocities are up-estuary (floods), and negative along-channel velocities are down-estuary (ebbs). Positive cross-channel (or along-breach) velocities are directed into the ponds (roughly northward), and negative cross-channel velocities are directed out of the ponds (roughly southward). Salinities varied from about 12 to 28 during this dry weather period (Figure 5-3c). The structure of the salinity signal recorded in the breach is quite distinct from that of the channel, and the details of both are discussed in the following sections.

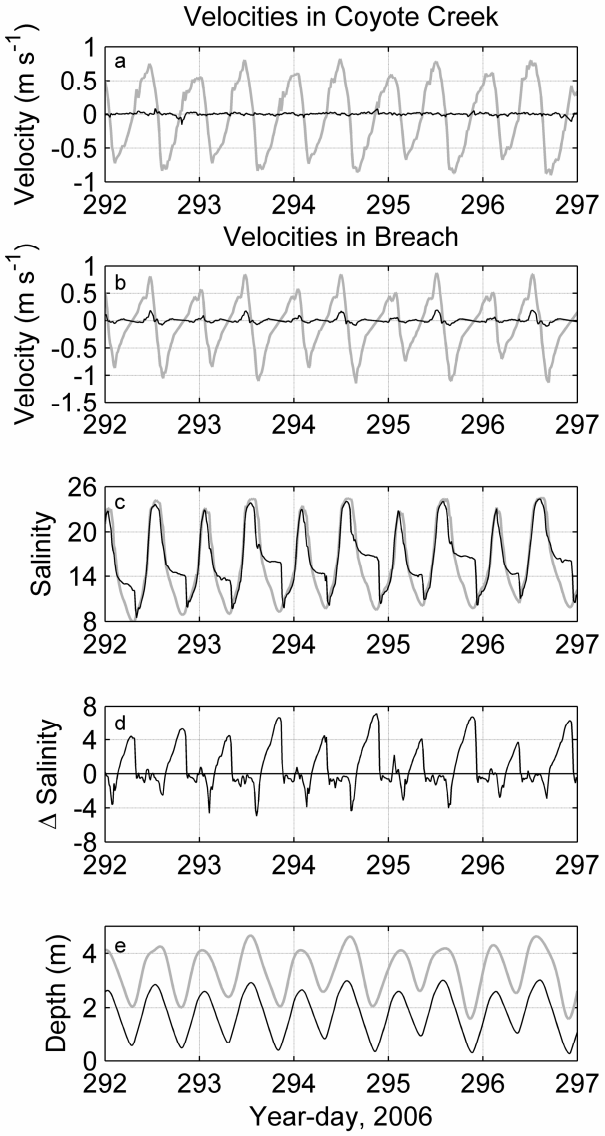

Figure 5-3: Conditions at Study Site: Velocities, Salinities, and Depths.
(a) Coyote Creek velocities (m s^{-1}) - gray line: along-channel, black line: across-channel. (b) Breach velocities (m s^{-1}) - gray line: along-breach, black line: cross-breach. (c) Salinities – gray line: Coyote Creek, black line: breach. (d) Breach salinity – Coyote Creek salinity. (e) Depths (mab) - gray line: Coyote Creek, black line: breach.

Lateral salinity gradient and exchange dynamics

Our observations show a periodically reversing lateral salinity gradient across Coyote Creek on each ebb tide, shown in Figure 5-3d as the difference in salinity. The salinity in the channel is essentially symmetric about high and low water, while the pond effluent has a very different salinity structure from the water that enters on the flood. Early in the ebb tide, the pond effluent has a lower salinity than that recorded in the main axis of Coyote Creek, resulting a

negative lateral gradient (for example, at day 294.5 in Figure 5-3c and 5-3d). Salinity drops quickly as the flow through the breach responds to the reversal in the barotropic pressure gradient, while the salinity in the main channel is sustained as the up-estuary momentum of the deeper flow must be overcome prior to changing direction. This lateral salinity gradient persists for the first half of the tidal cycle, and at its maximum has a value of -5 – -3 salinity units per 100 meters. Mid-way through the ebb-tide, when the water surface in the pond has reached the elevation of the intertidal interior island, the salinity in the channel continues to drop steadily, but the salinity in the pond effluent plateaus at an intermediate value, and diminishes only slightly for the remainder of the ebb tide (e.g. day 294.7 – 294.9). This produces a lateral salinity gradient of the opposite sign and results in higher salinities at the breach relative to the channel flow, with a typical maximum gradient of 6 – 7 salinity units per 100 meters separation between the two mooring stations. In summary, on every ebb tide, a reversing lateral salinity gradient sets up such that early in the ebb, the channel is more saline than the pond effluent, and later, the channel is fresher. The magnitude of this gradient depends on the spring-neap cycle and the daily inequality, where springs and the greater of the daily ebb tides produce the steepest gradients in salinity, as much as 8 salinity units over 100 meters.

Phasing in the channel and breach

The high-inertia flow in Coyote Creek is slower to respond to the tidal barotropic pressure gradient than the relatively shallow Island Ponds. A lagged correlation of the entire data record of along-channel velocity in Coyote Creek relative to water depth shows that velocity and depth are out of quadrature (where quadrature indicates a perfect standing wave) by 32 minutes. The phase lag for an individual tide deviates from this average value in response to the daily inequality as well as the spring-neap tidal forcing. The phase lags in the channel between velocity and depth, and velocity and salinity, for one 24-hour period are shown in Figure 5-4. The phase lags, in days, are shown by the width of the vertical gray bars, and each lag is labeled on the figure in minutes. On this day, high water occurs before high slack tide by 32 and 50 minutes, while low water leads low slack tide by 22 minutes, and later lags it by 5 minutes (Figure 5-4a).

The maxima and minima in salinity generally precede slack water by 12 minutes (Figure 5-4b) according to a lagged correlation of the salinity and velocity datasets in Coyote Creek. While 15-minute salinity data were used to calculate the phasing, Figure 5-4b shows the salinity after the application of a one-hour moving average. The elimination of fine-scale fluctuations in the salinity allows the tidal-scale sinusoidal structure and phasing relative to the velocity to be more readily visible in the figure. The observations are consistent with the tendency for the channel to freshen slightly just before high slack tide, as lower-salinity waters transported by the early ebb in low-momentum regions mix laterally, prior to the change in direction of channel flow. Equivalently, just before low-slack tide, channel salinity increases as the early flood transports more saline waters first into low-momentum areas, which then mix across the channel.

The flow through the breach, more heavily influenced by friction than the channel, responds more promptly to the tidal pressure gradient, and a lagged correlation shows that slack water lags maxima and minima in the depth by 8 minutes. Phasing in the breach during the same 24-

hour period, shown in Figure 5-5a, illustrates a range in the magnitude of lags between velocity and depth, from -4 minutes (where slack tide leads high water) to 34 minutes. The flood-to-ebb slack tide lags the maxima in velocity by 12 and 7 minutes during year-day 295, shown in Figure 5-5b.

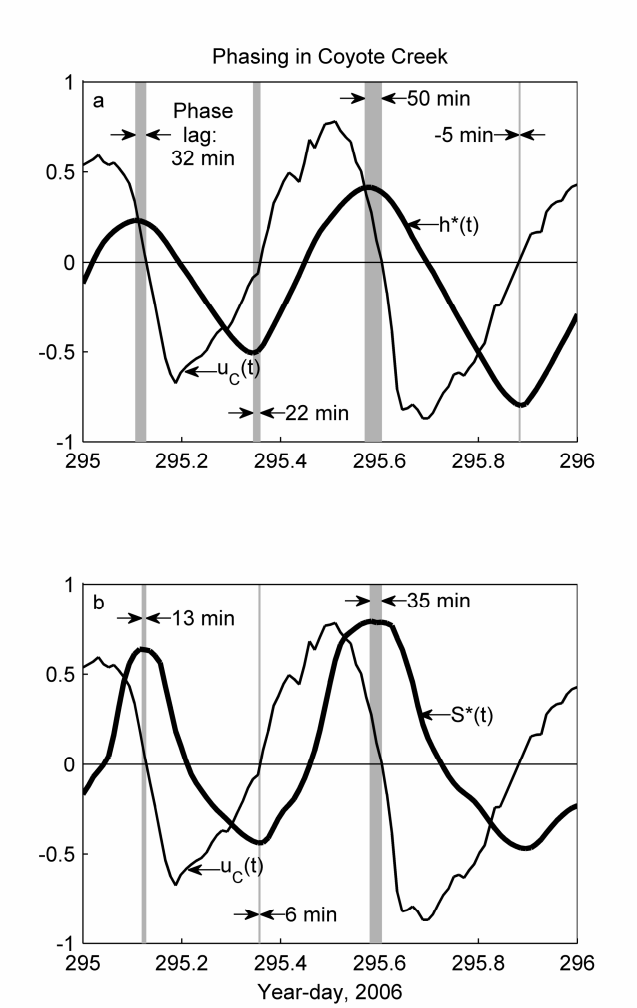

Figure 5-4: Phasing in Coyote Creek
(a): Thin black line: Depth-averaged along-channel velocity (m s^{-1}). Thick black line: Departure of water depth from the mean, scaled by the tidal range (h*). Solid gray band: Phase lag between time of slack water and time of maxima/minima of water depth. (b): Thin black line: Depth-averaged along-channel velocity (m s^{-1}). Thick black line: Departure of channel salinity from the mean, scaled by the salinity range (S*).

The salinity signal of water in the breach is distinct from that recorded in the channel (see figure 5-3c) because of differences in phasing, as well as mixing that takes place within the salt pond. The tidal asymmetries in the breach salinity preclude the use of a lagged correlation to determine the bulk phasing of salt concentration relative to velocity, however, individual phase lags are shown in Figure 5-5b. Flood tide salinities that enter the breach are very similar to those recorded in the channel, and the salinity peak occurs within a few minutes of the flood-to-ebb transition in the breach (Figure 5-5b). In contrast, the salinity of the pond effluent

recorded on the ebb-tide, shows the effects of mixing within the pond, and reaches a plateau of medium-salinity by the time the ebb is half over. At the end of the ebb tide, the salinity does not show an ebb-to-flood transition that is coincident with that of the velocity. This is attributed to the storage of late-ebb pond effluent in the broad mudflats that line the north (near-pond) border of Coyote Creek. The early flood tide washes the pond effluent stored on the mudflats up-estuary (and into the pond), and after this water mass has passed by, it is replaced by fresher channel water and the salinity drops sharply.

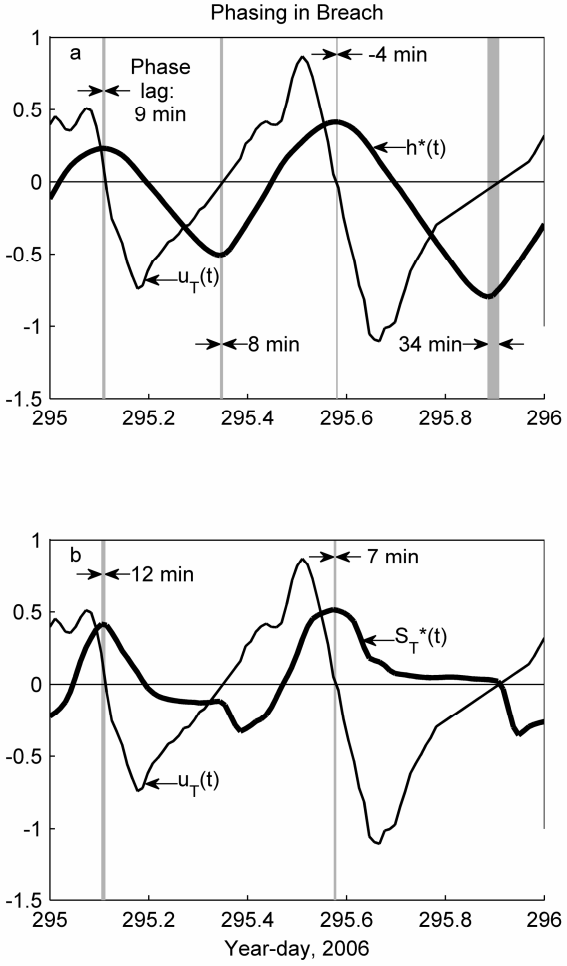

Figure 5-5: Phasing in Breach
(a): Thin black line: Depth-averaged along-breach velocity (m s^{-1}). Thick black line: Departure of water depth from the mean, scaled by the tidal range (h*). Solid gray band: Phase lag between time of slack water and time of maxima/minima of water depth. (b): Thin black line: Depth-averaged along-breach velocity (m s^{-1}). Thick black line: Departure of breach salinity from the mean, scaled by the salinity range (S*).

Mixing in the ponds

To explore the mixing that takes place within the ponds, we consider the time-series of breach salinity shown in Figure 5-5b. As noted in the previous section, by midway through the ebb-

tide, the salinity of the pond effluent reaches an intermediate value and decreases only minimally from this value for the rest of the ebb (e.g. year-day 295.2 and 295.7 in Figure 5-5b). Our data suggest that this transition to well-mixed pond effluent is dependent on pond bathymetry. The Island Ponds were constructed by excavating levee material from the inner perimeter of each pond, resulting in a "borrow ditch" surrounding an interior island. The borrow ditch is subtidal, approximately 25 meters wide and 1.65 meters deeper than the interior island plane, which itself is intertidal (shown schematically in Figure 5-6). The sustained medium salinity that we observe exiting the pond in the later portion of the ebb tide starts when water depth is approximately equal to the elevation of the pond's inner island (Figure 5-7). Salinities recorded at the 3 northern-most stations are identical, representing uniform conditions in the borrow ditch and the breach. This signal is distinct from that of the channel thalweg station, where the salinity drops evenly as the ebb decelerates, mirroring the flood tide. This suggests that mixing within the pond varies over the tidal cycle: trapped late-flood waters exit the pond early in the ebb with only slight dilution, effectively unwinding the flood tide, until only the borrow ditch remains full. At this point, the pond effluent is well-mixed, and the salinity exiting the pond departs significantly from salinities measured in the channel.

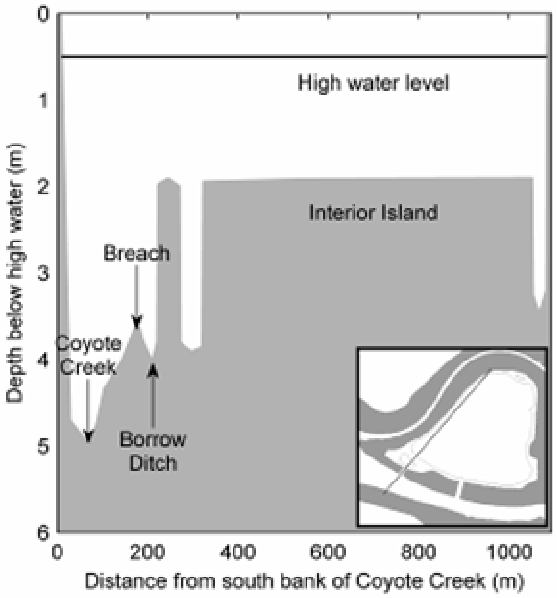

Figure 5-6: Schematic of Channel and Trap Cross-section
Elevation view of Coyote Creek, breach, borrow-ditch, and Pond A21. Inset: cross-section location. Bathymetry was measured via boat-mounted ADCP for distances up to 200 m, and estimated thereafter.

Longitudinal dispersion

A bulk estimate of the longitudinal spreading of a constituent may be reached by assuming a steady, one-dimensional balance of advection by freshwater flow and all other mechanisms (Fischer et al. 1979):

(5-2) $$U_{fresh} S = K_{bulk} (\partial S / \partial x)$$

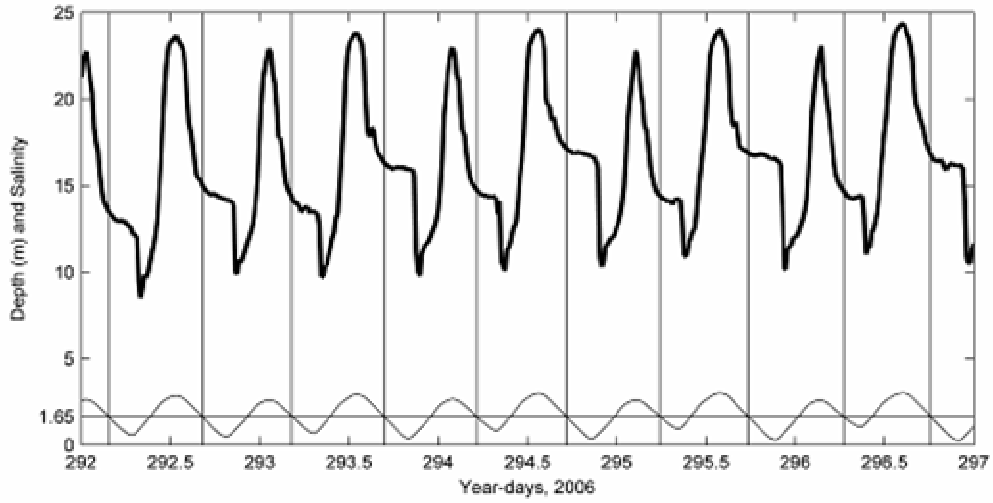

Figure 5-7: Transition to well-mixed pond-effluent: Depth and Salinity
Thin black line: depth (m), Thick black line: salinity, Vertical lines: onset of well-mixed pond outflow, Horizontal solid-line: depth coincident with onset of well-mixed conditions. It should be noted that the onset of well-mixed conditions is constant, in spite of the daily inequality and the neap-to-spring transition, both of which are evident in the salinity signal.

MacCready (1999) cautions that the assumption of steady-state is ill-advised when an estuary's response to changes in forcing is slow and significant, and we proceed in this case noting that the tidal channel is very shallow, and therefore more likely to have a rapid adjustment time. Additionally, this balance is applied to a long (2-month) dataset during which river input was low. Salinity measured as part of the present study was used as the tracer in order to estimate K_{bulk}, the aggregate dispersion coefficient. S was calculated as the average salinity over each tidal period, and the longitudinal concentration gradient was determined by the maximum change in salinity per tidal cycle divided by the tidal excursion. The freshwater velocity (U_{fresh}) was estimated using measurements of daily flow rates of freshwater (United States Geological Survey 2006), and the cross sectional area of Coyote Creek (Figure 5-8a). This velocity was interpolated onto the approximately twice-daily tidal timescale used for the concentration (Figure 5-8b) and concentration gradient (Figure 5-8c). The result of this calculation is an average bulk dispersion coefficient on the order of 500 $m^2 s^{-1}$, that varies over the range of 300 to 800 $m^2 s^{-1}$ with daily and spring-neap tidal forcing, shown in Figure 5-8d. The order of magnitude of this value will be referenced in the discussion as we compare dispersion due to tidal trapping to total dispersion in Coyote Creek.

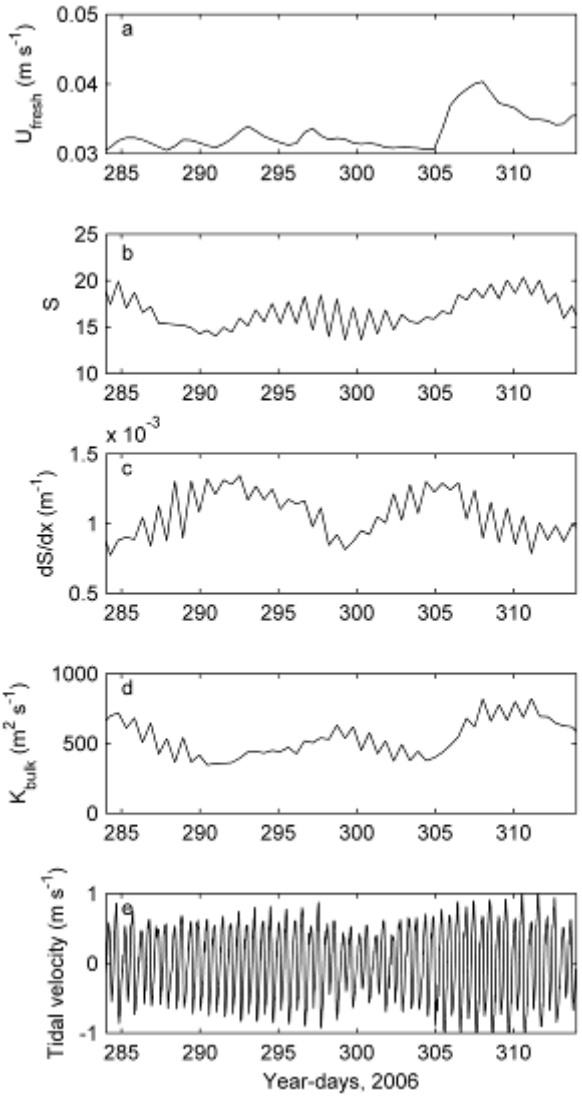

Figure 5-8: Bulk Dispersion in Coyote Creek
(a) Fresh water velocity: Qf/A, (m s^{-1}). (b) Average salinity per tidal cycle. (c) Longitudinal salinity gradient (m^{-1}), (d) Bulk dispersion coefficient (m^2 s^{-1}), (e) Depth-averaged along-channel velocity (m s^{-1}), showing spring-neap variability.

5.3 Application of traditional frameworks

5.3.1 Diffusive exchange

Classical analytical treatment of phase lags and the resulting tidal trapping flux has been directed toward quantifying an effective mass diffusivity coefficient to predict the effect of tidal trapping on longitudinal spreading. Okubo (1973) constructed a model of tidal trapping which predicts longitudinal dispersion in waterways with shoreline irregularities in both a uniform and oscillating flow. In this seminal work, Okubo described these irregularities as temporary traps of water and associated scalars. Okubo represented the exchange between the shoreline irregularity and the main channel as a source/sink term in a 1-dimensional advection-diffusion

equation, which is solved for the variance of the contaminant concentration as a function of time. The model, intended to elucidate the apparent diffusivity due to trapping, treats the source/sink term as diffusive, with a functional dependence on the concentration gradient between channel and trap. Okubo's definition of the source/sink term depends on the dimensions of the entrapment region relative to the channel, as well as a timescale which is described as a "characteristic residence time of a contaminant in the trap" (Okubo 1973). Okubo's analysis showed convincingly that this model is well-suited to environments such as the Mersey estuary, and the data Bowden (1965) collected there on observed longitudinal dispersion corroborates that model.

5.3.2 Limitations of the traditional framework

Okubo's (1973) effective diffusivity, as reproduced by Fischer et al. (1979), is shown in equation 5-3.

$$K_{effective,Okubo} = \frac{K}{1+r} + \frac{r u_C^{\,2}}{2k(1+r)^2(1+r+\varphi/k)} \tag{5-3}$$

K is the diffusivity due to turbulence and processes other than tidal trapping; r is the ratio of trap volume to channel volume; k^{-1} is the residence time of the trap; φ is $2\pi/T$, where T is the tidal period; and u_C is the amplitude of the velocity in the channel.

Using this model to estimate a diffusion coefficient for a trap that exchanges advectively with the main channel, rather than diffusively, is problematic. For example, we consider a trap that fills and drains with the tides. Any such trap has a characteristic residence time of T, the tidal period, making k equal to T^{-1}. The strength of the tidal advection which drives the exchange between the channel and trap is not represented in this formulation. The phase lag between the trap's response to the tidal pressure gradient and that of the channel, which has been observed to cause longitudinal scalar spreading as trapped water rejoins channel flow (Blanton & Andrade 2001), is also not captured by equation 5-3.

5.4 Development of new frameworks

5.4.1 Advective exchange

We propose that there are types of shoreline irregularities for which a distinct model of tidal trapping is better suited than Okubo's (1973) diffusive formulation. In particular, the source/sink term representing the exchange with the trap may be driven by tidal advection rather than diffusion for many environments. The breached Island Ponds in the present study represent such a case, as does the branching channel example discussed by Fischer et al. (1979). Later in this section, we discuss a dimensionless parameter useful for determining the suitability of an advective versus diffusive model.

Following Aris (1956; also Okubo 1973; Young et al. 1982; Wolanski & Ridd 1986), we calculate the time-dependent moments of the distribution of a pulse of solute released in a tidal channel subject to tidal trapping. The effective longitudinal dispersion coefficient in the channel is defined as one half of the derivative of the variance of the distribution with respect

to time, and the variance is the ratio of the second to the zeroth moment (equation 5-4). We evaluate the effective dispersion over one tidal cycle, from t = 0 to T, where $\Delta M_2 = M_2\big|_{t=T} - M_2\big|_{t=0}$ and $\overline{M_0}$ is the tidally-averaged zeroth moment in the channel.

$$(5\text{-}4) \qquad K_{effective} = \frac{1}{2}\frac{\partial \sigma^2}{\partial t} = \frac{1}{2}\frac{\partial}{\partial t}\left(\frac{M_2}{M_0}\right) = \frac{1}{2T}\left(\frac{\Delta M_2}{\overline{M_0}}\right)$$

Equation 5-5 represents the 1-dimensional (along-channel) transport equation for solute concentration in a tidal channel. This formulation is distinct from prior analyses (Okubo 1973; Wolanski & Ridd 1986; Ridd et al. 1990) in that the source/sink term employed in our transport equation is advective rather than diffusive. The terms in 5-5 are, from left to right, unsteadiness, advection of the solute concentration by an oscillating flow, turbulent diffusion, and an advective source and sink of solute into and out of the trap.

$$(5\text{-}5) \qquad \frac{\partial S}{\partial t} + u_C \sin(\varphi t - \alpha)\frac{\partial S}{\partial x} - K\frac{\partial^2 S}{\partial x^2} = -u_T \frac{H_T}{A_C}\sin(\varphi t) S_T(t)$$

S is the concentration of solute in the channel, u_C is the amplitude of the velocity in the channel, which is assumed to be driven by a single tidal constituent; K is the diffusivity for mass due to all other processes, e.g. shear, turbulence; u_T is the amplitude of the velocity into and out of the trap; $S_T(t)$ is the solute concentration entering and exiting the trap; H_T is the depth of flow into and out of the trap; A_C is the cross-sectional area in the channel; φ the inverse of the tidal period ($2\pi/T$), and α is the phase lag between flow into the trap and flow in the channel, in radians. On the time interval of 0 to T, the flood occurs from 0 to $T/2$, and the ebb occurs from $T/2$ to T. Equation 5-5 assumes that the main channel width is constant, and that the time-dependence of depth in the channel and depth in the breach is the same. This assumption is reasonable given the rapid adjustment to a lateral barotropic pressure gradient, which prevents any such gradient from persisting. No assumption is required about the phasing of the tidal pressure gradient relative to the other terms. The only phase lag specified in this 1-dimensional transport equation is that between the main channel flow velocity and the velocity entering and leaving the trap, α. The solute concentration entering and leaving the trap, $S_T(t)$, is not constrained in this transport equation. We first derive a general expression for the effective dispersion due to tidal trapping, and then examine particular formulations of $S_T(t)$.

The moments of any distribution may be calculated using equation 5-6.

$$(5\text{-}6) \qquad M_j = \int_{-\infty}^{\infty} x^j S(x,t)\,dx$$

We differentiate both sides with respect to time, resulting in:

$$(5\text{-}7) \qquad \frac{\partial M_j}{\partial t} = \int_{-\infty}^{\infty} x^j \frac{\partial S(x,t)}{\partial t}\,dx$$

Substituting 5-5 into this expression allows us to solve for the moments of the solute distribution without solving for *S(x,t)* explicitly (Aris 1956). While this integral must be evaluated over all of space, the source/sink term in 5-5 exists only within the width of the breach, which we define to be of length *2l* (centered on *x=0* for mathematical simplicity). We therefore evaluate each moment as follows:

$$\text{(5-8)} \quad \frac{\partial M_j}{\partial t} = -\int_{-\infty}^{\infty} x^j u_C \sin(\varphi t - \alpha)\frac{\partial S}{\partial x}dx + \int_{-\infty}^{\infty} x^j K \frac{\partial^2 S}{\partial t^2}dx - \int_{-l}^{l} x^j u_T \frac{H_T}{A_C}\sin(\varphi t) S_T(t)dx$$

Integrating equation 5-8 with *j*=0 with respect to time yields two terms in the zeroth moment, or the total mass of solute: the original amount released into the channel ($M_0(0)$), and a fluctuating component resulting from exchange with the trap (equation 5-9). Q_T is defined as the flow rate into and out of the trap: $u_T H_T 2l$.

$$\text{(5-9)} \quad M_0(t) = -\frac{Q_T}{A_C}\int_0^t \sin(\varphi t) S_T(t)dt + M_0(0)$$

Similar integrations with *j=1* and *j*=2, result in the first and second moments, (equations 5-10 and 5-11), which represent the location of the centroid of the solute cloud and the variance of the solute distribution, respectively.

$$\text{(5-10)} \quad M_1(t) = u_C \int_0^t \sin(\varphi t - \alpha) M_0(t)dt$$

$$\text{(5-11)} \quad \Delta M_2 = 2u_C \int_0^T \sin(\varphi t - \alpha) M_1(t)dt + 2K\int_0^T M_0(t)dt - \frac{l^2}{3}\frac{Q_T}{A_C}\int_0^T \sin(\varphi t) S_T(t)dt$$

Equation 5-11 is the discrete form of the second moment, evaluated over one tidal cycle, which allows us to simplify the effective dispersion coefficient by canceling sinusoidal terms. These terms represent periodic variations within the tidal cycle, while our interest is in the steady growth of the solute cloud over timescales greater than *T*. With this approach, the total effective diffusion coefficient can be calculated by substituting the equations for the concentration moments: 5-9, 5-10, and 5-11, into equation 5-4. The general effective dispersion coefficient is therefore:

$$\text{(5-12)} \quad K_{effective} = -\frac{{u_C}^2 Q_T}{\overline{M_0} T A_C}\int_0^T \sin(\varphi t - \alpha)\left(\int_0^t \sin(\varphi t - \alpha)\left(\int_0^t \sin(\varphi t) S_T(t)dt\right)dt\right)dt - \frac{l^2 Q_T}{6\overline{M_0} T A_C}\int_0^T \sin(\varphi t) S_T(t)dt + K$$

The last term on the right hand side represents the longitudinal dispersion due to other processes (turbulence, shear) as shown in the diffusive transport term in equation 5-5. The remaining terms in equation 5-12 represent the dispersion due to interaction with the trap, so

that $K_{effective} = K_{trap} + K$. The first term in this expression is analogous to the triple integration of Taylor (1953) for shear dispersion, but here the integration is in time, rather than in space. The contribution of this term depends on the phase shift of the flow into the trap relative to the tidal flows in the channel. The second term is non-zero only when the concentration in the source/sink term is different during the "sink" (flood) phase and the "source" (ebb) phase, which may result from mixing in the trap. Equation 5-12 simplifies considerably when we assume a form of $S_T(t)$, which we do in the following section.

5.4.2 Specific cases

We now consider the effective dispersion for four specific functional forms of $S_T(t)$. We start with two simplistic cases that are helpful for understanding the general equation, and then we examine two slightly more complex cases that approximate a branching channel system and a salt pond system. The structure of the velocities and concentrations in the channel and trap are shown in panels (a) through (d) of Figure 5-9.

Both the velocity of flow and solute concentration entering the trap are functions of conditions in the channel (S and u_C), however, in the present analysis, we are treating them as independent. We are able to approximate flows and concentrations in the channel reasonably well, and this approach allows us to solve for the dispersion resulting from exchange with the trap analytically. The soundness of this approach is confirmed by a comparison of the theoretical solutions derived below and a numerical solution to equation 5-12 using field measurements, presented subsequently.

The following scaling groups are helpful in presenting the results of the analytics: a ratio of the volume of flow into and out of the trap to the flow volume in the channel $r \sim Q_T T / A_C u_C T$; the tidal excursion $L \sim u_C / \varphi \sim u_C T$, and the ratio of the mass of solute entering and exiting the trap to that in the channel $\varepsilon \sim Q_T S_T L / A_C u_C \overline{M_0} \sim Q_T S_T / A_C u_C S$, where we assume that $\overline{M_0}$ may be scaled as SL.

S_T in quadrature with u_T

Although it may not occur naturally, the simplest form of the solute concentration entering and exiting the trap is the case in which S_T is a sinusoid in perfect quadrature with the flow into and out of the trap (u_T), shown in Figure 5-9a. While this phasing is realistic – the trap's solute concentration should depend on the velocity entering and exiting the trap – the concentration signal itself for this special case is lacking dependence on the channel concentration, which should be the source of solute during floods. Nevertheless, this case is illustrative of the main functional relationships that prove consistent for all four specific cases. Evaluating equation 5-12 assuming that $S_T(t) = -S_T \cos(\varphi t)$ yields:

(5-13a) $$\overline{M_0} = \frac{rLS_T}{4} + M_0(0)$$

(5-13b) $$K_{effective} = \frac{1}{2T}\frac{\Delta M_2}{\overline{M_0}} = \varepsilon L u_C \frac{\cos\alpha \sin\alpha}{8} + K$$

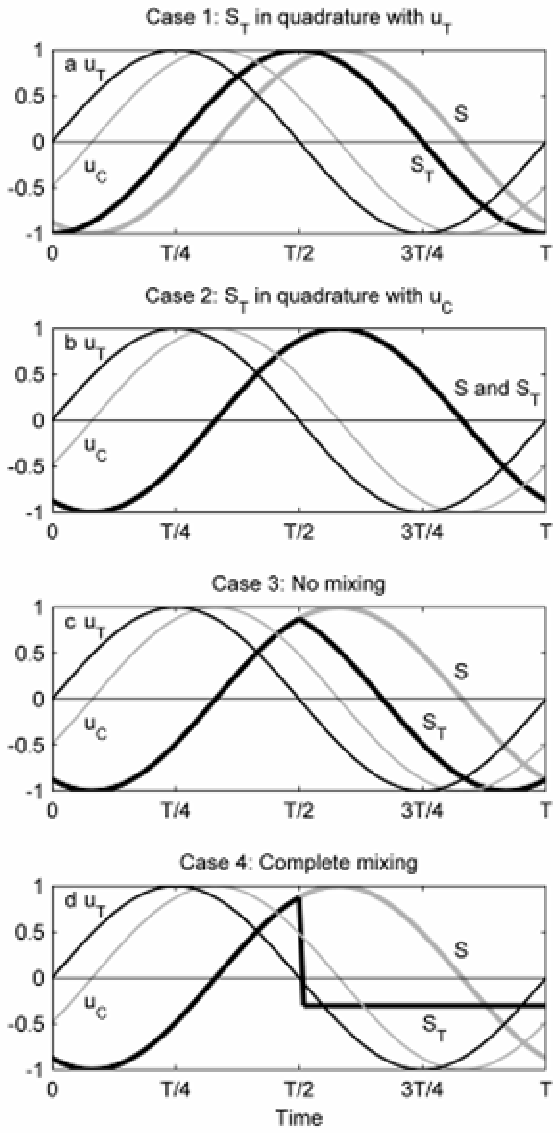

Figure 5-9: Theoretical velocities and concentrations for new tidal trapping framework
Concentrations are departures from the average, normalized from -1 to 1. For all panels: Thick black line: trap concentration, Thin black line: trap velocity (m s^{-1}), Thick gray line: channel concentration, Thin gray line: channel velocity (m s^{-1}). (a) Case 1: ST in quadrature with uT (b) Case 2: ST in quadrature with uC (c) Case 3: No mixing (d) Case 4: Complete mixing.

This result provides us with the simplest, clearest, mathematical statement regarding the effective diffusion coefficient due to tidal trapping, which is the first term on the right hand side of equation 5-13b. Here we see that the trapping coefficient is proportional to a velocity scale times a length scale (u_C , the tidal velocity scale in the channel, and L, the tidal excursion), as well as the mass trapped relative to the mass in the channel (ε). Finally, the diffusion

coefficient due to trapping is proportional to the product of the sine and cosine of the phase lag of the flow into the trap relative to the flow in the channel. At small phase lags, the cosine term is approximately 1, and the trap-induced diffusion coefficient increases linearly with phase lag. When the phase lag is precisely zero, the effect of trapping on dispersion vanishes, and $K_{effective}$ is simply equal to K.

S_T in quadrature with u_C

Rather than aligning the concentration in the trap with the exchange flow, in this case it is aligned it in time with flows in the channel. This achieves the opposite trade-off compared with the first special case: the phasing is now dependent on transport in the channel, but the channel can now serve as the source of solute while the trap is filling (Figure 5-9b). This is likely to be a correct formulation during the flood (sink) phase, but it will not be correct during the ebb; more realistic cases for that phase will be considered in the next two sections. Evaluating equation 5-12 assuming that the trap concentration is in quadrature with the channel velocity, or $S_T(t) = -S_T\cos(\varphi t-\alpha)$, yields:

(5-14a) $$\overline{M_0} = rLS_T\left(\frac{2\pi\sin\alpha+\cos\alpha\sin\alpha}{8\pi}\right)+M_0(0)$$

(5-14b) $$K_{effective} = \varepsilon L u_C\left(\frac{7}{16}\cos^2\alpha\sin\alpha+\frac{3}{16}\sin^3\alpha-\frac{1}{12}\frac{l^2}{L^2}\sin\alpha\right)+K$$

Just as in equation 5-13b, the trapping diffusion coefficient is proportional to the tidal velocity scale times the tidal excursion as well as the fractional mass retained in the trap. In this case, the dependence on the phase lag (α) is modified, and consists of three terms, but is essentially unchanged at small phase lags.

The no-mixing case: An idealized branching channel

As a step toward a more physically realistic scenario, we examine the case of an idealized branching channel. The phasing of the trap solute concentration is 90 degrees different from that of the trap velocity (they are in quadrature), but the concentration mimics that of the channel on the flood, and then reverses itself on the ebb, effectively unwinding the inflow in a mirror image, symmetric about slack water in the trap, as shown in Figure 5-9c. The symmetric structure of the salinity signal results when we invoke the assumption that no mixing occurs within the trap. The trap concentration is therefore described by: $S_T(t) = -S_T\cos(\varphi t-\alpha)$ for $0 < t < T/2$, and $S_T(t) = S_T\cos(\varphi(T/2-t)-\alpha)$ for $T/2 < t < T$.

(5-15a) $$\overline{M_0} = rLS_T\left(\frac{\cos\alpha-\pi\sin\alpha}{8\pi}\right)+M_0(0)$$

(5-15b) $$K_{effective} = \varepsilon L u_C\sin\alpha\cos\alpha\left(\frac{3\cos\alpha+32\sin\alpha}{24\pi}\right)+K$$

Once again, $\varepsilon L u_c$ is the fundamental dimensional group and the diffusion coefficient increases with phase lag, α.

The complete-mixing case: An idealized salt pond

Exchange with an idealized salt pond is represented by a trap solute concentration in quadrature with the trap velocity. It mimics the channel concentration on the flood, as with the no-mixing case. The ebb for the complete-mixing case, however, is simply the average of the inflow concentration. In other words, the inflow is assumed to be uniformly mixed within the trap as the flood progresses, such that the outflow on the ebb is a constant, average value (Figure 5-9d). For this case, the solute concentration in the trap is: $S_T(t) = -S_T\cos(\varphi t-\alpha)$ for $0 < t < T/2$, and $S_T(t) = \dfrac{1}{T/2}\int_0^{T/2} -S_T\cos(\varphi t-\alpha)dt$ for $T/2 < t < T$.

(5-16a) $$\overline{M_0} = rLS_T\left(\frac{\pi\cos\alpha + \pi^2\sin\alpha + 16\sin\alpha}{16\pi^2}\right) + M_0(0)$$

(5-16b) $$K_{effective} = \varepsilon L u_C \frac{1}{3\pi}\cos^3\alpha + \varepsilon L u_C\left(\begin{array}{l}\left(\dfrac{21\pi^2-128}{96\pi^2}\right)\cos^2\alpha\sin\alpha - \dfrac{5}{6\pi}\cos\alpha\sin^2\alpha \\ +\left(\dfrac{9\pi^2-64}{96\pi^2}\right)\sin^3\alpha + \left(\dfrac{\pi^2-8}{24\pi^2}\right)\dfrac{l^2}{L^2}\sin\alpha\end{array}\right) + K$$

Note that a ratio of squared length scales appears in this case, in the last $\sin(\alpha)$ term on the right hand side, where l/L represents half of the width of the breach or channel opening, scaled by the tidal excursion.

In this final example, the dependence on the phase lag is more complicated and a new dispersion process is represented. In the five terms that constitute the tidal trapping diffusion coefficient, four of them are proportional to $\sin(\alpha)$ and approach zero for small phase shifts; they can be interpreted similarly to the examples in the previous three sections. The first term, however, which depends only on $\cos(\alpha)$ is actually due to the diffusive effects of the mixing in the trap itself, which we have assumed here to be complete within the half tidal cycle that the trap is inundated.

5.5 Discussion of frameworks

5.5.1 Advection versus diffusion

The difference between the present framework and Okubo's (1973) is the structure of the source/sink term that represents exchange with the trap: this study uses a tidally driven advective flux that accounts for phase lags, while Okubo used a diffusive flux. A comparison of the important scaling groups in the present and traditional frameworks yields a Peclet number that may be useful in elucidating the distinct mechanisms represented in the

derivations, as well as the appropriateness of applying one formulation versus the other. The representative timescale for exchange is k^{-1} in Okubo's (1973) diffusive framework, and T in the present advective one, as discussed in section 5.3. The ratio of these timescales produces equation 5-17:

$$\frac{T^{-1}}{k} \sim \frac{Q_T V_{Prism}^{-1}}{D_y A_{Trap}^{-1}} \sim \frac{u_T l H_T \left(A_{Trap}\eta_0\right)^{-1}}{D_y A_{Trap}^{-1}} \sim \frac{u_T l}{D_y}\frac{H_T}{\eta_0} \tag{5-17}$$

Exchange in the advective model (in the numerator of 5-17) is represented by the time required for the trap to fill or drain the volume of the tidal prism, expressed as the flowrate into and out of the trap (Q_T), divided by the tidal prism of the pond (V_{Prism}). Diffusive exchange (shown in the denominator) is defined by the timescale for horizontal transport across the trap (A_{Trap}) driven by lateral diffusion (D_y). Replacing the flowrate into the trap with a velocity times the area of a rectangular breach ($u_T l H_T$), and the tidal prism with the trap area times the tidal amplitude ($A_{Trap}\eta_0$), we can cancel the trap area from the ratio. A Peclet number is reached: $u_T l / D_y$, scaled by the ratio of the average depth in the trap (H_T) to the tidal amplitude (η_0), that can be used to discern the relative suitability of each framework for a particular environment. For large Peclet numbers, advection dominates and the framework presented here should be the appropriate one for estimating dispersion from trapping; for small values of the Peclet number, the traditional, diffusion-based formulation should be used.

5.5.2 Variability with phase shift

The dependence of the dispersion due to trapping on the phase lag between the breach velocity and the channel velocity, α, is worth exploring (Figure 5-10). For each case, the important scaling group in K_{trap}, $\varepsilon L u_C$, is multiplied by a sum of sines and cosines of α. For cases 1-3, where no mixing takes place within the trap, K_{trap} is 0 when the trap and channel velocities are precisely in phase (α=0). In these cases, when α=0, the water removed from the channel on the flood rejoins its original neighbors on the ebb, resulting in no change to the original distribution of concentration in the channel. Contrastingly, when there is no phase lag, the complete-mixing case still alters the concentration distribution in the channel. On the ebb, the pond outflow contains a constant concentration (the volume average of the inflow), and results in the mixing of water masses of different concentrations as they are joined in the channel.

We consider Case 1, the simplest scenario, to demonstrate the influence of increasing α. As the phase lag grows, the ebb tide joins together water masses with concentrations that are increasingly mismatched. For this scenario, when α equals T/8, the trap returns flow to the channel such that the scalar concentration of trap effluent and that of flow in the channel are as different as possible, producing maximum spreading of the scalar cloud. The opposite is true when α is equal to T/4, or when u_T and u_C are 90 degrees out of phase. In this case, flow is removed from the channel at one location in the symmetric scalar cloud as it advects up- and down-estuary with the tides, and it is returned to the channel in the same location of the opposite side of the scalar cloud, such that the trapped flow rejoins channel flow of the exact same scalar concentration. In this way, no spreading is induced from the phase lags.

By mathematical definition, K_{trap} for each case is periodic in α, passing through zero and going negative for various values of the phase lag between 0 and T; however, it is important to note that physically, it is impossible to shuffle these water masses in a way that reduces the extent of the scalar cloud, and therefore dispersion from trapping should never be negative. Additionally, there is a physical maximum to α; the difference in response time to the barotropic pressure gradient of the velocity in the channel and the velocity in the trap cannot exceed a few hours. The physically realistic region of the relationship between K_{trap} and α is limited to low values of α (such as the range shown in Figure 5-10).

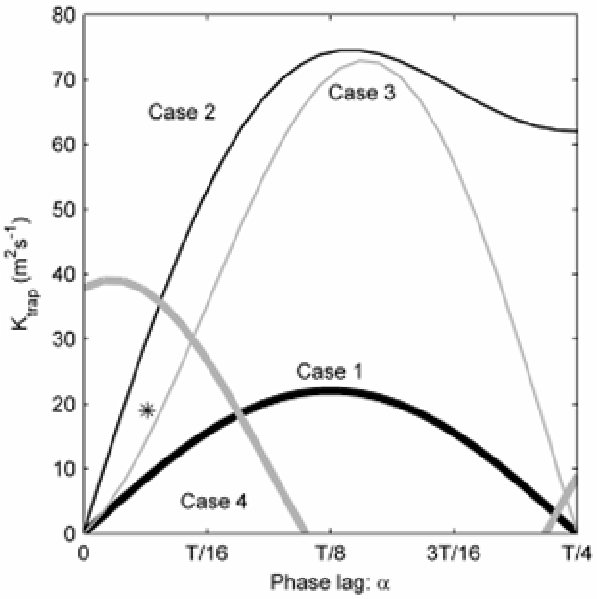

Figure 5-10: Theoretical dispersion coefficients as a function of phase lag
Thick black line: Case 1. Thin black line: Case 2. Thin gray line: Case 3. Thick gray line: Case 4. Asterisk: Data; numerical evaluation of the theory using measured salinities.

5.5.3 Comparison with field data

While the data collected in this study do not have fine enough temporal or spatial resolution to yield a complete decomposition of dispersive fluxes, it is possible to compare values of dispersion coefficients predicted from the new analytical framework to approximate, but still quantitative, values obtained through the field data. A summary of this comparison is presented in Table 5-1. Specifically, equation 5-12 is applied discretely to measurements of $S_T(t)$, the concentration of salt recorded at the pond entrance. The integrations are performed numerically by advancing through the data in time. To minimize the effects of higher order tidal harmonics, as only the M2 tide is accounted for in the present study, a repeating window of real data (of duration 12.4 hours) was used in this calculation (Figure 5-11). The window was selected such that the first point occurs at slack tide between ebb and flood, according to depth-averaged velocities measured at the breach entrance. Parameters representative of the field site are: amplitude of tidal velocities in the channel and into and out of the trap: 1 m s^{-1}, depth in the trap: 2 m; cross-sectional area of the channel: 200 m^2; breach width: 20 m; tidal

period: 12.4 hours; phase lag between trap and channel: 24 minutes. The initial concentration of solute in the channel, $M_0(0)$, is scaled as the average concentration of salinity in the channel, 15, times the tidal excursion. The discrete integration of equation 5-12 using measured values of $S_T(t)$ yields a coefficient for dispersion resulting from tidal trapping of 19 $m^2 s^{-1}$. This result represents the dispersion due to Coyote Creek's interaction with just one salt pond; accounting for all three Island Ponds would require increasing the values for the flowrate into and out of the ponds, the volume of the ponds, and the length of the combined breaches.

Table 5-1: Dispersion coefficients from data, existing, and new theoretical models

Source	K ($m^2 s^{-1}$)
Discrete integration of Equation 5-12	19
Case 1: S_T in quadrature with u_T	9
Case 2: S_T in quadrature with u_C	30
Case 3: No-mixing	15
Case 4: Complete-mixing	37
Okubo (1973)	3000
Aggregate K: $K_{bulk} = U_{fresh}S/(dS/dx)$	500

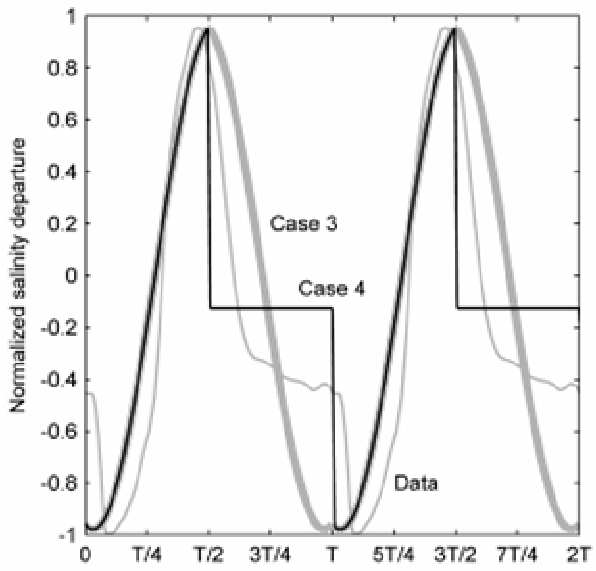

Figure 5-11: Data used in numerical evaluation of theoretical framework
Salinity is used as the solute, and the departure from the average, normalized by the range, is plotted.

Using these parameters and the new theoretical models for estimating dispersion from trapping in one salt pond produces values of 9, 30, 15, and 37 $m^2 s^{-1}$ for cases 1-4, respectively. The two cases representing no mixing and complete mixing within the trap envelop the estimate of dispersion from the data. The field measurements of $S_T(t)$ lie approximately between the theoretical formulations for $S_T(t)$ in the no-mixing and complete-mixing cases, shown in Figure

5-11. The relative structures of these real and contrived time-series support the assertion that a salt pond partly mixes the water it receives on the flood tide. As discussed previously, field data suggests that the pond effluent "unwinds", similar to case 3, until the depth in the pond reaches the surface of the interior island, at which point the remainder of the pond's discharge is well-mixed, as in case 4.

Since we propose that the salt pond environment is better approximated by an advectively driven form of trapping, it is useful to compare the values for K_{trap} thus obtained to Okubo's (1973) diffusive framework. The geometric parameter r is scaled as the trap volume ($A_{trap}\eta_0$) to the channel volume ($A_C L$). The timescale for exchange is T, making k equal to T^{-1}. Applying equation 5-3 produces a value of $K_{trap,Okubo}$ of more than 3000 $m^2 s^{-1}$. This unrealistic value, particularly in view of our estimated total diffusion of $\sim$500 $m^2 s^{-1}$, suggests that the diffusive model of exchange between the channel and the trap utilized by Okubo is not the appropriate framework for this environment. This conclusion was, of course, expected based on the strongly advective nature of exchange between the channel and the storage volume, or trap.

5.5.4 Other factors affecting longitudinal dispersion

It is important to note that tidal trapping can set up lateral processes that are not accounted for in either traditional or new frameworks for estimating dispersion. Specifically, in Coyote Creek, very strong, periodic lateral gradients of salinity have been observed, as described in section 2.3.2. The strongest gradients occur at the end of the ebb tide, where salinities recorded in the channel's thalweg are 2-6 ppt lower than those recorded in the pond effluent over a separation of approximately 100 meters. Surface salinity transects demonstrated that this is a frontal gradient, with a sharp change in salinity occurring over a distance of order 10 meters. A baroclinically-driven lateral circulation would be unsurprising, although depths late in the ebb (1-2 meters) made it impossible to resolve such a lateral flow with boat-mounted velocity measurements. If this lateral circulation exists, it would induce rapid cross-sectional mixing, which would diminish dispersion from shear, as discussed by Fischer et al. (1979), and as explored analytically by Smith (1976).

5.6 Summary and conclusions

Measurements of velocities and water properties in a tidal slough connected to former salt ponds in San Francisco Bay showed that tidal trapping is a locally important mechanism driving longitudinal dispersion and fluxes of salt. Observed phase lags between the tidal pressure gradient, velocities in the channel and pond, and salinity signals support the conceptual model of tidal trapping presented by Fischer et al. (1979). Specifically, velocities recorded in the thalweg of the channel lag the exchange flows through the breach by an average of 24 minutes. Maximum and minimum salinities recorded in the main channel occur before high- and low-slack tide, respectively, because of the relatively prompt response of the flow in the shallows to the change in tidal forcing. This serves to bring fresher waters to the channel perimeter around the flood-to-ebb transition (high-slack tide), and more saline waters around the ebb-to-flood transition (low-slack tide), which mix laterally before the flow in the main channel has changed direction. This process produces the observed phase lags between velocity and salinity in the

channel, with the result that those signals are out of quadrature. Additional salinity variation is created by mixing in the interior of the ponds prior to being discharged on the ebb tide.

High barotropic velocities (± 1 m s^{-1}) in the main channel and through the breach indicate that exchange between the channel and ponds is driven by tidal advection. Okubo's (1973) classical framework for dispersion from tidal trapping was derived based on diffusive exchange between the trap and channel, and if applied to this system, yields a dispersion coefficient from trapping that is greater than 3000 m^2 s^{-1}. Our measurements suggest that the total estuarine dispersion coefficient for this system fluctuates around an average value of 500 m^2 s^{-1}, reaching a maximum of 800 m^2 s^{-1}. These disparate estimates indicate that the classical treatment of dispersion from trapping is inappropriate for this advectively driven exchange.

To better assess dispersion from trapping for systems where exchange is forced by tidal advection, such as a branching channel system, as well as perimeter volumes that fill and drain with the tides, we rederived the expression for the dispersion coefficient replacing the diffusive flux between trap and channel with an advective one. The concentration moment method (following Aris 1956, and later Okubo 1973, Young et al. 1982, and Wolanski and Ridd 1986) was used to solve analytically for the variance of a scalar cloud in the channel due to exchange with a trap as a function of phase lag between flows in the channel and through the breach. This new framework, which is specified for four idealized scenarios, provides a dispersion coefficient from tidal trapping of 15-37 m^2 s^{-1} using physical parameters (the phase lag, the ratio of trap volume to channel volume, the tidal excursion, and the ratio of scalar mass in the trap to that in the channel) representative of the study site. Performing the analysis numerically on the observations yields a dispersion coefficient of 19 m^2 s^{-1}. These results indicate that a framework for dispersion from tidal trapping based on advective exchange is well-suited to the dynamics observed at our study site.

CHAPTER 6

Conclusions

The dynamics of flow and scalar transport through an estuary are dependent on its bathymetry, with irregular features causing departures from canonical estuarine physics. Perimeter habitats lining a tidal channel provide opportunities for exchange that modify scalar concentrations and gradients, as well as the momentum of the flow. Tidal exchange between an estuary and its perimeter combined with meteorological forcing define the residual fields of scalars and momentum, and thus the essential nature of the estuary. The research presented in this dissertation addresses the influence of a complex perimeter on concentrations of salt and sediment on tidal timescales, and on the long-term dispersion of scalars.

6.1 Effects of lateral exchange on stratification at tidal timescales

In-situ measurements of flow velocities and water properties were collected in a tidal slough that is flanked by intertidal mudflats and lined by breached former salt ponds. The observed pattern of stratification and mixing is in direct contrast with expected estuarine dynamics. Measurements show that while, typically, floods are well-mixed and ebbs are stratified, bathymetric irregularities such as channel-mudflat morphology can locally overwhelm the dynamics, resulting in a stratified flood and an unstably stratified or well-mixed ebb.

Observations along the axis of the channel indicate that the flood tides are stably stratified despite the destabilizing effects of tidal straining. Differential advection over the mudflats and channel laterally strain the longitudinal salinity gradient, concentrating the highest salinities in the channel center, with slower, fresher flow over the shallows. A lateral circulation is induced by the baroclinic pressure gradient which drives high-salinity water onto the mudflats and returns low-salinity, low-velocity flow into the channel at the water surface. This circulation is responsible for two mechanisms that create and maintain stable stratification on the flood tide. First, a source of buoyancy is directly provided to the channel surface by the return flow. Second, the velocity of the surface flow in the channel is retarded by the addition of low-momentum flow from the mudflats. The peak velocity is therefore located beneath the surface, and this pattern of shear strains the longitudinal salinity gradient such that stable stratification is produced above the velocity maximum. Measured velocity profiles indicate that the velocity

maximum is located at or below the middle of the water column. This stable stratification was consistently observed at instrument stations in the channel thalweg as well as near the channel-mudflat boundary.

On the ebb tide, the proximity to the channel-mudflat boundary controls the stratification. At the channel center, stable stratification intensifies as tidal straining advects fresh water down-estuary fastest at the surface; however, close to the channel-mudflat interface, unstable stratification on the order of 1 ppt m^{-1} was observed for the first 1.5-2 hours of each ebb, with weakened unstable stratification and well-mixed conditions thereafter. Exchange with the mudflat is again responsible for this departure from the expected ebb-tide stratification. In particular, measurements of velocity at two distances from the bed (0.5 m and 1.5 m) show that the flow nearer the bottom is bidirectional and confined to the channel, while the flow higher in the water column has a strong lateral component, directed away from the mudflat, early in the ebb tide. This lateral flow is representative of the draining of the mudflat and adjacent marsh into the channel surface. Differential advection causes the mudflats to freshen more slowly than the channel center, concentrating the highest salinities in the shallows. The combination of the lateral salinity gradient with the vertical shear in the lateral velocity creates and maintains unstable stratification during the early ebb at the channel-mudflat interface; simply stated, the mudflats are draining salty water into the channel at the surface, while the bottom layer freshens. Scaling the evolution of the potential energy anomaly using a balance of unsteadiness and longitudinal and lateral advection reproduces measured values and supports the conceptual model.

The duration of the instability is related to the strength of the flow off of the mudflats. The lateral velocity is highest early in the ebb when the storage (depth) on the mudflat is great. The momentum contained by this flow sustains strong lateral shear while turbulent stresses remain low at our instrument station; however, as the momentum diminishes and the mudflats lose volume of stored water, the mixing is elevated at the channel-mudflat boundary and turbulent stresses rise. Buoyancy and shear production are the inferred generators of turbulent kinetic energy during the late ebb. Well-mixed conditions are coincident with the rise in stresses. Late in the ebb, the potential energy anomaly depends on both horizontal advection components, as well as vertical mixing.

In summary, lateral exchange between a tidal channel and adjacent mudflats can overwhelm the typical pattern of stratification and mixing in the tidal channel. The physics represented by the classical view of straining are still applicable in the bathymetrically-controlled case, but they must be expanded to represent the cross-channel dimension in addition to the along-channel/vertical plane.

Future work will be focused on determining the parameters at which these dynamics may be observed. Geomorphic scales, including the depth and width of the mudflats and the slope between the mudflat and channel, are expected to be critical. In addition, the phasing of the barotropic pressure gradient relative to the velocity field (a standing or progressive wave) and its lateral variability, as well as the strength of the longitudinal salinity gradient, are also expected to play an important role. Finally, the implications of this exchange on residual fields of momentum and scalars will be investigated.

6.2 Bathymetric controls on tidal transport of suspended sediment

The intra-tidal variability of suspended sediment concentration was examined in the context of regular versus irregular local topography, as well as low versus high freshwater input. The objective was to determine the important transport mechanisms as represented by the sediment mass balance equation. Without information on grain size distributions, a simplistic, total-mass approach was employed. The validity of the commonly assumed balance between particle settling and turbulent resuspension was evaluated and found to be an inadequate representation of estuarine sediment transport in the presence of complex bathymetry and meteorological events.

During low freshwater inflow and in the channel center, concentrations of suspended sediment were slightly higher on flood tides than ebbs, despite the ebb-dominance of the flows. This is attributed to the settling lag, which is the length of time between the drop in velocity below the threshold for suspension and the deposition of the particle onto the bed. Assuming that velocities are damped with distance toward the head of the estuary, the settling lag allows particles to be advected up-estuary even after the flood velocity can no longer hold them in suspension, resulting in a tidal asymmetry and landward net transport of sediment. The importance of the settling lag requires unsteadiness to be accounted for in the sediment mass balance. In addition to unsteadiness, settling, and turbulent resuspension, longitudinal advection may be important at the channel center during dry weather. The rapid recovery of suspended sediment concentrations after slack tide one hour before any appreciable increase in turbulent stresses suggests that advection – and not local resuspension – is at work. Nevertheless, without additional information on particle size distributions, the possibility of resuspension of extremely fine sediment cannot be eliminated.

Settling lag exerts a greater influence with proximity to intertidal regions. Flood tides carry sediment into the shallows, where the subsequent ebb velocities are not adequate to resuspend it. The tidal asymmetry is much greater near the channel-mudflat boundary and near the intertidal island inside a breached former salt pond. In addition, these sharp geomorphic transitions result in lateral flows that require both horizontal advection terms to account for the relevant suspended sediment transport processes.

During wet weather, the tidal asymmetry is reversed, and there is seaward net transport of suspended sediment. This supports a conceptual model of sediment being supplied to the upper reaches of the system pulsatively (by rain events), and being redistributed on subsequent tides. Unsteadiness and horizontal advection, in addition to settling and resuspension, are important drivers of sediment transport during wet weather.

Future investigations will be directed toward more robust data collection in the vicinity of irregular topography, with grain size measurements as well as bed erodibility estimates using laboratory analyses of cores collected in the field. This additional information will be used to quantify the effects of horizontal advection and local resuspension from the bed.

6.3 The influence of the perimeter on subtidal estuarine dispersion

A theoretical analysis was employed to assess the long-term effects of tidally-driven exchange with the perimeter on the transport of scalars. The tidal trapping mechanism results in scalar dispersion from interaction with an irregular shoreline and associated bathymetry. The cases of a branching tidal channel and a tidal channel that exchanges with intertidal ponds through levee breaches were considered, and the scalar of interest was salt. A field study of the channel-intertidal pond case was used to validate the results of the analytical model. Tidal trapping produces dispersion in two ways. First, because of the higher frictional forcing in the shallowest regions relative to the main channel, phase lags are produced between the salinity field and the along-channel velocity. Maximum and minimum salinities in the main channel occur before high- and low-slack tide, respectively, because of the relatively prompt response of the flow in the shallows to the change in tidal forcing. This serves to bring fresher waters to the channel perimeter around the flood-to-ebb transition (high-slack tide), and more saline waters around the ebb-to-flood transition (low-slack tide), which mix laterally before the flow in the main channel has changed direction. This process results in the velocity and salinity signals in the channel being out of quadrature. Apart from the dispersion produced by phase differences, variations in mixing between the trap region (e.g. the intertidal pond) relative to the main channel results in the confluence of water masses with different salt concentrations, and causes additional dispersion independent of phasing.

High barotropic velocities (± 1 m s^{-1}) in the main channel and through the breach indicate that exchange between the channel and ponds is driven by tidal advection. The classical framework for dispersion from tidal trapping was derived based on diffusive exchange between the trap and channel, and if applied to this system, yields a dispersion coefficient from trapping that is greater than 3000 m^2 s^{-1}. Observations suggest that the total estuarine dispersion coefficient for this system fluctuates around an average value of 500 m^2 s^{-1}, reaching a maximum of 800 m^2 s^{-1}. These disparate estimates indicate that the classical treatment of dispersion from trapping is inappropriate for advectively driven exchange.

To better assess dispersion from trapping for systems where exchange is forced by tidal advection, such as a branching channel system, as well as perimeter volumes that fill and drain with the tides, the expression for the dispersion coefficient was rederived by replacing the diffusive flux between trap and channel with an advective one. The concentration moment method was used to solve analytically for the variance of a scalar cloud in the channel due to exchange with a trap as a function of phase lag between flows in the channel and through the breach. This new framework, which is specified for four idealized scenarios, provides a dispersion coefficient from tidal trapping of 15-37 m^2 s^{-1} using physical parameters (the phase lag, the ratio of trap volume to channel volume, the tidal excursion, and the ratio of scalar mass in the trap to that in the channel) representative of the study site. Performing the analysis numerically on the observations yields a dispersion coefficient of 19 m^2 s^{-1}. These results indicate that a framework for dispersion from tidal trapping based on advective exchange is well-suited to the observed dynamics.

At larger spatial scales, this framework is expected to be applicable cumulatively to trap regions located within the length of one tidal excursion from one another, producing an axially varying

estimate of the tidal trapping dispersion coefficient. Future work will be directed toward developing this framework for application to landscape scales, making it useful for engineering and management purposes.

Bibliography

Aris, R., 1956. On the Dispersion of a Solute in a Fluid Flowing through a Tube. *Proceedings of the Royal Society of London. Series A, Mathematical and Physical Sciences*, 235(1200), pp.67-77.

Banas, N. & Hickey, B., 2005. Mapping exchange and residence time in a model of Willapa Bay, Washington, a branching, macrotidal estuary. *J. Geophys. Res*, 110.

Banas, N. et al., 2004. Dynamics of Willapa Bay, Washington: A Highly Unsteady, Partially Mixed Estuary. *Journal of Physical Oceanography*, 34(11), pp.2413-2427.

Benilov, A., Kouznetsov, O. & Panin, G., 1974. On the analysis of wind wave-induced disturbances in the atmospheric turbulent surface layer. *Boundary-Layer Meteorology*, 6(1-2).

Blanton, J. & Andrade, F., 2001. Distortion of tidal currents and the lateral transfer of salt in a shallow coastal plain estuary (O estuário do Mira, Portugal). *Estuaries and Coasts*, 24(3), pp.467-480.

Bowden, K., 1965. Horizontal Mixing in the Sea Due to a Shearing Current. *Journal of Fluid Mechanics Digital Archive*, 21(01), pp.83-95.

Brand, A. et al., 2010. Wind-enhanced resuspension in the shallow waters of South San Francisco Bay: Mechanisms and potential implications for cohesive sediment transport. *Journal of Geophysical Research - Oceans*.

Bricker, J. & Monismith, S., 2007. Spectral Wave–Turbulence Decomposition. *Journal of Atmospheric and Oceanic Technology*, 24(8), p.1479.

Burchard, H. & Baumert, H., 1998. The Formation of Estuarine Turbidity Maxima Due to Density Effects in the Salt Wedge. A Hydrodynamic Process Study. *Journal of Physical Oceanography*, 28(2), pp.309-321.

Cacchione, D. & Drake, D., 1982. Measurements of Storm-Generated Bottom Stresses on the Continental Shelf. *Journal of Geophysical Research*, 87(C3), pp.1952-1960.

Callaway, J. et al., 2009. *Dynamics of sediment accumulation in Pond A21 at the Island Ponds*, Island Ponds, South San Francisco Bay: California State Coastal Conservancy.

Chatwin, P., 1976. Some remarks on the maintenance of the salinity distribution in estuaries. *Estuarine and Coastal Marine Science*, 4(5), pp.555-566.

Cheng, R.T. & Gartner, J.W., 1985. Harmonic analysis of tides and tidal currents in South San Francisco Bay, California. *Estuarine, Coastal and Shelf Science*, 21(1), pp.57-74.

City of San Jose, 2010. San Jose/Santa Clara Water Pollution Control Plant. *San Jose/Santa Clara Water Pollution Control Plant*.

Conaway, C. et al., 2004. Mercury deposition in a tidal marsh of south San Francisco Bay downstream of the historic New Almaden mining district, California. *Marine Chemistry*, 90(1-4), pp.175-184.

Conomos, T., 1979. San Francisco Bay: The Urbanized Estuary. Investigation into the natural history of San Francisco Bay and Delta with reference to the influence of man., San Francisco, California: Pacific Division of the American Association for the Advancement of Science.

Duke, R. et al., 2006. *Marsh Plant Associations of South San Francisco Bay: 2006 Comparative Study*, San Jose, California: City of San Jose. Available at: http://www.sanjoseca.gov/esd/marsh-studies.asp.

Dyer, K., 1986. Coastal and Estuarine Sediment Dynamics, John Wiley & Sons.

Dyer, K., 1973. *Estuaries: A Physical Introduction*, John Wiley & Sons.

Dyer, K. et al., 2000. An investigation into processes influencing the morphodynamics of an intertidal mudflat, the Dollard Estuary, The Netherlands: I. Hydrodynamics and suspended sediment. *Estuarine, Coastal and Shelf Science*, 50(5), pp.607-625.

El-Shaarawi, A. & Piegorsch, W., 2002. *Encyclopedia of environmetrics*, John Wiley and Sons.

Emery, W.J. & Thomson, R., 2001. *Data Analysis Methods in Physical Oceanography* 2nd ed., Elsevier Science.

Farmer, D. & Armi, L., 1999. Stratified flow over topography: the role of small-scale entrainment and mixing in flow establishment. *Proceedings of the Royal Society of London. Series A: Mathematical, Physical and Engineering Sciences*, 455(1989), pp.3221 -3258.

Fischer, H., 1972. Mass Transport Mechanisms in Partially Stratified Estuaries. *Journal of Fluid Mechanics*, 53(04), pp.671-687.

Fischer, H., 1976. Mixing and Dispersion in Estuaries. *Annual Reviews in Fluid Mechanics*, 8(1), pp.107-133.

Fischer, H. et al., 1979. *Mixing in Inland and Coastal Waters*, Academic Press.

Flegal, A. et al., 2005. A Review of Factors Influencing Measurements of Decadal Variations in Metal Contamination in San Francisco Bay, California. *Ecotoxicology*, 14(6), pp.645-660.

Folger, D., 1972. *Estuarine Sediments of The United States*, United States Geological Survey. Available at: http://pubs.er.usgs.gov/djvu/PP/pp_742.djvu.

Fortunato, A.B. & Oliveira, A., 2005. Influence of Intertidal Flats on Tidal Asymmetry. *Journal of Coastal Research*, 21(5), pp.1062-1067.

Fram, J., 2005. Exchange at the estuary-ocean interface: Fluxes through the Golden Gate Channel. Ph.D. University of California, Berkeley.

Fugate, D. & Friedrichs, C., 2003. Controls on suspended aggregate size in partially mixed estuaries. *Estuarine, Coastal and Shelf Science*, 58(2), pp.389-404.

Fugate, D. & Friedrichs, C., 2002. Determining concentration and fall velocity of estuarine particle populations using ADV, OBS and LISST. *Continental Shelf Research*, 22(11-13), pp.1867-1886.

Geyer, W., 1993. The importance of suppression of turbulence by stratification on the estuarine turbidity maximum. *Estuaries*, 16(1), pp.113-125.

Geyer, W. & Cannon, G., 1982. Sill Processes Related to Deep Water Renewal in a Fjord. *Journal of Geophysical Research*, 87(C10), pp.7985–7996.

Geyer, W., Chant, R. & Houghton, R., 2008. Tidal and spring-neap variations in horizontal dispersion in a partially mixed estuary. *Journal of Geophysical Research*, 113(c7), p.C07023.

Geyer, W. & Signell, R., 1992. A reassessment of the role of tidal dispersion in estuaries and bays. *Estuaries*, 15(2), pp.97-108.

Geyer, W., Trowbridge, J. & Bowen, M., 2000. The Dynamics of a Partially Mixed Estuary. *Journal of Physical Oceanography*, 30(8), pp.2035-2048.

Gibbs, R., 1985. Estuarine Flocs: Their Size, Settling Velocity and Density. *Journal of Geophysical Research*, 90(C2), pp.3249-3251.

Grossinger, R. et al., 2006. Coyote Creek Watershed Historical Ecology Study: Historical Condition, Landscape Change, and Restoration Potential in the Eastern Santa Clara Valley, California., Oakland, CA: San Francisco Estuary Institute.

Hansen & Rattray, 1965. Gravitational circulation in straits and estuaries. *Journal of Marine Research*, 23(2), pp.104-122.

HT Harvey & Associates, 2008. *Marsh Plant Associations of South San Francisco Bay: 2008 Comparative Study*, San Jose, California: City of San Jose. Available at: http://www.sanjoseca.gov/esd/marsh-studies.asp.

Hughes, F. & Rattray, M., 1980. Salt flux and mixing in the Columbia River Estuary. *Estuarine and Coastal Marine Science*, 10(5), pp.479-493.

Jassby, A. et al., 1995. Isohaline Position as a Habitat Indicator for Estuarine Populations. *Ecological Applications*, 5(1), pp.272-289.

Jay, D.A. & Musiak, J.D., 1994. Particle trapping in estuarine tidal flows. *Journal of Geophysical Research*, 99(C10), pp.20,445-20,461.

Kranck, K. & Milligan, T., 1992. Characteristics of Suspended Particles at an 11-Hour Anchor Station in San Francisco Bay, California. *Journal of Geophysical Research*, 97(C7), pp.11,373-11,382.

Krone, R., 1979. Sedimentation in the San Francisco Bay system. In *San Francisco Bay: The Urbanized Estuary*. San Francisco, California: Pacific Division of the American Association for the Advancement of Science c/o California Academy of Sciences, pp. 85-96.

Lacy, J., Schoellhamer, D. & Burau, J., 1996. Suspended-solids flux at a shallow-water site in South San Francisco Bay, California. In *Proceedings of the North American Water and Environment Congress*. North American Water and Environment Congress. Anaheim, California: American Society of Civil Engineers.

Lacy, J. et al., 2003. Interaction of lateral baroclinic forcing and turbulence in an estuary. *Journal of Geophysical Research - Oceans*, 108(C3).

Lerczak, J. & Geyer, W., 2004. Modeling the Lateral Circulation in Straight, Stratified Estuaries. *Journal of Physical Oceanography*, 34(6), pp.1410-1428.

Lerczak, J., Geyer, W. & Chant, R., 2006. Mechanisms Driving the Time-Dependent Salt Flux in a Partially Stratified Estuary. *Journal of Physical Oceanography*, 36(12), pp.2296-2311.

Li, M., Trowbridge, J. & Geyer, W., 2008. Asymmetric Tidal Mixing due to the Horizontal Density Gradient. *Journal of Physical Oceanography*, 38(2), p.418.

Lumborg, U. & Pejrup, M., 2005. Modelling of cohesive sediment transport in a tidal lagoon—an annual budget. *Marine Geology*, 218(1-4), pp.1-16.

MacCready, P., 1999. Estuarine Adjustment to Changes in River Flow and Tidal Mixing. *Journal of Physical Oceanography*, 29(4), pp.708-726.

MacCready, P. & Geyer, W., 2010. Advances in Estuarine Physics. *Annual Review of Marine Science*, 2(1), pp.35-58.

MacVean, L. & Stacey, M., 2010. Estuarine Dispersion from Tidal Trapping: A New Analytical Framework. *Estuaries and Coasts*. Available at: http://dx.doi.org/10.1007/s12237-010-9298-x.

McKee, L., Ganju, N. & Schoellhamer, D., 2006. Estimates of suspended sediment entering San Francisco Bay from the Sacramento and San Joaquin Delta, San Francisco Bay, California. *Journal of Hydrology*, 323, pp.335-352.

McKee, L. & Lewicki, M., 2009. Watershed specific and regional scale suspended sediment loads for Bay Area small tributaries, Oakland, CA: San Francisco Estuary Institute.

Mickett, J., Gregg, M. & Seim, H., 2004. Direct measurements of diapycnal mixing in a fjord reach—Puget Sound's Main Basin. *Estuarine, Coastal and Shelf Science*, 59(4), pp.539-558.

Nakagawa, H. & Nezu, I., 1993. *Turbulence in Open Channel Flows* 1st ed., Taylor & Francis.

NOAA, National Climatic Data Center, 2008. *Climatological Data Annual Summary - Calfornia - 2008*, California: NOAA.

NOAA, National Climatic Data Center, 2006. *Local Climatological Data - San Francisco International Airport*, Latitude: 37 ° 37'N, Longitude: -122° 23'W: NOAA.

NOAA, Tides and Currents, 2006. NOAA Coyote Creek 9414575 Tides. Available at: http://tidesandcurrents.noaa.gov/noaatidepredictions/NOAATidesFacade.jsp?Stationid=9414575.

Nunes, R. & Simpson, J., 1985. Axial convergence in a well-mixed estuary. *Estuarine, Coastal and Shelf Science*, 20(5), pp.637-649.

Okubo, A., 1973. Effect of shoreline irregularities on streamwise dispersion in estuaries and other embayments. *Netherlands Journal of Sea Research*, 6(1-2), pp.213-224.

Pejrup, M. & Mikkelsen, O., 2010. Factors controlling the field settling velocity of cohesive sediment in estuaries. *Estuarine, Coastal and Shelf Science*, 87(2), pp.177-185.

Pritchard, D., 2005. Suspended sediment transport along an idealised tidal embayment: settling lag, residual transport and the interpretation of tidal signals. *Ocean Dynamics*, 55(2), pp.124-136.

Pritchard, D., 1952. Estuarine Hydrography. *Advances in Geophysics*, 1, pp.243-280.

Ralston, D. & Stacey, M., 2005. Longitudinal dispersion and lateral circulation in the intertidal zone. *Journal of Geophysical Research - Oceans*, 110(C7).

Ralston, D. & Stacey, M., 2006. Shear and turbulence production across subtidal channels. *Journal of Marine Research*, 64(1), pp.147-171.

Ralston, D. & Stacey, M., 2005. Stratification and turbulence in subtidal channels through intertidal mudflats. *Journal of Geophysical Research - Oceans*, 110(C8).

Ralston, D. & Stacey, M., 2007. Tidal and meteorological forcing of sediment transport in tributary mudflat channels. *Continental Shelf Research*, 27(10-11), pp.1510-1527.

Ridd, P., Wolanski, E. & Mazda, Y., 1990. Longitudinal diffusion in mangrove-fringed tidal creeks. *Estuarine, Coastal and Shelf Science*, 31(5), pp.541-554.

Roussinova, V., Balachandar, R. & Biswas, N., 2009. Reynolds Stress Anisotropy in Open-Channel Flow. *Journal of Hydraulic Engineering*, 135(10), p.812.

Sanford, L.P., 1994. Wave-Forced Resuspension of Upper Chesapeake Bay Muds. *Estuaries*, 17(1), p.148.

Santa Clara Valley Urban Runoff Pollution Prevention Program, Coyote Watershed. *Coyote Watershed*. Available at: http://www.scvurppp-w2k.com/ws_coyote.shtml.

Santa Clara Valley Water District et al., 2010. *Island Ponds Mitigation Monitoring and Reporting: Year 4 - 2009*, Available at: http://www.southbayrestoration.org/monitoring/Island%20ponds%20mitigation%20monitoring%20report_Year%204_SCWD.pdf.

Schijf, J. & Schonfeld, J., 1953. Theoretical considerations on the motion of salt and fresh water. In *Proceedings of the Minnesota International Hydraulic Convention*. Minneapolis, Minnesota: IAHR, pp. 321-333.

Schoellhamer, D., 1996. Factors affecting suspended-solids concentrations in South San Francisco Bay, California. *Journal of Geophysical Research*. Available at: http://www.agu.org/pubs/crossref/1996/96JC00747.shtml.

Schuttelaars, H. & De Swart, H., 1997. An Idealized Long-Term Morphodynamic Model of a Tidal Embayment. *Eur. J. Mech., B/Fluids*, 15, pp.55-80.

Scully, M. & Friedrichs, C., 2007. The Importance of Tidal and Lateral Asymmetries in Stratification to Residual Circulation in Partially Mixed Estuaries. *Journal of Physical Oceanography*, 37(6), pp.1496-1511.

Simpson, J. et al., 1990. Tidal Straining, Density Currents, and Stirring in the Control of Estuarine Stratification. *Estuaries*, 13(2), pp.125-132.

Smith, R., 1976. Longitudinal Dispersion of a Buoyant Contaminant in a Shallow Channel. *Journal of Fluid Mechanics Digital Archive*, 78(04), pp.677-688.

Soulsby, R., 1981. Measurements of the Reynolds stress components close to a marine sand bank. *Marine Geology*, 42, pp.35-47.

Stacey, M., 2009. The Implications of Tidal Processes for the Subtidal Estuarine Circulation. Available at: http://www.sgmeet.com/cerf2009/.

Stacey, M., Burau, J. & Monismith, S., 2001. Creation of residual flows in a partially stratified estuary. *Journal of Geophysical Research - Oceans*, 106(C8), pp.17013-17037.

Stacey, M., Monismith, S. & Burau, J., 1999a. Measurements of Reynolds stress profiles in unstratified tidal flow. *Journal of Geophysical Research - Oceans*, 104(C5), pp.10933-10949.

Stacey, M., Monismith, S. & Burau, J., 1999b. Observations of turbulence in a partially stratified estuary. *Journal of Physical Oceanography*, 29(8), pp.1950-1970.

van Straaten, L. & Kuenen, P., 1958. Tidal action as a cause of clay accumulation. *Journal of Sedimentary Petrology*, 28(4), pp.406-413.

Talke, S., Deswart, H. & Schuttelaars, H., 2009. Feedback between residual circulations and sediment distribution in highly turbid estuaries: An analytical model. *Continental Shelf Research*, 29(1), pp.119-135.

Taylor, G., 1953. Dispersion of Soluble Matter in Solvent Flowing Slowly through a Tube. *Proceedings of the Royal Society of London. Series A, Mathematical and Physical Sciences*, 219(1137), pp.186-203.

Tennekes, H. & Lumley, J.L., 1972. *A First Course in Turbulence*, The MIT Press.

Turrell, W., Brown, J. & Simpson, J., 1996. Salt intrusion and secondary flow in a shallow, well-mixed estuary. *Estuarine, Coastal and Shelf Science*, 42(2), pp.153-169.

U.S. Fish & Wildlife Service et al., 2006. South Bay Salt Pond Restoration Project. *South Bay Salt Pond Restoration Project*. Available at: http://www.southbayrestoration.org/Project_Description.html.

United States Geological Survey, 2006. USGS Surface-Water Daily Data for the Nation. Available at: http://waterdata.usgs.gov/nwis/dv/?referred_module=sw.

US EPA, 1999. *Total Suspended Solids (TSS): EPA Method 160.2*, Region 9: US EPA. Available at: http://www.epa.gov/region9/qa/pdfs/160_2.pdf.

Valle-Levinson, A. & Atkinson, L.P., 1999. Spatial Gradients in the Flow over an Estuarine Channel. *Estuaries*, 22(2), pp.179-193.

Van Keuren, N., 2008. Discharge to Artesian Slough from SJWWTP.

Wahl, T., 2000. Analyzing ADV Data using WinADV. In *2000 Joint Conference on Water Resources Engineering and Water Resources Planning & Management*. Joint Conference on Water Resources Engineering and Water Resources Planning & Management. Minneapolis, Minnesota.

Wiberg, P., Drake, D. & Cacchione, D., 1994. Sediment resuspension and bed armoring during high bottom stress events on the northern California inner continental shelf: measurements and predictions. *Continental Shelf Research*, 14(10-11), pp.1191-1219.

Wolanski, E. & Ridd, P., 1986. Tidal mixing and trapping in mangrove swamps. *Estuarine, Coastal and Shelf Science*, 23(6), pp.759-771.

Young, W., Rhines, P. & Garrett, J., 1982. Shear-flow dispersion, internal waves, and horizontal mixing in the ocean. *Journal of Physical Oceanography*, 12(6), pp.515-527.